



HAL
open science

Doped Ag-In-Zn-S and Ag-In-Ga-Zn-S QDs: synthesis and potential as dual-modality probes for magnetic resonance and fluorescence imaging of cells

Perizat Galiyeva

► To cite this version:

Perizat Galiyeva. Doped Ag-In-Zn-S and Ag-In-Ga-Zn-S QDs: synthesis and potential as dual-modality probes for magnetic resonance and fluorescence imaging of cells. Chemical and Process Engineering. Université de Lorraine, 2021. English. NNT: 2021LORR0118 . tel-03368106

HAL Id: tel-03368106

<https://hal.univ-lorraine.fr/tel-03368106v1>

Submitted on 18 Oct 2022

HAL is a multi-disciplinary open access archive for the deposit and dissemination of scientific research documents, whether they are published or not. The documents may come from teaching and research institutions in France or abroad, or from public or private research centers.

L'archive ouverte pluridisciplinaire **HAL**, est destinée au dépôt et à la diffusion de documents scientifiques de niveau recherche, publiés ou non, émanant des établissements d'enseignement et de recherche français ou étrangers, des laboratoires publics ou privés.



AVERTISSEMENT

Ce document est le fruit d'un long travail approuvé par le jury de soutenance et mis à disposition de l'ensemble de la communauté universitaire élargie.

Il est soumis à la propriété intellectuelle de l'auteur. Ceci implique une obligation de citation et de référencement lors de l'utilisation de ce document.

D'autre part, toute contrefaçon, plagiat, reproduction illicite encourt une poursuite pénale.

Contact : ddoc-theses-contact@univ-lorraine.fr

LIENS

Code de la Propriété Intellectuelle. articles L 122. 4

Code de la Propriété Intellectuelle. articles L 335.2- L 335.10

http://www.cfcopies.com/V2/leg/leg_droi.php

<http://www.culture.gouv.fr/culture/infos-pratiques/droits/protection.htm>



**UNIVERSITÉ
DE LORRAINE**



Thèse

Présentée et soutenue publiquement pour l'obtention du titre de

DOCTEUR DE L'UNIVERSITE DE LORRAINE

Mention : Génie des Procédés, des Produits et des Molécules

par **Perizat GALIYEVA**

Sous la direction de Raphaël SCHNEIDER

Doped Ag-In-Zn-S and Ag-In-Ga-Zn-S QDs: synthesis and potential as dual-modality probes for magnetic resonance and fluorescence imaging of cells

12 juillet 2021

Membres du jury :

Directeurs de Thèse :	M. Raphaël SCHNEIDER	Professeur, Université de Lorraine, Nancy
Président du jury :	Mme. Lavinia BALAN	Directeur de Recherche CNRS, CEMHTI, Orléans
Rapporteurs :	Dr. Thomas PONS	Chargé de recherche, INSERM, ESPCI, Sorbonne Université, Paris
	Dr. Vincent MAUREL	Chercheur CEA, CEA-Grenoble/IRIG/SYMMES/CAMPE, Grenoble
Examineurs :	M. Jean-Louis CANTIN	Maître de conférences, Sorbonne Université, Paris
	Mme. Lina BEZDETNAYA-BOLOTINE	Professeur, Université de Lorraine, Nancy
	Mme. Lavinia BALAN	Directeur de Recherche CNRS, CEMHTI, Orléans
Invités :		
Co-directrice de la thèse	Mme. Halima ALEM-MARCHAND	Maître de conférences, Université de Lorraine, Nancy
Co-encadrant de la thèse	M. Bolat URALBEKOV	Professeur, Université Nationale Kazakhe al-Farabi, Almaty

Dedication

To my grandmother, Esqaiyrqyzy Zhibek,
who passed away during my doctoral studies
and who is an eternal inspiration to me

Acknowledgments

First of all, I would like to express my gratitude to my supervisor professor Raphaël Schneider, for his effective leadership, special interest in work and for the human and professional qualities that ensure a healthy working environment within the team. I sincerely thank you for your daily support, without which this work could not have seen the light and for your work, which prepared and guides us for further professional careers.

I would like to express my greatest appreciation to the co-directors of my dissertation Mrs. Halima Alem-Marchand, professor at the University of Lorraine and Mr. Bolat Uralbekov, professor at the al-Farabi Kazakh National University, for all the efforts you put in, for all the discussions and help during the writing of this manuscript.

I am also very grateful to the professor Henri-Pierre Lassale for agreeing to be the committee member and willingness to take part in the examining of this thesis. I thank you for advising, guiding and assisting in biological research in this thesis.

I would like to acknowledge the members of the Competence Center for Magnetism and Cryogenicity of the Jean Lamour Institute Crosby Chang, Stéphane Suire and Tom Ferte for their help and support in performing analyzes on the PPMS VSM instrument. I also thank Mr. Hervé Rinnert, professor at the Jean Lamour Institute (Nancy), for conducting time-resolved PL decay measurements and Mr. Jordane Jasniewski, associate professor at the University of Lorraine, for help and support in analyzes on a Zetasizer Nano ZS equipment. I also thank all other people, whom I did not know personally and who have provided their services for other analyzes and measurement of this work.

I would also like to express my gratitude to JSC “Center for International Programs” for the Bolashak International Scholarship, which financially supported my doctoral studies.

My warmest thanks go to all my fellows from the LRGP for their company and for the pleasant atmosphere throughout these years and, especially, Hatem Moussa, for his support from the day one of my arrival to France and thanks to whom I had a great time: Bilel, Rabeb, Maroua, Salima, Sarah and others.

Last but not the least, I express my respectful gratitude to my parents and family for the care, concern, especially for the inspiration and motivation. I would not want to go this path without your constant and sincere support.

I express my sincere gratitude to the reviewers Dr. Thomas PONS and Dr. Vincent MAUREL, and examiners M. Jean-Louis CANTIN, Mme. Lina BEZDETAYAYA-BOLOTINE, and Mme. Lavinia BALAN for their work in evaluating this dissertation, for valuable comments and suggestions.

Content

<i>Acknowledgments</i>	3
<i>Content</i>	5
<i>Abbreviations</i>	8
<i>General Introduction</i>	11
<i>Chapter 1. Literature review on quantum dots and doped quantum dots</i>	14
1.1. Introduction	14
1.2. Structure	16
1.2.1. Crystal structure of quantum dots	16
1.2.2. Crystal structure of semiconductor QDs of the I-III-VI ₂ group	17
1.2.3. Core/shell structure of quantum dots	20
1.2.4. Quantum confinement	22
1.2.5. Doping of quantum dots	23
1.3. Synthesis methods of quantum dots	25
1.3.1. Organic media synthesis.....	26
1.3.1.1. Hot-injection method.....	26
1.3.1.2. The non-injection method	30
1.3.1.3. Solvothermal method	31
1.3.1.4. Ag-In-Ga-S and Ag-Ga-Zn-S QDs synthesis in organic media.....	31
1.3.2. Aqueous media synthesis	34
1.3.2.2. Aqueous synthesis of Ag-In-Zn-S QDs	35
1.3.3. Aqueous phase transfer methods.....	37
1.4. Properties	39
1.4.1. Optical properties	39
1.4.2. Influence of synthesis parameters to the properties of QDs.....	44
1.4.2.1. Influence to the shape and size of QDs	44
1.4.2.2. Photoluminescence.....	45
1.4.2.3. Influence of the temperature	47
1.4.3. Magnetic properties.....	48
1.5. Applications	51
1.5.1. Optical applications.....	51
1.5.2. Biological applications.....	53

<i>Chapter 2. Organic phase synthesized AIZS and Mn-doped AIZS QDs.....</i>	<i>55</i>
2.1. Introduction	55
2.2. Experimental part	57
2.3. Morphology and structure characterization.....	62
2.4. Optical properties.....	73
2.5. Magnetic properties	81
2.6. Transfer of Mn:AIZS QDs in aqueous phase	83
2.7. Conclusion.....	88
<i>Chapter 3. Aqueous media syntheses of AIZS and Mn-, Gd-, or Fe-doped AIZS QDs</i>	<i>89</i>
3.1. Introduction	89
3.2. Experimental section.....	91
3.3. Morphology and structural characterization	95
3.4. Elemental analysis and EPR measurements	99
3.5. Optical properties.....	102
3.6. Magnetic properties	110
3.7. Preparation of AIZS QDs for biological applications.....	113
3.8. Colloidal and photostability	118
3.9. Cytotoxicity	119
3.10. Fluorescence imaging.....	122
3.11. Conclusion.....	124
<i>Chapter 4. Quinary Ag-In-Ga-Zn-S QDs synthesis</i>	<i>125</i>
4.1. Introduction	125
4.2. Experimental part	127
4.3. Morphology and structural characterizations.....	130
4.4. Optical properties.....	139
4.5. Aqueous phase transfer	146
4.6. Conclusion.....	148
<i>Chapter 5. Synthesis of AIGZS and Mn:AIGZS QDs</i>	<i>149</i>
5.1. Introduction	149
5.2. Experimental part	151
5.3. Morphology and structure characterization.....	153
5.4. Optical characteristics	160
5.5. Magnetic properties	165

5.6. Aqueous phase transfer	167
5.7. Mn:AIGZS QDs as MRI probes	169
5.8. Conclusion.....	171
<i>General conclusions and perspectives</i>	<i>172</i>
<i>References.....</i>	<i>175</i>
<i>List of figures.....</i>	<i>200</i>
<i>List of tables.....</i>	<i>208</i>
<i>Summary.....</i>	<i>209</i>
<i>Résumé.....</i>	<i>209</i>

Abbreviations

3-MPA	3-mercaptopropionic acid
AAS	Atomic Absorption Spectroscopy
AGS	AgGaS ₂
AIGS	Ag-In-Ga-S
AIGZS	Ag-In-Ga-Zn-S
AIS	Ag-In-S
AIZS	Ag-In-Zn-S
CAs	Contrast Agents
CB	Conduction Band
CIS	Cu-In-S
CIZS	Cu-In-Zn-S
CMC	Carboxymethylcellulose
CT	Computed Tomography
Cys	L-cysteine
D-A	Donor-Acceptor
DAPI	4', 6-diamidino-2-phenylindole
DDT	1-Dodecanethiol
DDTC	Diethyldithiocarbamate
DHLA	Dihydrolipoic acid
DI	Deionized
DLS	Dynamic Light Scattering
DMSA	<i>meso</i> -2, 3-Dimercaptosuccinic acid
DMSO	Dimethylsulfoxide
EDC	1-ethyl-3-(3- dimethylaminopropyl) carbodiimide
EDX	Energy-Dispersive X-ray
EPR	X-band Electron Paramagnetic Resonance
FA	Folic acid
FI	Fluorescence Imaging
FRET	Fluorescence Resonance Energy Transfer
FT-IR	Fourier-transform Infrared Spectroscopy
fwhm	full-width at half-maximum

GBCAs	Gadolinium-Based Contrast Agents
GSH	L-Glutathione reduced
GTMA	Glutathione tetramethylammonium
HA	Hyaluronic acid sodium salt
HDs	Hydrodynamic Diameters
HepG2	Hepatocyte Carcinoma
HR-TEM	High-Resolution Transmission Electron Microscope
ICP-OES	Inductively Coupled Plasma - Optical Emission Spectrometry
LED	Light-Emitting Diode
MAA	Mercaptoacetic acid
MNPs	Magnetic Nanoparticles
MRI	Magnetic Resonance Imaging
MTT	3-(4, 5-dimethylthiazol-2-yl)-2, 5-diphenyltetrazolium bromide
MUA	11-mercaptoundecanoic acid
NALC	N-Acetyl-L-cysteine
NCs	Nanocrystals
NHS	N-hydroxysuccinimide
NIR	Near Infra-Red
NPs	Nanoparticles
OA	Oleic acid
OAm	Oleylamine
ODE	Octadecene
OI	Optical Imaging
OTT	1-octanethiol
PAA	Polyacrylic acid
PEI	Polyethylenimine
PL	Photoluminescence
PLE	PL Excitation
PMAO	Poly(maleic anhydride-alt-1-octadecene)
QDs	Quantum Dots
QLED and QDLED	Quantum Dot Light-Emitting Diode
QY	Quantum Yield
SAED	Selected Area Electron Diffraction
TEM	Transmission Electron Microscope
TGA	Thermogravimetric Analysis

TGA	Thioglycolic acid
TLA	Thiolactic acid
TMAH	Tetramethylammonium hydroxide pentahydrate
TOP	Tri-n-octylphosphine
TOPO	Tri-n-octylphosphine oxide
UV	Ultra-Violet
UV-Vis	Ultraviolet-visible
VB	Valence Band
WLED	White Light-Emitting Diode
XPS	X-ray Photoelectron Spectroscopy
XRD	X-Ray Diffraction

General Introduction

‘There is Plenty of Room at the Bottom’. This was the title of lecture given by Richard Feynman in 1959, where he encouraged his fellow scientists and students to look down at the level of atoms and molecules. He was not talking about how it is going to be done, he was talking that this is possible to look down at the level of several atoms and molecules. This was the concept idea behind nanotechnology, the term, which first used by Norio Taniguchi over a decade after the Feynman's lecture. Even if the term began to be widely used among scientists during the last decades of the XXth century, the multi-colored stained-glass windows of medieval churches show that this technology used before the term was invented.

Looking back and studying the three industrial revolutions, each driven by manufacturing, electricity, and the Internet, one might think that downsizing could be one of the reasons for the fourth industrial revolution, which many believe we are already experiencing.

Nowadays, nanotechnology, which studies the synthesis methods, properties, characteristics and applications of nanoscale particles, finds its place in many areas of industry and life, from electronics and catalysis to agriculture, food processing and medicine.

Semiconductor particles ranging in size from 1 to 10 nm are called quantum dots (QDs). QDs are considered as intermediate materials between molecules and so-called bulk materials and their properties sharply differ from the bulk materials. For example, QDs due to their small size are subject to the so-called quantum confinement effect which results is a discretization of energy levels (increase in bandgap energy with decreasing size of QDs). Moreover, bulk materials are basically reflectors, whereas QDs absorb light. Once excited with an energy higher than the bandgap, they emit light at a wavelength longer than the absorbed light. Moreover, their physical, optical and magnetic properties are size, shape and composition dependent.

The multicomponent composition of modern fluorescent QDs (such as I-III-VI or I-II-III-VI QDs) allows changing the stoichiometry, which makes it possible to adjust the position of the photoluminescence (PL) peak in the visible and in the near-infrared zone. Doping QDs with additional ions is one of the ways to impart additional properties and/or change the existing ones. For example, to give magnetic properties to QDs, doping with paramagnetic ions such as manganese is used. In many cases, doping with Mn²⁺ ions was reflected in the PL emission spectrum with a peak at around 600 nm originating from the Mn²⁺ ⁴T₁ → ⁶A₁ transition. However, in some cases, the doping with Mn²⁺ ions can affect the PL emission peak position.

This shows that doping with Mn^{2+} not only imparts magnetic properties to the QDs, but also affects the fluorescence mechanism.

Due to the detection possibility by a conventional fluorescence microscope, QDs are potential materials for use in biology and/or medicine for observing processes at the single-molecular levels. If these particles also have magnetic properties, they can be used in diagnostics, therapy and separation. Separation is usually carried out using an external magnetic field.

The therapy is based on drug delivery, where magnetic nanomaterials have an advantage over other nanoparticles due to the possibility of drug movement using an external magnetic field and not only the targeting ligands.

Diagnosis, especially early diagnosis, is important in the fight against cancer. Fluorescence imaging (FI) and magnetic resonance imaging (MRI) are among the most effective diagnostic tools. Fluorescent QDs have already shown advantages over organic dyes as fluorescent probes due to their size-adjustable properties, modifiable surfaces, optical characteristics and so on. Magnetic QDs are of great interest in the use of MRI as contrast agents (CAs). Combining these properties in one probe would serve to improve the efficiency, sensitivity and accuracy of the diagnosis.

This work examines the synthesis and characterization of QDs for use in biomedicine, and especially as bimodal probes for fluorescence and magnetic resonance imaging.

The thesis is composed of five chapters.

Chapter 1, a literature review, covers general topics such as QDs structure, their synthesis methods, and their properties. In addition, widely studied application areas of QDs are also considered in the literature review.

In Chapter 2, the synthesis of highly fluorescent green- and orange-emitting Ag-In-Zn-S (AIZS) QDs and their doping with Mn^{2+} ions in organic media are described. The influence of Mn-doping on the QDs fluorescent and magnetic properties were discussed. Tuning the PL emission of Mn-doped AIZS QDs originating from a donor-acceptor (D-A) emission by changing the Mn-doping amount was demonstrated and the possible mechanism investigated. This chapter represents the article published in *Inorganic Chemistry Frontiers* in 2019 : P. Galiyeva, H. Alem, H. Rinnert, B. Lavinia, S. Blanchard, G. Medjahdi, B. Uralbekov and R. Schneider, *Inorg. Chem. Front.*, 2019, 6, 1422-1431. doi: 10.1039/C9QI00131J.

Chapter 3 describes the aqueous phase synthesis of Mn-, Gd-, Fe-doped AIZS QDs using L-Glutathione (GSH) as capping ligand. In this chapter, along with the morphology, elemental

analysis, optical and magnetic properties, the colloidal and photostabilities as well as *in vitro* cytotoxicities of these particles were investigated. Moreover, these particles were tested as the fluorescent probes in fluorescent imaging.

Chapter 4 describes the preparation of new quinary Ag-In-Ga-Zn-S (AIGZS) QDs using single precursors synthesized by varying the Ag/In/Ga/Zn molar ratio. The optical properties, structural characterizations as well as the aqueous phase transfer will be discussed.

Finally, in Chapter 5, the doping of AIGZS QDs with Mn^{2+} ions was considered. The optical and magnetic properties of Mn-doped AIGZS QDs along with the morphology and structural characteristics will be described. In addition, the aqueous phase transfer of these particles using two ligands was considered and the first trials for the use of these particles as MRI contrast agents will be presented.

The thesis was completed with a general conclusion, which shows the main results and prospects of the work done.

Chapter 1. Literature review on quantum dots and doped quantum dots

1.1. Introduction

Quantum dots are tiny semiconductor nanomaterials with sizes less than 10 nm. The QDs can be composed of several hundred to several thousands of atoms and their optical and electrical properties differ from the bulk materials. QDs were discovered in 1980s¹ during heat treatment of supersaturated solid solutions. Inspired by this study further investigations were conducted on QDs based on the explanations of their structure, properties, and the behaviour of these particles.

Currently, QDs are used in many industries where variable optical properties are convenient: in optoelectronics to expand the resolution of gadget screens, in medicine as various multimodal probes, in biomedicine for labeling, and also to convert solar energy to electrical energy, etc. All these properties of QDs differ from those of bulk materials with larger sizes.

Generally, the structure of QDs consists of a fluorescent inorganic core covered by an inorganic shell with similar dimensions as the core – shell may be missing depending on the properties of core material – and an organic ligand material is used to stabilize the QD and defines its polarity. Fig. 1.1 shows a schematic illustration of a QD. Every layer of the QDs plays a crucial role and can give additional properties to them. For example, while the main properties of the QDs are set by the core, the shell allows to reduce surface defects, which leads to improvement in optical properties. The surface ligand is usually bound to the shell and defines its polarity, as mentioned before, subsequently, it influences the stability and the solubility of QDs in various environments.

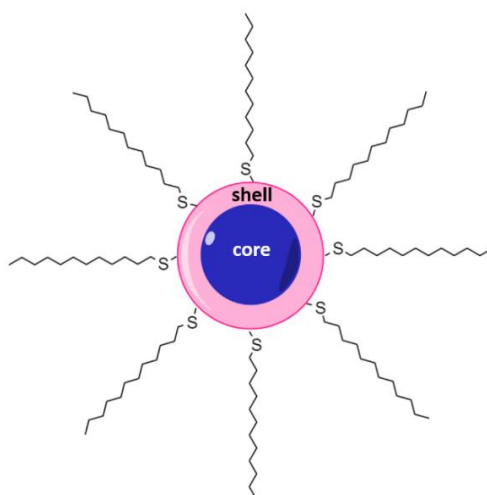


Figure 1.1. Schematic illustration of a QD stabilized with 1-Dodecanethiol (DDT)

The QDs can be fabricated in different way depending on the desired properties, the field of applications and according to the given structure: bottom-up or top-down approach; in a liquid phase or in a gas phase; in aqueous media or organic media; chemical synthesis or epitaxial growth, etc.

As a rule, each method has its own advantages and disadvantages. Usually the synthesis methods are selected according to the requirements for aimed nanoparticles (NPs). But, in general, it is desirable that the synthesis method be not expensive, easy to conduct, fast and reproducible.

Semiconductor nanoparticles have been of great interest in the past few decades. According to this, their applications are growing continuously. This leads to increasing demands for the quality and versatility of nanoparticles and, in addition, suitable adaptations of synthesis methods.

In the following parts of this work, more detailed information on the structure, properties, methods of preparation and applications with a focus on I-III-VI group elements-based nanoparticles, especially Ag-In-Zn-S QDs, since they are the subject of this research study.

1.2. Structure

The structure of QDs can be considered in two ways: first, the crystal structure of the unit cell; second, the structure of a dot. The crystal structure corresponds to the smallest structured part of QDs and follows the same pattern in all directions. The structure depends on several factors such as the composition of QDs, the synthesis methods, the starting materials, the synthesis conditions and the synthesis media. The following sections cover these topics in more detail.

1.2.1. Crystal structure of quantum dots

As it is well known, the core of QDs usually consists of an inorganic crystalline material (for carbon dots, the core is composed of carbon). While the binary QDs are II-VI, III-V compounds, Ti, In oxides and Pb, Hg iodides², while in ternary and quaternary QDs, the cationic part consists of metals of the first and third groups, and the anionic part – as in the binary ones – consists of chalcogenes. In many cases, ternary and quaternary QDs are considered as derivatives of binary QDs, since Group-I and Group-III metals replace the Group-II metal in binary QDs, increasing their range of properties and decreasing their toxicity, which is usually the highest weakness of Cd-based binary QDs. Further valence equivalent substitution of Group-III atoms with Group-II and Group-IV or Group-II and Group-III atoms leads to I₂-II-IV-VI₄ and I-II-III-VI quaternary quantum dots (Table 1.1).

Table 1.1. Evolution of QDs classes with examples

Class	Element groups	Examples
Binary	II-VI	CdS, CdSe, CdTe
Ternary	I-III-VI	Ag-In-S, Cu-In-S
Quaternary	I-II-IV-VI or I-II-III-VI	Ag-In-Zn-S or AgInS ₂ -ZnS

The crystal structure of solid substances is characterized by the Bravais lattices. Bravais lattices are spatial lattices that describe the arrangement of atoms in crystalline substances. Auguste Bravais, a French physicist, suggested that crystal lattices are constructed from points regularly placed in space – nodes (which are the locations of atoms), that can be obtained as the result of repeated parallel movements of that given point. If we consider a single crystal, where each repeated small part of this crystal is considered as a cell, atoms in these cells are arranged regularly and the positions of these atoms follow the certain pattern. There are 14 types of Bravais lattices, which, depending on the location of the elements in the unit cell, are divided into four groups called lattice types and, depending on the symmetry of the cells, are divided into seven groups called syngonies. There are four lattice types. In the primitive lattices, the nodes are located only in the corners of the cell. In the body-centered lattices, the nodes are located in the corners of the cell and a node in the cell center. In face-centered lattices, the nodes are located in the corners of the cell and the nodes in the center of every faces of the cell. In base-centered lattices, the nodes are located in the corners of the cell and the nodes in the centers of two opposite faces of a cell. Seven syngonies – cubic, tetragonal, orthorhombic, monoclinic, hexagonal, trigonal, and triclinic – differ from each other in the lengths of the cell sides and the angles between them.

1.2.2. Crystal structure of semiconductor QDs of the I-III-VI₂ group

Most of the binary QDs show zinc blende and wurtzite crystal structures, while ternary and quaternary QDs show zinc blende, wurtzite and chalcopyrite structures. Zinc blende structure refers to face-centered syngony of cubic crystal system. The name comes from the name of the zinc sulfide substance, which has two polymorphs: cubic zinc blende and hexagonal wurtzite. In both zinc blende and wurtzite crystal structures, every zinc atom coordinate to four sulfur atoms and every sulfur atom coordinates to four zinc atoms, but they differ in cell density. The hexagonal wurtzite QDs structure forms at higher temperature as the result of thermal rearrangement of the zinc blende structure. Chalcopyrite structure refers to a tetragonal symmetry system, its name comes from the name of copper iron sulfide (or chalcopyrite) mineral. In this tetragonal structure, every metal atom is surrounded by four sulfur atoms, so every sulfur atom is surrounded by four metal (two copper, two iron) atoms (Fig. 1.2).

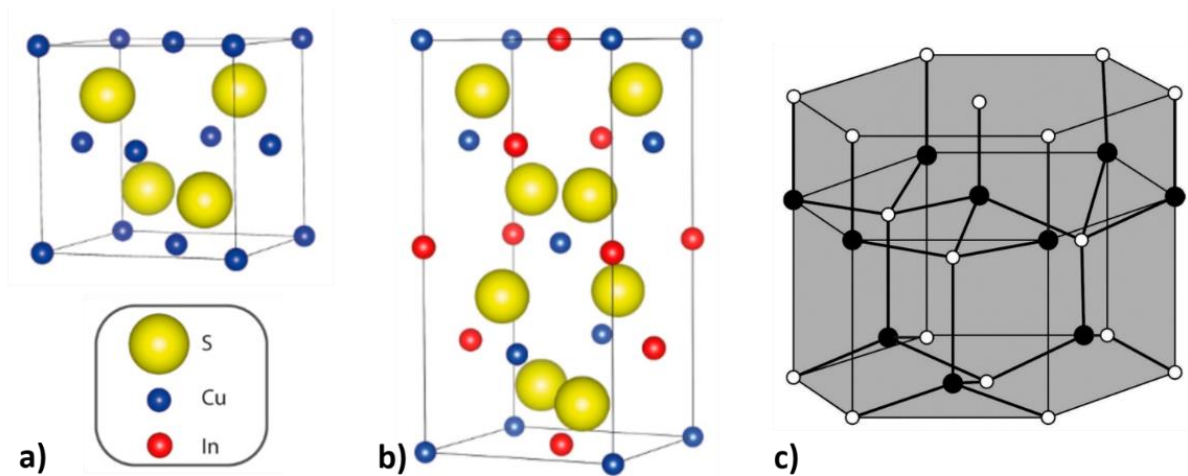


Figure 1.2. Schematic illustrations of a) binary zinc blende³; b) ternary chalcopyrite³ and c) binary wurtzite⁴ structures

It is possible to tune the crystal structure of QDs depending on the composition of these materials⁵ and/or depending on the synthesis temperature⁶.

The smaller the particle, the larger the surface-to-volume ratio. Surface-to-volume ratio is defined as the number of atoms (or what fraction of atoms in a particle) present on the surface of the particle. This is an important parameter of solids, which affects the reactivity and melting point of these particles, since the atoms on the surface are the ones to enter to the reaction first. Here is the visualisation of surface-to-volume ratio and graph shows how melting point of gold particles reduces with decreasing the particle diameter (Fig. 1.3)⁷.

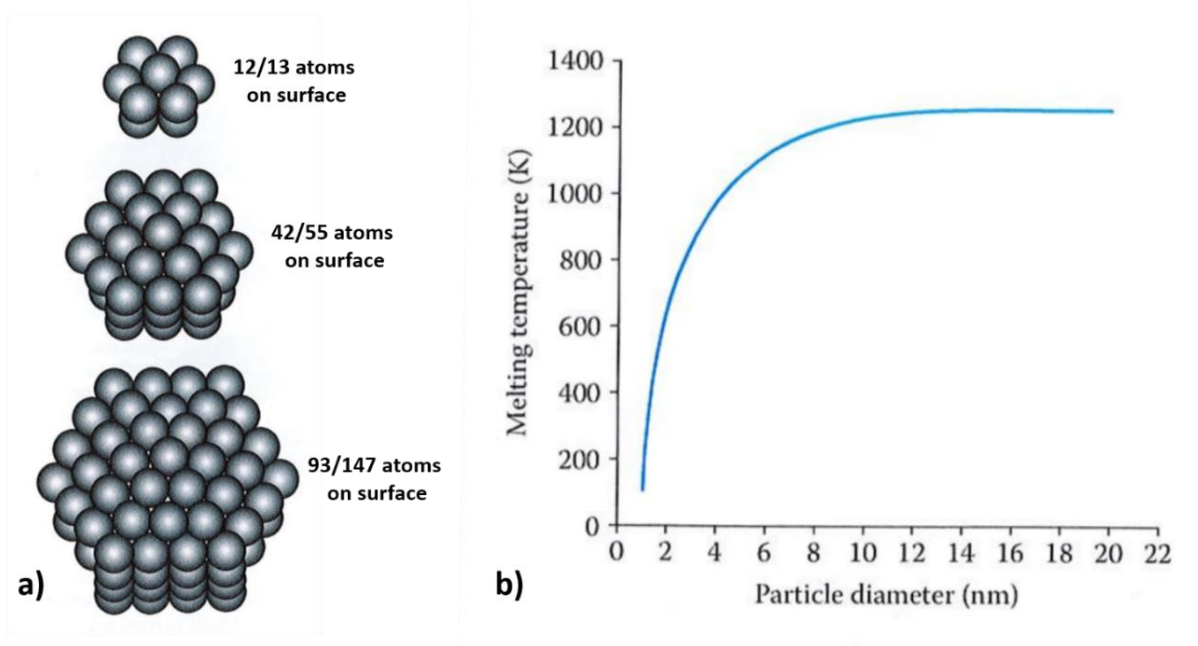


Figure 1.3. Schematic illustrations of: a) smaller the diameter the particle the more portion of atoms on the surface of particle; b) decreasing diameter decreases melting temperature of gold particles⁷

Very often researchers try to achieve as large surface-to-volume ratio as possible, since this reduces product consumption. For example, in catalytic reactions, a process takes place on the surface of a catalyst and thus the catalytic activity increases with the decrease of the nanoparticles size. Thus, there are two positive points: the rate of the catalytic reaction increases and the consumption of the catalyst decreases. In biological applications, surface-to-volume ratio of particles plays also an important role. According to their use, QDs can be of different sizes and structures. For biological studies, QDs are always covered with an organic ligand, the amount of which determines the QD size, and hence the surface-to-volume ratio.

Binary QDs have been a hot topic for the last decades thanks to their high fluorescence, size-dependent optical and electronic properties and facile synthesis methods. Following the development of binary QDs in terms of higher quantum yield, ternary and quaternary QDs have emerged due to their reduced toxicity. Among other advantages of multicomponent (ternary and quaternary) QDs, we can mention (i) the possibility of doping these nanocrystals with metal ions and (ii) their stability in both stoichiometric and in non-stoichiometric ratios⁶. Doping helps to give these particles additional properties such as magnetic properties when doping with

paramagnetic ions, which expands the horizon of their application. Stability at different ratios helps to adjust their properties, especially optical and electronic, to adapt them for the desired applications and enhance the interest in these particles.

1.2.3. Core/shell structure of quantum dots

The core/shell structure of nanoparticles appears when there is at least one substance in the core and another substance in the shell (or on the surface). The core/shell structure is used to improve the properties and characteristics of nanoparticles for specific purposes. The core and the shell are composed of different materials possessing similar properties, therefore core/shell materials own the properties of both core and shell materials. The core of nanoparticles is covered with a shell either to improve the core properties or to protect it. Namely, to increase its stability (thermal, reactive), its dispersibility, to impart additional properties (such as magnetic or photoluminescence), to modify the surface of QDs as passivating layer or to reduce the toxicity.

Core/shell nanoparticles are classified depending on core, shell and core/shell complex structures⁸. According to this classification, the core of these nanoparticles can be dense, porous or rattle, the shell can have continuous, dense, continuous and porous or particulate shell (patchy) nature. Another classification⁹ divides core/shell nanoparticles into four groups depending on their compositions: inorganic/inorganic, inorganic/organic, organic/inorganic and organic/organic. Their synthesis approaches and applications areas are also different.

Inorganic/inorganic core/shell nanoparticles include semiconductor nanoparticles also known as QDs. In the semiconductor nanoparticles either the core or the shell or both of them are made of semiconductor materials. Among these nanoparticles, a great interest falls on semiconductor/semiconductor core/shell particles. First, since both the core and the shell are semiconductors, the shell improves the optical properties of the core and increases its photostability. In other words, semiconductor nanocrystals have defects on their surface, which are traps for photogenerated electrons. This decreases the optical characteristics of QDs, especially the photoluminescence quantum yield (PL QY). To solve this problem, cores are covered with a shell material, which is also a semiconductor with a different band gap energy. Depending on the band gap energy differences and the position of the boundaries of the

conduction and valence bands, there are three different groups of core/shell nanoparticles¹⁰ (Fig. 1.4): 1. Type-I (higher band gap shell); 2. Quasi-type II reverse (lower band gap shell); 3. Type-II.

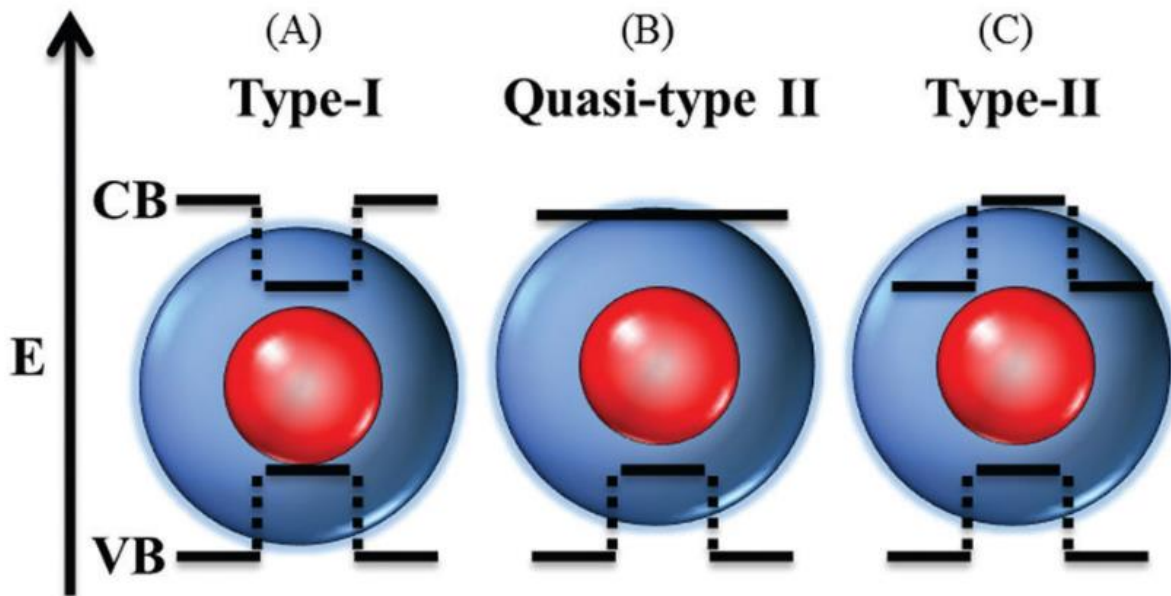


Figure 1.4. Type I and Type II band-edge alignments at the interface of core and shell semiconductors¹¹

In Type-I group semiconductors, the band gap of the shell material is wider than the band gap of the core material. Electrons and holes are trapped within the core region because both the conduction and the valence band edges of the core are located within the energy gap of the shell⁹.

In the Quasi-type II case, the shell material exhibits a narrower bandgap than the core material. Therefore, electrons and holes are partially localized/delocalized in the shell/core material.

In the case of Type-II core/shell semiconductors, there are two possible configurations, either the conduction and valence bands of the shell are higher than that of the core, or vice versa. Therefore, the energy gradient existing at the interfaces tends to spatially separate the electrons and the holes on the core and the shell materials¹².

1.2.4. Quantum confinement

When considering nanoscale particles, there is one concept that cannot be avoided. It is the quantum confinement effect. This effect is important because the size and the shape-dependent properties of QDs are the results of this effect. When the size of the bulk semiconductor materials is limited in three spatial directions, at a certain time the radius becomes equal to or less than the Bohr radius and, as a result, QDs are generated. In these QDs, the motion of electrons and holes randomly moving in different directions is limited and directed to certain energy levels, leading to a transition from continuous to discrete energy levels, which increases the band gap. Fig. 1.5 shows a schematic illustration of the relationship between particle sizes and bandgap energies.

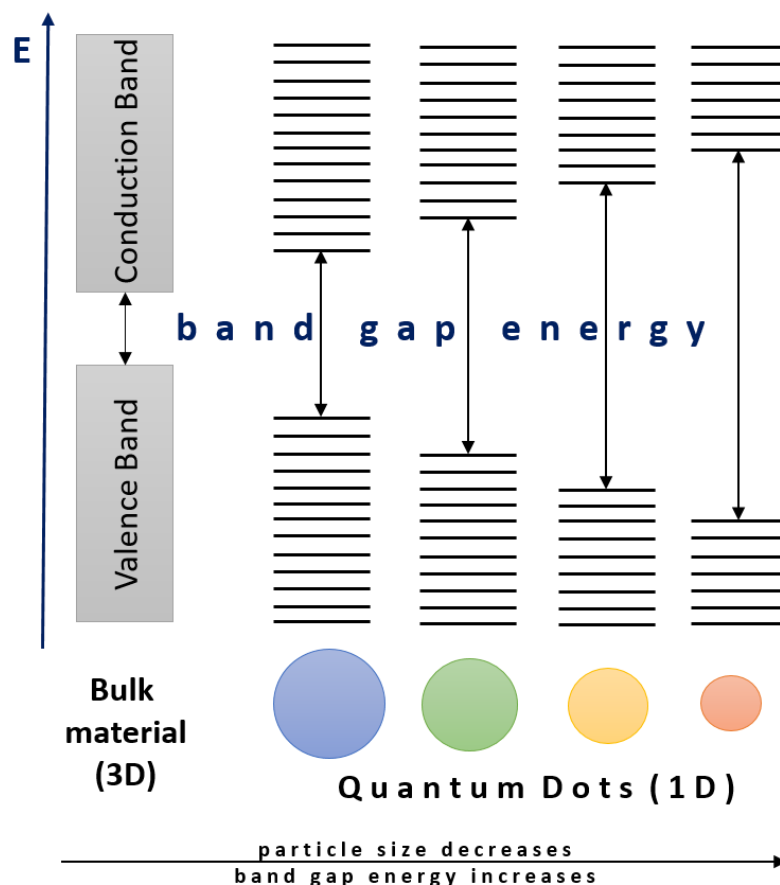


Figure 1.5. Figure of the bandgap energy dependence on particle size

1.2.5. Doping of quantum dots

Multinary QDs are the evolutionary derivatives of primary binary QDs. In the past decades, binary II–VI, III–V and IV–VI semiconductors (such as CdS, CdSe, CdTe, PbS and PbSe) and their alloys have been intensively studied because of their promising optical properties. But further development of such size and shape-dependent semiconductors have led to the preparation of ternary I–III–VI QDs (where I = Cu, Ag; III = In, Ga and VI = S, Se, Te etc.), which are less toxic due to the absence of Cd²⁺, Hg²⁺, Pb²⁺ ions in their compositions.

Compared to II-VI nanocrystals, I-III-VI nanocrystals have wider full-width at half-maximum (fwhm) of PL emission spectra, longer PL lifetime and larger Stokes shift, which diminish the self-absorption in optoelectronic and biotechnology applications¹³. Based on the quantum confinement effect, I-III-VI semiconductor particles exhibit a tunable bandgap and their PL spectra can be tuned by controlling the size of QDs, the synthesis temperature, and the chemical composition of the nanocrystals¹⁴. The main drawback of these QDs is that they exhibit a weak quantum efficiency (or quantum yield), but this defect can be removed by shelling or alloying with a higher bandgap material such as ZnS (noteworthy is that ZnS exhibits similar lattice parameters and crystal structure)^{15–17}. After that, more advanced quaternary I–II–III–VI QD materials appeared with the expanded opportunities for changing the composition and accordingly the properties and characterizations. One advantage of multinary semiconductor QDs is the possibility of introduction and/or substitution of other ions that are not part of these crystals to give them additional properties. This is called doping of semiconductor nanocrystals.

Doping of QDs is the process of introducing additional ions into the crystal structure of QDs to provide an additional property or to improve existing ones. This process is widely used to provide semiconductor QDs with magnetic properties, or to influence their optical, electrical properties. During the doping, one or more types of ions¹⁸ can be introduced and it is important to introduce doping ions into the core of nanocrystals, rather than adsorbing them on the surface of the nanoparticles.

It is important to know at what stage of the QDs formation, the doping materials are introduced as it affect the final product properties. For example, Y. Yang and co-workers¹⁹ tested three different approaches of doping Mn²⁺ ions into core/shell QDs : into the core, at the core-shell boundary and in the shell. The produced QDs exhibited dopant position dependent optical

properties: the red Mn emission peak showed different PL QY when varying the dopant position and the highest value was measured when the dopant was introduced during the shell formation.

Doping of semiconductor QDs with paramagnetic metal ions provides them magnetic and fluorescent properties simultaneously.

Spectroscopic analysis methods were used to determine the location of the dopant ions in nanocrystals and the location was found to depend on the synthesis method. The review reported that four types of methods are used to synthesize the doped QDs²⁰: (1) The growth of semiconductor QDs in a solution of the precursors of the QDs and of the dopant ion, in the presence of a passivating ligand; (2) The use of an inverse micelle solution in which the QDs grow inside water droplets from precursors dissolved in the water phase; (3) The well-known hot injection methods for the synthesis of undoped QDs can also be modified by including a dopant precursor in the reaction mixture; (4) The cluster method: (resembles the hot injection method) selected organometallic cation clusters used as precursors (similar coordinating ligands, growth at elevated temperatures) and the temperature is raised.

1.3. Synthesis methods of quantum dots

There are several methods to prepare QDs using either bottom-up or top-down approaches. In the top-down method, the bulk semiconductor material is crushed to the desired small size to obtain QDs, for example by ball milling, etc. The bottom-up approach describes the process when QDs are produced from precursors in the presence of a solvent. This method is widely used to synthesize semiconductor QDs. The next paragraphs will focus on bottom-up reactions.

Depending on the process environment, bottom-up synthesis methods can be divided into wet-chemical methods (liquid phase) or vapor-phase (gas phase) methods. Examples of vapor-phase synthesis method are molecular beam epitaxy, gaseous phase monomers aggregation, spraying of liquid metal sources. Sol-gel, hot-injection, microemulsion, solvothermal and electrochemical methods are examples of wet-chemical methods.

Almost all colloidal QDs used in bioresearch (biomedicine, bioimaging) are synthesized by wet-chemical methods. Depending on the solvent used, the wet-chemical synthesis methods may be organic phase synthesis and aqueous phase synthesis. A suitable synthesis method or synthesis medium is selected depending on the desired properties and the final applications of the QDs.

As mentioned above, there are the two ways to synthesize nanoparticles in colloidal form, in aqueous media or in organic media. Both approaches have their advantages and shortcomings. For example, aqueous phase synthesized particles can be directly sent to the surface modification step for the final applications unlike organic phase synthesized ones, which require an additional step in their preparation – aqueous phase transfer. On the other hand, organically synthesized particles have fewer surface defects and thus exhibit a higher PL quantum yield because they are usually processed at a higher-temperature than that used in aqueous synthesis.

Several approaches have been developed for the synthesis of colloidal QDs such as hot-injection, non-injection method, thermal decomposition, solvothermal method and aqueous methods including hydrothermal synthesis.

1.3.1. Organic media synthesis

As multinary QDs are the products of the change and development of binary and ternary QDs, most of multinary QDs synthesis routes are adapted versions of methods used for the preparation of binary/ternary QDs. Among the studies on I-III-VI₂ QDs, a one-pot synthesis was reported for orthorhombic phase AgInS₂ (AIS) nanorods, nanoparticles and worm-like shape nanoparticles¹⁶. Briefly, for the synthesis of AgInS₂ nanoparticles, analytical grade AgNO₃ (0.04 g), In(NO₃)₃ (0.1 g) and sulfur powder (0.01 g) were put into a warm solvent of octadecylamine (10 mL) at 120 °C, reaction lasted for 10 minutes. Using of 0.05 g sulfur powder resulted AgInS₂ nanorods; at 200 °C worm-like shaped AgInS₂ obtained. This thermal decomposition method allows the shape and size controllable synthesis of ternary QDs.

In 2007, Torimoto and co-workers reported a new protocol for the synthesis of ZnS-AgInS₂ (ZAIS) solid solution nanoparticles based on the thermal decomposition of metal ion-diethyldithiocarbamate complex¹⁷. This precursor was prepared by mixing a sodium diethyldithiocarbamate aqueous solution with silver, indium and zinc nitrates (mole ratio of $x/x/2(1-x)$, total concentration of Me ions is 0.025 mol/L) in water. ZAIS nanoparticles were obtained by heat treatment of this precursor in N₂ atmosphere: first for 30 min at 180 °C, then with addition of 3 mL oleylamine at the same temperature for 3 min. The PL emission of the obtained particles was blue shifted by increasing the Zn amount in precursor, which enabled to tune the desired emission color in visible spectrum. Later, the same researchers demonstrated the fluorescent enhancement of these QDs by post-synthesis heat treatment (after 30 min heating at 180 °C, PL QY reached 66 %, which is one of the highest value for quaternary QDs)²¹.

Over the years, various methods for the synthesis of ZAIS QDs were proposed and the initial research on their applications have been done. In particular, the so-called hot-injection and non-injection methods were used for the syntheses of ternary Ag-In-S (AgInS₂ or AgIn₅S₈) QDs²²⁻²⁸ and quaternary Zn-Ag-In-S (AgInS₂-ZnS or AgIn₅S₈-ZnS) QDs^{6,29}.

1.3.1.1. Hot-injection method

The hot-injection method is the largest spread method because of its simplicity. It was first demonstrated by Murray and co-workers³⁰ in 1993 in the synthesis of high quality CdE (E = S,

Se, Te) nanocrystals at 280 °C when using TOP/TOPO (tri-n-octylphosphine / tri-n-octylphosphine oxide) solvent coordinates. As the result, the nanomaterials with consistent crystal structure and diameter varying between 1.2 and 11.5 nm were produced. Fig. 1.6 shows the schematic illustration of simple equipment for hot-injection method. This method is based on the crystallization of a nanomaterial during the injection of cold precursors into a hot solvent in a flask.

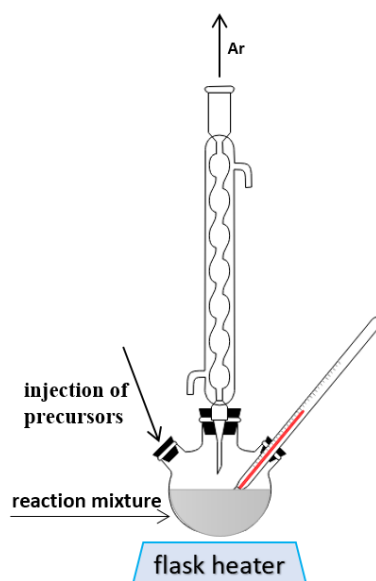


Figure 1.6. Schematic illustration of the equipment for the hot-injection synthesis of QDs

Some examples of using the hot-injection method for the synthesis of quaternary Zn-Ag-In-S ($\text{AgInS}_2\text{-ZnS}$ or $\text{AgIn}_5\text{S}_8\text{-ZnS}$) QDs are given below.

In 2009, Xie and co-workers demonstrated a versatile one-pot synthesis of CuInS_2 (CIS) NCs, which they also applied for the synthesis of the AgInS_2 semiconductor²³. Here, they used thiol ligands to control the reactivity of the cationic precursors. Further, the ZnS shell was grown on the surface of the particles, which was proved by the size increase in TEM (Transmission Electron Microscope) results. Briefly, CIS and AIS core nanoparticles were prepared in the presence of oleic acid (OA), n-dodecylthiol in octadecene (ODE) at 180 °C and 120 °C, respectively, followed by the ZnS shell growth at 210 °C. As-prepared AIS nanoparticles showed narrow size distribution and high crystallinity as evidenced by TEM and HR-TEM (High-Resolution Transmission Electron Microscope). They also showed that the PL emission

of the dots is pure bandgap emission. Moreover, by keeping the temperature below 100 °C, it was possible to produce rod-shaped nanoparticles since the lower temperature allows a slow rate of nucleation and the formation of elongated particles.

This approach with modifications was further used by Mao³¹ and co-workers to prepare AgInS₂ nanoparticles with tunable size and optical properties. Namely, oleic acid and toluene were used for the reaction and the core preparation was conducted at 90 °C. Shelling of AgInS₂ NCs with ZnS carried out in Teflon-lined stainless steel autoclave at 210 °C after injecting the as-prepared AIS NCs into Zn/S/dodecanethiol mixture. The PL lifetimes of AIS NCs were measured using a streak camera and two PL lifetime components were observed: short-lived from surface states and long-lived from intrinsic states (Fig. 1.7, left). The ZnS coating resulted in a slight increase in size (Fig. 1.7, right), but doubled the PL QY.

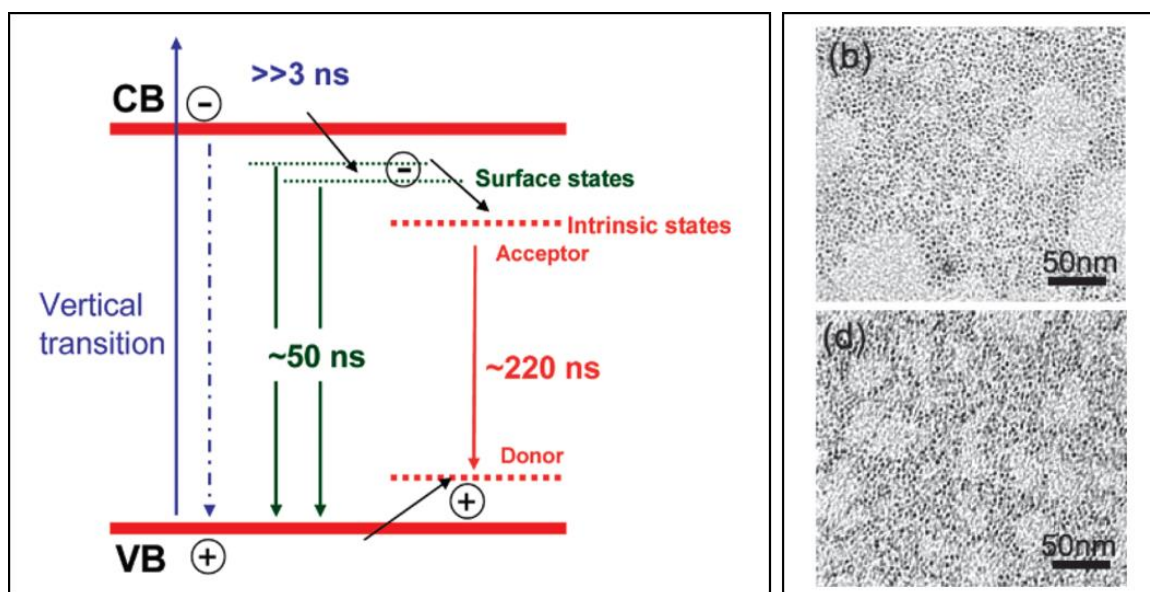


Figure 1.7. Left: schematic of the relaxation dynamics in the investigated AgInS₂ nanocrystals; Right: TEM images of the NCs: (b) AIS, 2.3±0.4 nm; (d) AIS/ZnS, 2.4±0.4 nm³¹

Hong and co-workers⁶ prepared cubic AgIn₅S₈ (c-AgIn₅S₈), orthorhombic AgInS₂ (o-AgInS₂) and tetragonal AgInS₂ (t-AgInS₂) nanocrystals by using the hot-injection method and changing the Ag/In ratio in AgIn_xS_{(3x+1)/2} core nanocrystals (NCs) as well as the reaction temperature. Silver and indium precursors with [In]/[Ag] molar ratio of 5 in the presence of oleylamine and ODE were purged for 20 min with N₂, after that the reaction mixture was heated to 90 °C and

DDT was added. Further, the temperature was increased (from 100 °C to 180 °C) followed by the injection of the sulfur precursor in oleylamine, then in 3 min reaction was stopped. Alloying with ZnS was carried out by addition of zinc stearate and sulfur mixture in trioctylphosphine to the AIS core at various temperatures (between 120 and 220 °C) for 2 h. The surface passivation by ZnS resulted in improved PL QY, for example, from 18.8 to 46.5% in the case of c-AgIn₅S₈-ZnS alloyed NCs prepared at 120 °C. The highest bandgap value (2.48 eV) was observed for the c-AgIn₅S₈ QDs when the synthesis temperature is 120 °C.

Another example of Ag-In-Zn-S QDs synthesis where all metal precursors were introduced simultaneously was reported by Mao et al.³². For synthesizing the AIZS NCs, they used a one-pot reaction involving the decomposition of the precursors at 60 °C with subsequent injection of dodecanethiol and raising the temperature to 90 °C, while sulfur dissolved in ODE was injected into the system. From the results of atomic absorption spectroscopy (AAS), it was found that Zn replaces Ag and that the incorporation of Zn is favored when Ag, In, Zn and S precursors are in the reaction medium compared to reactions in which the Zn precursor was injected to the AIS core. Regardless of synthesis conditions (zinc incorporated into the AIS core in a second step or introduced into the reaction simultaneously to the other metal precursors), the alloying with Zn has the same effect on the absorption and the PL peak position (blue shift).

Liu and co-workers²⁷ also proposed a synthesis procedure for these nanoparticles with emissions from red to near infrared (NIR) region to make them optimal for biological applications due to minimal absorption in biological tissues. Briefly, to prepare AIS QDs, a mixture of precursors in solution was heated to 90 °C, followed by injection of dodecanethiol and an oleylamine-sulfur solution at 170 °C. Separately, a mixture of zinc acetate, myristic acid and oleic acid was heated to 150 °C, then the dispersed nanocrystal solution was injected into the hot reaction mixture. Upon reaching the desired temperature, TOP-sulfur was added dropwise into the reaction mixture. An emission tunability of AgInS₂/ZnS QDs to the near infrared region was observed by tuning the composition. The QDs were made water dispersible by micelle-encapsulation.

Ko and co-workers³³ used a multistep hot-injection method to synthesize ZAIS QDs with intermediate ZIS shell, outer ZnS shell and PL QY as high as 87%. To synthesize the AIS core, the precursors were purged with N₂ gas and heated to 90 °C, after that 1-octanethiol (OTT) was added. Then, sulfur dissolved in OAm was quickly injected at 120 °C. For the first alloying/shelling process, the zinc precursor dissolved in OA and OTT were injected into the

AIS core at 180 °C. The second alloying/shelling process and the two-step outer-shelling process were carried out at 230, and at 180 and 180 °C, respectively.

The hot-injection method was also used for the preparation of doped QDs. For instance, in 2012, Manna and co-workers³⁴ doped Mn²⁺ ions in CIZS and AIZS QDs using the hot-injection method and explained the change in PL emission mechanism, namely, the appearance of the Mn d-d emission. In terms of morphology, according to TEM and XRD results, the sizes and the crystal structure of undoped and doped particles remained unchanged (Fig. 1.8).

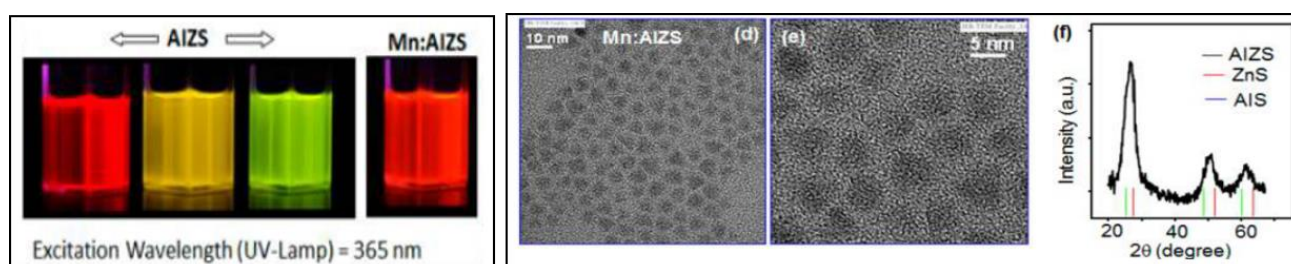


Figure 1.8. Left: digital images of PL tunable AIZS and their Mn-doped NCs obtained under UV irradiation; Right: (d) and (e) are TEM and HR-TEM images of Mn-doped AIZS QDs, respectively, (f) is the XRD pattern of AIZS QDs³⁴

Another study on Mn-doped Ag-In-Zn-S QDs came out in 2017 by Chen and co-workers³⁵, the protocol of their synthesis as follows: Ag and In salts and DDT were heated to 125 °C under vacuum until a clear solution was obtained, and to 200 °C under a flow of argon. Then, Zn and Mn precursors were added into the AIS core solution to form AIZS QDs and Mn doped AIZS NCs. By using this heat-up method to synthesize the NCs, it was demonstrated that with increasing the amount of Mn ions amount, the PL peak red-shifts due to interactions of Mn ions with host QD lattices.

1.3.1.2. The non-injection method

The non-injection method (or heating-up method) is based on the thermal decomposition of precursor metal salts in the presence of a high boiling point solvent and a capping ligand. This method is also useful for the synthesis of multinary QDs, in which it is important to control and maintain the reactivity of all precursors. In this method, the reaction temperature is usually high

and depends on the reactivity of precursors. In the non-injection method, the precursors are already in the system when the temperature rises. The absence of injection and the possibility to control the reaction temperature are the main advantages of this method in scaling up development.

There are only a few studies describing the synthesis of ZAIS QDs by the non-injection method and among the studies, the size and composition controllable synthesis of ZAIS QDs developed by Kameyama and co-authors³⁶ should be mentioned. In brief, metal acetates were added into a tube with thiourea. After adding a mixture solution of OAm and DDT, the solution was heated at 250 °C for 10 min with vigorous stirring under N₂ atmosphere. Then, the resulting solution was cooled down to room temperature.

1.3.1.3. Solvothermal method

The solvothermal method requires an autoclave, involves organic solvents and has many advantages over hot injection or non-injection synthesis methods¹¹: (1) low emission of harmful vapors, (2) use of low boiling point organic solvents that provide moderate synthesis temperature. This moderate synthesis temperature allows to produce highly crystalline QDs with relatively few structural defects. Despite all these efforts toward green chemistry, the main shortcoming of QDs' organic synthesis for biological applications remains the hydrophobicity of produced QDs.

1.3.1.4. Ag-In-Ga-S and Ag-Ga-Zn-S QDs synthesis in organic media

First attempt on the synthesis of Ag-based I-III-VI nanocrystals containing Ga started at the end of the last century, but those syntheses afforded large sized particles with significant shape irregularity and agglomeration^{37,38}. In the beginning of the last decade, T. Uematsu and co-workers³⁹ synthesized Ag-In-Ga-S nanoparticles by thermal decomposition of metal precursors in the presence of diethyldithiocarbamate which produced solid-solution nanoparticles of AgInS₂-AgGaS₂. With the increase of the Ga/In ratio, the PL peaks shifted to lower wavelengths due to the larger bandgap of AgGaS₂ (AGS) (2.7 eV) compared to AgInS₂ (1.8 eV).

Further, the same researchers⁴⁰ studied the thermal stability of these AgInS₂-AgGaS₂ solid-solution semiconductor nanoparticles compared to ZnS-AgInS₂ solid-solution nanoparticles. AgInS₂-AgGaS₂ were synthesized by the previous mentioned diethyldithiocarbamate

thermolysis method with slight changes. Dispersing the resulting nanoparticles in methacrylate resin did not affect their optical properties and the nanocrystals showed good fluorescent properties after 1000 h of heating.

Bulk AgGaS₂ shows the highest bandgap among I-III-VI nanoparticles and possesses unique optical properties such as nonlinearity. This increases the application interest of these particles in some fields. But, their PL peak emission at around 500 nm originating from exciton recombination in AgGaS₂ limits their potential. F. Huang and co-workers⁴¹ attempted to solve this issue. While synthesizing monodisperse AgGaS₂ nanoparticles through a one-pot synthesis in solution, they introduced Mn²⁺ ions into the solution. During this one-pot co-precipitation reaction, Ag₂S appeared as an intermediate phase and played a key role in the fabrication of final AgGaS₂ nanoparticles. Introducing Mn²⁺ ions into the AgGaS₂ NPs synthesis complex did not affect the crystal structure. However, introducing Mn²⁺ ions into the structure changed the fluorescence mechanism: when 5% of Mn²⁺ ions were introduced, the exciton recombination almost disappeared and an intense emission of Mn²⁺ ions (⁴T₁ → ⁶A₁) appeared at around 650 nm, making these NPs red emitting. These changes occurred while increasing the Mn amount from 0.5 to 5.0%. Further increasing the Mn dopant to 7.0% of caused a decrease of the intensity of the emission peak at 650 nm due to concentration quenching. This process allows to tune the emission color of AgGaS₂ nanoparticles to higher wavelengths and to increase the potential of these NPs for LEDs and biolabeling.

The photocatalytic activity of AgGaS₂ NPs was studied by C-M. Fan and co-workers⁴². A one-pot colloidal synthesis was carried out to fabricate the orthorhombic phase of AgGaS₂ with lattice parameters smaller than that of AgInS₂, due to the difference in ionic radius of Ga³⁺ (0.62 Å) compared to In³⁺ (0.80 Å). In this study, the influence of coordinating solvents on the structure of synthesized NPs during metal dithiocarbamate thermolysis is reported. Using primary alkylamines and long-chain alkanethiols leads to orthorhombic AgGaS₂ while ternary alkylamines resulted in a mixture of tetragonal AgGaS₂ and Ag₉GaS₆.

Further studies of these nanoparticles led to the preparation of quaternary QDs containing Ag and Ga. S. J-H. Kim and co-workers⁴³ prepared Zn-Ag-Ga-S and Ag-In-Ga-S QDs by alloying Zn²⁺ and In³⁺ ions into AGS QDs, respectively. Then the QDs were surface passivated by ZnS-shelling. Blue shift of the absorption spectra when alloying with Zn²⁺ and red shift when alloying with In³⁺ indicated the formation of quaternary Zn-Ag-Ga-S and Ag-In-Ga-S QDs. According to the synthesis requirement for highly fluorescent I-III-VI QDs, the deficiency in

monovalent cation relative to trivalent cation is respected and the optimal Ag/Ga ratio was found to be 1/8.

The optical properties of I-III-VI semiconductor nanoparticles are characterized by the presence of a broad defect-site PL peak with a large Stokes shift and this might limit their application range. There is a well-spread way to preclude the recombination sites on the surface of nanoparticles and at the same time increase the PL QY. T. Kameyama and co-workers⁴⁴ applied this approach while using solution-phase synthesis to prepare Ag-In-S nanoparticles coated by an amorphous GaS_x shell. Preparing non-stoichiometric (Ag deficient) Ag-In-S resulted in a narrow band edge PL peak and the PL wavelength can be tuned from 610 to 500 nm while increasing the doping in Ga³⁺ ions into QDs. Also shelling with GaS_x of Ag-In-S significantly decreased the intensity of the broad defect-related PL peak and enhanced the PL QY of the band-edge emission peak up to 30 % from 3.6 % after 180 min of GaS_x shell coating. XRD results proved that the obtained Ag-In-Ga-S (AIGS) QDs are the solid solution between AgInS₂ and AgGaS₂ and amorphous shell coating did not affect the crystal structure.

Later, T. Uematsu and co-workers⁴⁵ developed the surface coating of AgInS₂ QDs with a III-VI semiconductor shell material. They capped AgInS₂ QDs with InS_x and GaS_x shells by using a two-step thermal decomposition method. While comparing the PL spectra of InS_x-coated and GaS_x-coated AIS QDs, some differences were noticed. During GaS_x-shelling, the intensity of the broad-band-defect emission originating from uncoated AgInS₂ QDs decreased and a new narrow peak appeared at a lower wavelength. With InS_x-shelling, the broad-band-defect emission peak remained with a slight blue shift, assuming that some amount of In, which was supposed to produce the shell, was incorporated into the core structure producing indium-rich AgIn₅S₈. According to these results, when choosing a shelling semiconductor material, it is necessary to select the material that will not form alloys or solid solutions with the core material.

In later studies, J. Song and co-workers⁴⁶ synthesized water dispersible Ag-In-Ga-S QDs for the first time. They used a cation exchange approach where Ga³⁺ and In³⁺ precursors were injected into the solution containing AgInS₂ QDs. Synthesized QDs showed excellent biocompatibility and the PL emission can be tuned between 502 and 719 nm depending on QDs composition.

In another study, W. Hoisang and co-workers⁴⁷ synthesized Ag-In-Ga-S QDs by GaS_x-shelling of AgInS₂ QDs using a hot injection method. The tetragonal crystal phase was obtained at 140 °C and the orthorhombic phase at 180 °C. Both crystal phases, tetragonal and orthorhombic,

emitted narrow luminescence that originated from band-edge transition of AgInS₂. The high PL QY (49.2%) of the tetragonal phase was further enhanced by alkylphosphine surface passivation until 72.3 %.

1.3.2. Aqueous media synthesis

All of previous methods use organic solvents at high temperature and afford high quality QDs with high PL quantum yields and narrow size distributions. As mentioned before, one of the most important parameter for bio-applicable QDs is their water solubility. Before being used in biological applications, organic synthesized QDs should be surface modified to be soluble in water media. One way to avoid this extra step in QDs preparation for bio-applications is to synthesize these QDs directly in aqueous media. Compared to the organometallic synthesis, numerous hydrophilic ligands can be used for the aqueous synthesis of Ag-In-Zn-S QDs : reduced glutathione (GSH)^{48,49}, 3-mercaptopropionic acid (3-MPA)⁵⁰, polyacrylic acid (PAA)⁵¹, thioglycolic acid (TGA), mercaptosuccinic acid and sodium citrate⁵², L-cysteine or mercaptoacetic acid (MAA)^{51,53}.

The advantages of the aqueous synthesis are as follows⁵⁴ : (i) as-prepared products are suitable for biological applications being surface functionalized with water-soluble ligands during the synthesis process, (ii) this method uses less toxic reagents and solvents, and (iii) lower reaction temperatures (usually 100 °C) that are beneficial for large scale synthesis. The latter can also be a disadvantage of the aqueous synthesis because the low temperature is not effective for removing surface defects and the QDs usually have modest luminescence efficiency. To improve the luminescence properties, hydrothermal processes at temperatures higher than 100 °C were proposed.

Hydrothermal synthesis requires an autoclave and the water is heated at a temperature higher than 100°C⁵⁵ increasing the reaction environment pressure, which helps to produce QDs with better crystallinity than those prepared via aqueous synthesis at 100°C. There are numerous examples of ternary Ag-In-S and quaternary Ag-In-Zn-S QDs produced by hydrothermal synthesis.

Compared with the synthesis in organic media, the aqueous synthesis is more environmental-friendly⁵¹, biocompatible⁵⁶, of low-cost⁵², reproducible⁵⁷, and the as-prepared nanomaterials are water soluble⁵⁸.

There are other methods of QDs synthesis such as microwave-assisted synthesis⁵⁹ or biosynthesis⁵⁴ which are only scarcely used for the synthesis of Ag-In-Zn-S nanoparticles.

1.3.2.2. Aqueous synthesis of Ag-In-Zn-S QDs

Luo and co-workers²⁵ were the first to prepare AgInS₂ nanocrystals in water in the presence of GSH as capping ligand using a one-step synthesis. According to synthetic protocol, silver and indium acetates were dissolved in water in the presence of GSH before increasing to reaction temperature to 95 °C. Then sodium sulfide was injected. To prepare AIZS QDs, the Zn precursor was injected to reaction after 60 min at 95 °C. Zn treatment of AIS affected the PL peak position and PL QY.

Microwave-assisted synthesis of aqueous soluble AgInS₂/ZnS nanocrystals has been demonstrated by Xiong and co-workers⁴⁹. The typical protocol is as follows: silver and indium precursors were added to GSH in water, and a Na₂S solution was injected before microwave irradiation to 100 °C. Then to prepare AgInS₂/ZnS QDs, the Zn precursor and Na₂S were injected. The highly fluorescent QDs with PL lifetime of 424.5 ns showed promising results for application as fluorescent probes.

The teams of Regulacio⁵¹ and Deng⁴⁸ both prepared highly fluorescent AIZS QDs in aqueous media using different approaches and capping ligands and both showed their potential for biological applications, such as low toxicity, long lifetimes, appropriate colloidal and optical stabilities and modifiability with specific-cell-targeting ligands.

Due to its scalability, to the moderate synthesis temperature and the use of a “green” solvent, aqueous-based synthesis is of high potential. In 2015, Kang and co-workers⁵⁷ scaled up the aqueous synthesis of Ag-In-Zn-S QDs synthesis and demonstrated the method as facile, reproducible, of low cost and eco-friendly. The PL emission tunability of QDs can be controlled by varying the Ag/In ratio in the range from 535 to 607 nm. In addition, the as-prepared QDs showed photostability and biocompatibility.

In 2017, Mansur and co-workers⁵⁶ made a development by synthesizing QDs capped with carboxymethylcellulose (CMC) whose surface is already modified for biological applications. A shelling with ZnS was conducted to improve optical properties.

The precipitation technique was used to obtain size-selected AIZS QDs⁶⁰. The synthesis of the AIS core was conducted in the presence of MAA at 90-95 °C. Then, the core was covered with a ZnS shell. After concentration of the reaction mixture using a rotary evaporator, the precipitation was carried out in 6 steps using 2-propanol as non-solvent.

The other approach to aqueous synthesis was made by Lui and co-workers⁵⁰, when they prepared AIZS QDs in aqueous media under open air using MPA as a capping ligand. The QDs with high QY of 41% and diameter of 3 nm were prepared, and emission color of these nanomaterials can be tuned by adjusting the Ag or Zn precursors.

The ZAIS QDs demonstrated high potential in photocatalytic hydrogen generation. Chen and co-workers⁵⁵ produced 2D ZAIS nanosheets at 180 °C applying hydrothermal method and introduced oxygen into structure which reduced surface defects and non-radiative decay, but did not affect on the band structure.

Lately, Mrad and co-workers⁶¹ have synthesized AIZS QDs in aqueous phase synthesis using 3-MPA as a capping ligand. It is known, that by adjusting the Ag/In ratio it is possible to tune the PL emission, but atypical blue-shift with increasing this ratio obtained, which was explained by forming Ag-3-MPA and In-3-MPA complexes. It was also been reported that the PL emission is possible by varying the synthesis temperature and amount of Zn²⁺ introducing. It should be noted that the synthesized QDs were size-selectively precipitated, one of the fractions showing the highest PL QY value (78%) reported for aqueous synthesized AIZS QDs. Obtained AIZS QDs exhibited long PL lifetime, good colloidal and photostabilities presenting good candidate for biological applications.

1.3.3. Aqueous phase transfer methods

QDs synthesized in organic phase must be transferred into aqueous phase for biological applications. There are two main aqueous phase transfer strategies: (i) ligand exchange and (ii) ligand overcoating on the QDs surface⁶².

In the case of the ligand exchange strategy, the original hydrophobic ligand is replaced by new hydrophilic ligand. In the case of ligand overcoating, a new amphiphilic ligand is coated over the existing QDs surface ligands (Fig. 1.9).

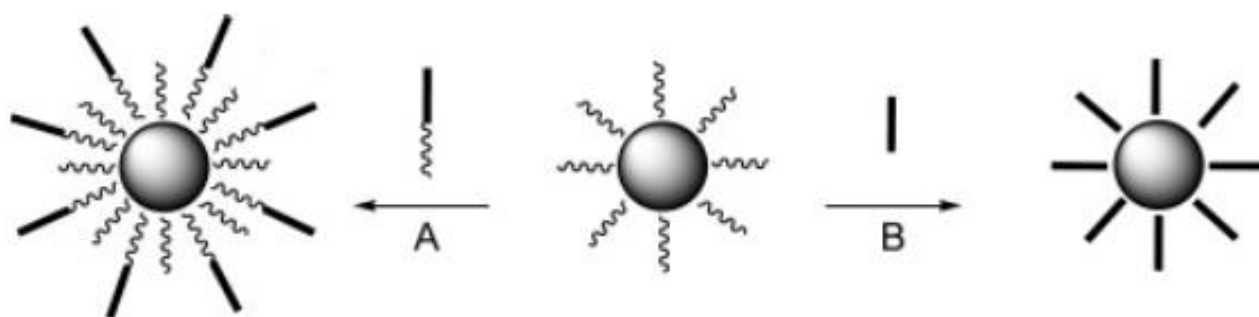


Figure 1.9. Schematic illustration of aqueous phase transfer methods: A – ligand overcoating; B – ligand exchange⁶²

Thioalkylated oligo ethyleneglycols⁶³, histidine⁶⁴, dihydrolipoic acid⁶⁵ and monothiolated ligands⁶⁶ like reduced glutathione (GSH)⁶⁷, L-cysteine (L-Cys)⁶⁸, 11-mercaptoundecanoic acid (MUA)^{69,70} and 3-mercaptopropionic acid (MPA)⁷¹, are the most commonly used ligands for ligand exchange. The ligand exchange method has some disadvantages such as the decrease of the colloidal stability and of the PL QY. But these shortcomings can be prevented by controlling the reaction conditions like the pH⁶⁸, the temperature, the concentration of ligands and of the QDs. The advantages of this aqueous transfer approach are the small hydrodynamic diameter of resulting products, which make them advantageous for biological applications^{72,73}, and cheaper ligands as well as easy procedure.

In the ligand overcoating on the QDs surface, amphiphilic polymers with hydrophobic end (to connect with the hydrophobic surface of QDs) and hydrophilic end (to ensure the water solubility of QDs) are used⁷⁴. This approach requires the dispersion of capping polymer and

QDs in a nonpolar solvent such as chloroform and subsequent solvent evaporation followed by the dispersion of the assembly in a buffer solution⁷⁵. Even though the QDs aqueous transferred by ligand overcoating have thicker hydrodynamic diameters, they have some advantages over ligand exchanged QDs in terms of optical properties, and can be concentrated by slight heating. This approach was developed to overcome the disadvantage of TOPO-capped QDs for biomedical imaging. Indeed, this ligand can be replaced by proteins in living systems, which may cause the degradation of QDs and the deactivation of the proteins⁷⁶.

1.4. Properties

1.4.1. Optical properties

The mechanism of PL for I-III-VI₂ QDs was explained by D-A recombination model and still under debate⁷⁷. Measurements of PL quantum efficiencies for I-III-VI₂ QDs showed that their values were significantly below that recorded for II-VI QDs. In addition, optical spectra recorded for I-III-VI₂ QDs are characterized by broad PL spectra as well as large Stokes shifts between the PL and absorption peaks. These observations led to conclusion that PL emission for I-III-VI₂ QDs does not result from conventional exciton recombination. One of the suggestions was that the recombination of carriers originates from trapped intragap levels formed by structural defects⁷⁸. In their study, the authors showed that the broad PL band of AgInS₂ QDs is due to D-A pair recombination based on detected shift in the time-resolved PL spectrum and the dependence on excitation intensity. They attributed the measured broad PL band to electron-phonon coupling, while observed strong electron-phonon interaction were attributed to the large Stokes shift.

The same D-A model was proposed for I-II-III-VI₂ NCs (such as ZnS_{1-x}(AgInS₂)_x) to describe the PL origin, where different emission energies obtained by the change in the coulomb interaction due to the change in the distance between the D-A pair.

Further explanation of the PL emission of I-III-VI₂ QDS was done by M. Jagadeeswara Rao and co-workers⁷⁹. Observing that the PL peak blue-shifts by 0.57 eV while changing the composition of the dots (while increasing the ZnS content) cannot be explained by D-A transitions model, they proposed two pathways of transition mechanisms (Fig. 1.10). The Path-1 with shorter lifetime (ca. 25 ns) with higher emission energy involves transitions between delocalized conduction/valence band and localized defects, while the Path-2 with longer lifetime (≥ 185 ns) and lower emission energy involves transitions between two localized or defect levels. Their model also explained the blue shift in emission of path-1 with changing ZnS content as its content affect the bandgap value, while deep midgap defect levels remain unaltered.

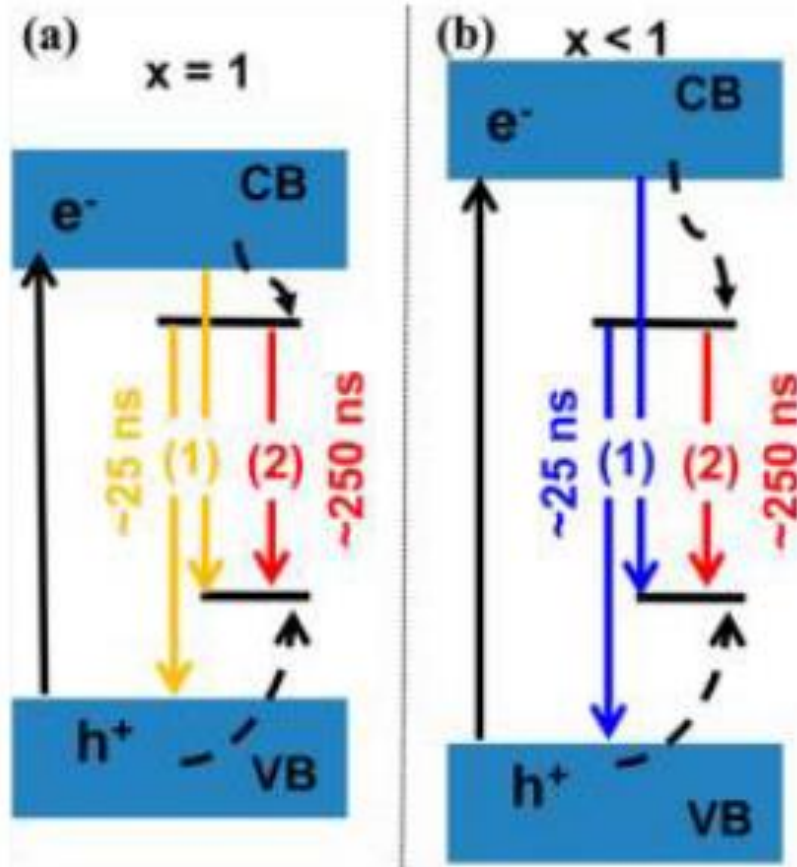


Figure 1.10. Schematic diagram of PL mechanism for $(\text{ZnS})_{1-x}(\text{AgInS}_2)_x$ NCs when a) $x = 1$; and b) $x < 1$ ⁷⁹

Near-infrared emitting $\text{AgInS}_2/\text{ZnS}$ nanocrystals were synthesized and their PL mechanism was explained by the results of time-resolved PL study⁶⁹. According to the results, two components contribute to their photoluminescence, and the fast decay component corresponds to surface trap state recombination and the slow decay component corresponds to the deep donor–acceptor recombination. The same mechanism was applied to describe the origin of the PL emission of AgIn_5S_8 nanoparticles⁸⁰. There are three time constants that describe the PL lifetime of these particles: two long constants (τ_2 and τ_3) related to the lifetimes of the defect states and one short time constant (τ_1) related to lifetime of band gap state.

Another study on aqueous synthesized glutathione-capped Ag-In-S and ZnS -shelled Ag-In-S QDs⁸¹ proposed that the PL bands of AIS QDs originate from the dynamics of the electron-phonon interaction and the vibrational relaxation in the QDs rather than from energy factors (depth and distribution of trap states).

The effect of Mn^{2+} ions doping on the photoluminescence mechanism in multinary quantum dots has also been investigated. When using a sufficient amount of Zn^{2+} ions and doping Mn^{2+} ions into CIZS or AIZS QDs, the trap-state emission was quenched by Mn d-state emission and only the latter was detected at ca. 600 nm^{34,82} (Fig. 1.11). To prove that the emission at 600 nm originated from $\text{Mn}^{2+} \ ^4\text{T}_1 \rightarrow \ ^6\text{A}_1$ transition, excited-state lifetime and time delay PL spectra measurements for both undoped and Mn-doped QDs were carried out. The excited-state lifetime was measured at different positions of the emission spectrum of undoped and Mn-doped NCs: in Mn-doping, since the emission peak is untunable, the lifetime values remain constant, while in undoped NCs, the lifetimes of the emission are different at different NC compositions. In delay time PL spectra, different delay times behave differently in two (trap-state and Mn d-state) emissions.

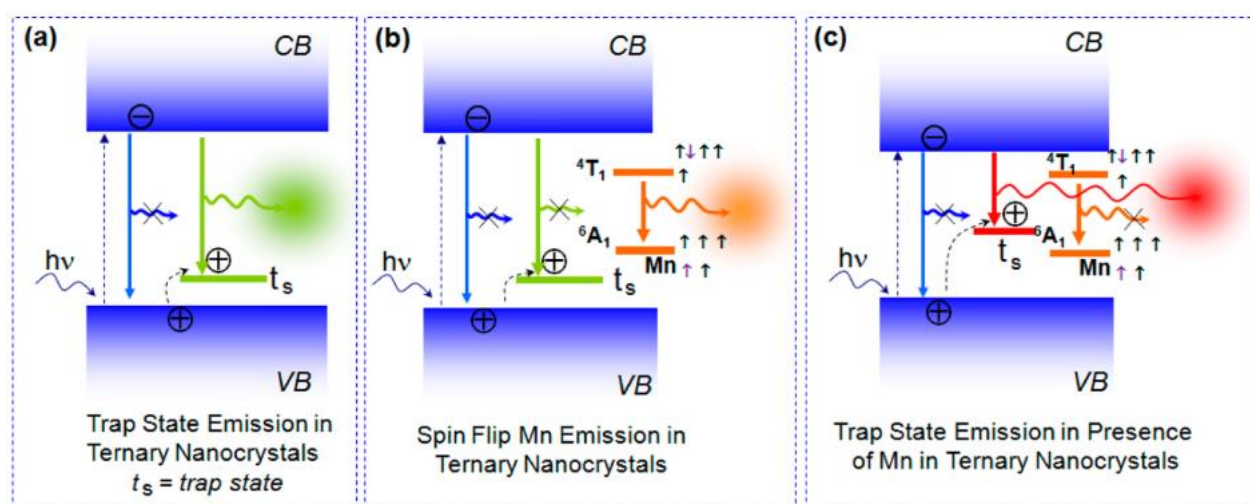


Figure 1.11. Schematic diagram of PL mechanisms: a) original hole transfer and appearance of defect levels in ternary NCs that emits trap-state emission; b) quenching of trap-state emission with $\text{Mn}^{2+} \ ^4\text{T}_1 \rightarrow \ ^6\text{A}_1$ transition in CIZS and AIZS QDs, while Zn content is sufficient; c) case in CIZS and AIZS QDs, while Zn content is insufficient for dopant emission to evolve³⁴

Mn-doped CIZS QDs can be prepared as following : the CIS core is covered with a ZnS shell and Mn^{2+} ions were adsorbed on the surface of this shell. Next, a second ZnS shell covering is conducted^{83,84}. In some cases, two emissions – green from CIZS and orange from Mn^{2+} – appear simultaneously in the PL spectrum (Fig. 1.12). It was suggested that the green PL peak

at 528 nm is related to the trap-state emission and the orange one at 590 nm to the Mn d-state transitions. The millisecond lifetime (ca. 2 ms) of Mn-doped QDs is the proof of Mn²⁺ ion contribution in PL.

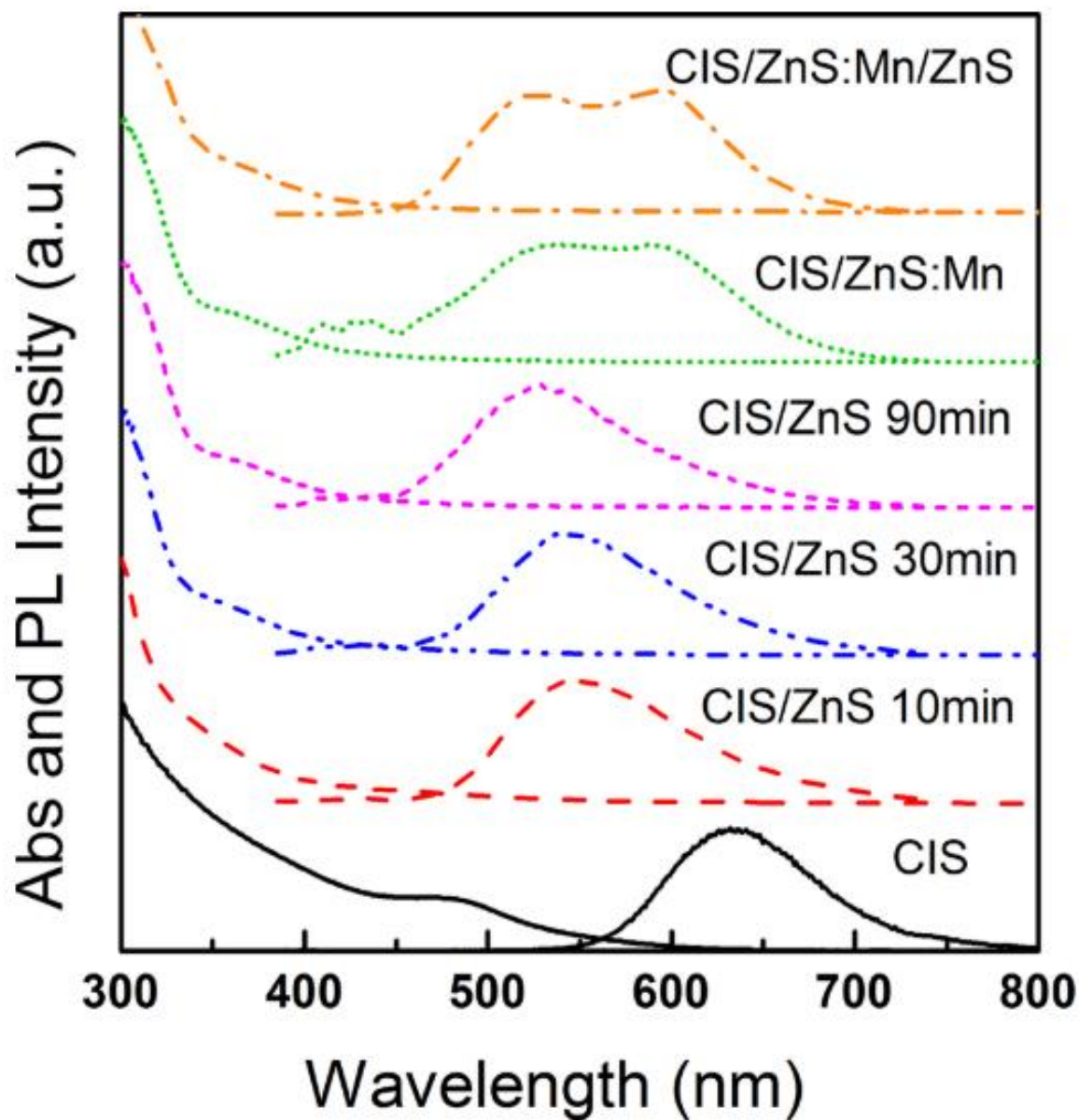


Figure 1.12. Absorption and PL spectra of CIS, CIS/ZnS, CIS/ZnS:Mn, and CIS/ZnS:Mn/ZnS nanocrystals⁸⁴

The photoluminescent properties of Mn-doped CIZS QDs were investigated at different temperatures⁸⁵. The results show that with increasing the temperature from 20 K to 300 K, there

is a slight red-shift in the PL peak position and the PL intensity falls rapidly. The mechanism is in accordance with the one described here above (Fig. 1.13).

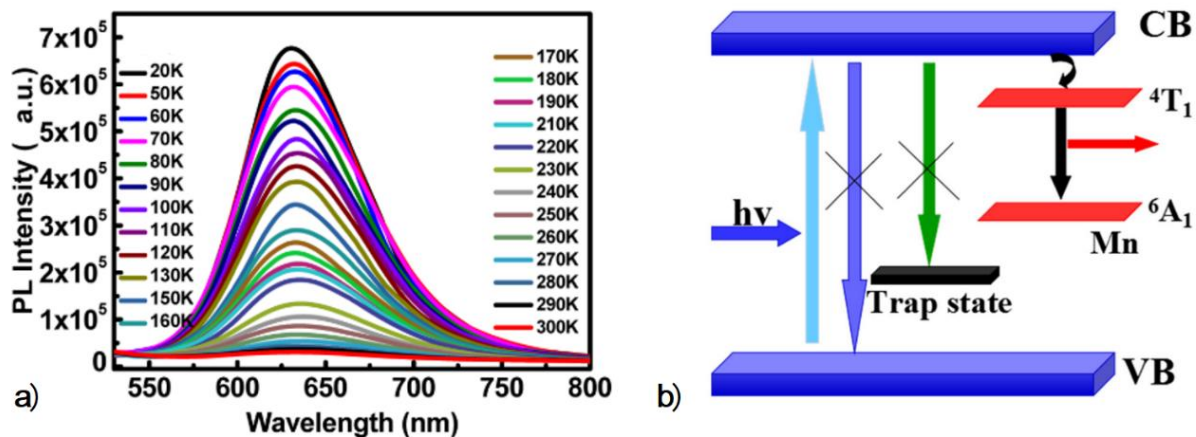


Figure 1.13. a) Temperature-dependent PL spectra of Mn:CIZS QDs; b) Schematic diagram of PL mechanism for Mn:ZCIS nanocrystals⁸⁵

While increasing the Mn-doping³⁵ in Mn:AIZS/ZnS NCs, a red-shift in the PL peak position, a decrease of the PL QY, and short excited-state lifetimes became predominant. It was suggested that the incorporation of Mn^{2+} ions into host NCs lattices is the reason of the red-shift⁸⁶ in the PL peak position. The short lifetime refers to the defect-related emission while the long lifetime corresponds to the Mn emission from Mn pairs or diluted Mn dopants in host NCs. In addition, the possible effects of Mn^{2+} ion on the PL mechanism were discussed. (Fig. 1.14).

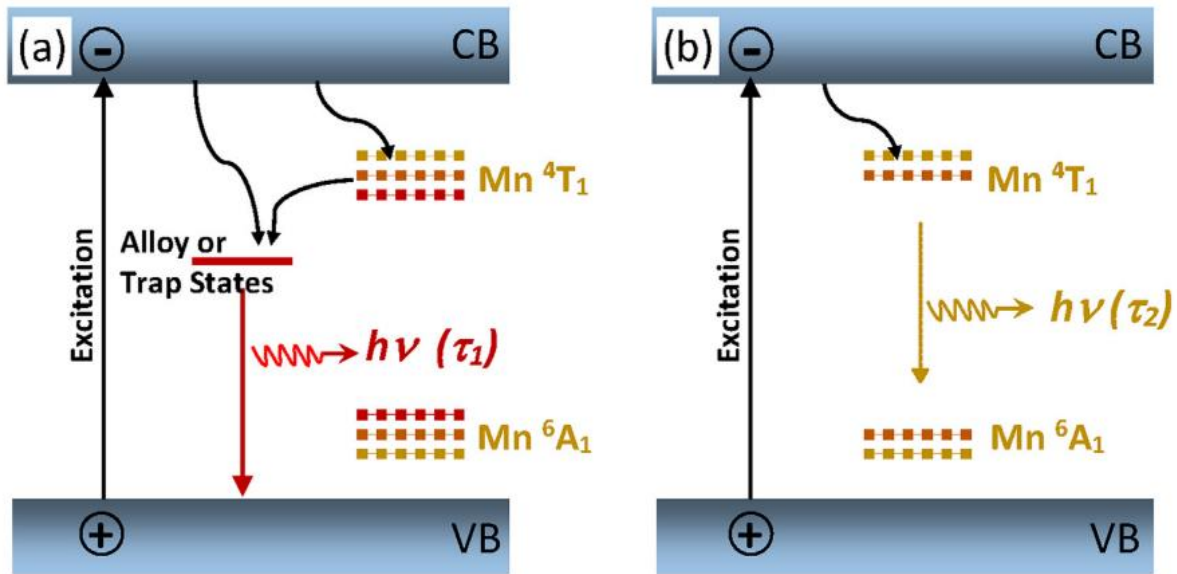


Figure 1.14. Illustration of two possible pathways for electron-hole recombination in Mn doped AIZS/ZnS NCs (a) one is from the alloy or trap states (caused by Mn-AIZS alloying or Mn-induced defects in the Mn-doped layer) to the valence band, which contributes to the fast PL decay; and (b) the other one is Mn ⁴T₁ to ⁶A₁ from a few of Mn pairs or diluted Mn dopants out of the Mn-doped layer, which is responsible for the slow PL decay³⁵

1.4.2. Influence of synthesis parameters to the properties of QDs

The synthesis of multinary nanoparticles is more challenging than the synthesis of binary or ternary QDs due to the well-known factors such as the difficulty of controlling the reactivity of all the ions, adjusting the reaction temperature for each precursor and finding the appropriate ligands to control the nucleation and growth of the particles.

1.4.2.1. Influence to the shape and size of QDs

In the studies^{69,87} related to Ag-In-Zn-S QDs, the researchers investigated the optimal conditions for the shape and size controlled synthesis. It was found that when an auxiliary sulfur precursor is used, alloyed Ag-In-Zn-S NCs can be prepared without impurities such as ZnS

particles⁸⁷. Additionally, changing the ratios of precursors allows to control the composition, the shape and the size of resulting QDs.

A study on Ag-In-Zn-S QDs was published in 2019 by Bujak et al.⁷⁰, and the authors investigated the growth and the surface chemistry of these materials. The influence of the used solvents and of sulfur precursors on the properties of QDs was reported. The growth mechanism of these QDs was described in detail and it was concluded that the core of these quaternary QDs is composed of orthorhombic AgInS₂ and hexagonal ZnS with an indium-rich surface and that changing the solvent or the sulfur precursors does not affect the indium content on the QDs surface. Moreover, these factors do not significantly affect the nanocrystals size and shape.

Jeong and co-workers studied the bandgap states⁸⁰ and photoluminescence⁸⁸ of ZnS-AgIn₅S₈ nanoparticles. It was demonstrated that the stable crystal structure of these nanoparticles is cubic and that their crystal structure and stoichiometry affect their electronic band structure.

1.4.2.2. Photoluminescence

Changes in the stoichiometry of reactants during the preparation of AIS and ZAIS NCs allows to tune the photoluminescence. Dai et al.⁸⁹ prepared a series of non-stoichiometric AIS NCs using the previously mentioned¹⁷ one precursor thermal decomposition method (where the precursor is $(\text{Ag}_x\text{In}_{(1-x)}[\text{S}_2\text{CN}(\text{C}_2\text{H}_5)_2]_{(3-2x)})$ and the molar ratio of metals was controlled $\text{Ag/In} = x/(1-x)$). The authors found that a $N_{\text{Ag}}/N_{\text{metal}}$ ratio of 0.37 is the optimal ratio of precursors to prepared highly fluorescent QDs (PL QY reaches 70%). The synthesized AIS NCs have also a tunable PL emission (Fig 1.15).

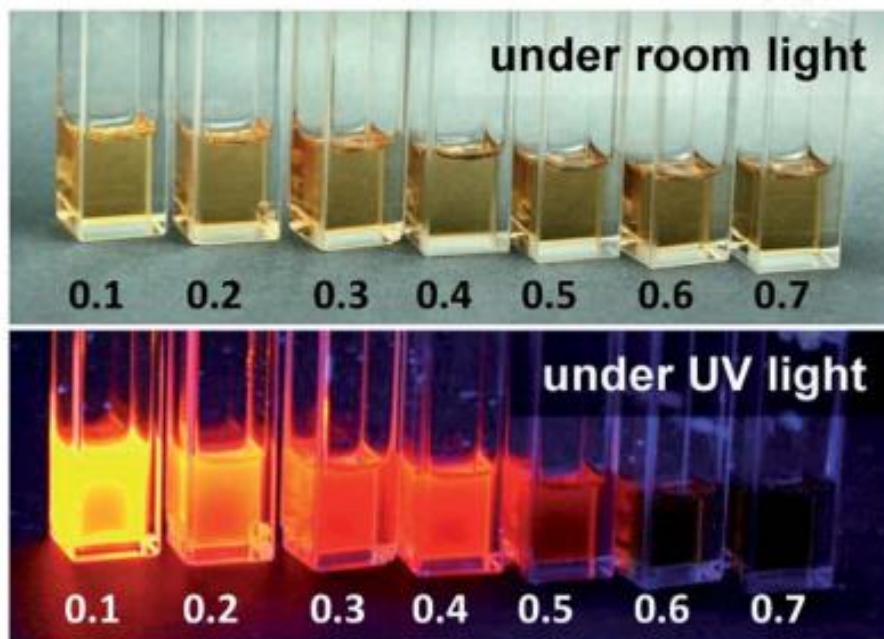


Figure 1.15. Photographs of the chloroform solution containing AIS particles under room (upper) and UV (lower) light irradiation (numbers show x value in $(\text{Ag}_x\text{In}_{(1-x)}[\text{S}_2\text{CN}(\text{C}_2\text{H}_5)_2]_{(3-2x)})$)⁸⁹

When considering AIZS nanoparticles, it was shown that to increase their luminescence, a ZnS coating is the best option due to its higher bandgap and that a high synthesis temperature is required for better particle crystallinity. Hamanaka and co-workers⁹⁰ carried out a detailed examination of the structure of these particles and indicated that a high temperature is mandatory for effective Zn-doping/alloying.

In another study, the effect of the S/In feed ratio on the PL emission was demonstrated for water synthesis⁹¹. The increase of this ratio caused a blue shift in the PL peak. In this study, $\text{AgInS}_2/\text{ZnS}$ QDs were prepared with a defect in Zn compared to other precursors in order to engineer near infrared emitting particles for biological applications⁶⁹.

Chang and co-workers⁹² developed strategies to increase the photoluminescence of AgInS_2 QDs, reported a one-pot synthesis of $\text{AgInS}_2\text{-ZnS}$ core-shell QDs and their potential bio-application. According to their results, a higher amount of In precursors decreases the density of Ag vacancies and subsequently reduces the intrinsic defects and the possible nonradiative recombinations. Regarding the surface ligands, the situation is as follows: with the increase of the DDT ligand concentration, the PL QY increases and a blue shift of the PL peak maximum

position is observed. This was explained by a decrease of the particle sizes with the increase of the DDT concentration.

In 2019, Zeng and co-workers⁹³ carried out the synthesis of ternary AIS and quaternary AIZS QDs using a cation exchange method. Ag₂S was first prepared and further used as a seed for multinary QDs preparation. By adjusting the Ag/In ratio, it was possible to tune the PL emission and by introducing Zn²⁺ ions into the structure, the band gap and the PL QY values increased.

Lately, Martynenko and co-workers⁹⁴ reported the excitation energy dependent photoluminescence properties of AIZS QDs prepared by an aqueous method adopted from Raevskaya et al.⁶⁰. In this study, the dependence of the PL peak positions, PL spectral bandwidths, and PL QYs of AIZS QDs on the excitation energy was investigated. Results show that only the PL QY is not dependent on the excitation energy.

1.4.2.3. Influence of the temperature

Another parameter affecting the optical properties is the synthesis temperature. It is well known that the higher the synthesis temperature, the better the crystallinity of NCs and the narrower the size distribution. The study⁹² also showed that the reaction temperature affects the luminescent properties of the QDs. If the temperature is low, a decrease of the PL QY is observed. On the contrary, if the temperature is too high, the NCs growth occurs at high rate and their precipitation may be observed and thus a rapid decrease in PL QY. Two reasons were proposed for this PL QY decrease: (1) particles sizes become higher than the Bohr exciton radius and (2) the high reaction temperature partially removes the ligands from the QDs surfaces, which conducts to surface defects. Finally, shelling with the higher bandgap ZnS material dramatically increases the photoluminescent properties of QDs by decreasing the amount of surface defects and the quenching the nonradiative recombinations.

To demonstrate the effect of the temperature on the fluorescent properties of QDs, it is interesting to discuss the preparation of Zn-doped AIS QDs. In 2011, Tang and co-workers⁹⁵ synthesized Zn-doped AgInS₂ QDs in two steps: (i) the AIS core synthesis was conducted by thermal decomposition, and (ii) Zn was doped into the AIS core. In the second step, four different reaction temperatures were tested resulting in different color emitting QDs: 120 °C – red, 150 °C – orange, 180 °C – yellow, 210 °C – green-emitting QDs (Fig. 1.16). The results

show that with the increase of the temperature, the incorporation level of Zn into AIS core increases.

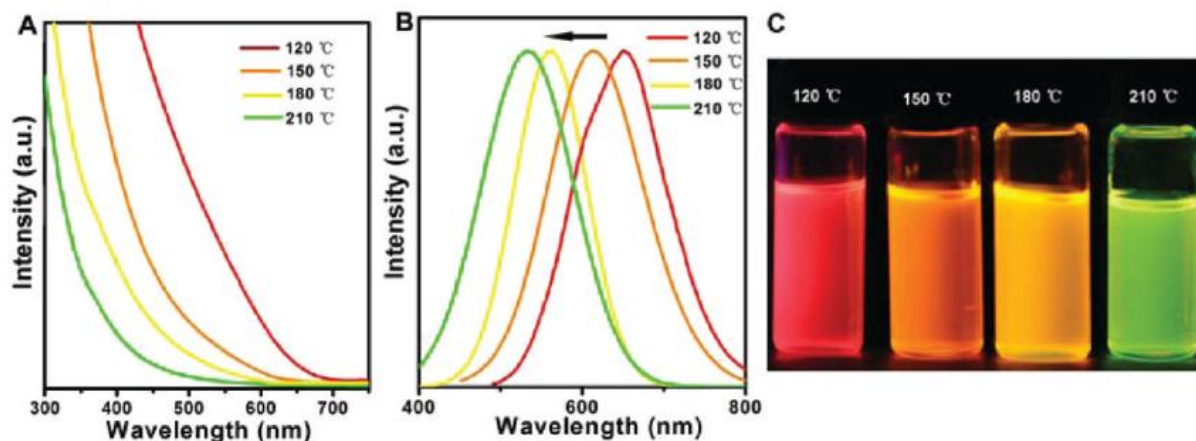


Figure 1.16. Absorption (A), PL (B) spectra and photographs of Zn-doped AIS QDs prepared at different temperatures⁹⁵

1.4.3. Magnetic properties

In general, magnetic materials include various types of materials depending on their compositions and applications. These materials are useful in diverse range of areas from producing electricity to data storage, from sound recording to body scanning.

Nanotechnology gets also interested in the miniaturization of magnetic materials. Magnetic nanoparticles are abbreviated MNPs and their properties differ from the bulk materials. Generally, the magnetic structure consists of small regions called domains. A domain contains spins that are aligned in the same directions, in other words, in every domain the magnetism of all atoms is pointed in this direction, but in different domains all the spins are pointed differently, the regions between the domains are called walls. Usually, when MNPs exhibit a size smaller than the single domain limit, they show superparamagnetic properties at room temperature⁹⁶. This means that MNPs can be ferromagnetic or ferrimagnetic, but due to their small size, they became superparamagnetic below the Curie temperature and consist of one magnetic domain.

Superparamagnetic materials are useful in ferrofluids owing their tunable viscosity and biomedical applications. Depending on the applications, MNPs must possess adequate morphology, size or shapes, surfaces and physical properties.

The magnetic properties of substances are characterized by a magnetic moment. The magnetic moment is related to the spin and angular momentum of electrons, whose orbital and spin motions determine the magnetic properties. Bulk magnetic materials are classified in terms of their response to magnetic fields. There are five main categories to which all magnetic materials can be classified: ferromagnetism, ferrimagnetism, antiferromagnetism, paramagnetism and diamagnetism. As described above, the bulk magnetic materials consist of magnetic domains, within each domain the aligned magnetic moments. In the case of MNPs, the decrease of the particle volume affects the magnetic properties as quantum confinement affects the electronic properties of QDs, which means that the nanoparticles may possess only one domain and that the properties are different from those of bulk materials.

Many nanoparticles show superparamagnetic properties due to their small sizes, which means the magnetization of these particles may change directions with the temperature. When there is no external magnetic field, the magnetic moment of superparamagnetic materials is equal to zero. However, when an external magnetic field is applied, the magnetic moment aligns like in paramagnetic materials but with a higher value.

The other factors characterizing MNPs are the susceptibility (χ) and the coercivity (H_C). In bulk magnetic materials, their composition, crystallographic structure, vacancies and defects and magnetic anisotropy characterize their magnetic behaviors. In MNPs, in addition to the previously described factors, the synthesis method can also affect the magnetic properties. As turned out, the superparamagnetic property of MNPs depends on their size (the smaller the size of the MNP, the lower is the temperature required for the ferromagnetic-to-superparamagnetic transition).

MNPs are usually produced in two ways: (i) using magnetic elements in the synthesis and (ii) doping with paramagnetic ions. Doping paramagnetic metals into QDs provides them magnetic and fluorescent properties simultaneously. It is important to introduce doping ions into the core of the nanocrystals, rather than adsorbing them on the surface of the nanoparticles. Spectroscopic analysis methods were used to determine the location of dopants which depends on the synthesis method.

Mn (II) is a well-known dopant for tuning the PL emission of semiconductor materials to the red region, in the 585 to 650 nm range⁸⁶. Since the Mn²⁺ ion has a high magnetic moment of 5 μ_B , it is of high interest for producing magnetic materials⁹⁷.

In general, doping or co-doping of nanomaterials with Mn showed that when the concentration of Mn increases, the net magnetic moment increases^{98,99}. It was suggested that the main role of the Mn cations is not to influence the magnetic ordering, but rather only modify the paramagnetism and suppress the ferromagnetism. In another study on Mn-doping of BiFeO₃ nanomaterials, it is reported that the Mn-doping improves the overall electrical and magnetic properties¹⁰⁰.

The doping of Ag-In-Zn-S QDs with Mn²⁺ ions has been studied over the past few years and only a few publications focusing on the effect of doping on the optical properties have been published^{34,35,82,101}.

1.5. Applications

1.5.1. Optical applications

Fluorescent semiconductor nanoparticles exhibit longer PL life-time, broad absorbance and higher (photo)stability compared to organic dyes,¹⁰² which make their application area wider.

The following studies proposed to use AIZS QDs in optical and solar cell applications. Ruan¹⁰³ and Kim¹⁰⁴ studied the applications of Ag-In-Zn-S QDs in white LEDs and organic-inorganic solar cells, respectively. In their studies, they used the hot-injection⁶ (Ruan) and thermal decomposition¹⁷ (Kim) methods to prepare the QDs. The application of hydrothermally synthesized AIZS QDs in white light emitting diodes was reported by Chen and co-workers¹⁰⁵. The particle sizes were controlled by the duration of the shell coating and the composition of particles were adjusted by changing the ratio of zinc to silver and indium. These particles can be used as the yellow emitting part of white LEDs. The ability of tuning the emission color by changing the reaction temperature was also used by Chung et al.¹⁰⁶ to fabricate white LEDs, and by Zhu et al. to fabricate QLEDs¹⁰⁷.

AIS NCs were also evaluated as heavy metal-free photosensitizer for QDs-sensitized solar cells¹⁰⁸, where the TiO₂/AgInS₂ electrode was prepared by attaching the QDs to a mesoporous TiO₂ surface. Photoelectrochemical measurements indicate that the electron injection from photo-excited AgInS₂ QDs to TiO₂ is energetically favorable. The use of the hot-injection method for the preparation of green emitting Zn–Ag–In–S and red emitting Zn–Cu–In–S alloyed QDs was demonstrated by Yoon and co-workers²⁹. These ZAIS and ZCIS QDs with a wide fwhm PL emission and high PL QYs were prepared by triple and double ZnS shelling for ZAIS and ZCIS, respectively, and demonstrated potential use in visible light LEDs.

Choi and co-workers¹⁰⁹ modified the synthesis temperature and its duration to prepare ZAIS NCs emitting in the green (reaction at 90 °C), yellow (reaction at 160 °C) and amber (reaction at 180 °C) for LEDs engineering. Li and co-workers¹¹⁰ synthesized Ag–In–Zn–S/ZnS core/shell QDs using the so called continuous-flow synthesis using diethyldithiocarbamate precursors of each metals and their subsequent heating in a needle. The obtained QDs were demonstrated to be of high potential in QD-LEDs. From the latest data on ZAIS QDs, the thermal

decomposition¹¹¹ and hot-injection¹¹² prepared QDs were used in WLEDs and QLEDs, respectively.

The other application area of ZAIS QDs is photocatalysis. Photocatalytic activity of dumbbell shape ZAIS nanoparticles was studied by Kameyama and co-workers¹¹³ and the NPs showed an improved photocatalytic H₂ evolution rate compared to nanorod or ellipsoidal ZAIS nanoparticles. Yang and co-workers¹¹⁴ also improved the photocatalytic activity of these QDs by mixed-ligand capping.

Lui and co-workers¹¹⁵ prepared ZAIS QDs by doping Zn²⁺ ions into the AIS core using a thermal decomposition method at 120°C in the presence of oleic acid, 1-dodecanethiol, 1-octadecene and trioctylphosphine. Then, the aqueous phase transferred particles were used for detection of Cu²⁺ ions^{115,116}.

In another study on AgInS₂/ZnS QDs, Matsuda and co-workers¹¹⁷ investigated their application as temperature sensors (Fig. 1.17). The temperature sensitivity of the luminescence of AgInS₂/ZnS QDs is similar to that of other luminescent particles. In addition, the AgInS₂/ZnS QDs synthesized via the thermal decomposition method are less toxic and more photostable than CdSe/ZnS QDs used as reference, which makes them of interest for bio-applications.

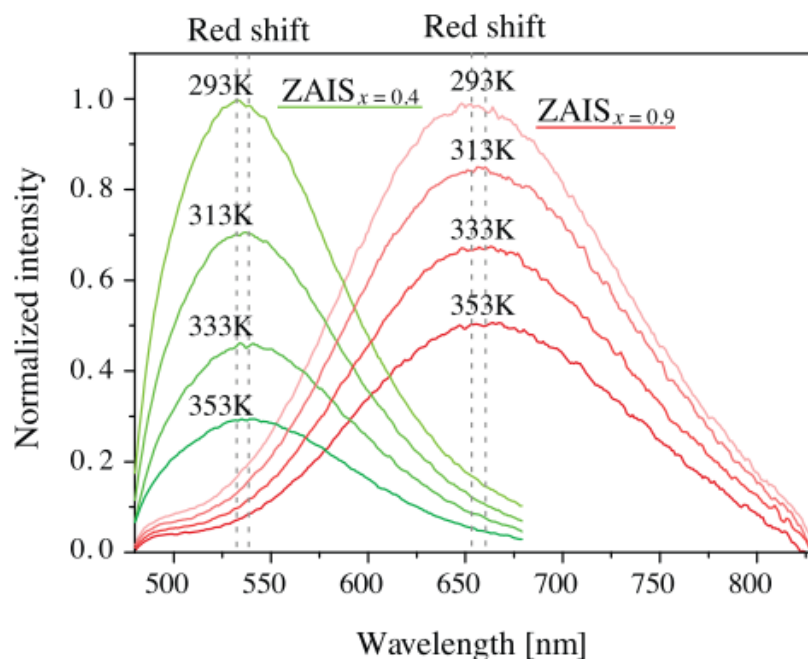


Figure 1.17. Temperature variation of ZAIS ((AgIn)_xZn_{2(1-x)}(S₂CN(C₂H₅)₂)₄) QDs luminescent spectra¹¹⁷

1.5.2. Biological applications

As mentioned before, Ag-In-Zn-S QDs are of high potential for biological applications due to their low toxicity compared to Pb-, Hg-, Cd-based binary QDs. Besides non-toxicity, to be useful in biological applications, the nanoparticles must meet some important requirements such as stability, biocompatibility, water solubility, and reproducibility of synthesis methods. The most suitable emission wavelengths for biological applications are in the range from 600 to 900 nm.

The toxicity of QDs is the most important factor when their biological and/or biomedical applications are considered. The toxicity of QDs is influenced not only by their physico-chemical properties, but also by the environmental conditions¹¹⁸, the QDs size, charge, concentration, outer coating bioactivity (capping material, functional groups), and oxidative, photolytic, and mechanical stability have each been shown to be determining factors. Biocompatible means not harmful to living cells. Making QDs water-soluble is one way for improving their biocompatibility. Moreover, engineering nanoparticle-biomolecule conjugates capable of participating in biological processes is crucial in QDs functionalization for biological applications. While choosing a bioconjugation ligand for a specific application, it is important to find a ligand with suitable functional groups and that will not alter the stability, the size, and the photophysical properties of QDs.

The biological applications of ZAIS QDs are focused in the fields of bioimaging and biolabeling. Bioimaging is based on a non-invasively contrast in diverse tissues and organs due to the molecular difference. Magnetic resonance imaging (MRI) along with computed tomography (CT), optical imaging (OI), fluorescence imaging, fluorescence resonance energy transfer (FRET) and others serve as bioimaging technique. MRI is a technique used for monitoring full body or local soft tissues based on the differences in rotational axis directions of protons in tissues in response to strong magnetic field. Biolabeling means labeling and tracking the biological cells commonly using fluorescent nanoparticles.

Recently, many studies on ZAIS QDs focused on biological applications such as biodistribution, biocompatibility and bioimaging. In a recent study¹¹⁹, aqueous synthesized GSH-capped ZAIS QDs were demonstrated to exhibit no harmful effect on body mass dynamics and basic hematological parameters of rats for 30 days. In 2015, Chen and co-workers¹²⁰ reported the use of AIZS QDs for tumor cell targeting after chlorotoxin-conjugation.

This work demonstrated that the scalable synthesis and the easily tunable surface chemistry of AIZS QDs pave the way for their application in cells targeting and/or tissue-based theranostics. Chang and co-workers⁹² demonstrated the potential of PMAO-coated and FA-conjugated AgInS₂/ZnS QDs, for HepG2 intracellular entry via receptor-mediated endocytosis (Fig. 1.18).

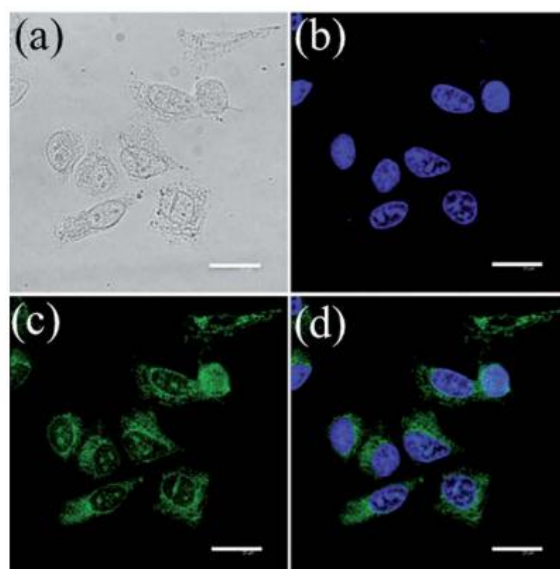


Figure 1.18. Confocal images of HepG2 cells stained with a solution of FA-conjugated AgInS₂-ZnS QDs for 1 h as well as fixed with alcohol and subsequently stained with DAPI: a) under visible light; b) DAPI emission at 460 nm, showing the location of the HepG2 cell nuclei; c) red fluorescence originating from AgInS₂-ZnS QDs; d) composite image. Scale bar represents 20 μm ⁹²

Chapter 2. Organic phase synthesized AIZS and Mn-doped AIZS QDs

2.1. Introduction

In recent years, I-III-VI₂-based semiconductor quantum dots like CuInS₂ (CIS) or AgInS₂ (AIS) and their alloys with ZnS (ZCIS and AIZS, respectively) have gained high interest as alternatives to binary QDs like CdSe or CdTe because these nanocrystals are composed of weakly toxic elements and their optical properties can be controlled by varying their size and their composition^{11,13,16,121,122}. The bandgap of these QDs can be tuned from the visible to the near-infrared spectrum making them suitable for applications like photocatalysis,^{36,123} light-emitting diodes,^{109,124} solar cells,¹²⁵ bio-imaging^{75,126} or bio-sensing.^{49,127,128} Although the full-width at half-maximum (fwhm) of the photoluminescence emission, and thus the color purity, of I-III-VI₂ QDs is larger (ca. 100 nm) than that of binary QDs like CdSe, these nanocrystals not only exhibit long PL lifetimes but also large Stokes shift between the absorption and the PL emission and thus do not suffer from self-absorption or non-radiative Förster resonance energy transfer.

For II-VI QDs, the PL emission usually originates from exciton recombination. For I-III-VI₂ QDs, the PL emission mechanism is more complex and still under debate.^{31,69,78–81} Due to their heterogeneous composition, these dots contain high native defect densities which make their electronic band structures difficult to determine. For AIZS QDs, silver vacancies (V_{Ag}), sulfur vacancies (V_{S}), silver interstitial atoms (Ag_{int}) and sulfur interstitial atoms (S_{int}) have been reported and V_{S} and Ag_{int} behave as donors while V_{Ag} and S_{int} as acceptors.^{78,129,130} Therefore, the recombination of carriers trapped by intragap levels originating from surface defects, also called donor-acceptor pair recombination, markedly contributes to the PL emission. The PL emission of AIZS QDs was demonstrated to exhibit two components: (1) a fast transition with a PL lifetime of ca 25 ns originating from a delocalized valence/conduction band transition and (2) a slower component (PL lifetime higher than 185 ns) originating from the deep D-A pair transition, its contribution being dependent on the composition of the nanocrystals.⁷⁹

The incorporation of transition metal cations like Mn^{2+} in QDs allows not only to confer to these nanocrystals new properties like magnetism but also to tune their optical properties. To date, the doping of ZCIS or AIZS QDs with Mn^{2+} ions has only scarcely been investigated. When using a low amount of Mn^{2+} and a high level of Zn^{2+} ions in ZCIS or AIZS QDs, the D-A emission was suppressed and only the PL emission originating from the $\text{Mn}^{2+} \ ^4\text{T}_1 \rightarrow \ ^6\text{A}_1$ transition located at ca. 600 nm was observed.^{34,82} The temperature-dependent PL properties of Mn-doped ZCIS was also demonstrated.⁸⁵ When Mn^{2+} were adsorbed at the periphery of the CIS cores followed by the ZnS shell coating and the alloying, the obtained nanocrystals exhibited both the Mn^{2+} and the D-A pair emissions.⁸⁴

In this chapter, we report the incorporation of Mn^{2+} ions in green- or orange-emitting AIZS QDs via a one-pot reaction conducted in OAm. The loading in Mn^{2+} was varied from 25 to 75% relative to the total amount of metal cations in the dots to prepare quaternary $(\text{AgInS}_2)_x(\text{MnS})_y(\text{ZnS})_{1-x-y}$ QDs, thereafter noted Mn:AIZS. Our results show that the PL emission of Mn:AIZS QDs, originating from the D-A pair recombination, can be tuned by varying the Mn^{2+} content of the dots. Time-resolved PL was used to investigate the PL behaviors of Mn:AIZS QDs at different Mn^{2+} loadings. The small sized, highly fluorescent and magnetic Mn:AIZS QDs can easily be transferred in aqueous solution using poly(maleic anhydride-alt-1-octadecene) and other ligands, which make them of high potential for bio-imaging or cells labeling and sorting.

2.2. Experimental part

Materials

Silver acetate ($\geq 99.0\%$, Sigma-Aldrich), indium acetate (99.99%, Sigma-Aldrich), zinc acetate dihydrate ($\geq 98\%$, Sigma-Aldrich), thiourea ($\geq 99.0\%$, Sigma-Aldrich), oleylamine (OAm, technical grade, 70%, Aldrich), 1-dodecanethiol (DDT, 98%, Alfa Aesar), stearic acid (SA, 97%, Acros organics), methanol ($\geq 99.9\%$, Carlo Erba Reagents), manganese chloride tetrahydrate ($\geq 99.0\%$, Sigma), tetramethylammonium hydroxide pentahydrate (TMAH, $\geq 97\%$, Sigma), poly(maleic anhydride-alt-1-octadecene) (PMAO, 30000-50000, Sigma-Aldrich), 3-mercaptopropionic acid (MPA), dimercaptosuccinic acid (DMSA), dihydrolipoic acid (DHLA), L-cysteine (L-Cys), thiolactic acid (TLA), N-acetyl-L-cysteine (NAC), N,N-dimethylformamide (DMF), propanol, borate buffer solution and chloroform ($\geq 99\%$, Carlo Erba Reagents).

Synthesis of $(\text{AgInS}_2)_x(\text{ZnS})_{1-x}$ (AIZS) and $(\text{AgInS}_2)_x(\text{MnS})_y(\text{ZnS})_{1-x-y}$ (Mn:AIZS) QDs

$(\text{AgInS}_2)_x(\text{ZnS})_{1-x}$ (AIZS) and $(\text{AgInS}_2)_x(\text{MnS})_y(\text{ZnS})_{1-x-y}$ (Mn:AIZS) QDs were prepared according to a facile one-step method recently described³⁶, with slight modifications (Fig. 2.1). Green emitting nanocrystals were prepared by heating 0.02 mmol of AgOAc, 0.02 mmol of In(OAc)₃, 0.16 mmol of Zn(OAc)₂ and 0.2 mmol of thiourea in 3 mL of OAm containing 2 mol% of DDT. Red emitting nanocrystals were prepared by heating 0.06 mmol of AgOAc, 0.06 mmol of In(OAc)₃, 0.08 mmol of Zn(OAc)₂ and 0.2 mmol of thiourea in 3 mL of OAm containing 2 mol% of DDT. The Mn(St)₂ loading was varied (25, 50 or 75 mol% relative to the total amount of salts used). The precursors and ligands were mixed in a four-necked flask and the mixture stirred under an argon atmosphere until dissolution. Next, the temperature was increased to 180 °C and maintained for 10 min. The reaction mixture was then cooled to room temperature and centrifuged to remove large aggregates. AIZS or Mn:AIZS QDs were precipitated from the supernatant using methanol and further purified by washing with methanol and centrifugation (at least 10 times). The nanocrystals were dried under vacuum at room temperature and stored in a dark place for further characterizations.

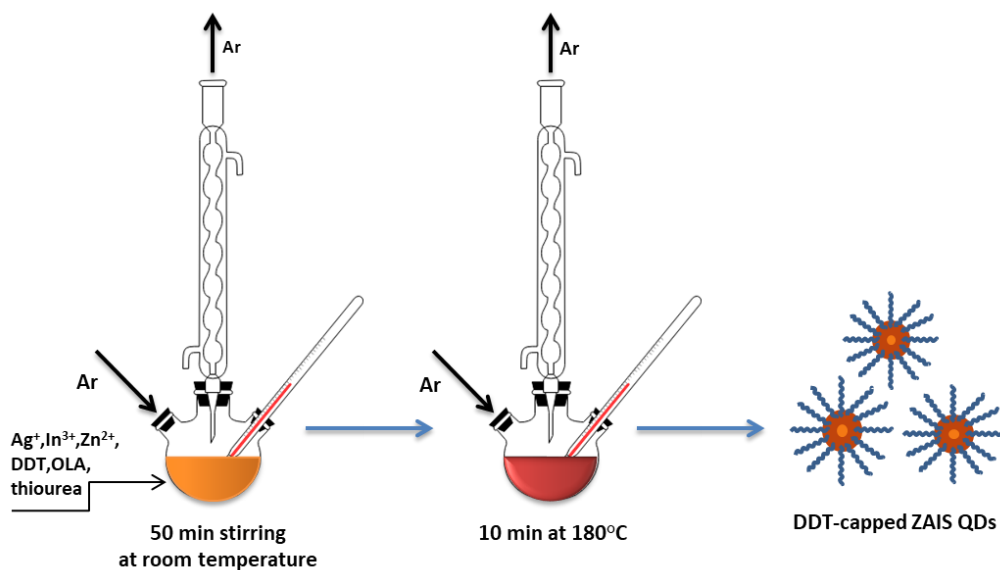


Figure 2.1. Schematic illustration of DDT-capped $(\text{AgInS}_2)_x(\text{ZnS})_{1-x}$ (AIZS) QDs synthesis

Synthesis of Mn(+2) stearate (MnSt_2)

Under a nitrogen atmosphere, stearic acid (10 mmol) in 15 mL of methanol was heated to 50–60 °C to make a homogeneous solution. After cooling the reaction mixture to room temperature, TMAH (10 mmol) in 20 mL of methanol was added and the mixture was further stirred 15 min. Next, $\text{MnCl}_2 \cdot 4\text{H}_2\text{O}$ (5 mmol) in 10 mL of methanol was added dropwise under vigorous stirring. The white MnSt_2 precipitate was collected by centrifugation, washed several times with methanol and dried under vacuum. The dried MnSt_2 was stored at 4 °C under N_2 before use.

Hydro-dispersion of AIZS@DDT QDs with PMAO

To disperse Mn:AIZS@DDT QDs in water, the amphiphilic polymer poly(maleic-alt-1-octadecene) (PMAO) was used⁷⁵ (Fig. 2.2). A mixture of Mn:AIZS@DDT QDs (6 mg), PMAO (9.4 mg) and 10 mL of chloroform was stirred vigorously for 2 h at ambient temperature. Next, the solvent was removed at room temperature by using a rotary evaporator. The obtained product was dissolved in 1 mL of chloroform and 6 mL of a 0.05 M aqueous solution of NaOH were added. This mixture was sonicated for 1 h at 50°C and next centrifuged for 15 min at 5000

rpm to remove aggregates. Next, the supernatant was centrifuged for 30 min at 15000 rpm and the pellet obtained was dispersed in a Borate Buffer solution (pH = 9) and stored at 4°C.

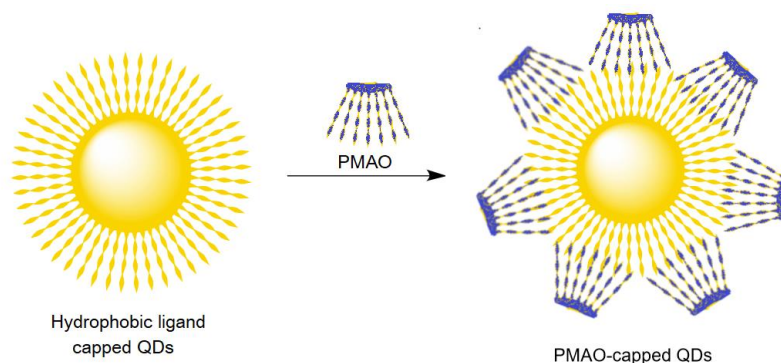


Figure 2.2. Schematic illustration of aqueous phase transfer of hydrophobic ligand capped QDs by overcoating with PMAO

Aqueous phase transfer using L-Cys

The aqueous phase transfer by ligand exchange approach was achieved by replacing the starting DDT surface ligands by L-Cysteine (or MPA (3-Mercaptopropionic acid) and GSH (Glutathione), or DMSA (Dimercaptosuccinic acid) and MPA, or DHLA (Dihydrolipoic acid) and MPA, or L-Cys (L-Cysteine) and MPA, or TLA (Thiolactic acid), or NAC (N-acetyl-L-cysteine)) (Fig. 2.3). A mixture of L-Cysteine (1.266 g, ~10.45 mmol) and 100 mg QDs were added into 3 mL of N,N-dimethylformamide (DMF) and a turbid solution was obtained. Then, the mixture was heated up slowly to 130°C, then stirred under protection of nitrogen. After 15 min the mixture became transparent. Finally, the product was precipitated by adding 10 mL of methanol (or propanol) and centrifugated at 6000 rpm for 3 min. The precipitate was dissolved in borate buffer solution (pH~9) and the solution stored. UV-Visible and PL spectra were measured in borate buffer solution.

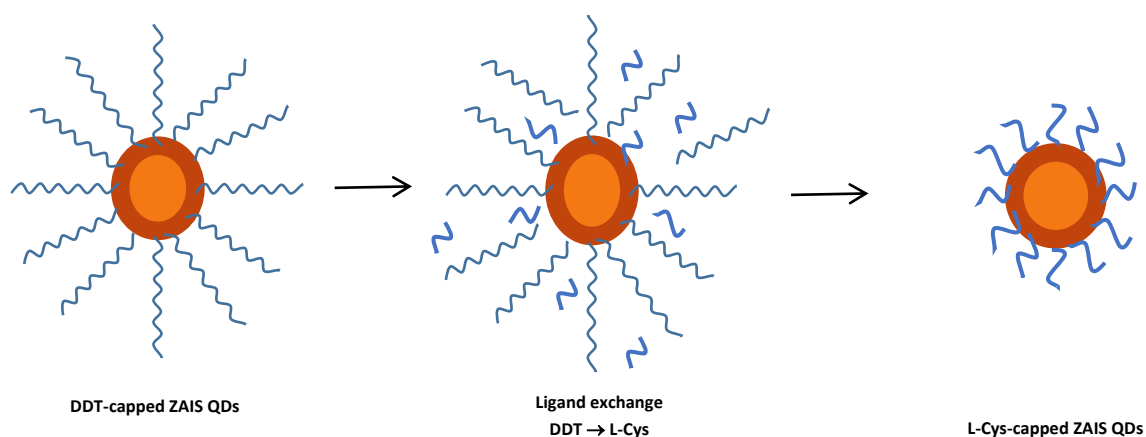


Figure 2.3. Schematic illustration of aqueous phase transfer by ligand exchange using L-Cysteine

Preparation of DHLA

In two-necked flask 0.4 mg of thioctic acid mixed with 7.8 mL (0.25 M) sodium hydrocarbonate at 0-5 °C. Then, to this mixture powder of sodium tetrahydridoborate (80 mg) was slowly added, after that the mixture was stirred for 1 hour and mixture became clear. Then, 6.7 mL toluene was added and solution appeared to be two-layered. After that solution was acidified to pH = 1 using 20% HCl. The reduced thioctic acid fully transferred to the organic phase and this whitish milky organic phase collected, then magnesium sulfide added to the solution and solution became transparent. After filtration, this solution treated solvent evaporation. Pure DHLA is a colorless transparent liquid⁶⁵.

Characterizations

TEM and HR-TEM images were taken by placing a drop of the particles in water onto an ultrathin carbon film-supported gold grids. XRD studies were carried out by using an X'Pert MPD diffractometer (Panalytical AXS). The samples were placed on zero background quartz sample holders and the XRD patterns were recorded at room temperature using Cu K α radiation ($\lambda = 0.15418$ nm). A Jeol ARM 200F microscope equipped with EDX spectrometry was used for the energy-dispersive X-ray (EDX) analysis. The actual compositions of Mn:AIZS QDs was also determined using an inductively coupled plasma-optical emission spectrometer (ICP-OES) (Thermo). The samples were prepared by digestion of the dried QDs with HCl/HNO₃ 3 : 1 (v/v)

for 12 h, followed by dilution with Milli-Q water. TGA was conducted under O₂ atmosphere from room temperature to 800 °C at a heating rate of 10 K/min using a TGA/DSC1 STAR equipment (Mettler-Toledo). X-band EPR spectra were recorded in non-saturating conditions on a Bruker ELEXSYS 500 spectrometer equipped with an Oxford instrument continuous-flow liquid–helium cryostat and a temperature control system. Typical conditions were: 5G amplitude modulation, 9.402 GHz, microwave power: 2.52 mW. Hydrodynamic QDs sizes, polydispersity indexes (PDI), and Zeta potential measurements were determined by dynamic light scattering (DLS) on a Zetasizer Nano ZS (green laser beam 532 nm) (Malvern Panalytical, UK), Cuvette DTS1070.

All the optical measurements were performed at room temperature (20±1 °C) under ambient conditions. FT-IR spectra were recorded on a Bruker ALPHA spectrometer. Absorption spectra were obtained with a Thermo Scientific Evolution 220 UV-visible spectrophotometer, while PL spectra were measured on a Horiba Fluoromax-4 Jobin Yvon spectro- fluorimeter. PL spectra were spectrally corrected and PL QYs were determined relative to Rhodamine 6G in ethanol (PL QY = 94%). For the PL excitation measurements, a Horiba Jobin Yvon Fluorolog spectrofluorimeter equipped with a Xe lamp source was used. The PL signal was analyzed by a monochromator equipped with a 150 grooves per mm grating and by a CCD detector cooled at 200 K. For the time resolved photoluminescence (TR-PL) experiments, the QDs were pumped by the 355 nm line of a frequency-tripled YAG (yttrium alu- minium garnet):Nd laser. The laser pulse frequency, energy and duration were typically equal to 10 Hz, 50 μJ and 10 ns, respectively. The PL signal was analyzed by a monochromator equipped with a 600 grooves per mm grating and by a photomultiplier tube cooled at 190 K. The rise time of the detector is equal to around 3 ns.

Magnetic properties were characterized with vibrating sample magnetometry (VSM) at temperatures of 10 and 300 K, with applied magnetic field (H) up to ±9 T. The magnetic moment values are reported in electromagnetic units (emu) per mass unit of sample.

2.3. Morphology and structure characterization

Mn:AIZS QDs were prepared via a one-pot synthetic protocol developed for AIZS QDs,³⁶ in which AgOAc, In(OAc)₃, Zn(OAc)₂ and Mn(St)₂ and thiourea precursors were thermally decomposed in the presence of a mixture of DDT and OAm used as capping ligands. Green and orange-emitting AIZS QDs were prepared using Ag/In/Zn molar ratios of 0.02/0.02/0.16 and 0.06/0.06/0.08, respectively. The amount of DDT used to control the size of the nanocrystals was fixed at 2 mol% and the loading of Mn(St)₂ was varied (25, 50 or 75 mol% relative to the total amount of salts in the reaction medium). Further increasing the loading in Mn(St)₂ was found to be deleterious on the QDs optical properties (*vide infra*). In preliminary experiments, we observed that after complete dissolution of the precursors at room temperature, the best optical properties were obtained when heating the reaction mixture at 180°C and this temperature was kept in further experiments. The reaction mixture was maintained at 180°C for 10 min before cooling to room temperature and purification of the QDs. Only weak shifts of the UV-visible absorption and of the PL emission to lower energy were observed during the 10 min of heating indicating that no significant growth of the nanocrystals occurred during that period.

Fig. 2.4 and Fig. 2.5 show X-ray diffraction patterns of orange- and green-emitting AIZS and Mn:AIZS QDs, respectively. The broadness of the peaks is indicative of the small size of the nanocrystals. The peaks located at 25.4, 26.8, 28.8, 37.4, 44.9, 48.8 and 53.2° correspond to the (120), (002), (121), (122), (320), (123) and (322) planes of the AIS orthorhombic structure, respectively (JCPDS card No 25-1328, *Pna*2₁ space group, a = 0.7008 nm, b = 0.8162 nm and c = 0.6585 nm), as demonstrated by the Rietveld refinements using the Fundamental Parameters approach built in the Topas application (Bruker XAS) shown in Fig. 2.6.

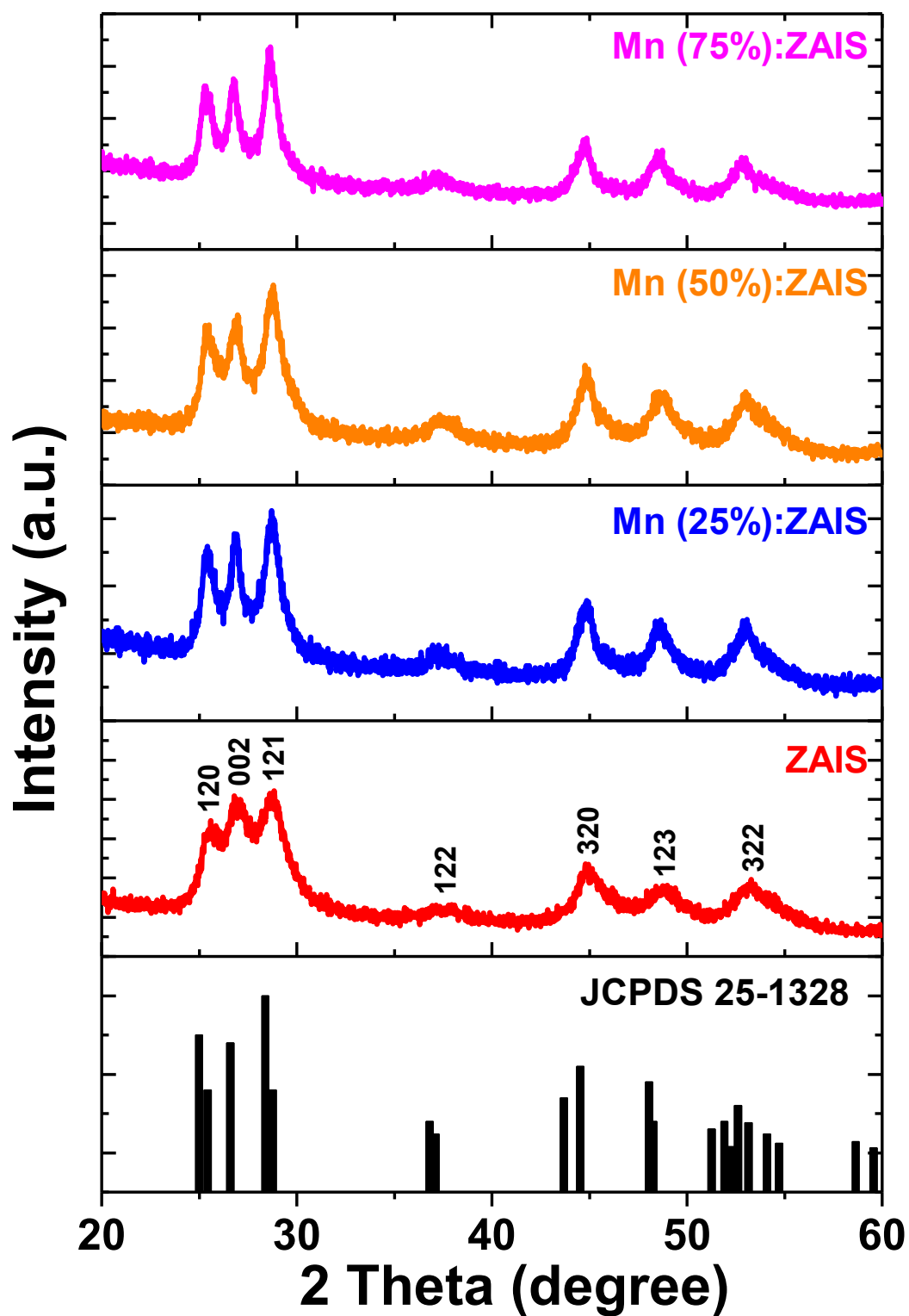


Figure 2.4. XRD patterns of red-emitting AIZS and Mn:AIZS QDs when varying the Mn^{2+} loading

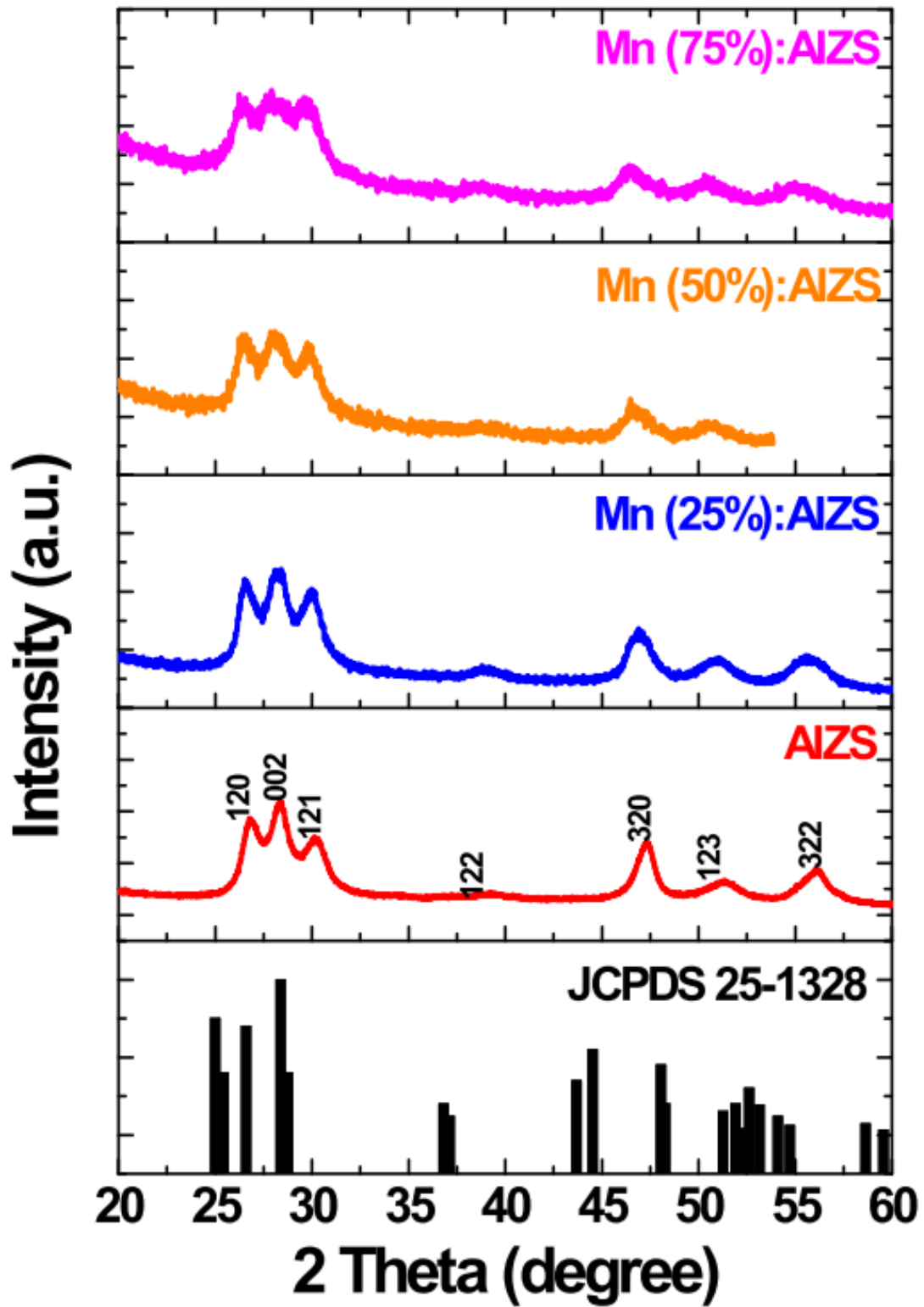


Figure 2.5. XRD patterns of green-emitting AIZS and Mn:AIZS QDs when varying the Mn^{2+} loading

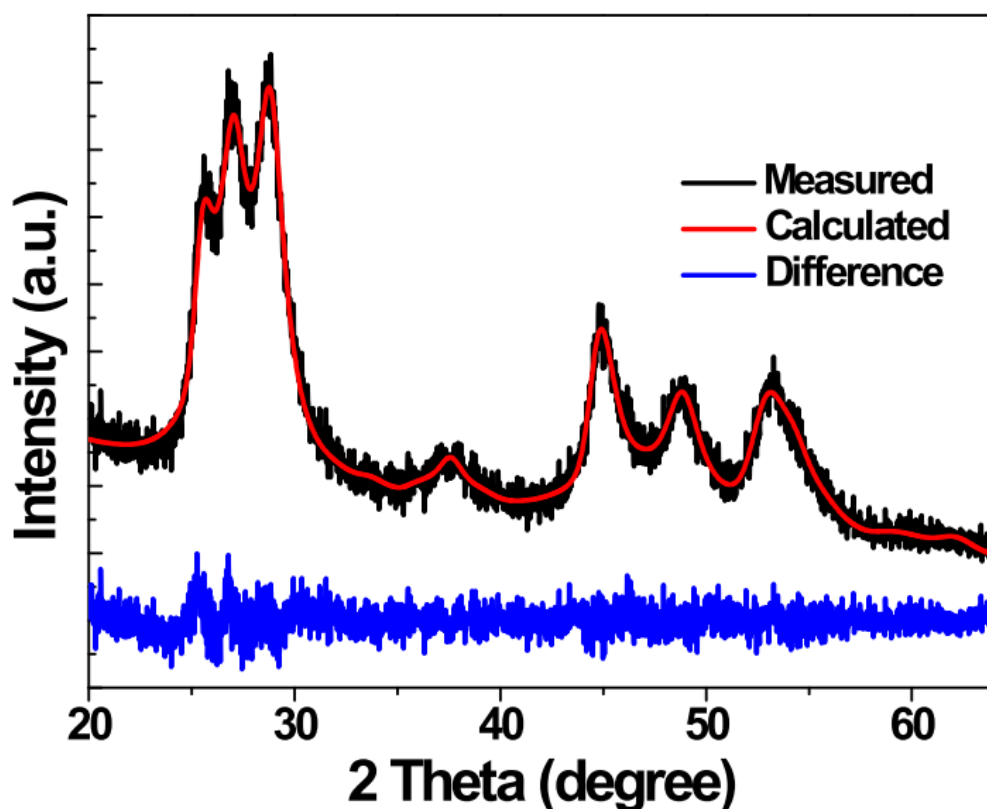


Figure 2.6. Rietveld refinement result (red curve) of the powder XRD data of AIZS QDs (black curve) using the orthorhombic phase of AgInS₂. The blue curve corresponds to the difference between the experimental data and the simulation. Data were obtained considering the lattice parameters $a = 0.7008$ nm, $b = 0.8162$ nm and $c = 0.6585$ nm and an average size of 5 nm for the QDs

These results are in accordance with the synthetic method used.³⁶ The orthorhombic phase is stable above 620°C while the tetragonal chalcopyrite structure is stable below 620 °C.¹⁶ This phase reversion likely originates from the use of OAm as solvent which modifies the chemical growth environment of the nanocrystals.¹⁶ The peaks are shifted towards larger angles compared to pure AIS crystals, due to the diffusion of Zn²⁺ and Mn²⁺ ions into the AIS core which conducts to a lattice shrinkage as the ion radii of Zn²⁺ (0.075 nm) and Mn²⁺ (0.070 nm) are smaller than that of In³⁺ (0.094 nm) and Ag⁺ (0.115 nm). No significant shift of XRD peaks was observed when varying the Mn²⁺ loading, indicating that Mn²⁺ ions were incorporated in the QDs without significant changes in their crystal structure. Finally, no impurity like Ag₂S, In₂S₃ or MnS was detected indicating that phase separation did not occur even using a high loading in Mn²⁺.

Both energy-dispersive X-ray (EDX) and inductively coupled plasma-optical emission spectrometer (ICP-OES) analyses confirm the presence of Zn, Ag, In, Mn and S elements in Mn:AIZS QDs, but the stoichiometry is different from that used for the synthesis (Table 2.1 for ICP-OES results where the actual ratios of Ag/In/Mn/Zn are normalized to the molar amount of the Ag element, and Fig. 2.7, 2.8 and Table 2.2 for EDX results). According to EDX and ICP-OES analyses, the QDs have a non-stoichiometric composition with an excess of S compared to metal ions and a defect in Ag compared to In and Zn. The high amount of S detected originates from the presence of S both in the core and in the DDT capping ligand. While equimolar amounts of Ag and In were charged in the reaction flask, AIZS QDs obtained after purification appear significantly richer in the In element (In/Ag atomic ratio of 1.54). Although In^{3+} is a hard Lewis acid according to the Pearson theory while Ag^+ and S^{2-} exhibit a soft character, this result may be related to the difference of chemical reactivity of Ag and In precursors towards S^{2-} in the reaction solution. When Mn^{2+} was loaded in the AIZS nanocrystals, the contents in Ag^+ and In^{3+} of the QDs decrease while that of Zn^{2+} remains almost constant, suggesting that a cation exchange allowing the replacement of Ag^+ and In^{3+} by Mn^{2+} occurs.

Finally, EDX analyses show that the amount of Mn^{2+} ions loaded in the nanocrystals is significantly lower than the amount used for the synthesis (1.82, 5.37 and 11.89 at.% of Mn^{2+} were detected when using 25, 50 and 75% of Mn^{2+} relative to the total amount of metallic salts used for the synthesis), suggesting that Mn^{2+} ions poorly incorporate into the AIZS crystal lattice.

Table 2.1. Theoretical and actual Ag/In/Mn/Zn ratios determined by ICP-OES for orange-emitting AIZS QDs when varying the Mn^{2+} loading QDs

QDs	Ag/In/Mn/Zn ratio in precursors	Actual ratios of Ag/In/Mn/Zn
AIZS	1/1/0/1.33	1/1.54/0/1.80
Mn (25%) : AIZS	1/1/0.83/1.33	1/1.55/0.17/1.97
Mn (50%) : AIZS	1/1/1.66/1.33	1/1.62/0.55/2.02
Mn (75%) : AIZS	1/1/2.5/1.33	1/1.47/1.44/2.38

Table 2.2 Atomic ratios in AIZS and Mn:AIZS QDs determined by EDX analyses

Element	Theoretical dopant percentage in Mn			
	0%	25%	50%	75%
Zn	20.57	20.82	19.51	19.62
Ag	11.41	10.54	9.62	8.24
In	17.64	16.43	15.63	12.18
S	50.04	50.39	49.85	48.07
Mn	-	1.82	5.37	11.89

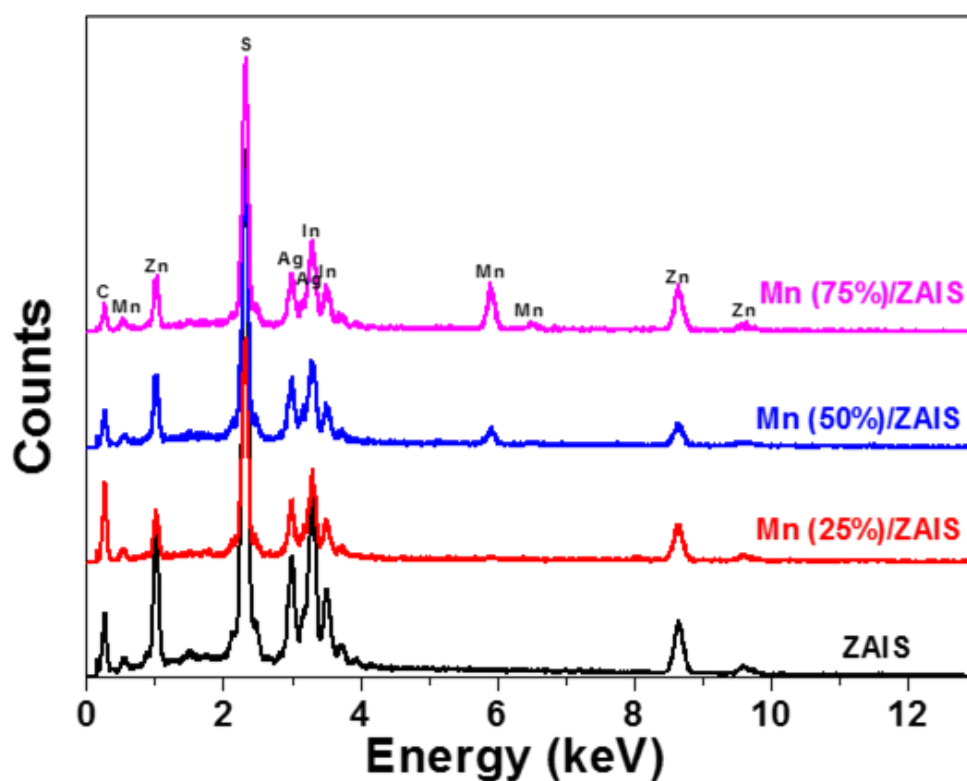


Figure 2.7. EDX analyses of orange-emitting AIZS and of Mn:AIZS QDs loaded with 25, 50 and 75% Mn²⁺, respectively

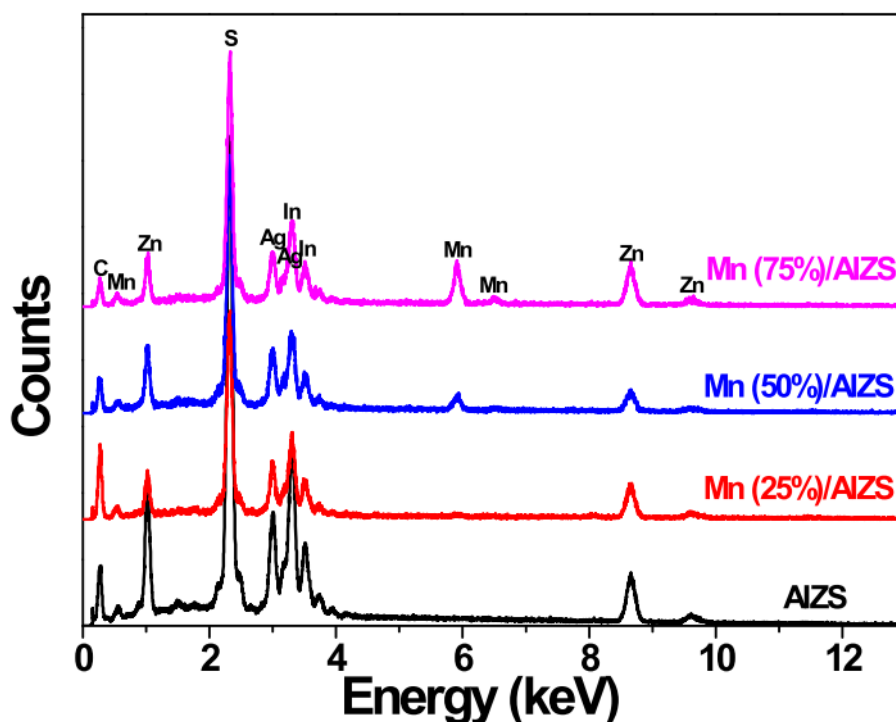


Figure 2.8. EDX analyses of orange-emitting AIZS and of Mn:AIZS QDs loaded with 25, 50 and 75% Mn²⁺, respectively

Low temperature (20 K) X-band electron paramagnetic resonance (EPR) spectra recorded on the Mn : AIZS QDs further support the loading of Mn²⁺ in the nanocrystals (Fig. 2.9). In all cases, a broad signal centered on $g = 2$ is detected. The broadness of the signal is typical for Mn-doped AIZS or CIZS QDs and originates from the complex environment of Mn²⁺ surrounded by Ag⁺, In³⁺ and Zn²⁺ ions³⁴. While poorly resolved hyperfine coupling can be observed for 50% and 75% loading in Mn²⁺, the spectrum of the Mn (25%):AIZS QDs displays a set of six lines separated by about 80 G, which is related to the coupling of the electronic spin with the 5/2 nuclear spin of Mn²⁺.

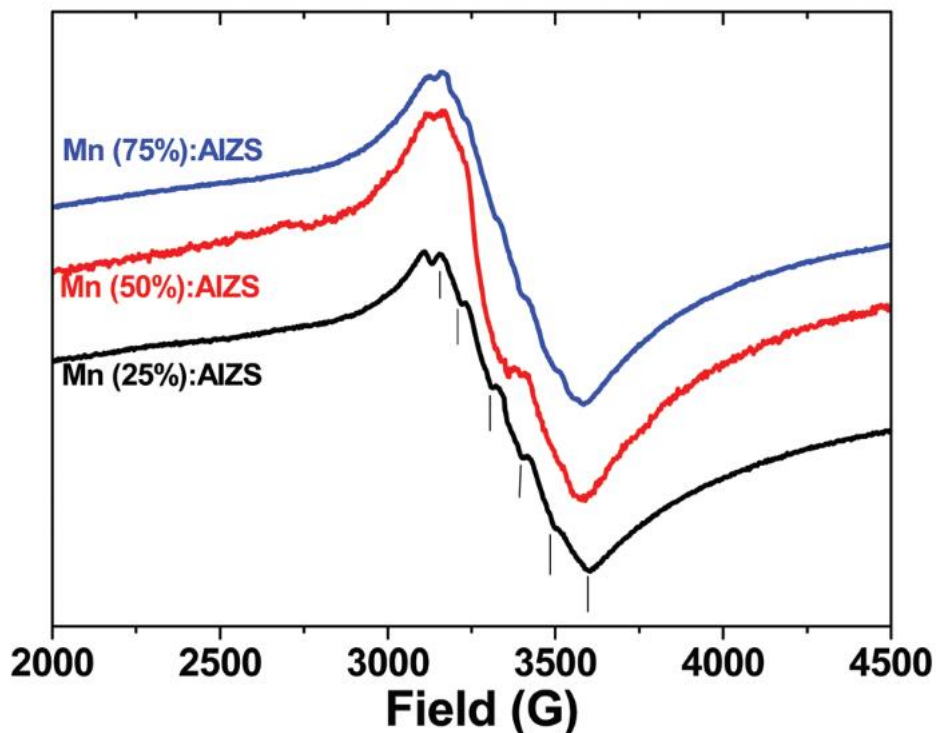


Figure 2.9. EPR spectra recorded at 20 K of orange-emitting AIZS QDs loaded with 25, 50 and 75% Mn^{2+}

Transmission Electron Microscopy and High-Resolution TEM were used to characterize the size and the shape of AIZS and Mn:AIZS QDs. Fig. 2.10 shows the results obtained with orange-emitting AIZS QDs when increasing the loading percentage in Mn^{2+} from 25 to 75%. The average size of the nanocrystals was determined by analyzing at least 100 nanocrystals in the TEM images and, regardless of the Mn-loading percentage, was found to vary between 3.3 and 3.7 nm (see Fig. 2.11 for the size distributions). Mn:AIZS QDs shape is irregular and spherical, ellipsoidal and triangular particles can be observed in each sample. The clear lattice fringes in the associated HR-TEM images confirm that Mn:AIZS QDs are single crystals. The lattice space measured is of ca. 0.35 nm and corresponds to the (120) crystal plane of orthorhombic AgInS_2 . The high crystallinity of the dots is further evidenced from the selected area electron diffraction (SAED) patterns (insets of Fig. 2.10) which show a set of concentric rings corresponding to the diffraction of the various crystalline planes of the nanocrystals.

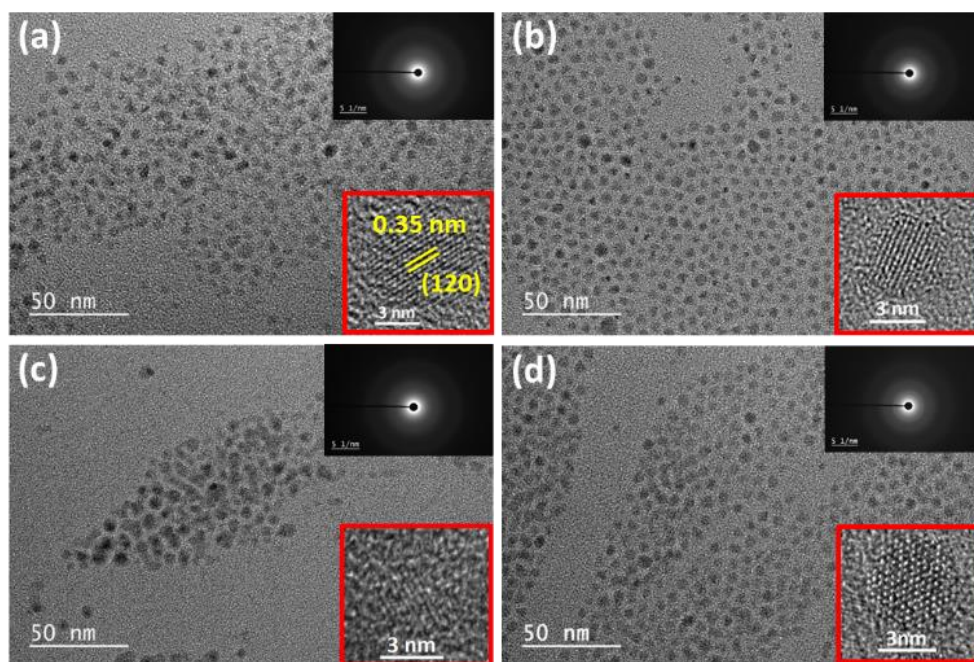


Figure 2.10. TEM and HR-TEM images of (a) orange-emitting AIZS and (b-d) Mn:AIZS QDs loaded with 25, 50 and 75% Mn²⁺, respectively. The insets show SAED patterns

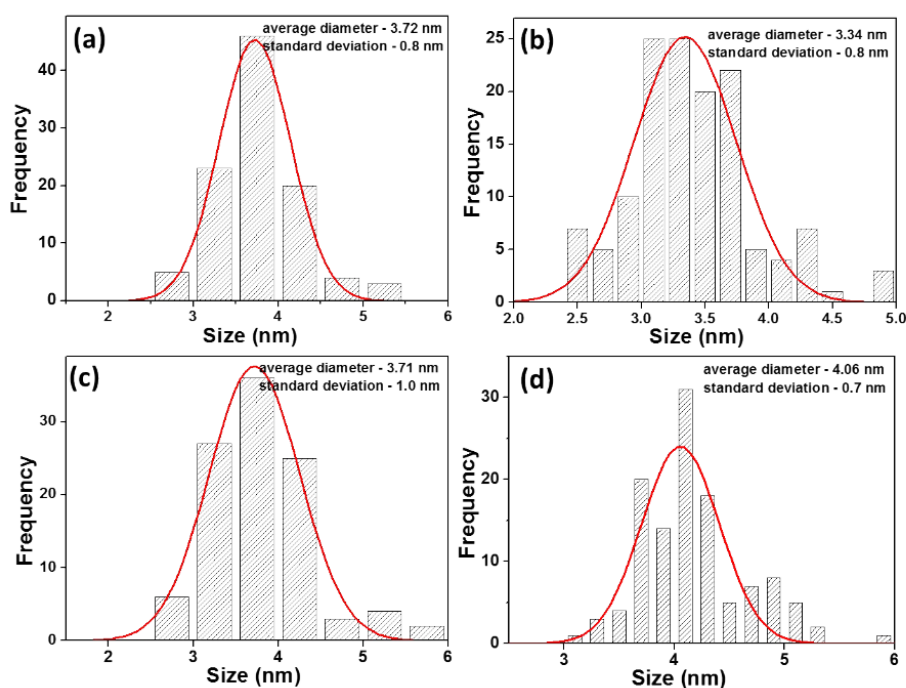


Figure 2.11. Average sizes and standard deviations of (a) orange-emitting AIZS, (b) Mn (25%):AIZS, (c) Mn (50%):AIZS and (d) Mn (75%):AIZS QDs

A representative thermogravimetric analysis (TGA) of the Mn (50%):AIZS QDs is given in Fig. 2.12a and shows three mass loss regions. The two first mass losses (between 250-350°C and 360-460°C) likely originates from the removal of neutral ligand (DDT and OAm) anchored at the surface of the dots while the third weight loss might originate from the removal of ionic ligand (DDT covalently bound to surface Zn atoms). The remaining mass (ca. 73%) corresponds to the inorganic Mn:AIZS core and indicates that the QDs are covered by a relatively thick shell of ligands. The presence of the DTT and OAm ligands at the periphery of the dots was further confirmed by FT-IR (Fig. 2.12b). The symmetric and antisymmetric C-H stretching of methylene groups of OAm and DDT can be observed at 2916 and 2850 cm^{-1} , respectively, while the in-plane deformation of these bonds can be observed at 1453 cm^{-1} . The weak signal at 3002 cm^{-1} is characteristic of the ethylenic C-H stretching of OAm. The N-H stretching and bending appear at 3209 and 1614 cm^{-1} , respectively. The C-S stretching of DDT at 1375 cm^{-1} further confirms the co-capping of the dots with OAm and DDT.

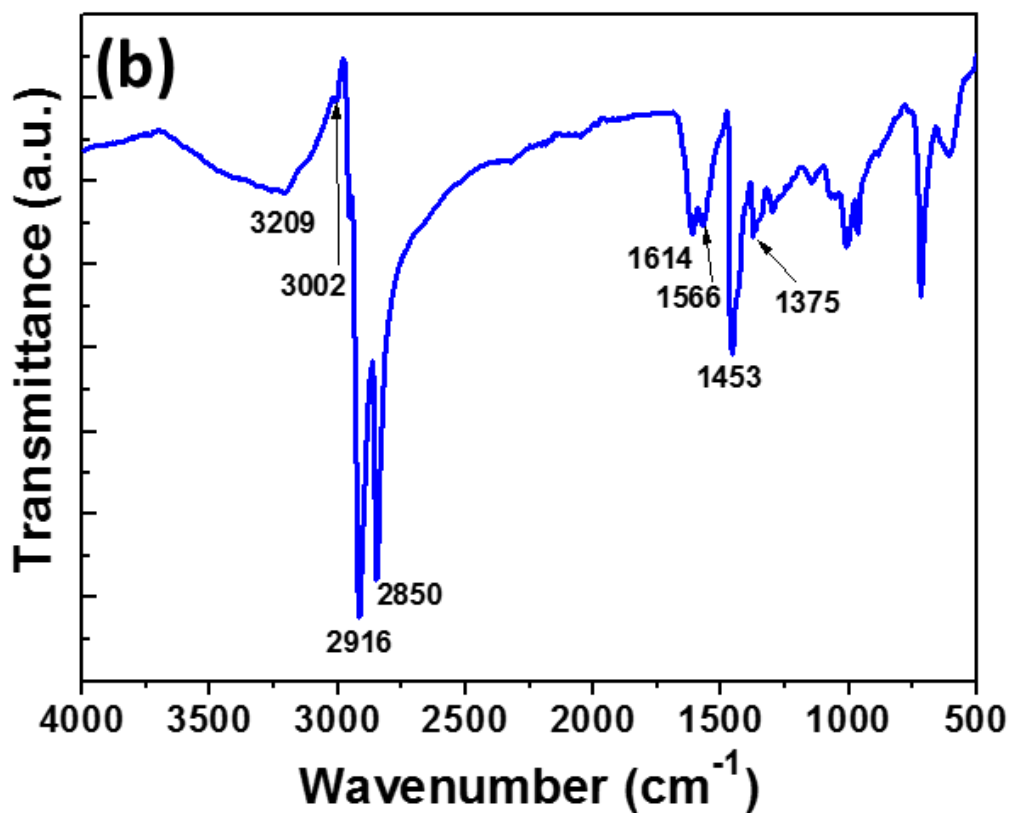
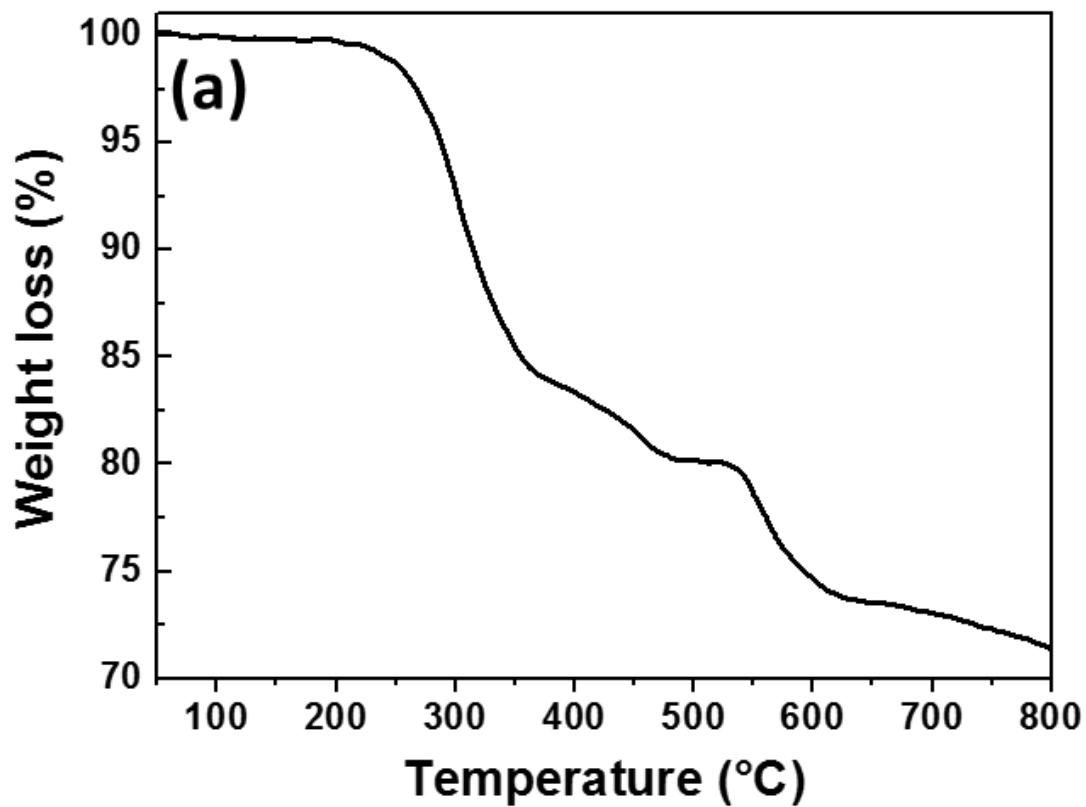


Figure 2.12. TGA trace (a) and FT-IR spectrum (b) of Mn (50%):AIZS QDs

2.4. Optical properties

Fig. 2.13 shows the UV-vis absorption and the PL emission spectra of green- and orange-emitting AIZS QDs and the evolution of these spectra when increasing the loading in Mn^{2+} from 25 to 75%. All spectra were recorded using nanocrystals obtained after 10 min heating at 180°C and purified by precipitation and washing with methanol. The broad absorption without a marked exciton band is typical of ternary like AIS and quaternary like AIZS QDs and originates from the distribution of vibrational states rather than from size and/or composition inhomogeneity of the dots.^{13,16,131} A slight shift to lower energies is observed when increasing the loading in Mn^{2+} , which suggests a decrease of the bandgap. The bandgap values were determined from the Tauc plots of $(\alpha h\nu)^2$ vs $h\nu$ (where α is the absorption coefficient and $h\nu$ is the photon energy) and were found to decrease from 2.52 to 2.31 and from 2.93 to 2.83 eV for orange- and green-emitting AIZS QDs, respectively, when loading these nanocrystals with 25, 50 and 75% Mn^{2+} (Fig. 2.15). These values are higher than that of bulk AgInS_2 in orthorhombic phase (1.87 eV) due to the quantum confinement effect in AIZS and Mn:AIZS QDs. The steady state PL emission spectra of green- and orange-emitting AIZS QDs are broad and their fwhm are of ca. 100 and 138 nm, respectively (Fig. 2.13a-b). The maximum of the PL peaks are located at 540 and 660 nm and the PL QYs are 46 and 62% for the green and the orange-emitting QDs, respectively. As previously mentioned, the broadness and the asymmetry of the spectra originate from the numerous D-A transitions and trap-state emissions in these nanocrystals.^{31,69,78-81} For both QDs, a marked Stokes shift is observed, indicating that the self-absorption is minimal and further corroborating that the PL emission is not a bandgap emission.

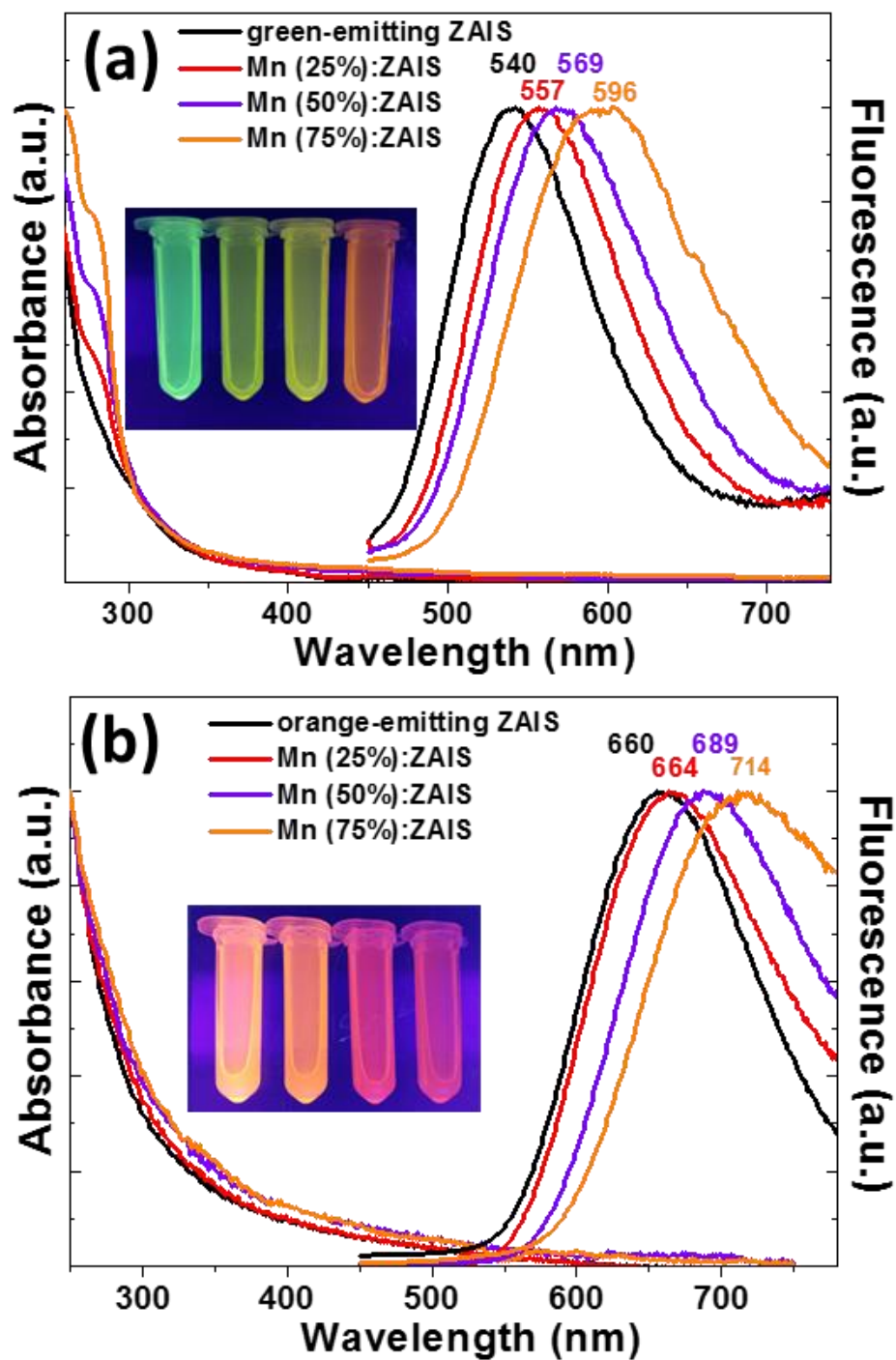


Figure 2.13. UV-visible absorption and normalized PL emission spectra of (a) green and (b) orange emitting QDs when increasing the Mn²⁺ loading from 25 to 75% ($\lambda_{\text{exc}} = 400$ nm). The insets are digital photographs of the dots dispersed in chloroform under UV light illumination

When loading these AIZS QDs with Mn^{2+} , a continuous red-shift from 540 to 596 nm and from 660 to 714 nm is observed compared to green- and orange-emitting QDs, respectively, indicating that Mn^{2+} ions contribute to the PL emission mechanism. However, contrary to previous reports describing the preparation of Mn-doped AIZS QDs, the ${}^4\text{T}_1 \rightarrow {}^6\text{A}_1$ emission of Mn^{2+} ions in the AIZS host was not observed at ca. 600 nm, which suggest that Mn^{2+} ions incorporated in AIZS QDs via the synthetic method developed in this work do not quench the D–A pair emission.^{34,82} PL excitation (PLE) spectra of AIZS and Mn (25%):AIZS QDs are shown in Fig. 2.14. A broad signal with a maximum located at ca. 520 nm was observed for both QDs, which is in good agreement with previously described PLE spectra of AIZS QDs emitting in red region.^{49,69} PLE have been also measured (not shown here) for an emission from 550 nm to 900 nm with a step equal to 4 nm for AIZS and Mn:AIZS and the spectra show the same shape. The similar profiles confirm that the Mn^{2+} -related ${}^4\text{T}_1 \rightarrow {}^6\text{A}_1$ transition is not involved in the PL excitation and emission of Mn:AIZS QDs. We assume that the PL red-shift observed when increasing the dopant loading likely originates from the Mn^{2+} position in the AIZS host and thus from the synthetic method used.

The PL shifts do not originate from a size increase of the dots as previously demonstrated by TEM (Fig. 2.10 and 2.11) but rather from a decrease of the bandgap as previously demonstrated. Simultaneously, their shape was also found to be dependent on the Mn^{2+} loading and the fwhm of the PL peak increases up to 144 and 170 nm for Mn:AIZS QDs emitting at 596 and 714 nm, respectively, while it should be of ca. 60 nm for the Mn d-state emission.²⁴ The PL intensity of Mn:AIZS QDs remains high but a continuous decrease of the PL QY is observed when increasing the Mn^{2+} content. For green-emitting AIZS, the PL QY decreases from 46 to 38, 31 and 13% for theoretical loadings in Mn^{2+} of 25, 50 and 75%. A similar behavior is observed starting from orange-emitting QDs (decrease from 62 to 53, 41 and 16%, respectively).

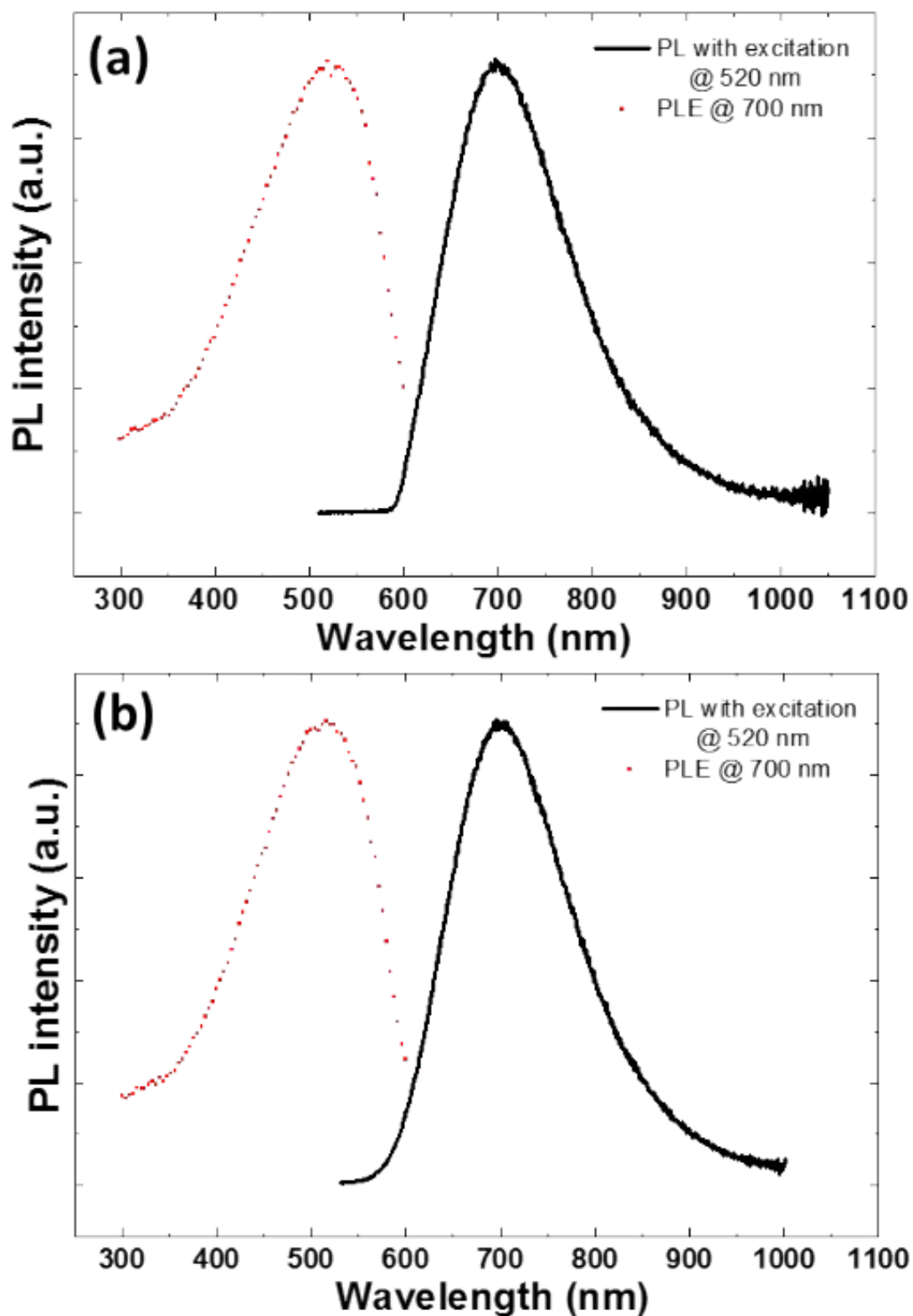


Figure 2.14. PL excitation (dotted red lines) and PL emission (black lines) spectra of (a) AIZS and (b) Mn (25%):AIZS QDs in chloroform. Excitation spectra were monitored at the corresponding emission peak of each sample taken from Fig. 2.13

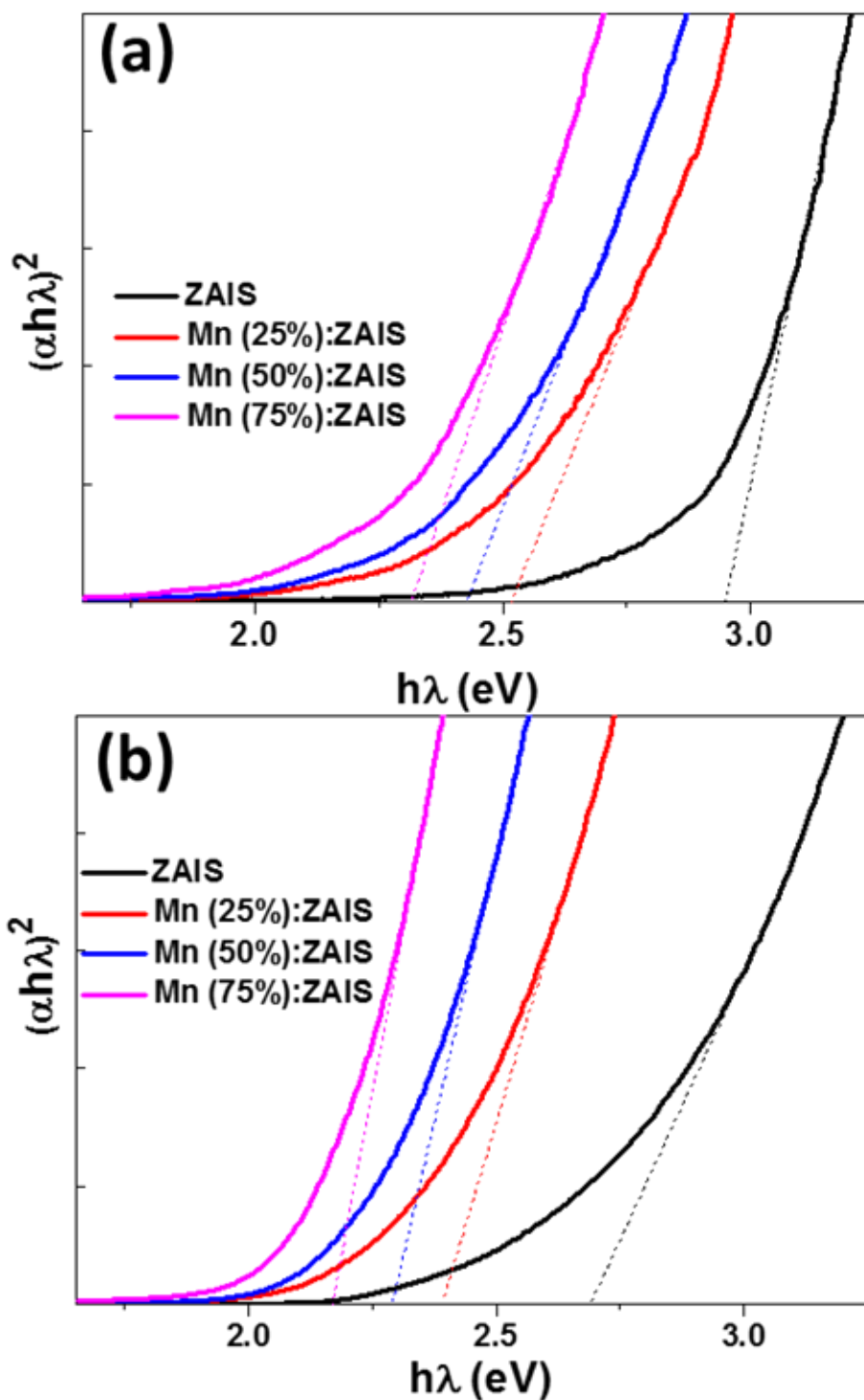


Figure 2.15. Determination of the optical bandgap of AIZS and Mn:AIZS QDs when increasing the loading in Mn^{2+} ions in (a) green-emitting AIZS QDs and (b) orange-emitting AIZS QDs

The PL mechanism for AIZS QDs is presented schematically in Fig. 2.16a and shows the radiative D-A pair recombination. On the basis of the previously described results, the position

of the trap state A relative to the $\text{Mn}^{2+} {}^6\text{A}_1$ state determines the recombination process.^{31,34,69,78-81} If the trap state A is located below the $\text{Mn}^{2+} {}^6\text{A}_1$ state, the typical ${}^4\text{T}_1 \rightarrow {}^6\text{A}_1$ transition of Mn^{2+} yielding an orange PL at ca. 600 nm should be observed (Fig. 2.16b).³⁴ The dependence of the PL emission peak with the Mn^{2+} content suggests that a new Mn^{2+} dependent trap state located above the ${}^6\text{A}_1$ state and with a gradually higher energy appears while increasing the Mn^{2+} loading of AIZS QDs as demonstrated by the continuous red-shift of the PL peak with the increase of the Mn^{2+} content (Fig. 2.16c).

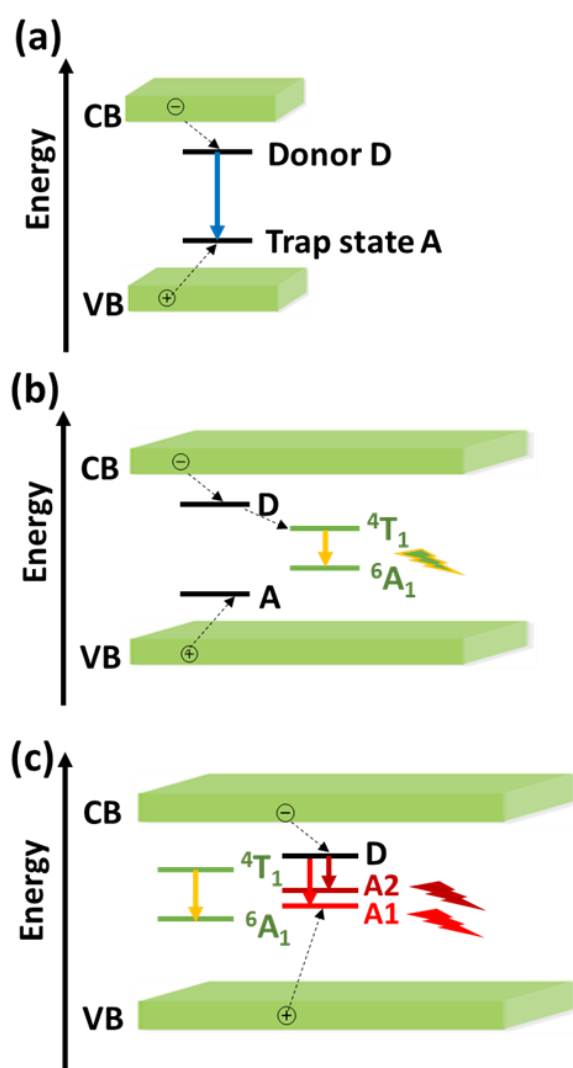


Figure 2.16. Schematic illustration of the PL mechanism of (a) AIZS and (b-c) Mn:AIZS QDs. The solid arrows correspond to radiative relations while the dotted arrows show the non-radiative relaxations

To further study the mechanism of the PL emission, time-resolved PL decay measurements were carried out. Representative time-resolved PL decay spectra were recorded at the PL emission maxima of orange-emitting AIZS and Mn:AIZS QDs obtained from Fig. 2.13a and results are shown in Fig. 2.17. The data were best fitted using a bi-exponential function $I(t) = A_1 \exp(-t/\tau_1) + A_2 \exp(-t/\tau_2)$ where τ_1 and τ_2 are the time constants of the PL and A_1 and A_2 the normalized amplitudes of the components. The fitting parameters are summarized in Table 2.3. The average PL lifetimes (τ_{av}) were determined using $\tau_{av} = (A_1\tau_1 + A_2\tau_2) / (A_1 + A_2)$ and are in the typical range of 1 to 10 μs^{-1} generally observed for AIZS nanocrystals due to the numerous intrinsic trap states (V_S and $A_{g_{int}}$ acting as donors while V_{Ag} and S_{int} as acceptors).^{31,69,78–81,89,126} These results further confirm that the PL emission does not originate from Mn^{2+} ions which exhibit a millisecond PL lifetime.^{132,133}

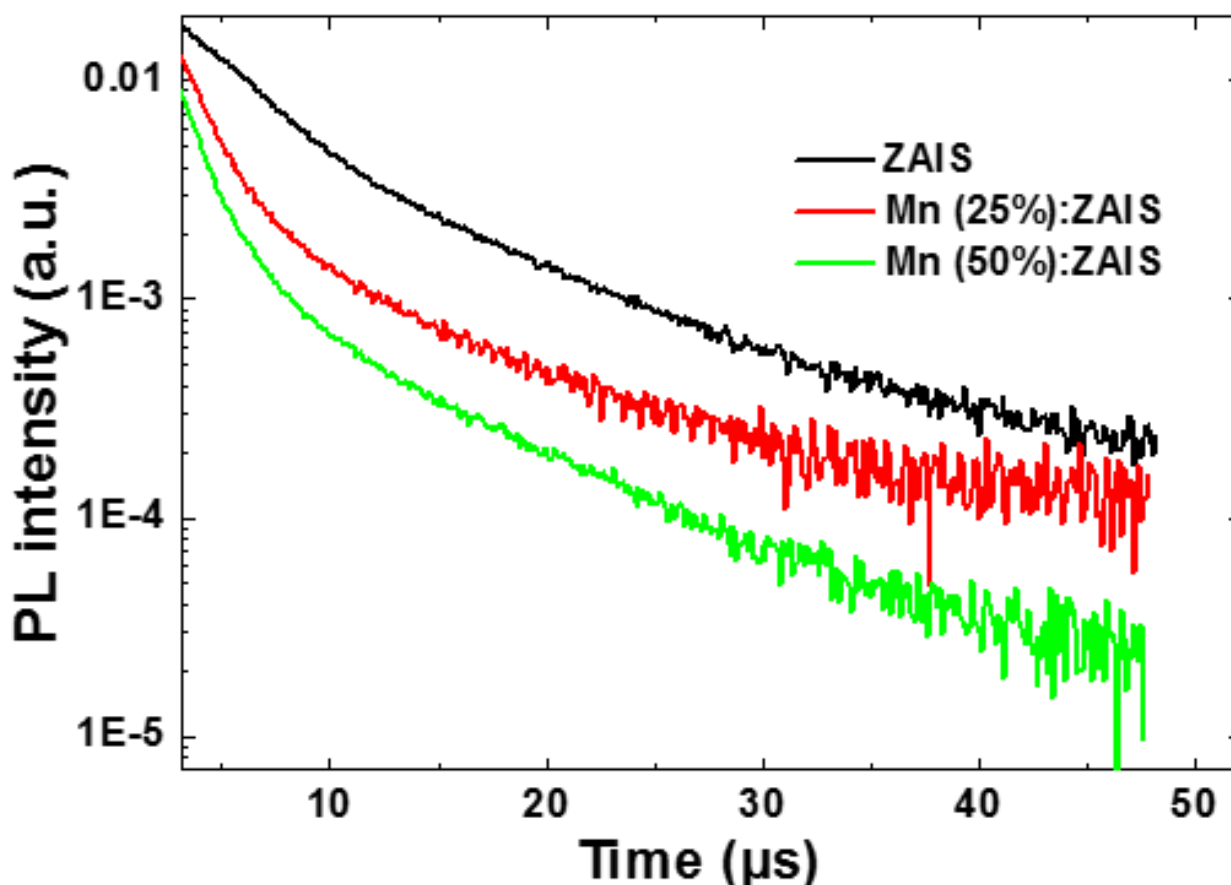


Figure 2.17. PL lifetimes of orange-emitting AIZS and of the corresponding Mn:AIZS QDs at the PL maximum wavelength

Table 2.3. Lifetimes and fitting parameters of orange-emitting AIZS and Mn:AIZS nanocrystals

Sample	A₁ (%)	τ_1 (μs)	A₂ (%)	τ_2 (μs)	τ_{av} (μs)
AIZS	54.1	2.738	45.9	10.143	6.14
Mn (25%):AIZS	75.8	1.471	24.2	8.146	3.09
Mn (50%):AIZS	87.8	1.344	12.2	7.832	2.14

These long PL lifetimes clearly differentiate AIZS QDs from binary QDs like CdSe or CdTe that exhibit a short PL lifetime of tens of nanoseconds originating from band to band emission.¹³⁴ As previously described, two radiative channels were observed.⁹⁵ The fast decay component τ_1 corresponds to surface trap state recombination and the slow decay component τ_2 to the D-A recombination originating from the defect states within the bandgap. Until 50% loading in Mn²⁺, which corresponds to the dots with a PL QY only weakly affected by the Mn²⁺ incorporation (*vide supra*), a decrease of the decay time of both components is observed. This decrease is however more pronounced for the fast component, suggesting a more pronounced influence of Mn²⁺ ions on the surface-related states. Moreover, its amplitude A₁ increases, indicating that the observed evolution of the time-resolved PL can be interpreted by the promotion of energy migration from Mn²⁺ to the surface quench centers as observed in previous studies.⁸⁴

2.5. Magnetic properties

AIZS QDs do not display any magnetic response with the applied field. When Mn^{2+} is incorporated within the nanocrystals, and regardless of the loading percentage, the magnetic moment (M) is the merge of a ferromagnetic signal (evident from the hysteresis at low fields in the inset of Fig. 2.18b, d and f) and of a paramagnetic and/or superparamagnetic signal (evident from the overall Langevin-like shape of the curves at high fields). Previous works demonstrated that nanocrystals doped with Mn^{2+} display a ferromagnetic behavior^{135–138} whereas the Mn^{2+} ions are well known to be paramagnetic.^{133,139} The coercivity H_c (the applied field required for zero net moment) and the remanence M_r (the magnetic moment at zero applied field) can both be trivially extracted from the hysteresis loops (Fig. 2.18b and d). The samples synthesized at high concentration of Mn^{2+} exhibit the highest saturation magnetization, up to 0.25 emu/g (at 10 K) (Fig. 2.18a), and decrease above 0.02 emu/g at room temperature. The decrease of the amount of Mn^{2+} leads to the decrease of the M_s values below 0.17 emu/g, and the temperature dependence is drastically increased. All Mn:AIZS QDs exhibit remanent magnetization (Fig. 2.18a and c), up to 0.001 emu/g at 10 K. Fig. 2.18e depicts the behavior of the Mn (25%):AIZS doped sample, no influence of the temperature on the magnetic behavior of the QDs can be evidenced. The extraction of saturation magnetization (M_s) from the curves is non-trivial, since saturation was not achieved in the system due to persisting paramagnetic signal on top of the ferromagnetic signal of interest.

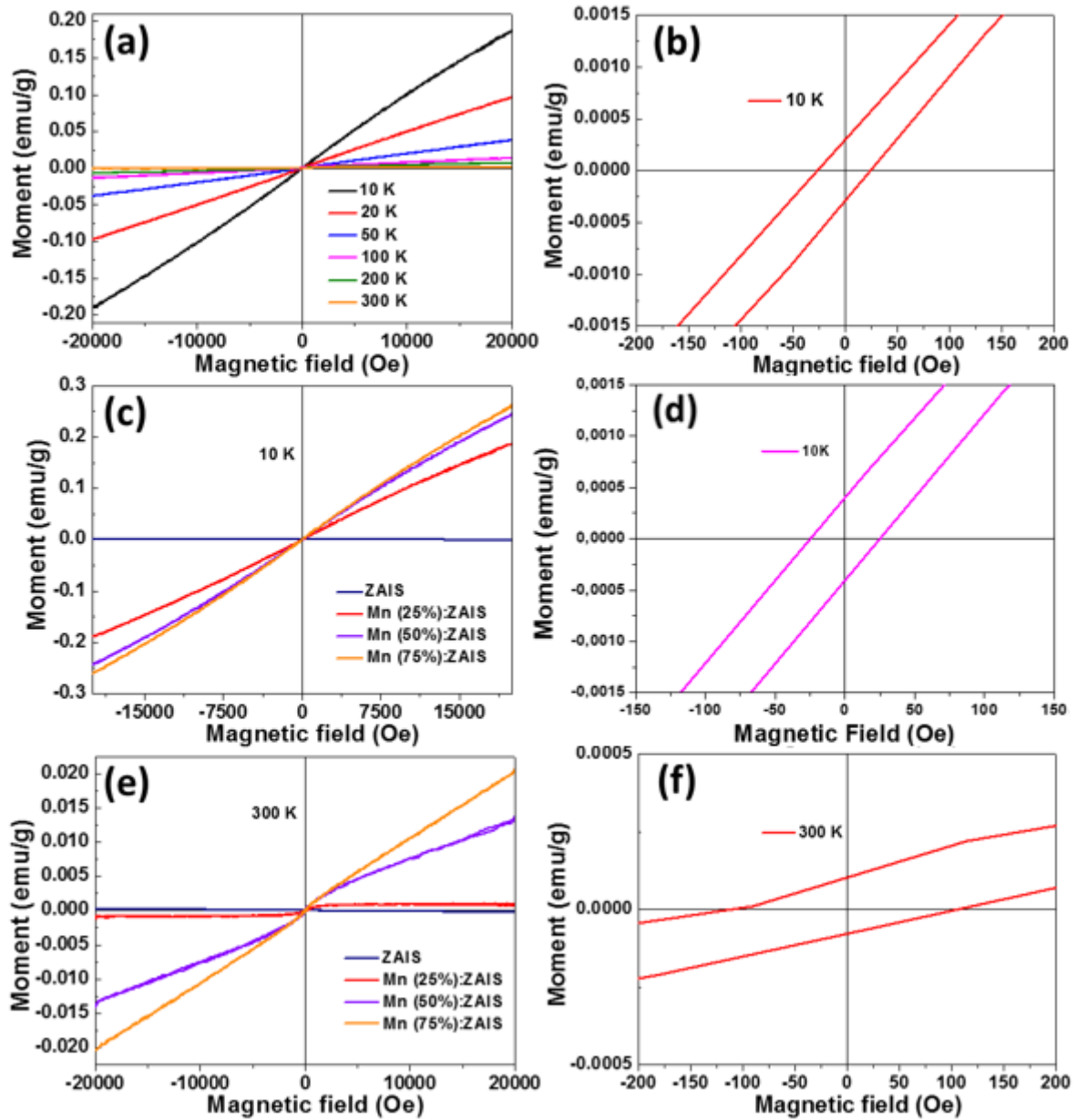


Figure 2.18. (a) M(H) loop curves of Mn (25%):AIZS QDs at different temperatures and (b) the magnetic properties at zero field. (c) and (e) are the M(H) loop curves of AIZS and Mn:AIZS QDs at 10K and 300K, respectively. (d) and (f) describe the magnetic properties at zero field of 75% and 25% Mn-doped AIZS QDs, respectively

2.6. Transfer of Mn:AIZS QDs in aqueous phase

To demonstrate the potential of Mn:AIZS QDs for biological applications, the DDT and OAm-capped Mn:AIZS QDs were transferred into aqueous phase using the amphiphilic PMAO polymer.⁷⁵ Micelles were first produced by the association of the hydrophobic alkyl chains of PMAO with those of DDT and OAm through self-assembling in chloroform (Fig. 2.2). After evaporation of the solvent, maleic anhydride units were hydrolyzed into carboxylate functions. This hydrophilic corona allows the successful transfer of Mn:AIZS QDs in water without alteration of their optical properties. Empty micelles were removed by ultracentrifugation at 15000 rpm and the PMAO-encapsulated Mn:AIZS QDs can easily be dispersed in water, PBS or borate buffer. These colloidal dispersions can be stored for months at 4 °C indicating the high stability of the micelles. Except for the Mn (75%):AIZS QDs, a red-shift of the PL emission is observed but the PL QYs were not significantly altered (59, 51, 40 and 11% for AIZS and Mn:AIZS loaded with 25, 50 and 75% Mn²⁺, respectively) (Fig. 2.19). The red-shift observed likely originates from the compact association of QDs in the core of the micelle in which the light emitted by the smallest nanocrystals is adsorbed by the largest ones that emit a higher wavelength like a Förster resonance energy transfer process.^{120,140}

The stability of PMAO-coated undoped AIZS QDs was also studied in the pH range from 3 to 13 (Fig. 2.20). As can be seen from the figure, the positions of the PL peaks change only insignificantly. The PL intensity of the particles increased and reached the highest value at pH of 9 and decreased, but shows the highest values within the physiologically appropriate pH range of 5 to 9 and stays stable in the basic medium until pH of 12.

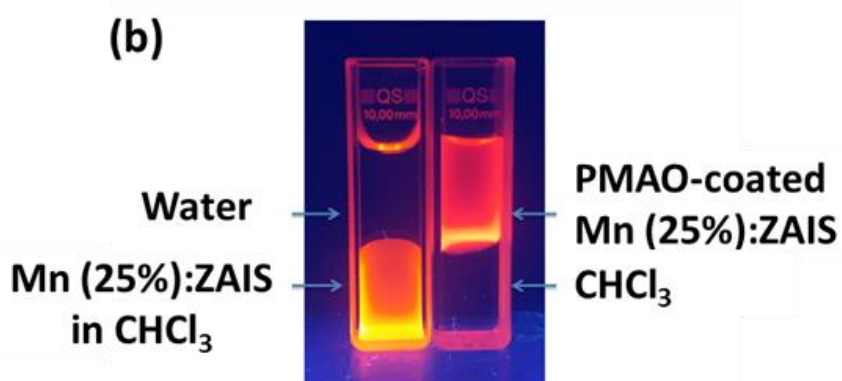
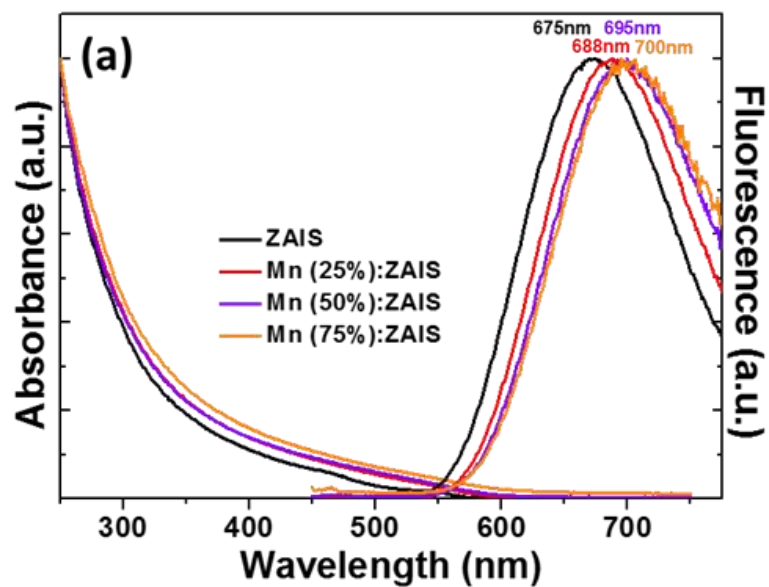


Figure 2.19. (a) UV-visible and PL emission spectra of AIZS and Mn:AIZS QDs after transfer in water using the PMAO polymer and (b) digital photograph taken under UV light illumination of Mn (25%):AIZS QDs before and after their transfer into water

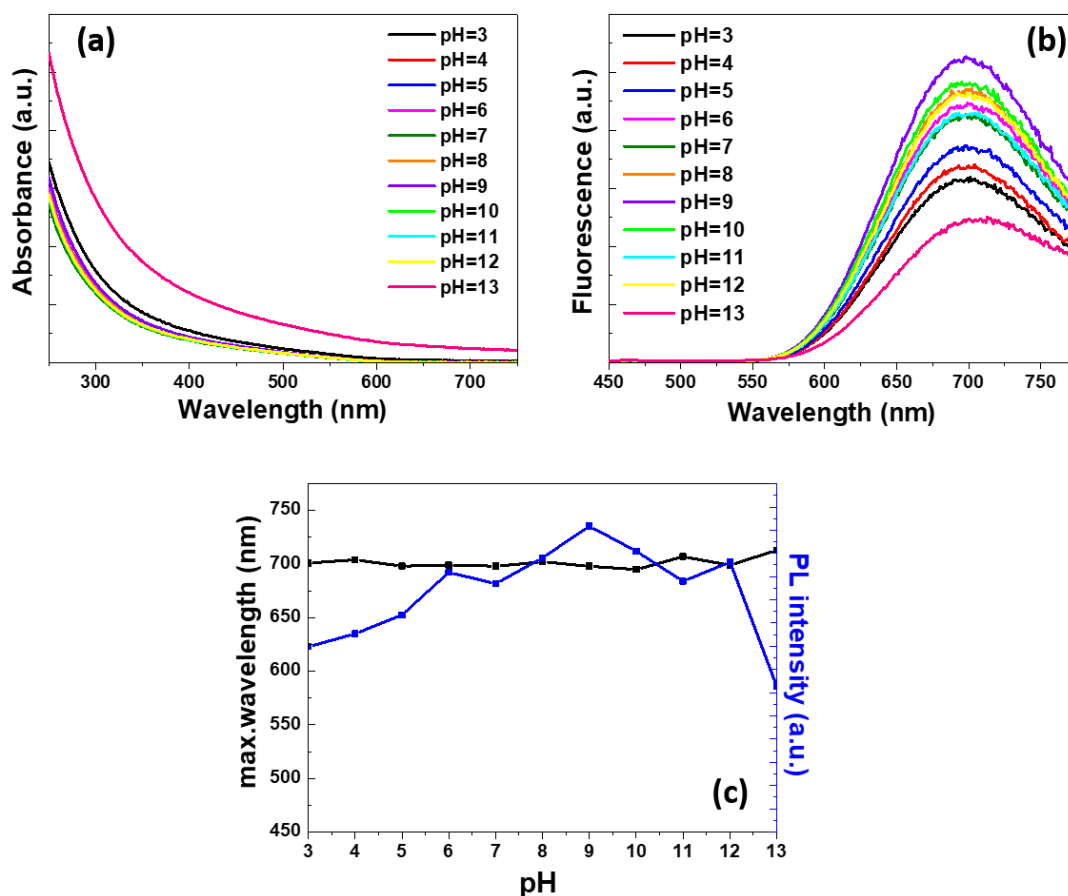
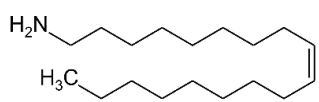
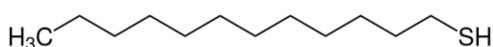
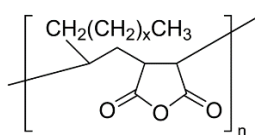
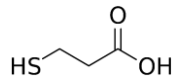
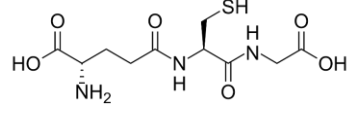
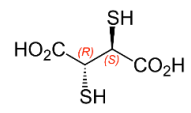
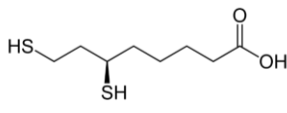
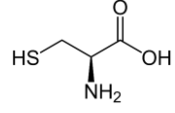
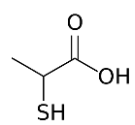
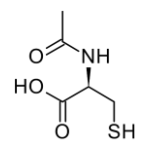


Figure 2.20. UV-Vis (a) and PL (b) spectra of undoped AIZS QDs water transferred using PMAO at different pH, and the PL peak positions and the PL intensities changing (c) in media with different pH values

The other ligands, listed in Table 2.4, were used to transfer DDT and OAm-capped AIZS QDs into aqueous media using the ligand exchange approach (Fig. 2.21). The hydrodynamic diameters and zeta-potential values of the water transferred AIZS QDs are demonstrated in Fig. 2.22.

The stability of the undoped AIZS QDs water transferred by L-Cys-coating was tested at pH range between 3 to 13 (Fig. 2.23). According to the results, the PL intensity of these QDs stays stable at the physiological relevant pH range of 5 to 9, with highest PL QY value of 40% at pH of 9. The PL peak positions also can be considered not changed in this physiological relevant pH range of 5 to 9, which demonstrates the suitability of these particles for use in biological applications.

Table 2.4. The structural and chemical formulas of the ligands used for the synthesis and ligand exchange

Names	Chemical formulas	Structural formulas
Oleylamine	$C_{18}H_{37}N$	
1-Dodecanethiol	$C_{12}H_{26}S$	
Poly(maleic anhydride- <i>alt</i> -1-octadecene)		
3-Mercaptopropionic acid	$C_3H_6O_2S$	
Glutathione	$C_{10}H_{17}N_3O_6S$	
<i>meso</i> -2,3-Dimercaptosuccinic acid	$C_4H_6O_4S_2$	
Dihydrolipoic acid	$C_8H_{16}O_2S_2$	
L-cysteine	$C_3H_7NO_2S$	
Thiolactic acid	$C_3H_6O_2S$	
N-Acetyl-L-cysteine	$C_5H_9NO_3S$	

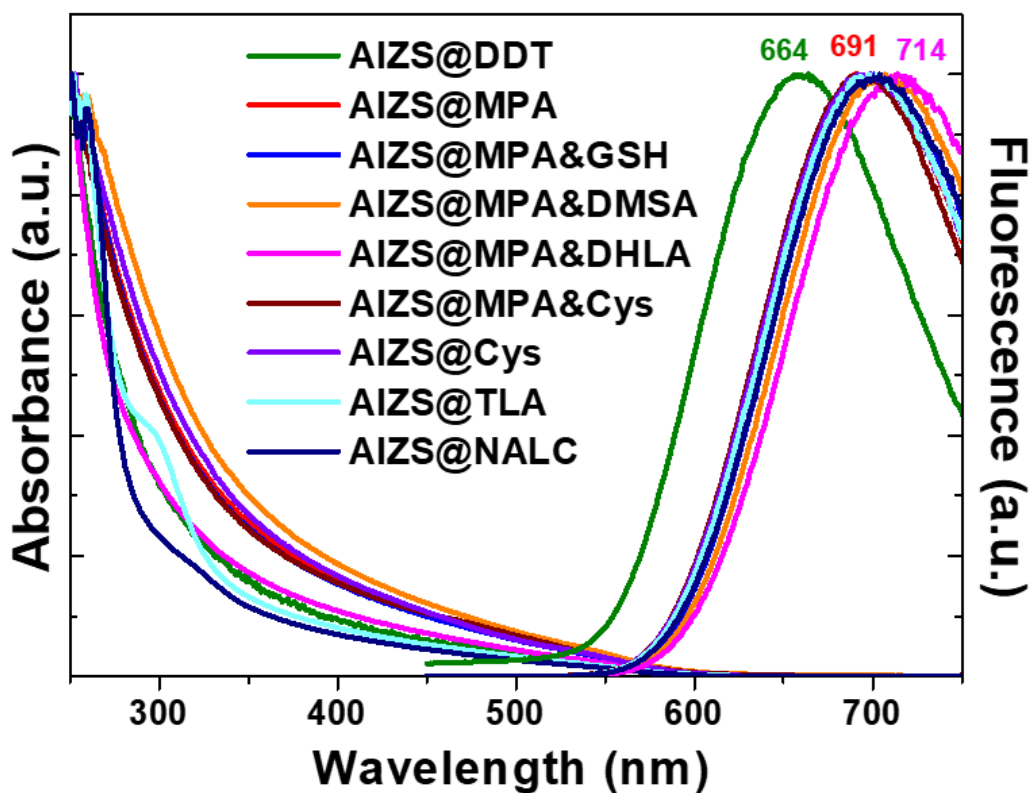


Figure 2.21. UV-visible and PL emission spectra of undoped AIZS QDs after transfer in water using different ligands

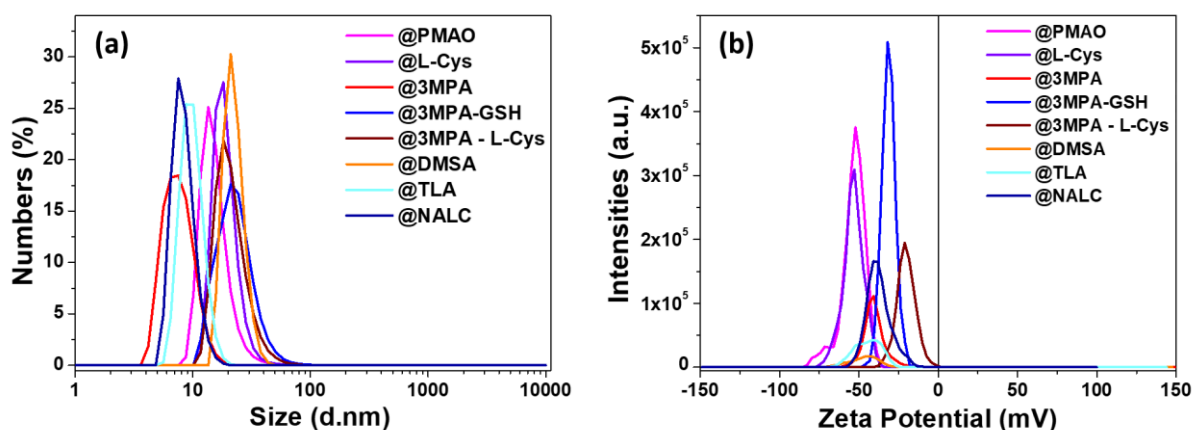


Figure 2.22. DLS and zeta-potential curves of AIZS QDs after transfer in water using different ligands

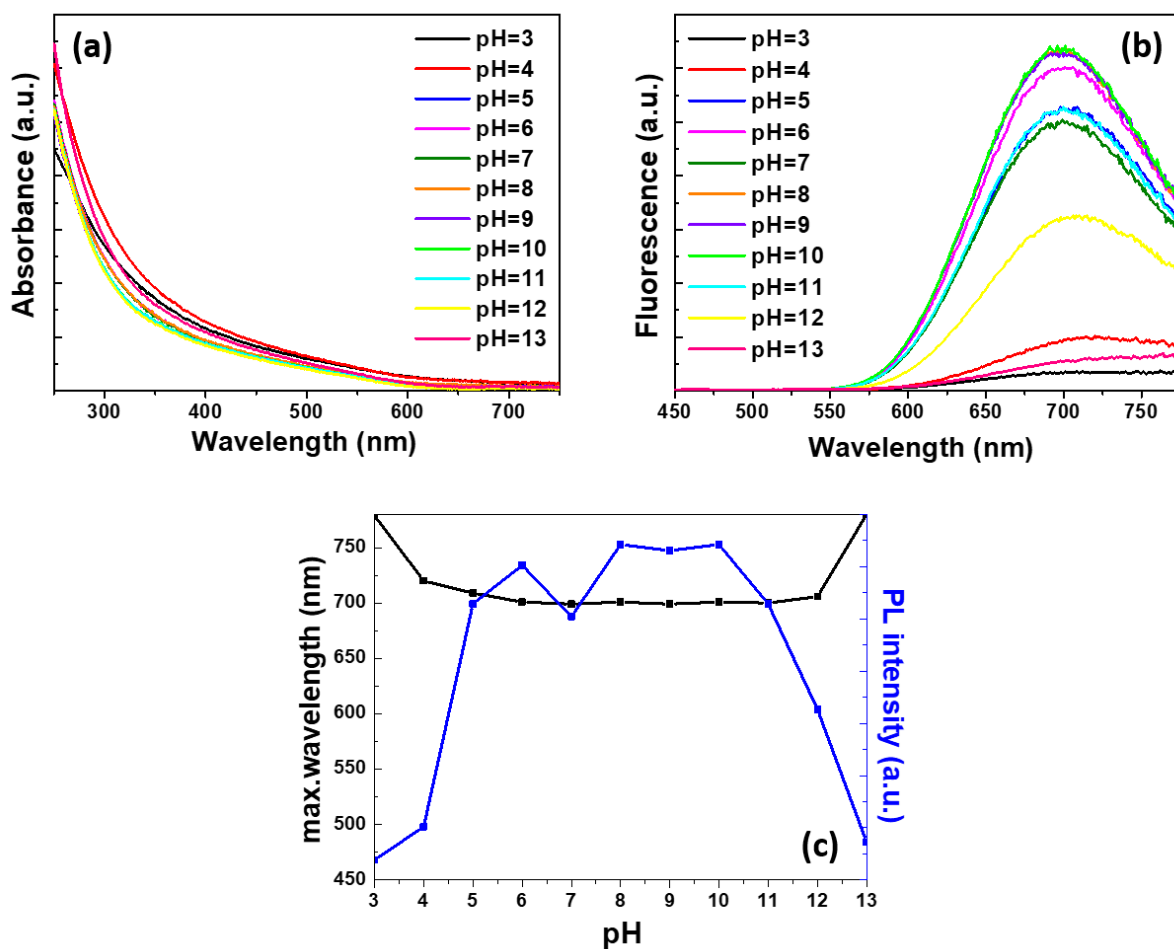


Figure 2.23. UV-Vis (a) and PL (b) spectra of undoped AIZS QDs water transferred using L-Cys recorded at different pH, (c) shows the PL peak position and PL intensity changing in media with different pH values

2.7. Conclusion

In summary, Mn:AIZS QDs were easily prepared via a one-step approach using AgOAc, In(OAc)₃, Zn(OAc)₂, Mn(St)₂ and thiourea as precursors DDT and OAm as capping ligands. The PL emission of Mn:AIZS originates from D-A transitions and can easily be tuned by varying the Ag/In/Zn/Mn stoichiometric ratio. A red-shift of the PL emission is observed when increasing the Mn²⁺ loading likely due to the generation of Mn²⁺ dependent trap states. Mn:AIZS QDs were also demonstrated to exhibit ferromagnetic and paramagnetic properties. Their long PL lifetimes which allow to differentiate their signals from the fast decaying background and biological systems PL and their magnetic properties should allow Mn:AIZS QDs to be of high potential for bioimaging applications.

Chapter 3. Aqueous media syntheses of AIZS and Mn-, Gd-, or Fe-doped AIZS QDs

3.1. Introduction

Recently, ternary I-III-VI₂ QDs have been demonstrated to be very attractive for biological and biomedical applications due to their small size and composition tunable optical and electrical properties and to their reduced toxicity compared to binary Cd-based QDs. In order to improve their photoluminescence properties, shelling with higher band gap ZnS is well developed, which led to the development of quaternary I-II-III-VI QDs.

Various methods were applied to synthesize high quality Ag-In-Zn-S QDs such as hot-injection²³, non-injection³⁶ and single source precursor thermal decomposition¹⁷. Ko and co-workers³³ proposed a multi-step shelling approach resulting in a PL QY of 87% for AIZS QDs. Consequently, the use of AIZS QDs for optical applications has increased¹⁴¹⁻¹⁴⁴. In addition, the possibility to control their sizes, and their properties during the synthesis and customize their compositions due to their multi-component nature expand the field of their application to biology and biomedicine.

The synthesis of quaternary Ag-In-Zn-S QDs in aqueous media is developing because the obtained particles do not require a post-preparative step for their water solubility since the as-prepared particles are soluble in water, hence biocompatible. Furthermore, aqueous synthesis is of low-cost and environmental-friendly. AIZS QDs can also be synthesized by hydrothermal⁵⁵ or microwave-assisted⁴⁹ methods. The simplicity of the synthesis methods along with the mild synthesis conditions allowed for the large-scale synthesis of these QDs⁵⁷. Luo and co-workers²⁵ synthesized water-soluble AIZS QDs using a one-step method, where silver and indium acetates were dissolved in water containing the GSH ligand followed by the injection of Na₂S to prepare the AIS core. To prepare the AIZS NCs, zinc acetate as precursor was injected into the heated AIS core solution at 95 °C. Moreover, the influence of the ratio of precursors, the amount of ligand used on the optical properties of the synthesized QDs were studied.

The doping of fluorescent QDs with paramagnetic metal ions in order to prepare multimodal contrast agents is having huge interest¹⁴⁵⁻¹⁴⁷. This is due to the possibility of obtaining a contrast agent combining two properties in one nanomaterial for two imaging tools, such as fluorescent imaging and magnetic resonance imaging.

In this work, we synthesized highly fluorescent AIZS and Mn²⁺, Gd³⁺ and Fe³⁺-doped AIZS QDs in aqueous media using reduced L-glutathione as a capping ligand. This easy to conduct and reproducible synthesis method allowed us to prepare QDs with superparamagnetic and paramagnetic properties. Moreover, synthesized QDs showed no toxicity towards KB cells when incubated for one day at a concentration of 1 mg/mL.

3.2. Experimental section

Materials

Silver nitrate, indium nitrate, zinc acetate dihydrate, sodium sulfide nonahydrate, manganese acetate, gadolinium nitrate hydrate, iron chloride, L-glutathione reduced (GSH), ethanol, polyethylenimine (PEI), hyaluronic acid sodium salt (HA), 1-ethyl-3-(3-dimethylaminopropyl)carbodiimide (EDC), N-hydroxysuccinimide (NHS), folic acid (FA), (3-(4,5-dimethylthiazol-2-yl)-2,5-diphenyltetrazolium bromide) (MTT), dimethylsulfoxide (DMSO) were used as received.

Aqueous phase synthesis of Ag-In-Zn-Me-S (Me=Mn, Gd, Fe) QDs

In a typical procedure for the synthesis of the Ag-In-S core QDs (Ag/In ratio of 1:5; total metal amount of 0.5 mmol), 0.083 mmol silver nitrate and 0.417 mmol indium nitrate hydrate were dissolved in 25 mL water in a 100 mL three-neck flask under magnetic stirring. Then, to this solution GSH (0.02 M) was added. Afterwards, the pH of the mixture was adjusted to 8 by adding a 2 M NaOH solution. Then the mixture was kept under argon flow for 30 min. Next, sodium sulfide nonahydrate (1 mmol in 2 mL of water) was injected quickly in the flask. Then, after 5 min of vigorous stirring, the heating was started. After reaching 100 °C, the mixture was kept this temperature for 35 min. After the core synthesis, the first shell precursors (0.5 mmol of zinc acetate dihydrate and 0.5 mmol of sodium sulfide nonahydrate, each dissolved in 1 mL of DI water) were simultaneously dropwise added to the reaction and kept at 100 °C for 1 h. The second shell was injected with the doping element. The precursor of the doping element replaced the corresponding amount of zinc acetate (Fig. 3.1). Thus, in the second shell, 0.5 mmol of zinc acetate dihydrate with manganese (II) acetate (gadolinium (III) acetate or iron (III) chloride) and 0.5 mmol of sodium sulfide nonahydrate – each dissolved in 1 mL of DI water – were introduced dropwise into the reaction flask. The growth of the second shell lasted for 1 h. After the synthesis, the QDs solution was naturally cooled down to room temperature and centrifugated for 10 min at 5000 rpm. Next, the precipitate was removed, the supernatant precipitated with ethanol and washed with ethanol several times. The wet product was stored in the fridge.

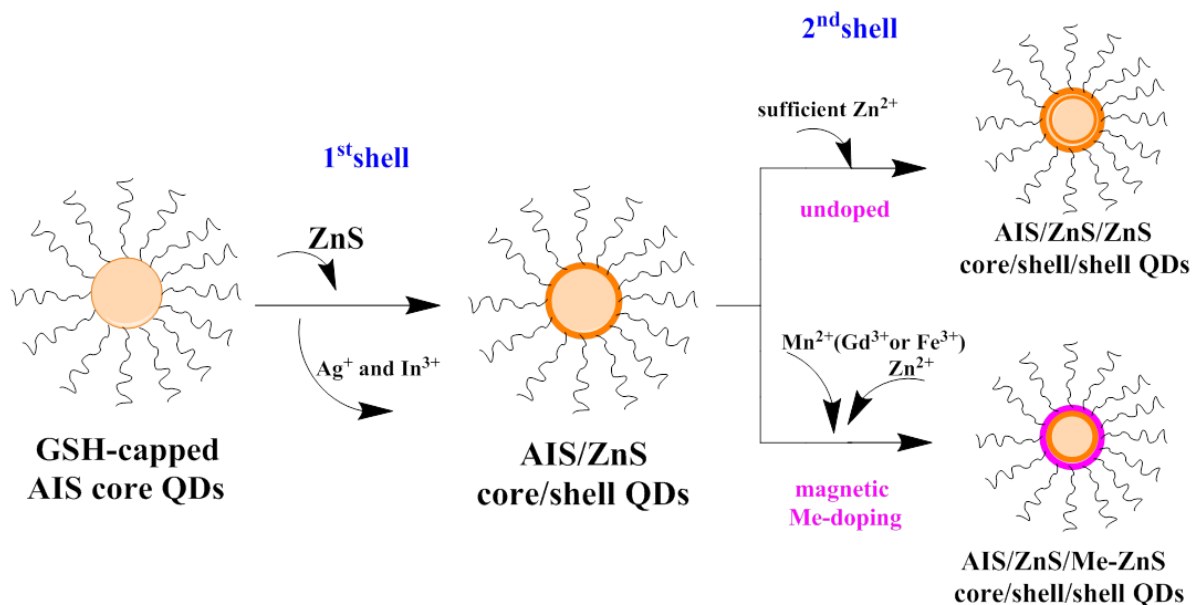


Figure 3.1. Schematic illustration of aqueous phase synthesis of magnetic metal doped GSH-capped quaternary Ag-In-Zn-Me-S QDs

Surface modifications

PEI-capping of aqueous phase synthesised AIZS@GSH QDs

10 mg of GSH-capped QDs were dissolved in 1 mL of DI water. Then, to this solution of the QDs, 9 mL (1 mg/mL) water solution of polyethylenimine (PEI, pH 8) was added dropwise. The mixture was sonicated for 2 h under ambient conditions (after sonication, the solution should be transparent). The sonication was followed by an ultracentrifugation (20 min at 30000 rpm). The supernatant was removed and the precipitate dissolved in 10 mL of DI water. UV-Vis absorption and PL emission spectra of PEI-capped QDs solutions were recorded. The product was stored in the fridge before hyaluronic acid capping (HA).

HA-capping of PEI-capped AIZS@GSH QDs

To the water solution of hyaluronic acid sodium salt (0.25 mL, 0.5 mg/mL), the solution of the PEI-capped QDs (2 mL, 1 mg/mL) was slowly added and the mixture stirred for 40 min under ambient conditions. The schematic illustration of PEI-capping and HA-capping of AIZS@GSH QDs is depicted in Fig. 3.2.

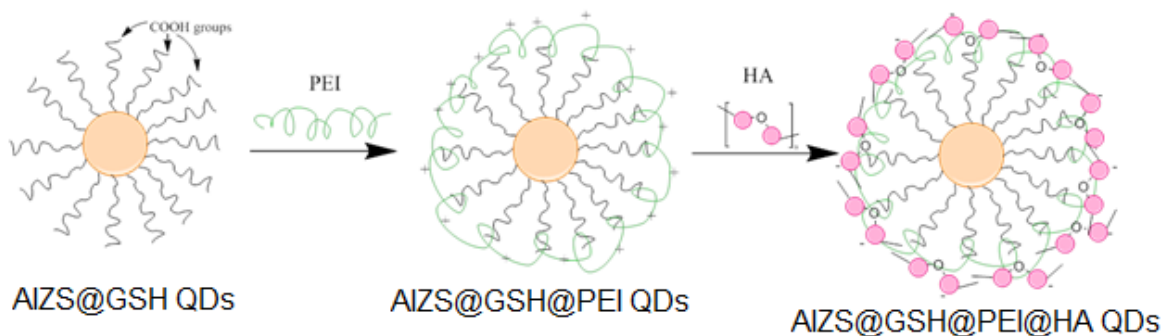


Figure 3.2. Schematic illustration of cationization with PEI and HA-capping of GSH-capped AIZS QDs

Folic acid (FA) capping through PEI-FA conjugate

The PEI-FA conjugate was prepared using an earlier published procedure¹⁴⁸. 100 mg of folic acid were added by small portions into 5 mL of DMSO. Then, to this solution, 70 mg of EDC and 200 mg of NHS in 5 mL of DMSO were added. After that, the mixture was stirred in the dark for 2 h, then 800 mg of PEI in 20 mL of DI water were added to the mixture, followed by pH adjustment to 8 using 0.2 M NaOH. Afterwards, the solution stirred for the next 3 days followed by a dialysis against DI water for 5 days to remove excess by-products. Then, the solution was collected, the solvent evaporated using a rotary evaporator, and the product was stored at 4°C before use.

To prepare PEI-FA conjugate capped QDs, the QDs and the PEI-FA conjugate (10 mg of each) were dissolved separately in 1 mL and 9 mL DI water, respectively. Then the conjugate solution was dropwise added to the QDs solution and sonicated for 2 h.

In Vitro Cytotoxicity

The *in vitro* cytotoxicity of QDs was determined by MTT (3-(4,5-dimethylthiazol-2-yl)-2,5-diphenyltetrazolium bromide) assays. In a typical procedure, KB cells were cultured in 96-well plates at the density of 1.10^5 cells/mL with 200 μ L/well for 12 h to allow the cells to attach. Then, the cells were exposed to different concentrations of QDs (1, 0.5, 0.25, 0.1 mg/mL) for 24 h. At the end of the incubation time, the media containing the QDs was removed, and the cells were treated with 50 μ L of MTT for 3 h. Then, the cells were lysed by the addition of 50

μL DMSO. Further, the absorbance was measured at a wavelength of 540 nm. Averages and standard deviations were based on six experiments.

Preparation of KB cells for the experiment

The KB cell line was purchased from ATCC (CCL-17). Cells were cultured in Roswell Park Memorial Institute 1640 medium (RPMI-1640, Invitrogen, Carlsbad, California, USA), supplemented with 9% (v/v) heat-inactivated fetal bovine serum (FBS, Sigma-Aldrich, St. Louis, MO, USA), penicillin (10,000 IU) streptomycin (10,000 mg/mL) and 1% (v/v) 0.2 M glutamine (Invitrogen, Carlsbad, California, USA). Cells were kept as a monolayer culture in a humidified incubator (5% CO_2) at 37°C. Cell culture was reseeded every week to ensure exponential growth.

KB cells were seeded ($@3 \times 10^4$ cells/mL) in 4 well Lab-Tek II Chamber Slide System during 3 days. QDs were incubated during 3 h in the cell culture medium with 2% SVF.

Fluorescent imaging equipment

Images were acquired with an upright Olympus AX-70 Provis fluorescence microscope equipped with a Hamamatsu Orca-flash 4.0 LT Plus camera. Fluorescence filters were: Ex: 405-445 nm band pass; Ex: 590 nm high pass; Dichroic mirror: 570 nm

3.3. Morphology and structural characterization

Water-soluble GSH-capped AIZS QDs were synthesized via a one-pot three-step method at 100 °C. Silver nitrate and indium nitrate hydrate with the molar ratio of 1/5 were dissolved in water solution of GSH (0.02 M) followed by pH adjusting at 8. Then, the mixture was stirred under argon flow for 30 min, after which Na₂S.9H₂O was quickly injected to the mixture and the heating started. After reaching 100 °C, the core preparation lasted for 35 min. For the first shell deposition, Zn(OAc)₂ and Na₂S.9H₂O, each dispersed in water, were injected dropwise, followed by the shell growth for one hour. The second shell is installed using the same synthetic protocol. For the doped QDs, various amounts of Zn(OAc)₂ were replaced by the doping ion (manganese (II) acetate, gadolinium (III) acetate or iron (III) chloride). The growth of the second shell lasted for another hour. Then the synthesized QDs solution was cooled down to room temperature, centrifugated to remove large particles, precipitated using ethanol, cleaned several times using ethanol and finally stored in the fridge.

X-Ray diffraction analysis was used to characterize the chemical structure and crystallinity of synthesized QDs. In Fig. 3.3, the XRD patterns of Mn-, Gd-, and Fe-doped AIZS@GSH QDs are shown. The broadness of the peaks originates from the small sizes of the nanoparticles. The peaks located at 2θ values of 28.63, 47.63, and 56.52° correspond to the (111), (220), and (311) planes, respectively, of the cubic ZnS blende structure (JCPDS 03-065-0309, F-43m space group, a = 5.4 Å). The shift of diffraction peaks towards high angles is attributed to the decrease in the lattice parameters due to the smaller ionic radii of Zn²⁺ (0.74 Å) ions compared to those of Ag⁺ (1.15 Å) and In³⁺ (0.80 Å) and it is an evidence of the alloying of the AIS core with the ZnS shell and of the formation of a core/shell structure. The incorporation of Zn²⁺ ions as a first shell reduces the cationic vacancies in the AIS core crystal lattice and consequently, the non-radiative recombination centers are reduced leading to the improvement of the quantum efficiency. It should be mentioned that the introduction of the different doping ions did not affect the crystal structure of the QDs. Moreover, no impurities such as Ag₂S, In₂S₃, AgInS₂ or ZnS were detected, which confirms the optimal conditions for the preparation of doped AIZS QDs synthesis.

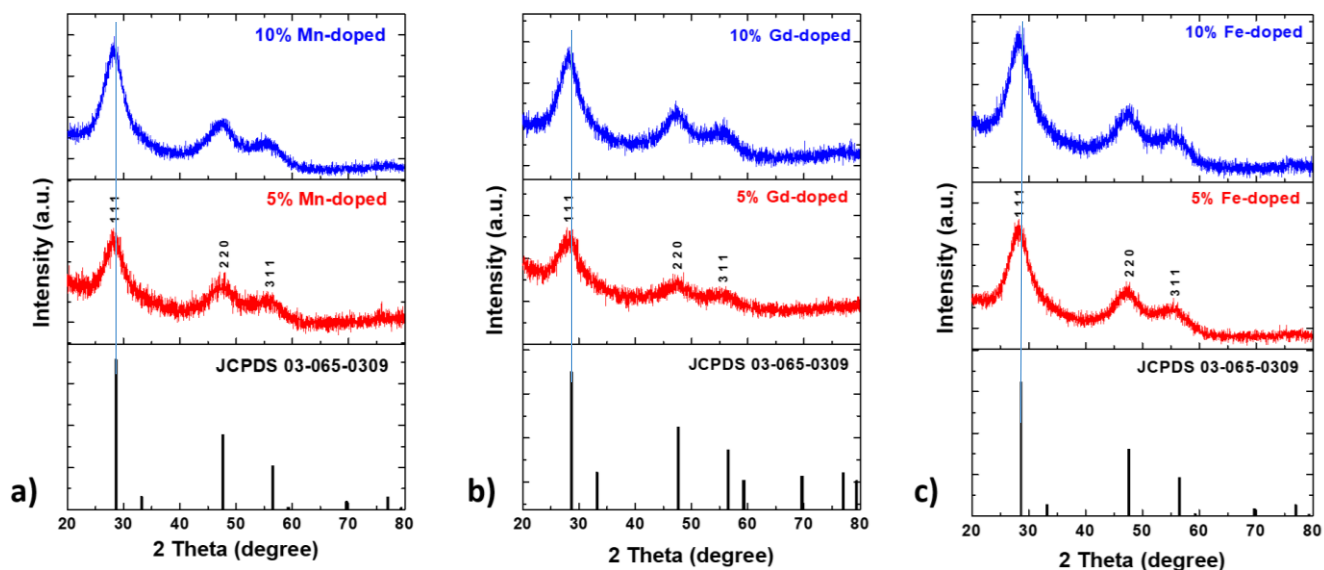


Figure 3.3. XRD patterns of aqueous synthesized AIZS@GSH QDs when varying the metal-doping percentage: a) Mn-doped; b) Gd-doped; c) Fe-doped

The nanosize of doped AIZS QDs was further confirmed by TEM. The TEM images show relatively narrow size distributions (at least 100 nanoparticles counted) and confirm the high crystallinity of doped AIZS QDs (see SAED patterns) (Fig. 3.4, 3.5 and 3.6). The average diameters of the QDs are in the range of 2.2 nm to 2.5 nm. The shapes of these nanoparticles are mostly spherical but some irregularly shaped particles were found. The increase of the doping elements (Mn, Gd, or Fe) concentration in AIZS QDs does not significantly affect the size of nanoparticles.

TGA results show around 20% weight loss for undoped and Mn-, Gd-, and Fe-doped AIZS QDs, which indicates a thin layer of the GSH ligand at the surface of the QDs (Fig. 3.7). Two weight-loss regions, first below 100°C and the second around 300°C, were observed. The weight-loss below 100°C may originate from water molecules bound to the surface of the samples while the second weight-loss corresponds to the removal of the GSH surface ligand.

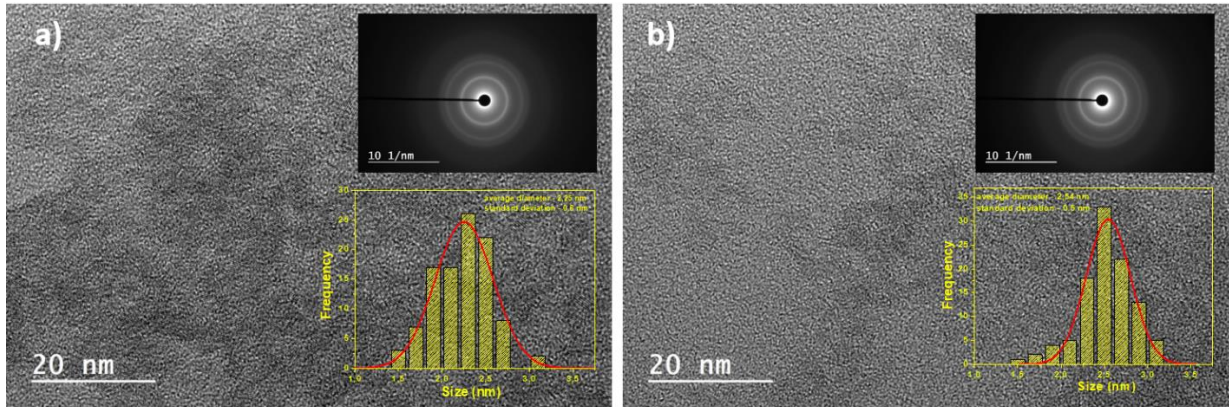


Figure 3.4. TEM images, SAED patterns and size distributions of 5% Mn-doped (a) and 10% Mn-doped (b) AIZS@GSH QDs

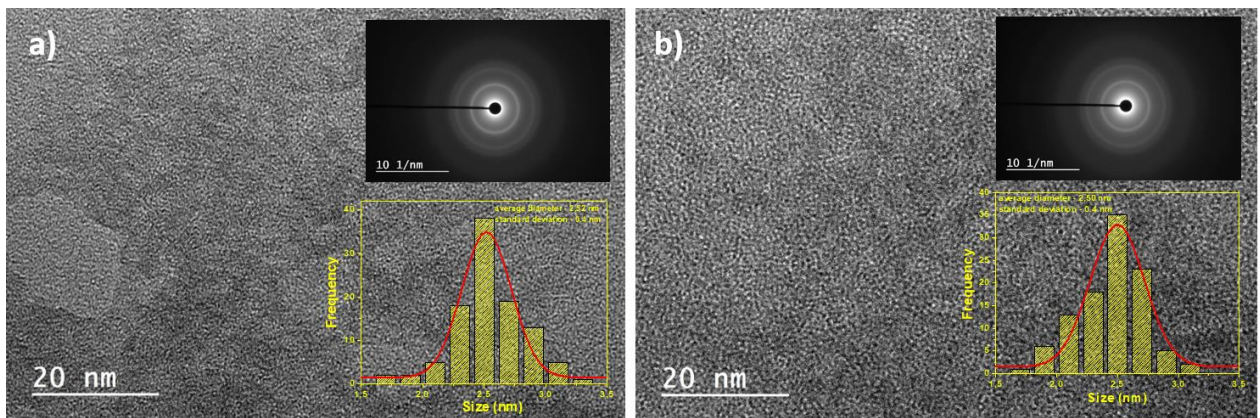


Figure 3.5. TEM images, SAED patterns and size distributions of 5% Gd-doped (a) and 10% Gd-doped (b) AIZS@GSH QDs

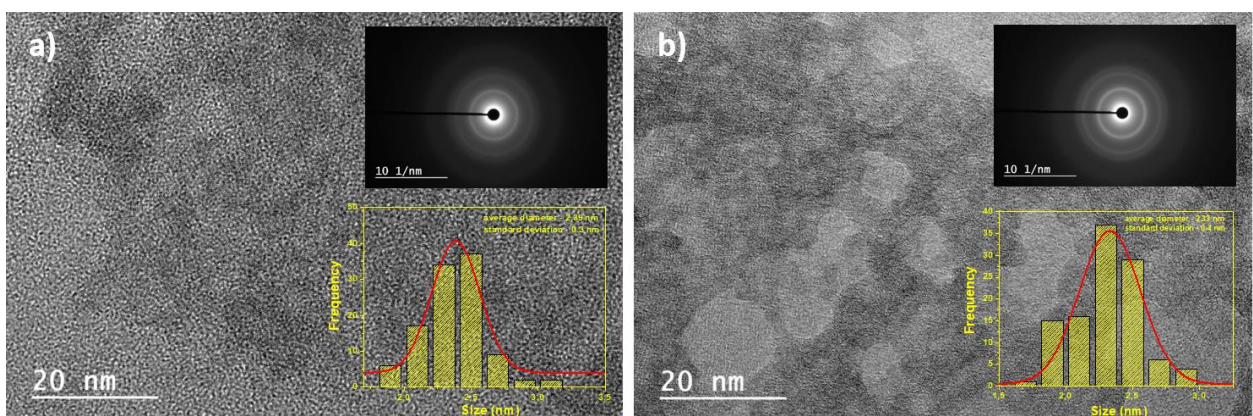


Figure 3.6. TEM images, SAED patterns and size distributions of 5% Fe-doped (a) and 10% Fe-doped (b) AIZS@GSH QDs

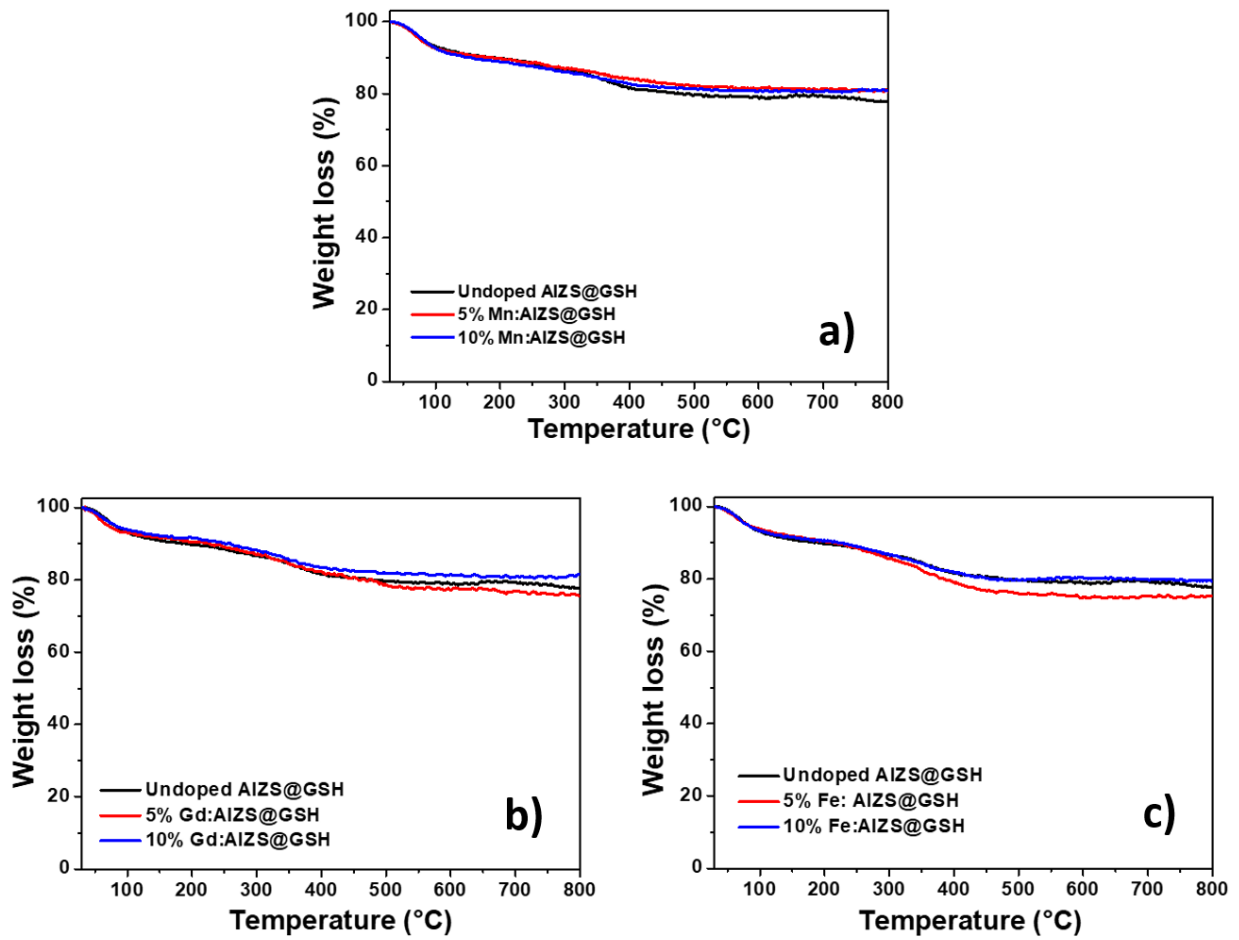


Figure 3.7. TGA curves of AIZS@GSH QDs when varying the: a) Mn-doping, b) Gd-doping, and c) Fe-doping

3.4. Elemental analysis and EPR measurements

Energy-dispersive X-ray was used for the elemental analysis of synthesized QDs and it confirms the presence of Ag, In, Zn, Mn elements and of Gd, Fe and S dopants in the AIZS QDs (Fig. 3.8, Table 3.1). The detected amount of Mn and Fe elements was found to be lower than the amount used for the synthesis, while amount of Gd was higher than used for the synthesis (Table 3.2). However, results show that the dopants are successfully incorporated into the crystal structure of the QDs. Based on EDX analysis (Table 3.1 and Table 3.2), the prepared Mn and Fe-doped QDs have a non-stoichiometric composition with a defect in In compared to Ag and Zn. Furthermore, in the case of the Gd-doping, the dopant replaces zinc in the structure (defect in Zn compared to Gd) (Table 3.2).

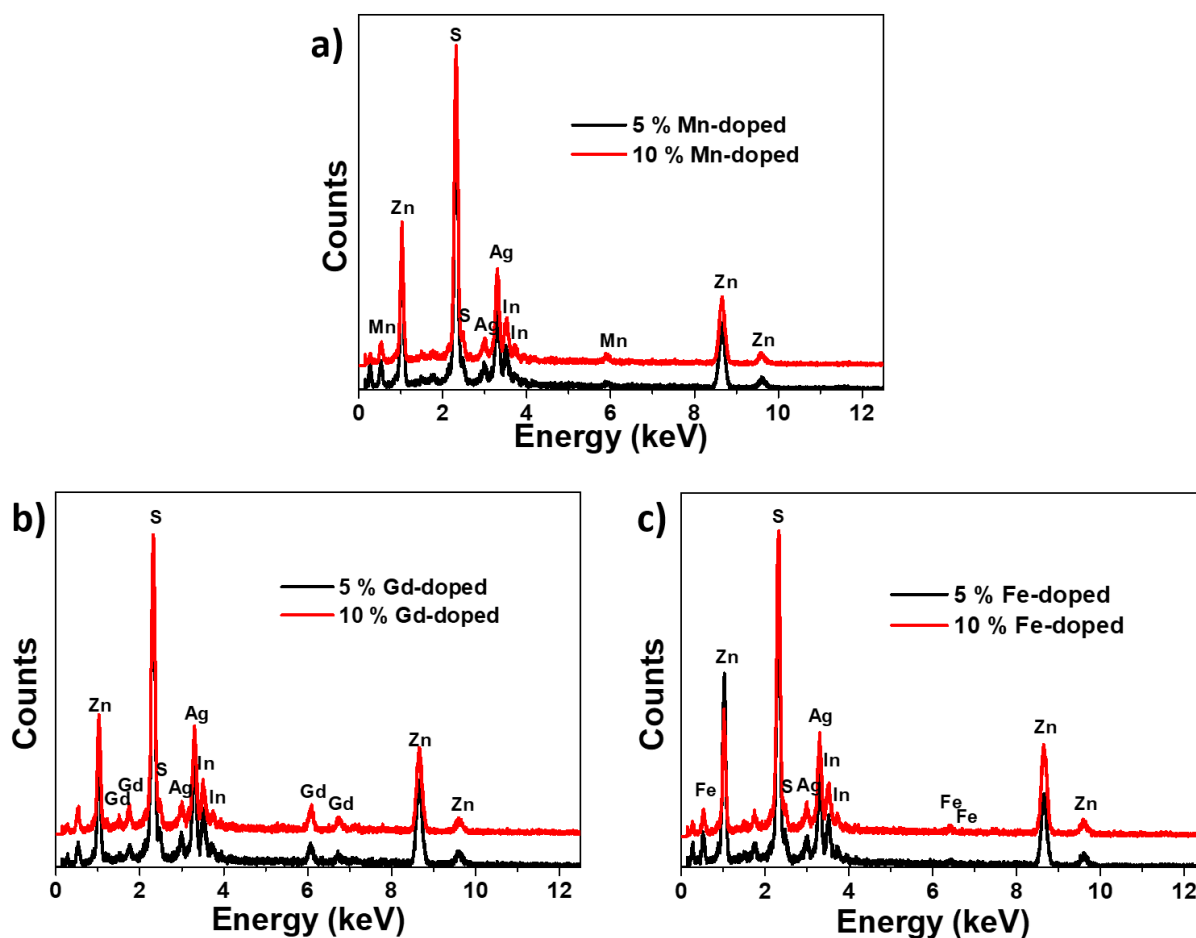


Figure 3.8. EDX analyses of AIZS@GSH QDs when varying the: a) Mn-doping, b) Gd-doping, and c) Fe-doping

Table 3.1. EDX results of AIZS@GSH QDs when varying the metal-doping

Element	at%					
	5 % Mn	10 % Mn	5 % Gd	10 % Gd	5 % Fe	10 % Fe
Ag	2.43	2.80	3.07	3.25	2.87	2.79
In	11.94	13.02	14.72	15.94	12.49	12.00
Zn	46.68	37.70	27.14	26.56	40.56	44.96
S	38.22	45.53	51.21	48.44	43.58	39.49
Mn	0.73	0.95	-	-	-	-
Gd	-	-	3.86	5.81	-	-
Fe	-	-	-	-	0.50	0.76

Table 3.2. Theoretical and actual Ag/In/Zn/Me ratios determined by EDX for Me-doped AIZS QDs

	Ag/In/Zn/Me ratio in precursors	Actual ratios determined by EDX		
		Ag/In/Zn/Mn	Ag/In/Zn/Gd	Ag/In/Zn/Fe
5 % doping	1/5.21/11.88/0.63	1/4.91/19.21/0.30	1/4.79/8.83/1.26	1/4.35/14.13/0.17
10 % doping	1/5.21/11.25/1.25	1/4.65/13.46/0.34	1/4.90/8.17/1.79	1/4.30/16.11/0.27

To further confirm the Mn ions incorporation into the AIZS structure, X-band electron paramagnetic resonance spectra were recorded. Fig. 3.9 shows the EPR spectra of 5% and 10% Mn-doped AIZS QDs with the broad signal centered on $g = 2$. These spectra of Mn-doped AIZS

QDs display a set of six lines separated by about 80 G, which is related to the coupling of the electronic spin with the $5/2$ nuclear spin of Mn^{2+} . The broadness of the signals observed is likely due to the complex environment of Mn ions in the presence of indium, silver and zinc ions.

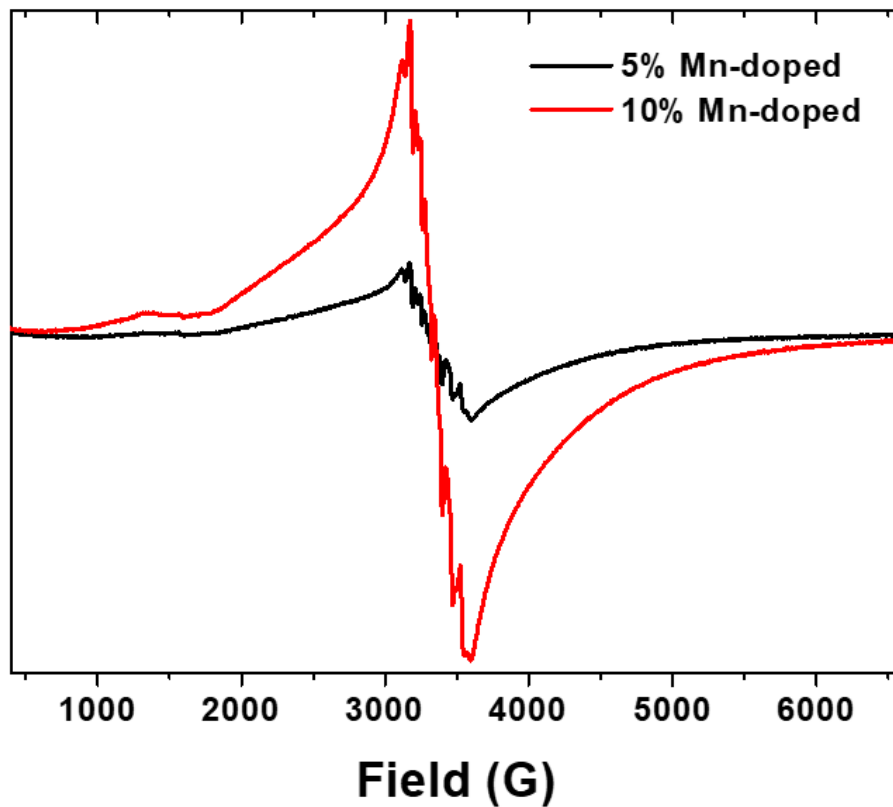


Figure 3.9. EPR spectra of Mn-doped AIZS@GSH QDs

3.5. Optical properties

Fig.3.10 shows the UV-vis absorption and the PL emission spectra of 5% Mn-doped AIZS@GSH QDs during the aqueous phase synthesis. A PL peak centered at 624 nm was observed for the AIS core, which is attributed to defect-related transition¹⁴⁹. Furthermore, the broad absorption is typical for AIS and AIZS QDs, and is usually explained by the distribution of vibrational states rather than from size and/or composition inhomogeneity of the dots.

A slight blue-shift of the PL peak from 624 nm to 600 nm can be observed after the first ZnS shell introduction as compared to the PL spectra of the AIS core. This can be explained by the cationic interdiffusion between the narrower bandgap AIS core ($E_g = 1.87$ eV) and the wider bandgap ZnS shell ($E_g = 3.68$ eV)⁹². The same behavior was observed in other studies when a ZnS shell was introduced on CIS and AIS cores^{105,150}. The quantum confinement effect resulted in increasing the bandgap values of core/shell QDs compared to the AgInS₂ core (Fig. 3.11). These values for AIZS QDs determined from the Tauc plots of $(\alpha h\nu)^2$ vs $h\nu$ (where α is the absorption coefficient and $h\nu$ is the photon energy) were found to be in the range 3.27 eV (AIZS) to 2.86 eV (Mn(10%):AIZS).

The introduction of the second shell containing Zn and Mn onto the AIS core did not change the PL peak position, indicating that no subsequent alloying occurred (Fig. 3.10).

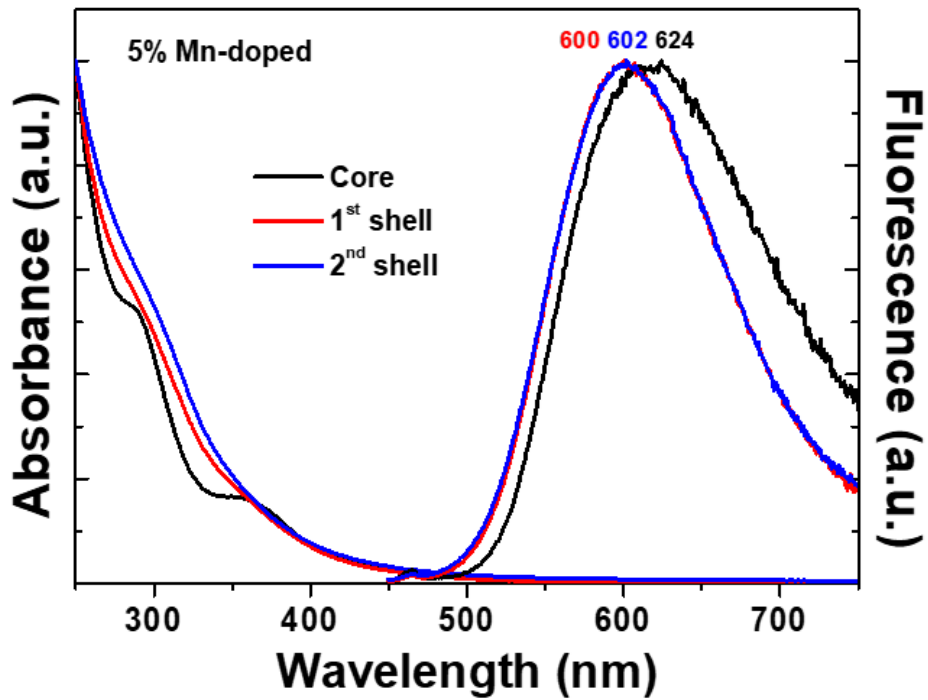


Figure 3.10. UV-Vis absorption and PL emission spectra of 5% Mn-doped AIZS@GSH QDs during core, 1st shell and 2nd shell processing

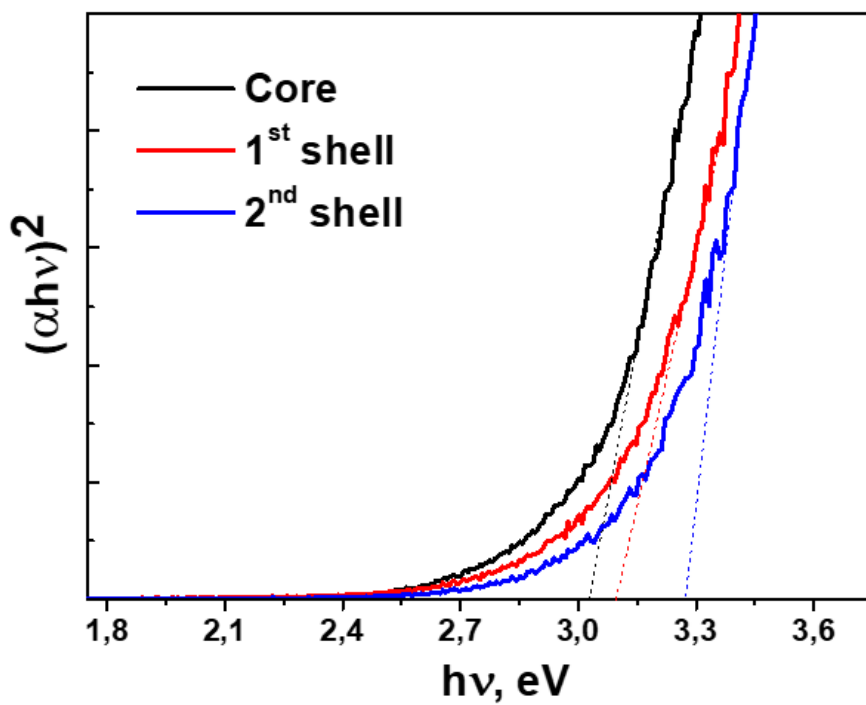


Figure 3.11. Determination of the optical bandgap of AIZS QDs during nanoparticles growth

A shift to higher wavelengths (lower energies) was observed when increasing the loading in Mn^{2+} ions. This increase of the dopant loading also influences the electronic states of the AIZS QDs as seen from the bandgap values decrease upon Mn-content increasing (Fig. 3.13). This shift to lower energies may be caused by the lattice shrinkage originating from the diffusion of Mn^{2+} ions into the AIS/ZnS core/shell structure (Fig. 3.12) as also indicated by XRD. The red shift was observed from 588 nm for undoped AIZS QDs to 602 nm and 604 nm when the nanocrystals were doped with 5 % and 10 % Mn, respectively. The PL emission of doped AIZS QDs is not a bandgap emission, which is noticeable from the observed large Stokes shift. The peaks centered at ca. 600 nm are also not the Mn d-state emission (${}^4\text{T}_1 \rightarrow {}^6\text{A}_1$ transition)³⁴, which was found by microsecond PL lifetimes. It was concluded, that this emission is more likely a radiative D–A pair emission with Mn-content dependent trap state.

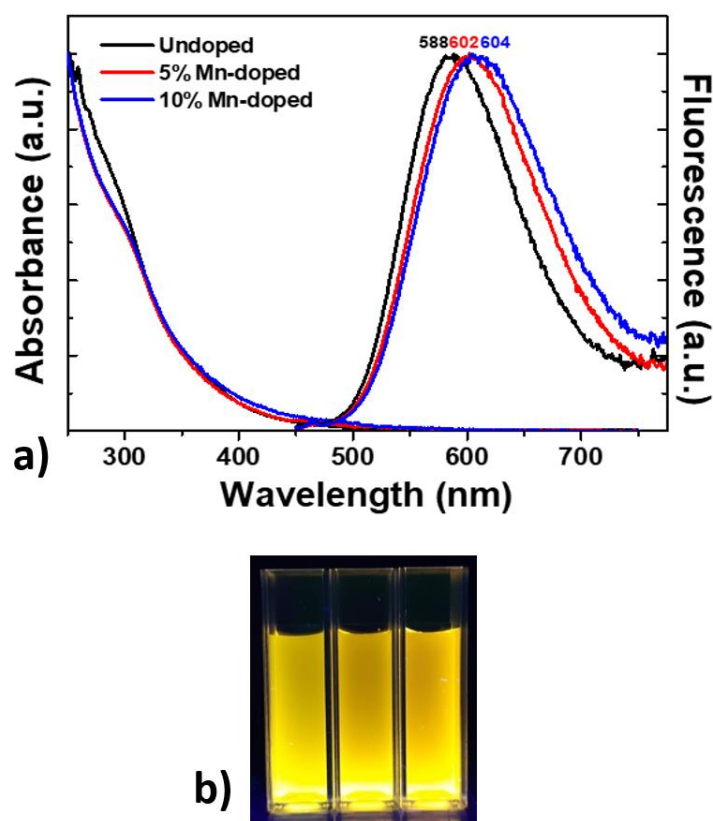


Figure 3.12. (a) UV-Vis absorption and PL emission spectra undoped and Mn-doped AIZS@GSH QDs and (b) photograph of aqueous dispersions of the dots under UV light irradiation

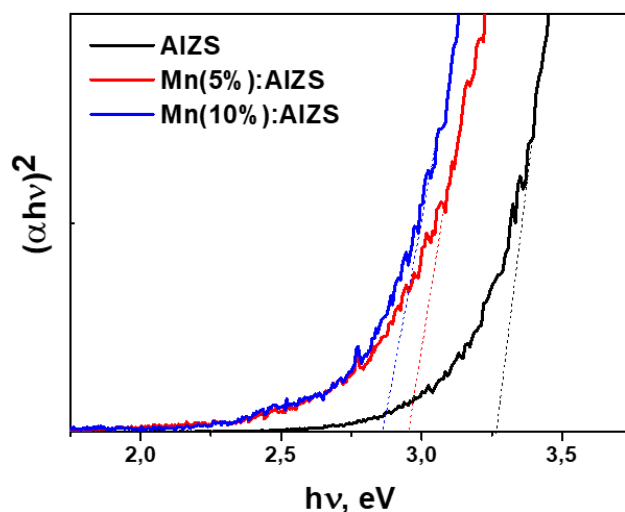


Figure 3.13. Determination of the optical bandgap of AIZS and Mn:AIZS QDs when increasing the loading in Mn²⁺ ions

The PL QY of AIZS and metal-doped AIZS QDs at room temperature was determined from the integrated fluorescence intensities of the QDs and of the reference (Rhodamine 6G, QY=95% in water, at 400 nm excitation). All the samples for spectral measurement were diluted to yield an absorbance between 0.01-0.02 at the excitation wavelength. The QYs of the AIZS QDs (Table 3.3) were calculated using the formula:

$$QY = \frac{F_s \times A_r \times QY_r}{F_r \times A_s}$$

where F is the integrated fluorescence emission, A is the absorbance at the excitation wavelength of samples (s) and reference (r).

Table 3.3. PL QYs of aqueous synthesized AIZS@GSH QDs doped with different metals

AIZS@GSH QDs	Mn-doped		Gd-doped		Fe-doped	
	5%	10%	5%	10%	5%	10%

PL QY, %	42.4	23.9	69.3	55.5	12.94	14.09
----------	------	------	------	------	-------	-------

When doping Gd^{3+} ions into AIZS QDs, the PL emission peak position was not changed, indicating that there are no significant structural defects and that the PL peaks can be attributed to the emission of AIZS QDs (Fig. 3.14). For the Fe^{3+} doping, there is a shift to higher wavelengths with the increasing of the doping percentage (Fig. 3.15).

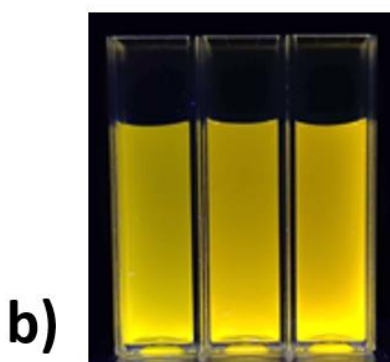
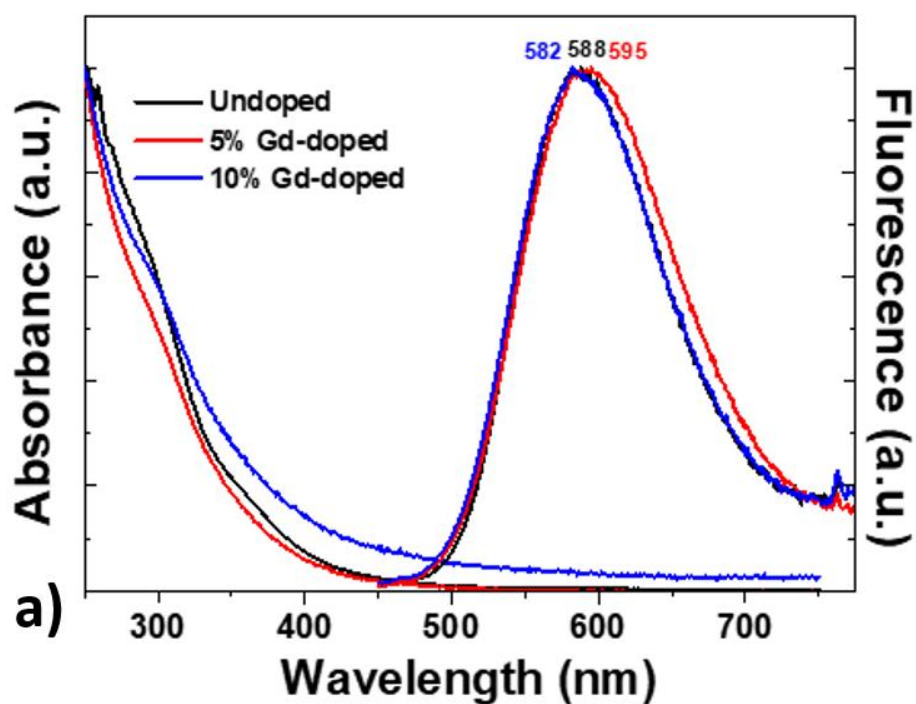


Figure 3.14. (a) UV-Vis absorption and PL emission spectra of undoped and Gd-doped AIZS@GSH QDs and (b) photograph of aqueous dispersions of the dots under UV light irradiation

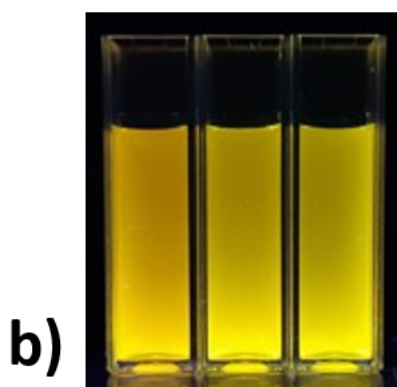
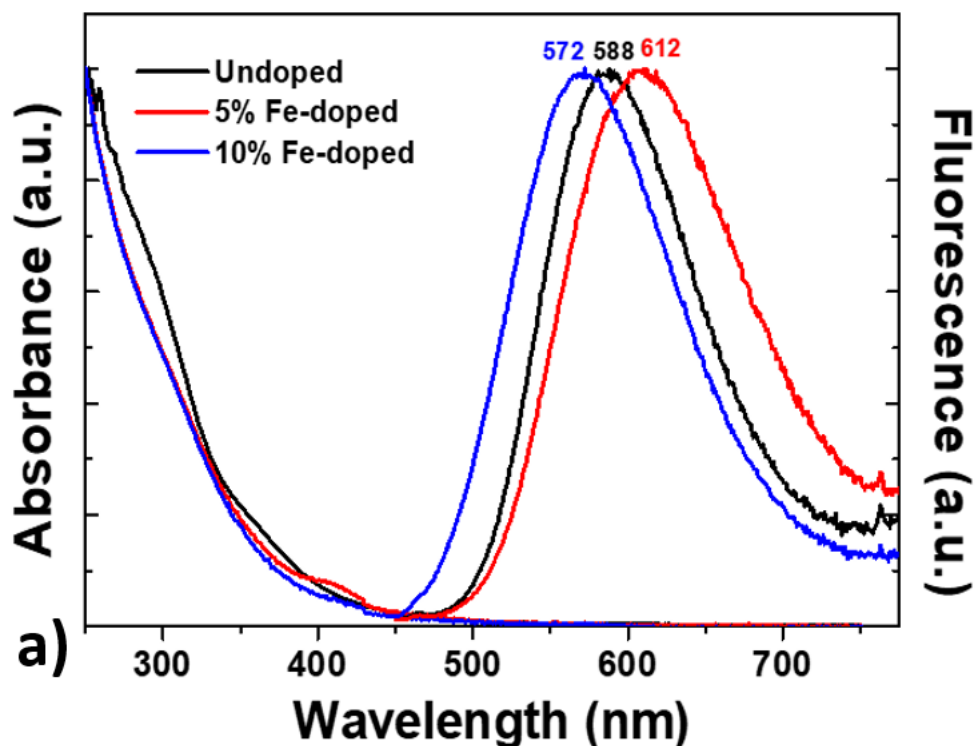


Figure 3.15. (a) UV-Vis absorption and PL emission spectra of undoped and Gd-doped AIZS@GSH QDs and (b) photograph of aqueous dispersions of the dots under UV light irradiation

PL lifetimes. As it was reported in the first chapter, there are two luminescent mechanisms in AIZS QDs⁷⁹: the first with shorter lifetimes (ca. 25 ns) and with higher emission energy involves transitions between delocalized conduction/valence band and localized defects. The second with longer lifetime (≥ 185 ns) and lower emission energy involves transitions between two localized or defect levels.

The fast decay component τ_1 corresponds to surface trap states (dangling bonds or vacancies), and the slow decay component τ_2 relates to the D-A recombination originating from the intragap defect states.

To identify the optical transfer path in doped AIZS QDs, the time-resolved PL measurements were recorded at the wavelengths corresponding to the PL emission maxima (from Fig. A, B and C). The data were best fitted using a bi-exponential function $I(t) = A_1 \exp\left(-\frac{t}{\tau_1}\right) + A_2 \exp\left(-\frac{t}{\tau_2}\right)$ where τ_1 and τ_2 are the time constants of the PL, and A_1 and A_2 are the normalized amplitudes of the PL components. The fitting parameters are summarized in Table 3.4, Fig. 3.16. The average PL lifetimes (τ_{av}) were determined using the following equation : $\tau_{av} = (A_1\tau_1 + A_2\tau_2)/(A_1 + A_2)$.

The PL decay curves measured for AIZS QDs (as well as the calculated PL lifetime) further confirm that the PL emission is not a simple bandgap emission. The PL lifetime is in the range of 0.275 and 0.326 μs , which corresponds to the D-A recombination originating from the intragap defect states.

Table 3.4. Lifetimes and fitting parameters of AIZS and Mn:AIZS, Gd:AIZS, Fe:AIZS QDs

Samples	A_1 , %	τ_1 , μs	A_2 , %	τ_2 , μs	τ_{av} , μs
AIZS	59,900	0,142	40,099	0,482	0,278
Mn(5%):AIZS	67,169	0,155	32,830	0,518	0,274
Mn(10%):AIZS	66,419	0,156	33,580	0,532	0,282
Gd(5%):AIZS	60,063	0,175	39,936	0,552	0,326
Gd(10%):AIZS	60,472	0,166	39,527	0,533	0,311
Fe(5%):AIZS	59,827	0,168	40,172	0,525	0,312
Fe(10%):AIZS	61,000	0,170	38,999	0,527	0,309

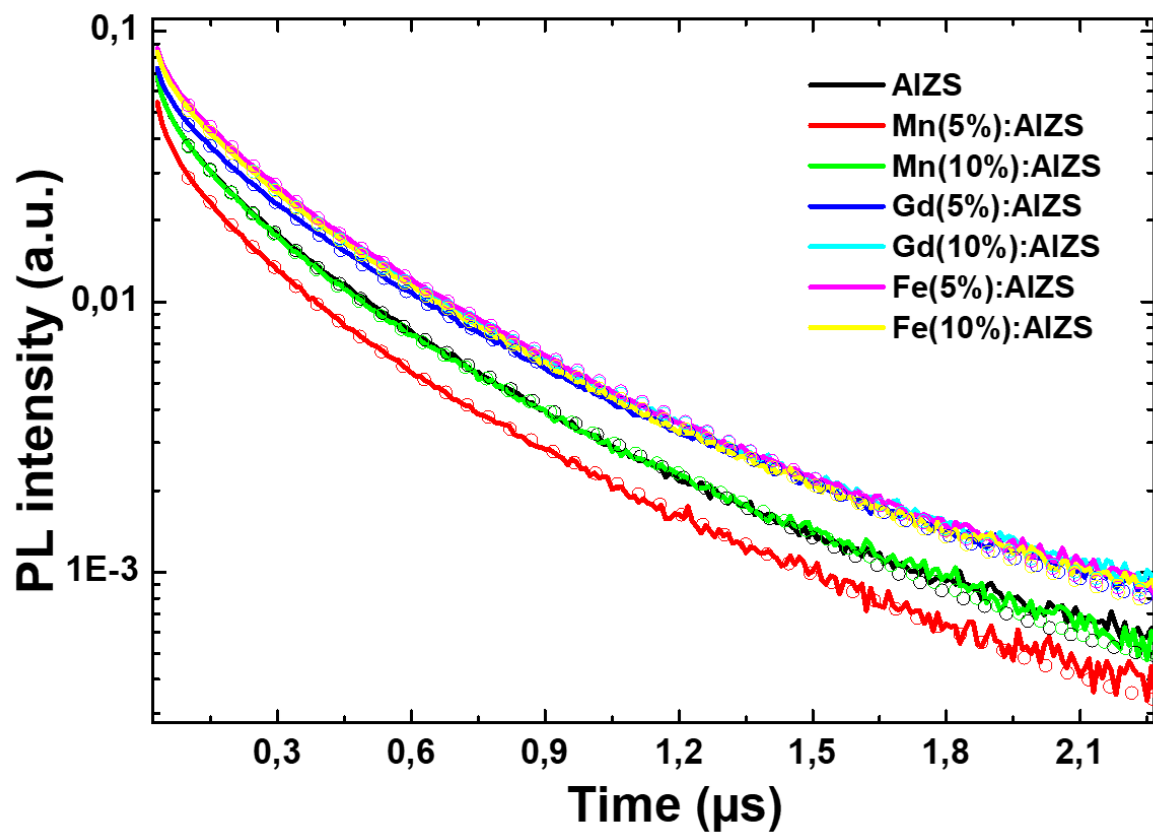


Figure 3.16. PL lifetimes of AIZS and Mn-, Gd-, Fe-doped AIZS QDs at PL maximum wavelength

3.6. Magnetic properties

Undoped AIZS QDs do not present any magnetic response to the applied field. When Mn^{2+} , Gd^{3+} or Fe^{3+} ions are introduced into the nanocrystals structure, regardless of the loading percentage, the magnetic moment (M) of these particles is the combination of ferromagnetic, paramagnetic and/or superparamagnetic signals (Fig 3.17, 3.18 and 3.19). These Mn^{2+} , Gd^{3+} or Fe^{3+} ions are known to be paramagnetic, but several studies reported nanoparticles doped with these ions to be ferromagnetic^{136,151–153} or the coexistence of paramagnetic and ferromagnetic¹⁵⁴ signals.

From the (a) and (b) parts of the Fig. 3.17, it can be seen that the samples synthesized at high concentration of Mn^{2+} ions exhibit the highest saturation magnetization, up to 1.5 emu/g (when 10% Mn-doped, at 10 K) (Fig. 3.17b), and the saturation magnetization decreases at room temperature. The same trend was observed for Gd^{3+} -doped and Fe^{3+} -doped AIZS QDs, with the highest saturation magnetizations of 10 emu/g (when 10% Gd-doped, at 10 K) (Fig. 3.18b) and 0.175 emu/g (when 10% Fe-doped, at 10 K) (Fig. 3.19b, respectively. Fig. 3.17 and 3.18 (c) and (d) parts show the magnetic moments of Mn-doped and Gd-doped AIZS QDs at 10 K and 310 K when zero field is applied. The results demonstrate that both the amount of doped paramagnetic ion, but also the temperature affect the magnetic properties of the nanoparticles. The extraction of the saturation magnetization (M_s) from the curves is non-trivial, since saturation was not achieved in the system due to persisting paramagnetic signal on the top of the ferromagnetic signal of interest.

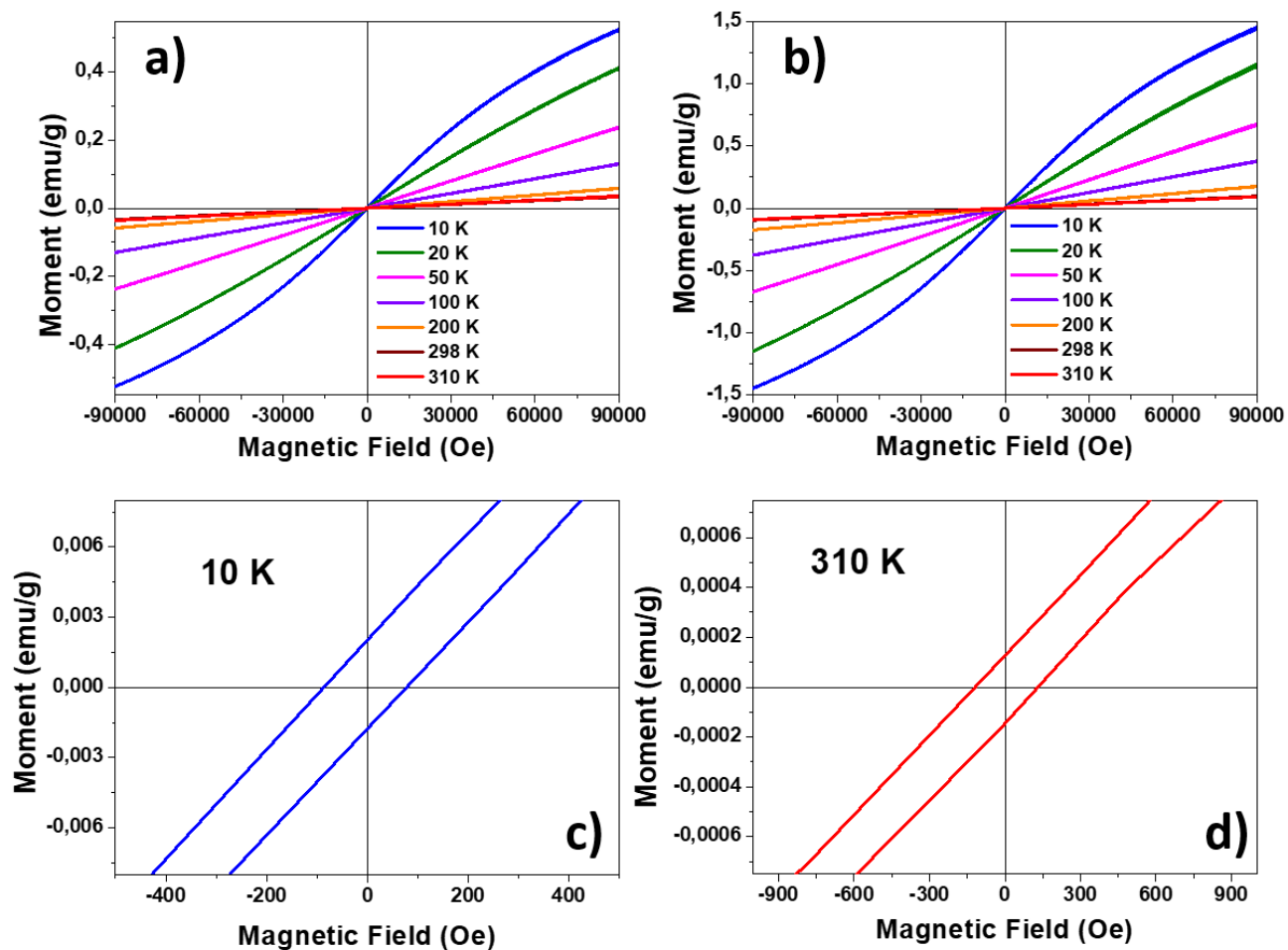


Figure 3.17. M(H) loop curves of 5 % (a) and 10 % (b) Mn-doped AIZS QDs at different temperatures and the magnetic properties of 10% Mn-doped QDs at zero field at 10 K (c) and 300 K (d)

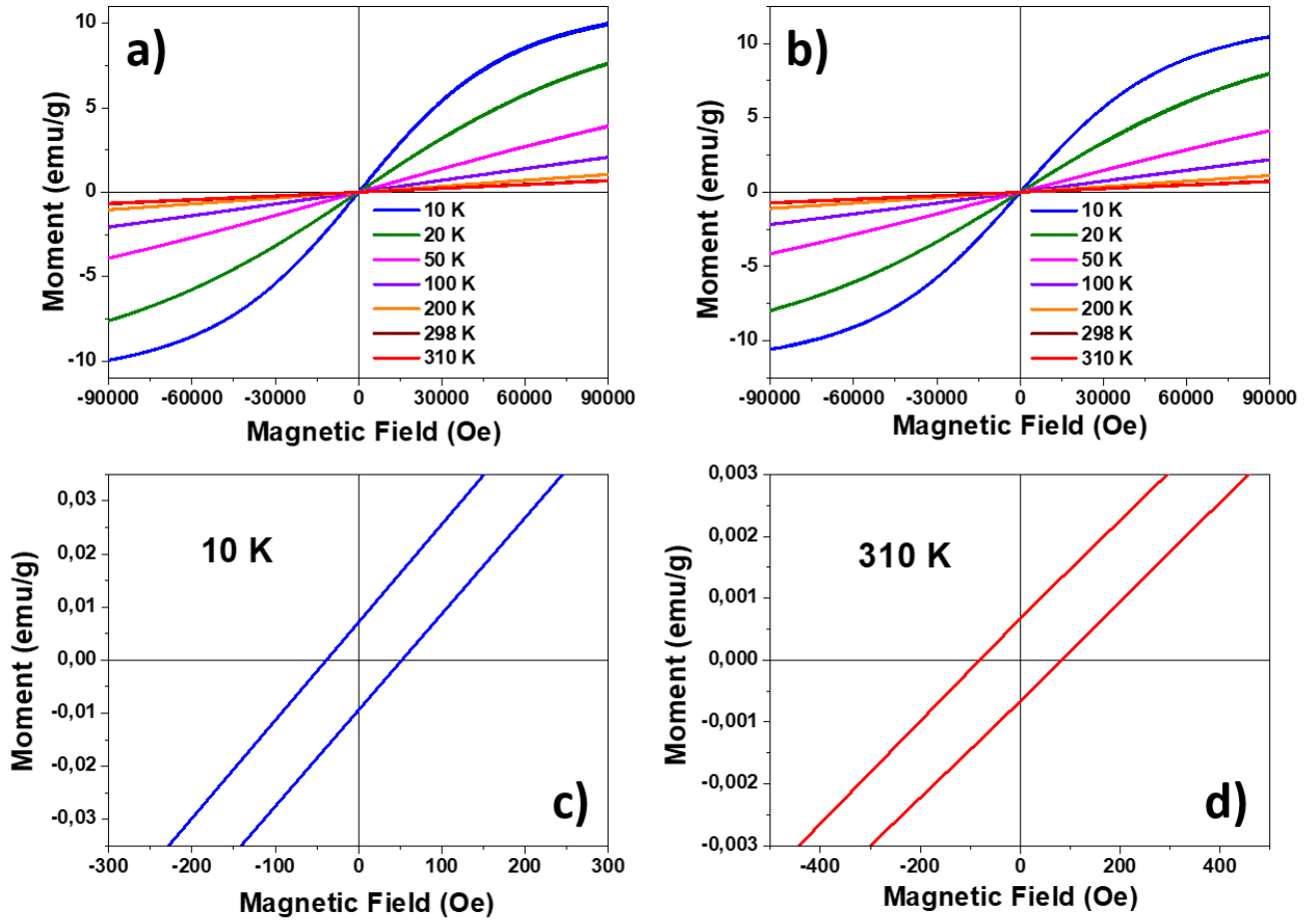


Figure 3.18. M(H) loop curves of 5 % and 10 % Gd-doped AIZS QDs at different temperatures (a and b, respectively) and the magnetic properties of 10% Gd-doped QDs at zero field at 10 K and 300 K (c and d, respectively)

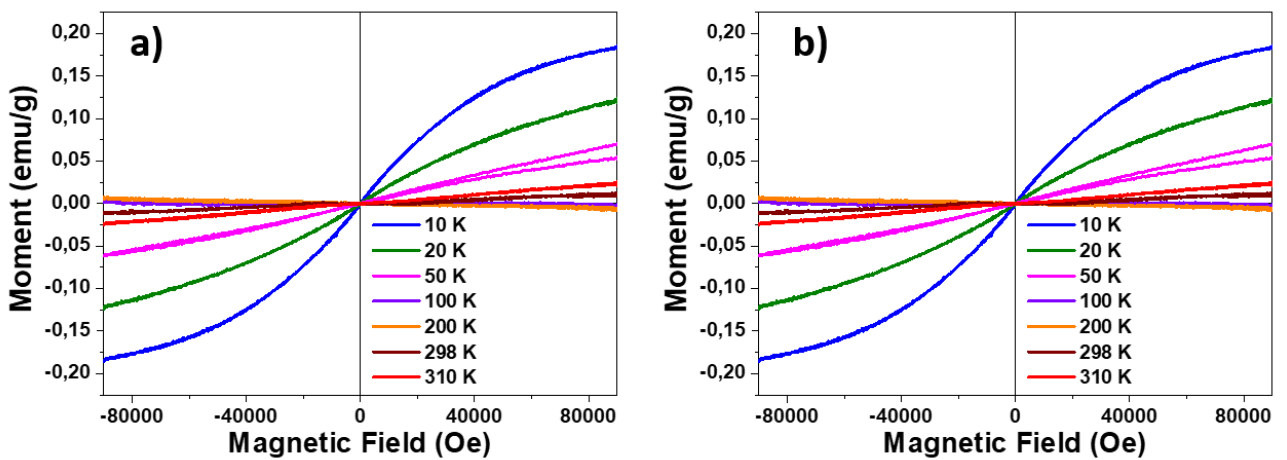


Figure 3.19. M(H) loop curves of AIZS QDs at different temperatures: a) 5 % and b) 10 % Fe-doped

3.7. Preparation of AIZS QDs for biological applications

Hyaluronic acid is one of the major components of vertebrate tissue and body fluid. It has been used in different nanomedical studies as a targeting ligand to cancer cells^{155–157}. Its structure is shown in Fig. 3.20a and its FT-IR spectrum in Fig. 3.23a. To associate hyaluronic acid (negatively charged at physiological pH) with GSH-capped AIZS QDs that are also negatively charged at pH 7.2, we chose PEI as interface layer.

Polyethylene imine is a water-soluble cationic polymer. The branched PEI possesses primary, secondary and tertiary amino groups (Fig. 3.20b). This amine-rich molecule makes it one of the most promising cationic ligand for drug delivery¹⁵⁸. On the other hand, the abundance of amine groups is also responsible of the cytotoxicity of PEI, resulting in cellular internalization by membrane destabilization¹⁵⁹. Hence, to reduce this cytotoxicity, several methods describing the covalent modification of PEI amines groups were reported, including the modification of PEI with acetic anhydride, succinic anhydride, glycidol, and with poly(ethylene glycol) (PEG) associated to acetic anhydride^{160,161}.

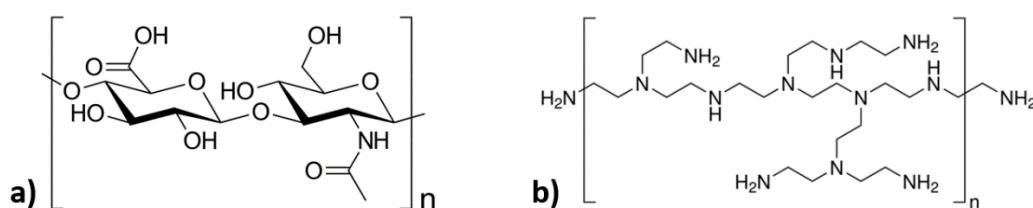


Figure 3.20. Structures of (a) hyaluronic acid and (b) branched polyethylene imine

Folic acid (Fig. 3.21) or vitamin B₉, apart from its important role as a food supplement, is also widely used as a tumor cells targeting ligand due to its ability to attach to folate receptor^{162–165} and the folate receptor was found in a large number of tumors such as brain, breast, lung and

ovarian cancers¹⁶⁶. In this study, FA was also used as the surface targeting ligand to adapt the AIZS QDs for biomedical applications.

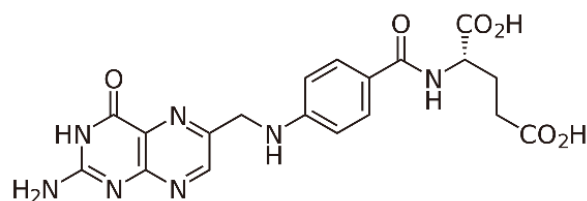


Figure 3.21. Structure of folic acid

Association of HA with the QDs was carried out through the intermediate PEI-capping step. The two-step electrostatic association was used due to the self-assembly of the negatively charged HA with the positively charged PEI-capped QDs. As mentioned above, the branched PEI has primary, secondary and tertiary amino groups which are positively charged at neutral pH and that will associate with carboxylate (-COO^-) groups of GSH-capped QDs.

In the case of the FA assembly onto the QDs surface, the PEI-FA conjugate was first prepared. During the formation of the PEI-FA conjugate, the primary amine groups of PEI react with the carboxylic groups of FA using 1-ethyl-3-(3-dimethylaminopropyl)carbodiimide (EDC) as coupling agent and N-hydroxysuccinimide (NHS) as activator (Fig. 3.22). Then, the positively charged PEI-FA conjugate associates to negatively charged carboxylate groups of GSH-capped QDs.

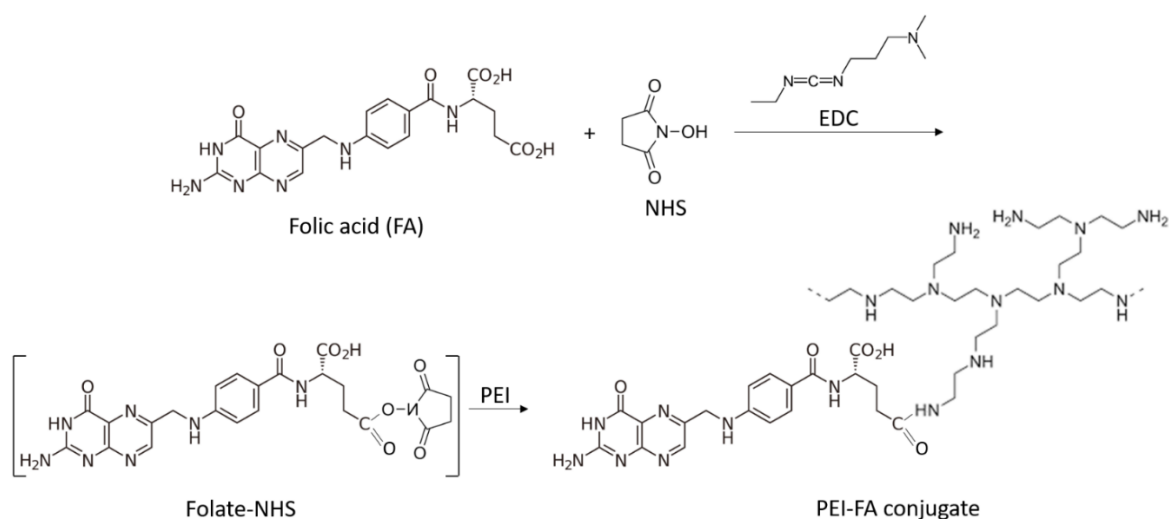


Figure 3.22. Schema of PEI-FA conjugate preparation

FT-IR and zeta-potential characterizations were carried out to determine the nature of surface ligands. Fig. 3.23 shows the FT-IR spectra of the as-synthesized GSH-capped QDs (b), PEI-capped QDs (c) and a spectrum of hyaluronic acid sodium salt (d) as a reference for the spectrum of HA-capped QDs (a). From the FT-IR spectrum of GSH-capped QDs, we can see a wide and intense peak centered at 3197 cm^{-1} which is characteristic of the $-\text{OH}$ functions that likely originates from water molecules bounded at the surface of QDs. The signals at 1574 cm^{-1} and 1538 cm^{-1} prove the existence of $-\text{N-H}$ amide and $-\text{COO}^-$ carboxylic groups. The absence of the characteristic peak of the $-\text{S-H}$ stretching at around $2535\text{-}2564\text{ cm}^{-1}$ indicates that the GSH ligand was bounded to QDs via the sulfur atom.

The FT-IR spectrum of PEI-capped QDs shows more intense peaks for C-H stretching at $\sim 2950\text{ cm}^{-1}$, 2850 cm^{-1} and at 1473.67 cm^{-1} and new signals appear and between 1650 and 1580 cm^{-1} (N-H bending). The characteristic peaks of the amine group also exist at $\sim 3400\text{ cm}^{-1}$ and $\sim 1630\text{ cm}^{-1}$. The sharp peak at 1020 cm^{-1} observed for HA-capped QDs is the characteristic peak of C-O-C bonds of HA, which is a proof of successfully capping of the QDs surfaces with HA.

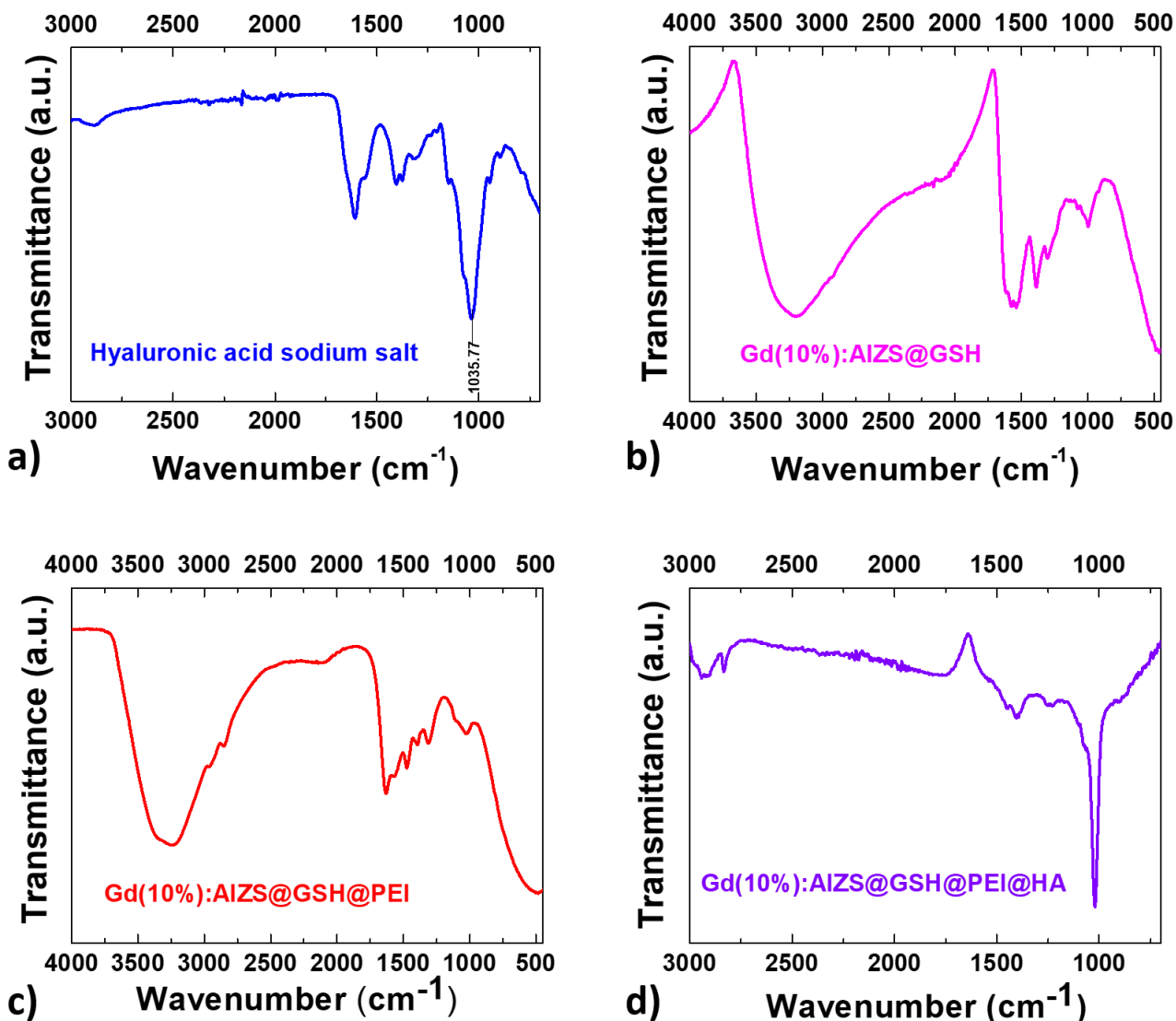


Figure 3.23. FT-IR spectra of (a) hyaluronic acid sodium salt and 10% Gd-doped AIZS QDs capped with (b) GSH, (c) GSH-PEI and (d) GSH-PEI-HA

Fig. 3.24 shows the results of DLS analyses and zeta potentials measurements of the different ligand capped AIZS QDs using 10% Mn-doped particles as representative. According to the results, GSH-capped QDs have minus zeta-potential (-50 mV in deionized water), which is in consistent with the presence of carboxylate groups on their surfaces. The QDs were further capped with PEI, which provided cationic properties to the surface of the QDs (zeta-potential +50 mV) and facilitated electrostatic interactions with negatively charged hyaluronic acid (Fig. 3.24b).

Moreover, according to the dynamic light scattering analysis, the hydrodynamic diameters (HDs) of QDs increased in the order of GSH < GSH-PEI < GSH-PEI-HA, which further proves the successful capping of the QDs (Fig. 3.24a).

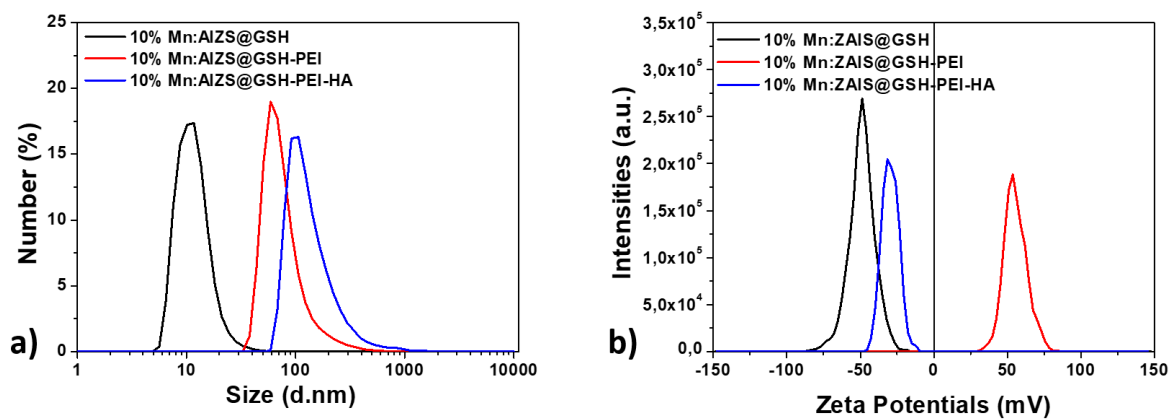


Figure 3.24. (a) DLS and (b) zeta-potential analyses of 10% Mn-doped AIZS QDs capped with glutathione, polyethylene imine and hyaluronic acid

3.8. Colloidal and photostability

The colloidal and the photostability of nanoparticles are crucial factors for their application in biological or medical purposes. The colloidal stability of as-prepared and cationized QDs was evaluated in phosphate buffer saline (0.1 M, pH 7.4) and the pH was adjusted by using 1 M NaOH and 1 M HCl in the range of 3 and 9. As can be seen from the results, PL QYs of glutathione-capped QDs increase with the pH from 5 to 9 (Fig. 3.25a). The pKa values of GSH are 2.12 (CO₂H), 3.59 (CO₂H) and 8.75 (NH₃⁺). When the pH increases, both carboxylic acids are in their carboxylate form and the NH₂ group in its ammonium form until pH 8.75. This explains why the colloidal stability and thus the PL QY are the highest at pH values ranging from 5 to 9.

The photostability of these QDs was determined by measuring the irradiation time dependence of the PL QY values. The photostability assessment has conducted for 3 h under UV light illumination with a fluence of 50 W/cm², and results show that the PL QY of QDs only slightly decreases with the irradiation time (Fig. 3.25b).

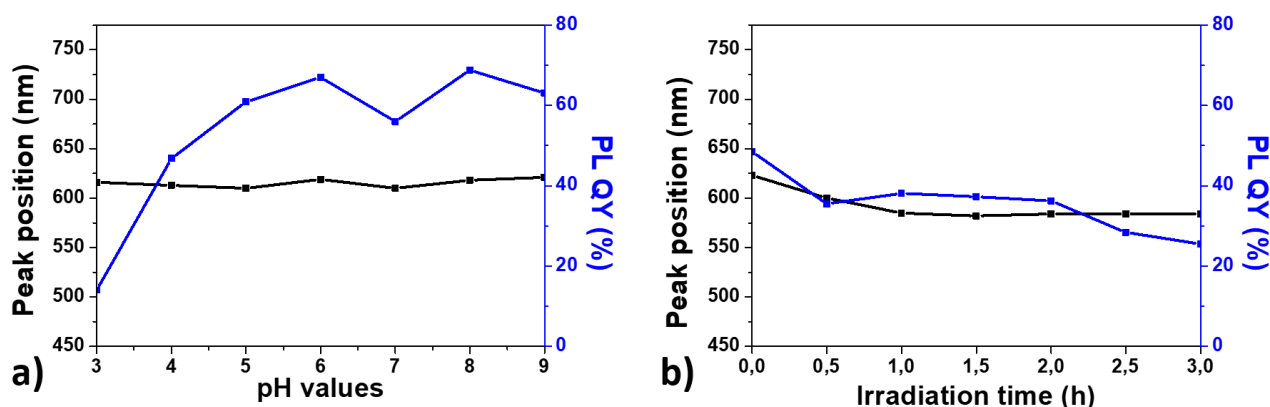


Figure 3.25. (a) Colloidal and (b) photostability of aqueous phase synthesized 10% Mn-doped AIZS@GSH QDs

3.9. Cytotoxicity

The nanoparticles used in biological applications must also be nontoxic. For this reason, the cytotoxicity of as-synthesized GSH-capped AIZS QDs and positively charged PEI-capped AIZS QDs was determined.

For the cytotoxicity test of QDs, the viability of KB cells was measured as a function of QDs concentrations. The KB cell line is widely used in biomedical research for MTT assay, where the cytotoxicity of potential drugs and/or imaging probes is studied¹⁶⁷. Standard cell viability assay is based on the reduction of yellow 3-(4,5-dimethylthiazol-2-yl)-2,5-diphenyltetrazolium bromide (MTT) to purple formazan in living cells.

MTT assay results indicate that Mn-, Gd- or Fe-doped, GSH-capped and GSH-PEI-capped AIZS QDs exhibit a good biocompatibility: all particles show only weak toxicity until a concentration of 1 mg/mL (Fig. 3.26). The same cytotoxicity results were found for GSH@PEI-FA capped AIZS QDs (Fig. 3.27).

The determined cell viability for GSH-capped AIZS QDs was higher than 60% at a concentration of 1 mg/mL, while for PEI-covered QDs higher than 80%. Fig. 3.26 shows that the capping with PEI increases the biocompatibility for all prepared QDs. Furthermore, to investigate the potential application of these QDs in bioimaging, the cytotoxicity of the QDs capped with FA was studied and the results are presented in Fig. 3.26. To connect FA with the QDs, the PEI-FA conjugate was first prepared¹⁴⁸, then the positively charged conjugate was associated to the negatively charged GSH-capped AIZS QDs. We can see that the capping with FA does not decrease the cell viability (the lowest cell viability, 76.4 %, being found for 5% Mn-doped AIZS QDs). These results confirm the high potential of AIZS QDs for bio-imaging applications.

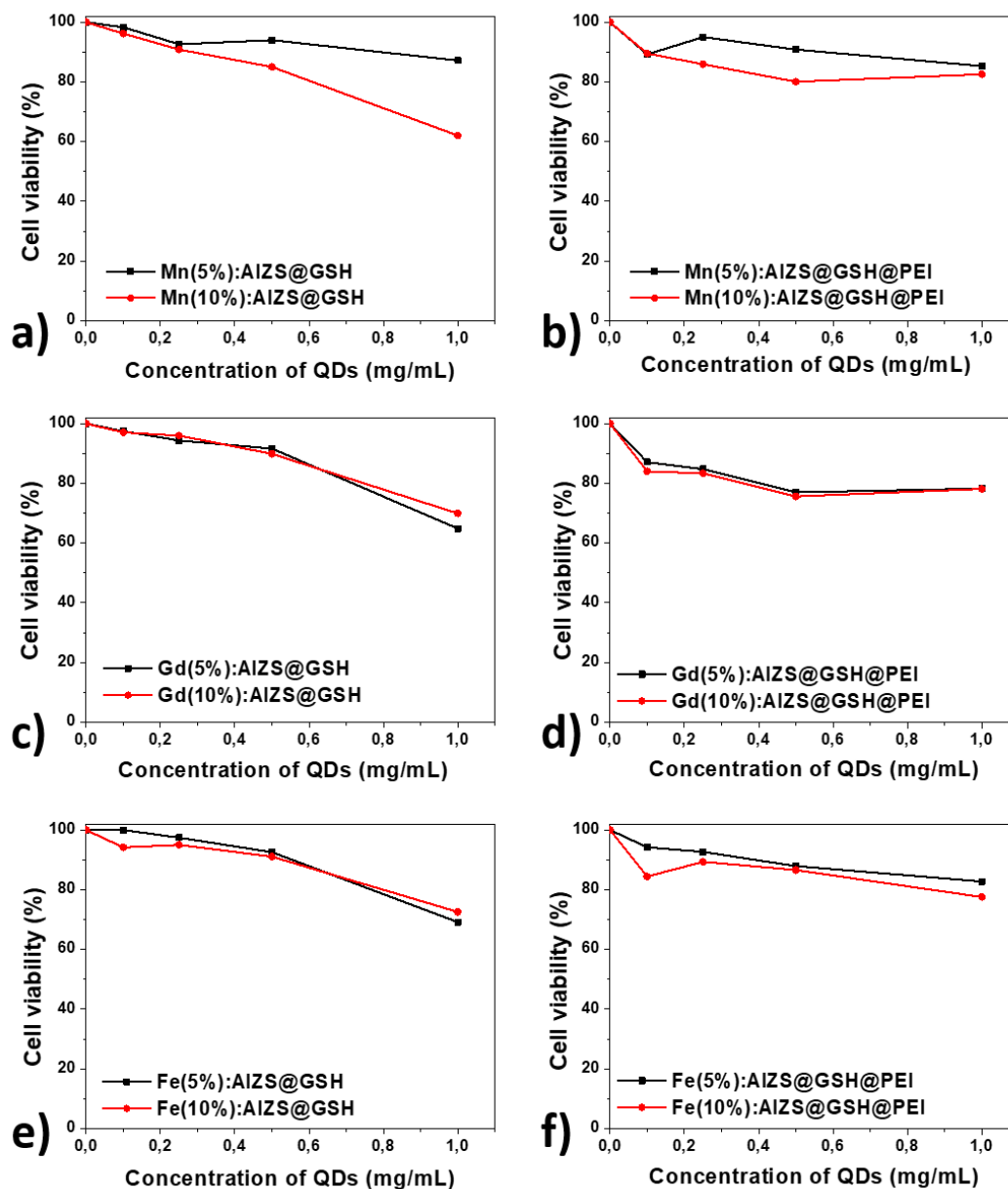


Figure 3.26. KB cells viability detected by the MTT assay after 24 h incubation in GSH and GSH@PEI-capped Mn-doped (a and b, respectively), Gd-doped (c and d, respectively), and Fe-doped (e and f, respectively) AIZS QDs at different concentrations

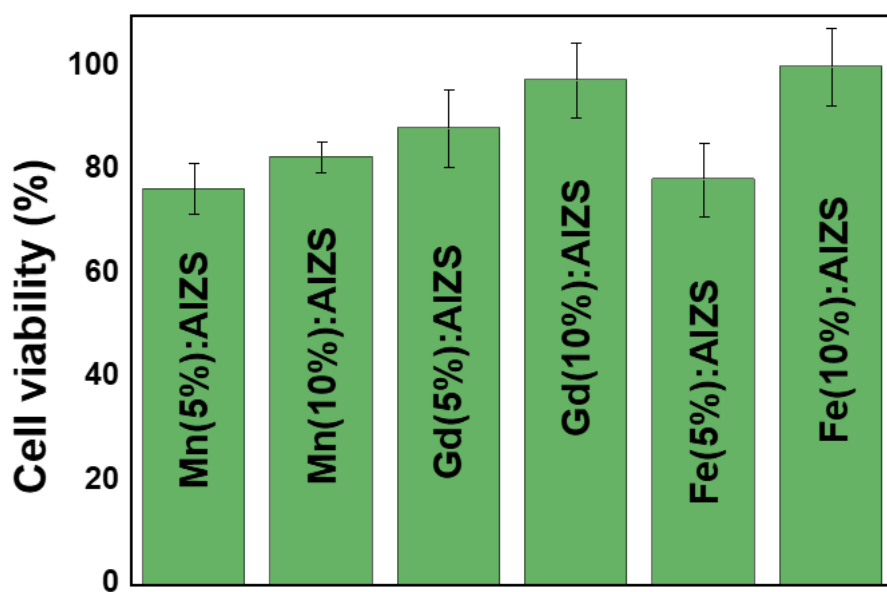


Figure 3.27. KB cells viability determined by MTT assay after 24 h incubation with GSH-PEI-FA-capped AIZS QDs (concentration of 1 mg/mL)

3.10. Fluorescence imaging

GSH-PEI-FA-capped AIZS QDs were used for *in vitro* bioimaging tests. The GSH-capped AIZS QDs were used as controls. *In vitro* bioimaging experiments using KB cells and AIZS QDs were carried out as follows: the KB cells (the folate receptors were found to be highly overexpressed in KB cell lines) were stained for 3 h with a 0.1 mg/mL solution of FA-conjugated AIZS QDs, then the cells were rinsed to remove noninternalized QDs. The cells were also stained with DAPI to visualize their nuclei. Results are described in Fig. 3.28: the first column shows KB cells under visible light, the second column the fluorescence of the cell nuclei stained with DAPI, the third column shows the fluorescence from the AIZS QDs into the cells, while the fourth column, the merged images when cells were stained with DAPI and AIZS QDs.

As can be seen from the merged images, when using the targeted QDs, the dark points in images in visible light corresponds to the red parts in QDs fluorescent images. They are likely internalized via endocytosis vesicles and they do not enter into the nucleus and thus should not generate genotoxicity. (Fig. 3.28b, c, d). In the case of control QDs (GSH-capped AIGZS QDs, not linked to FA), a fluorescence could be observed in both nuclei and the cytoplasm of the cells (Fig. 3.28a). The efficient labeling of cells using GSH-PEI-FA-coated AIZS QDs indicates that the FA conjugation has been successful and facilitates specific intracellular uptake, which occurs mainly through receptor-mediated endocytosis⁹².

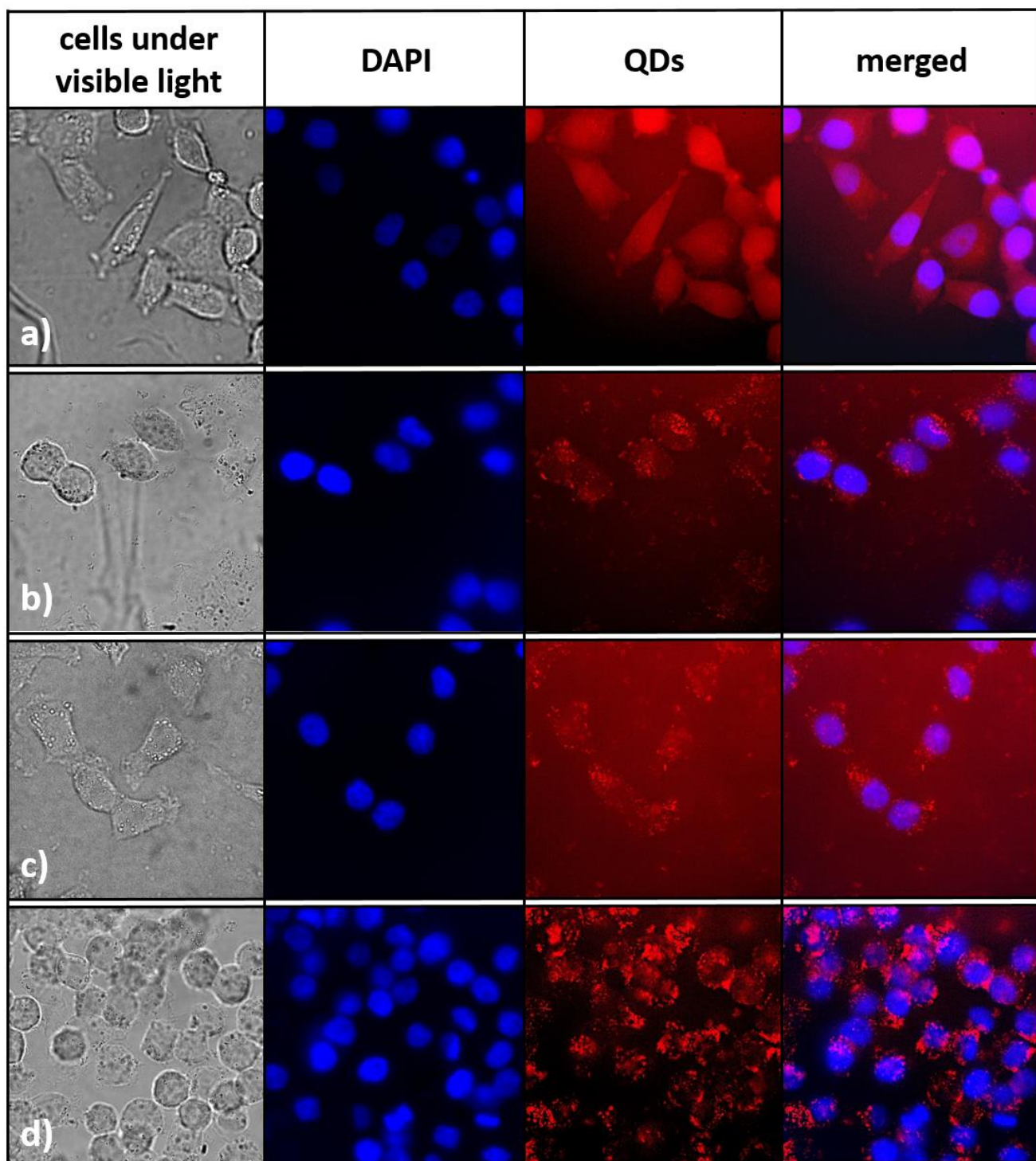


Figure 3.28. Confocal microscopic images of AIZS QDs: a) 10 % Mn, GSH; b) 10% Mn, GSH-PEI-FA; c) 10% Gd, GSH-PEI-FA; d) 10% Fe, GSH-PEI-FA

3.11. Conclusion

Highly fluorescent water-soluble Ag-In-Zn-S QDs and their paramagnetic Mn-, Gd-, and Fe-doped derivatives were synthesized in the presence of GSH as a capping ligand using a three-step synthesis method. Their structural, optical, magnetic properties were studied. Doped QDs exhibit paramagnetic and superparamagnetic properties due to their small sizes. Their suitable physico-chemical properties and their fluorescence and magnetic properties make these probes of high potential as fluorescent or/and fluorescent and magnetic labels.

Chapter 4. Quinary Ag-In-Ga-Zn-S QDs synthesis

4.1. Introduction

Ternary I-III-VI₂ semiconductor QDs (where I = Ag or Cu, III = In or Ga and VI = S, Se or Te) and quaternary ones of general formula I-II-III-VI₂ (where II = Zn) obtained after shelling and alloying with ZnS have widely been investigated in recent years due to their unique chemical and optical properties^{11,122,168–170}. Much of the studies on these QDs have been limited to the direct bandgap CuInS₂/ZnS (CIZS)^{171,172} and AgInS₂/ZnS (AIZS)^{61,173,174} semiconductors that have been demonstrated to be of high promise for photovoltaic or photocatalytic applications,^{36,175,176} solid-state lighting devices^{106,177} or bio-imaging.^{75,178} Moreover, these QDs are considered to be safe and environmentally benign as they do not contain toxic elements such as Cd or Pb.

One of the key advantages of these QDs is their high degree of compositional flexibility by varying monovalent and/or trivalent cations which allows to finely tune their bandgap energy and thus the PL emission wavelength over all the whole visible region and even in the near infrared.^{11,122,168–170} In recent years, different quaternary compositional and structural variants such as green to orange emitting CuInGaS₂,^{179,180} green to red emitting CuGaZnS₂¹⁸¹ or CuGaZnSe₂,¹⁸² blue to orange emitting Mn²⁺-doped CuGaZnS₂,^{183,184} violet to aqua emitting AgGaZnS₂^{185,186} or blue to orange-emitting AgGaInS₂^{187,188} have been reported. Only one report describes the synthesis of quinary CuGaInZnS₂ QDs with a PL emission tunable from the orange to the red by varying the Cu/Ga molar ratio.¹⁷⁹ The synthesis of these quaternary and quinary nanocrystals is classically performed like that of AIZS and CIZS QDs by thermal decomposition of metal salts or organometallic precursors in the presence of S or Se precursors using dodecanethiol, oleylamine or ethylenediamine as capping ligand.^{179–186,188} AgInS₂ QDs were also used as template to prepare AgGaInS₂ by cation exchange between In³⁺ and Ga³⁺.¹⁸⁷ Some of the synthetic protocols require the injection of Na₂S or NaHSe, multiple injections of the shell precursors (generally ZnS or ZnSe) or the handling of air-sensitive reagents.

In recent years, single-source molecular precursor synthesis of QDs has emerged due to its simplicity and safety when compared to multi-step processes.^{17,89,189,190} In this context,

transition metal dithiocarbamates are well known to decompose under inert atmosphere into metal sulfide nanocrystals.¹⁹¹ This approach has successfully been used to prepare binary like Ag₂S, ZnS or CdS, ternary like Zn_{1-x}Mn_xS or Zn_xCd_{1-x}S nanocrystals using a mixture of dithiocarbamates of each of these metals.¹⁹¹⁻¹⁹⁵ However, the use of a single dithiocarbamate complex containing more than one metal for the production of corresponding sulfides is far unexplored. Herein, a facile method allowing the production of highly fluorescent AgInGaZnS (AIGZS) QDs with PL QY up to 48.3% is presented. Using a single dithiocarbamate complex of Ag⁺, In³⁺, Ga³⁺ and Zn²⁺ and OAm as solvent and capping ligand, a series of AIGZS QDs could be produced by varying the Ag/In/Ga/Zn ratio in the precursor. The obtained QDs exhibit a low size (ca. 2 nm) and their PL emission could be tuned from the visible to the near-infrared. Moreover, the optical properties could be maintained after ligand exchange and transfer into water.

4.2. Experimental part

Materials

Silver nitrate AgNO_3 (ReagentPlus, >99%, Sigma), gallium nitrate hydrate $\text{Ga}(\text{NO}_3)_3 \cdot x\text{H}_2\text{O}$ (>99.9%, Sigma), indium nitrate hydrate $\text{In}(\text{NO}_3)_3 \cdot x\text{H}_2\text{O}$ (>99.9%, Alfa Aesar), zinc diethyldithiocarbamate $\text{Zn}(\text{DDTC})_2$ (97%, Sigma), oleylamine (80-90%, Acros), glutathione (99%, Sigma), tetramethylammonium hydroxide pentahydrate (97%, Sigma), glycine (99+%, Acros), carbon disulfide (>99.9%, Sigma) were used as received without any purification.

Preparation of $\text{Ag}_x\text{In}_y\text{Ga}_{2-x-y}\text{Zn}_2(\text{S}_2\text{CN}(\text{C}_2\text{H}_5)_2)_4$ precursors

AgNO_3 , $\text{In}(\text{NO}_3)_3$ and $\text{Ga}(\text{NO}_3)_3$ with a defined Ag/In/Ga ratio were mixed with $\text{Zn}(\text{DDTC})_2$ in 10 mL of a 1:1 water-methanol mixture. The solution was stirred for 2 h at room temperature to form $\text{Ag}_x\text{In}_y\text{Ga}_{2-x-y}\text{Zn}_2(\text{S}_2\text{CN}(\text{C}_2\text{H}_5)_2)_4$ precursors when the (Ag + In + Ga)/Zn ratio is of 1. The product was collected by centrifugation (4000 rpm for 15 min), dried under vacuum and stored at 4°C before use.

Preparation of Ag-In-Ga-Zn-S QDs

The AIGZS QDs were synthesized by thermolysis of $\text{Ag}_x\text{In}_y\text{Ga}_{2-x-y}\text{Zn}_2(\text{S}_2\text{CN}(\text{C}_2\text{H}_5)_2)_4$ precursors in OAm. First, the precursor (100 mg) was dispersed in OAm (6 mL) and the mixture was stirred under argon flow until homogenization. Then, the solution was heated (190, 220 or 250°C) for 10 min and the color changed to dark. After cooling, the large sized crystals were removed by centrifugation (5000 rpm for 10 min). The supernatant was precipitated by adding an excess of methanol and the powder was collected by centrifugation (5000 rpm for 10 min) and dried under vacuum. Next, the dried product was redispersed in OAm (6 mL) and the solution was heated (190, 220 or 250°C) for 30 min. The obtained AIGZS QDs were precipitated by adding an excess of methanol, recovered by centrifugation (5000 rpm for 10 min) and purified by washing with methanol.

Transfer of AIGZS QDs into water

Glutathione tetramethylammonium (GTMA) coating. GTMA-coating was conducted using a previously described method.¹⁹⁶ Briefly, GTMA was prepared by dissolving GSH (30 mg) and TMAH (54 mg) in 1 mL of methanol. Separately, 5 mg of AIGZS@OAm QDs were dispersed in 1 mL toluene, then 5 mL chloroform was added. Next, 0.5 mL of GTMA solution was dropwise added to the QDs solution and the mixture was vigorously stirred for 2 h. Then, water (4.5 mL) was added and the two-layer mixture was slightly shaken to transfer QDs into the water layer before being left for 1 h to reach equilibrium. Finally, the top water layer containing GTMA-capped AIGZS QDs was collected.

Glycine diethyldithiocarbamate (Gly-DDTC) capping.⁶² AIGZS@OAm QDs (2 mg) dispersed in a methanol/chloroform mixture (3 mL, 1:1 vol.) were added to glycine (80 mg) in a methanol/chloroform mixture (2 mL, 1:1 vol.) containing TMAH (384.2 mg) and CS₂ (81 mg). The mixture was stirred for 12 h at room temperature followed by centrifugation for 3 min at 4000 rpm. Then, 5 mL of diethyl ether were added to the supernatant and the mixture centrifuged for 10 min at 5000 rpm. Next, the fluorescent bottom layer was dispersed in methanol (2 mL), precipitated with THF (5 mL) and centrifuged (5000 rpm, 10 min). The obtained solid was dispersed in Tris buffer (0.1 M, pH 8.5).

Characterization

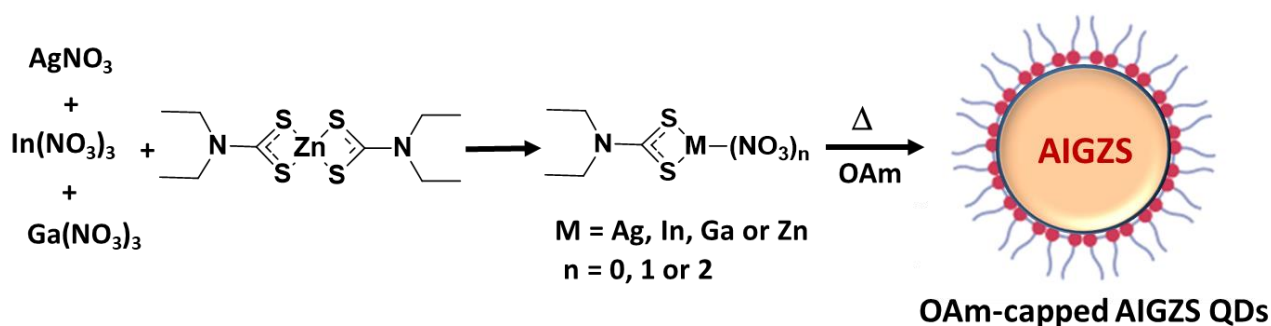
The morphology of the QDs was investigated by transmission electron microscopy (TEM) and high-resolution TEM (HR-TEM) using a Philips CM200 instrument operating at 200 kV. A drop of the QDs dispersed in toluene was deposited onto a carbon-coated copper grid. The crystal structure of AIGZS QDs was examined by X-ray diffraction (XRD) using a Panalytical X'Pert Pro MPD diffractometer with Cu K α radiation ($\lambda = 0.15418$ nm). The dried samples were placed on a silicon zero-background sample holder and the XRD patterns were recorded at room temperature. XRD patterns were analyzed using TOPAS (Bruker AXS, Version 4-2). X-ray photoelectron spectroscopy (XPS) measurements were carried out with a Gamdata Scienta SES 200-2 spectrometer. Thermogravimetric analysis (TGA) was conducted under air atmosphere from room temperature to 800°C at a heating rate of 10°C/min using a TGA/DSC1 STAR equipment (MettlerToledo). Inductively Coupled Plasma-Optical Emission

Spectrometer (ICP-OES) measurements were conducted on a Varian 720-ES equipment. Hydrodynamic QDs sizes and Zeta potential measurements were determined by dynamic light scattering (DLS) on a Zetasizer Nano ZS (green laser beam 532 nm) (Malvern Panalytical, UK), Cuvette DTS1070.

FT-IR absorption spectra were collected on a Bruker ALPHA spectrometer. Optical absorption and PL emission spectra were recorded on a UV-visible absorption spectrometer (Thermo Scientific Evolution 220) and spectrofluorometer (Horiba Fluoromax-4 Jobin Yvon), respectively. PL spectra were spectrally corrected and PL QYs were determined relative to Rhodamine 6G in ethanol (PL QY = 94%). For the time resolved photoluminescence (TR-PL) experiments, the QDs were pumped by the 355 nm line of a frequency-tripled YAG (yttrium aluminium garnet):Nd laser. The laser pulse frequency, energy and duration were typically equal to 10 Hz, 50 μ J and 10 ns, respectively. The PL signal was analysed by a monochromator equipped with a 600 grooves/mm grating and by a photomultiplier tube cooled at 190 K. The rise time of the detector is equal to around 3 ns.

4.3. Morphology and structural characterizations

The AIGZS QDs precursors were prepared by mixing AgNO_3 , $\text{Ga}(\text{NO}_3)_3$ and $\text{In}(\text{NO}_3)_3$ with $\text{Zn}(\text{DDTC})_2$ ($n\text{Ag}^+ + n\text{In}^{3+} + n\text{Ga}^{3+}/n\text{Zn}^{2+} = 1$ or 0.5) in a water/methanol mixture (Scheme 4.1). The powders obtained after centrifugation and drying were stored at 4°C before use and can be handled in open air without any protection. The thermolysis of the precursors in the presence of OAm produces AIGZS QDs, DDTC serving as sulfur source and OAm as capping ligand.



Scheme 4.1. Schematic representation of AIGZS QDs synthesis

According to the hard and soft acids and bases theory, Ag^+ is a soft Lewis acid, Ga^{3+} and In^{3+} are hard Lewis acids while Zn^{2+} can be considered as borderline.¹⁹⁷ The reaction of $\text{Zn}(\text{DDTC})_2$ with AgNO_3 , $\text{Ga}(\text{NO}_3)_3$ and $\text{In}(\text{NO}_3)_3$ should favor the exchange of Zn^{2+} by Ag^+ as DDTC is a soft base. Once dispersed in OAm, In^{3+} and Ga^{3+} likely coordinate more strongly with OAm which is a harder Lewis acid. ICP-OES and XPS analyses conducted on AIGZS QDs indicate that the Ag/In/Ga/Zn ratio is close to the feeding ratio used to prepare the precursors (*vide infra*), suggesting that all metal cations incorporate well in the precursors either as mono-, bis- or tris-complexes of DDTC.

The cation exchange between Ag, In and Ga nitrates and $\text{Zn}(\text{DDTC})_2$ during the $\text{Ag}_x\text{In}_y\text{Ga}_{2-x-y}\text{Zn}_2(\text{S}_2\text{CN}(\text{C}_2\text{H}_5)_2)_4$ precursors synthesis was first evidenced by TGA. Pure $\text{Zn}(\text{DDTC})_2$ is stable until ca. 250°C and a sharp weight loss is observed above 300°C , which corresponds to the decomposition of $\text{Zn}(\text{DDTC})_2$ into ZnS (Fig. 4.1). For all precursors, the decomposition is more complex and takes place in successive steps between 100 and 300°C . The remaining mass (ca. 35%) is higher than that measured after thermolysis of $\text{Zn}(\text{DDTC})_2$ (ca. 10%), indicating the formation of higher molecular weight metal sulfides. The precursors powders were also examined by XRD. While pure $\text{Zn}(\text{DDTC})_2$ exhibits a monoclinic structure (JCPDS No 44-

1815),¹⁹⁸ new signals appear in the XRD patterns of the precursors, further confirming that a reaction occurred between Zn(DDTC)_2 and Ag, In and Ga nitrates (Fig. 4.2).

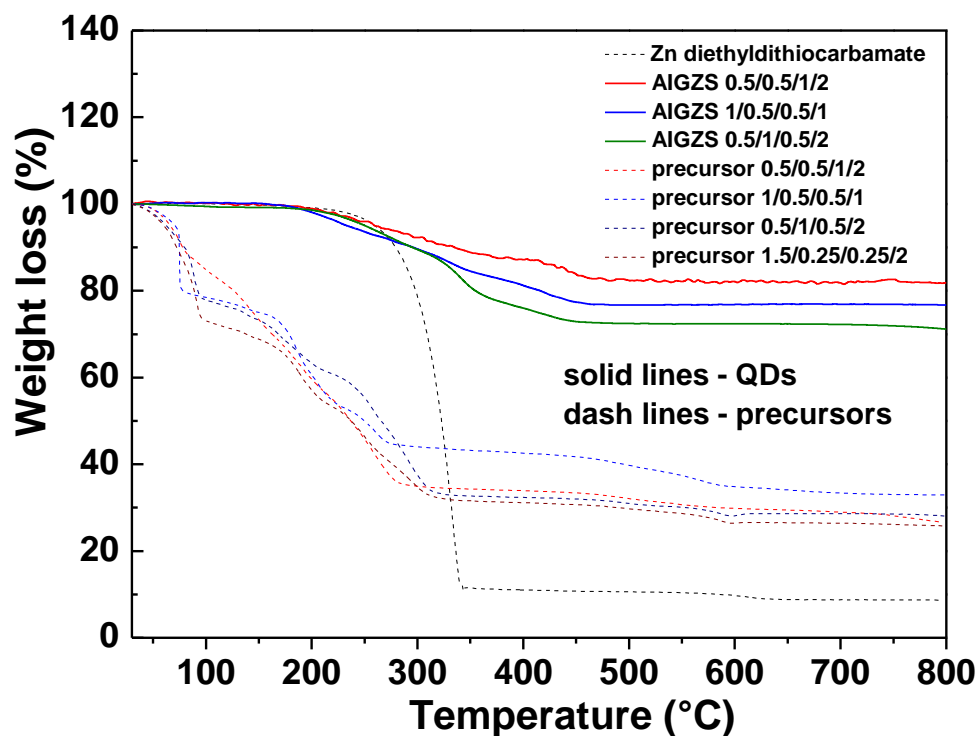


Figure 4.1. TGA traces of Zn(DDTC)_2 , AIGZS precursors prepared with Ag/In/Ga/Zn ratios of 0.5/0.5/1/2, 1/0.5/0.5/1, 0.5/1/0.5/2 and 1.5/0.25/0.25/2 and the corresponding AIGZS QDs

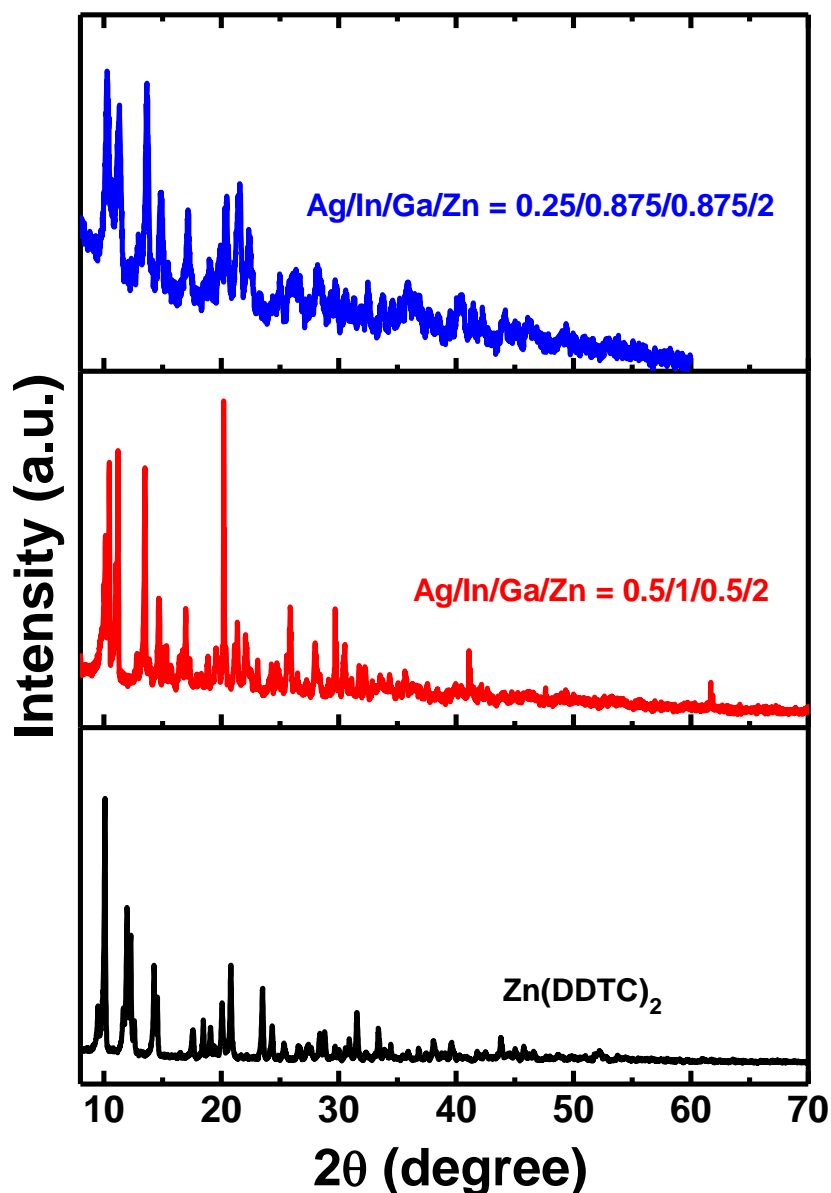


Figure 4.2. XRD patterns of Zn(DDTC)_2 and of the precursors prepared with Ag/In/Ga/Zn ratios of 0.25/0.875/0.875/2 and 0.5/1/0.5/2

The FT-IR spectra of the precursors show signals at ca. 3360 cm^{-1} ($\gamma_{\text{O-H}}$ from adsorbed water molecules), $2967\text{-}2867\text{ cm}^{-1}$ ($\gamma_{\text{C-H}}$), 1638 cm^{-1} ($\delta_{\text{O-H}}$) and numerous signals between 1497 and 1270 cm^{-1} originating from C-H and C-N stretchings (Fig. 4.3).¹⁹⁹ The signals at 1204 , 1134 and 1057 cm^{-1} can be attributed to $\gamma_{\text{C-S}}$, $\gamma_{\text{N-CS}_2}$ and $\gamma_{\text{C=S}}$ bonds, respectively.¹⁹⁹ The weak signals below 500 cm^{-1} originate from metal-S bonds. All these signals disappear after heating at 220°C and only the characteristic vibrations of the OAm ligand can be observed for AIGZS QDs ($\gamma_{\text{N-H}}$ at 3212 cm^{-1} and $\gamma_{\text{C-H}}$ at 2935 and 2848 cm^{-1}) (Fig. 4.4). Finally, it can also be noted that

depending on the Ag/In/Ga/Zn ratio, the precursors absorb in the UV and in the visible region until ca. 450 nm (see Fig. 4.11 for representative UV-visible absorption spectra). After thermolysis, the absorption in the visible region is significantly extended, which further confirms the decomposition of the precursors into AIGZS QDs.

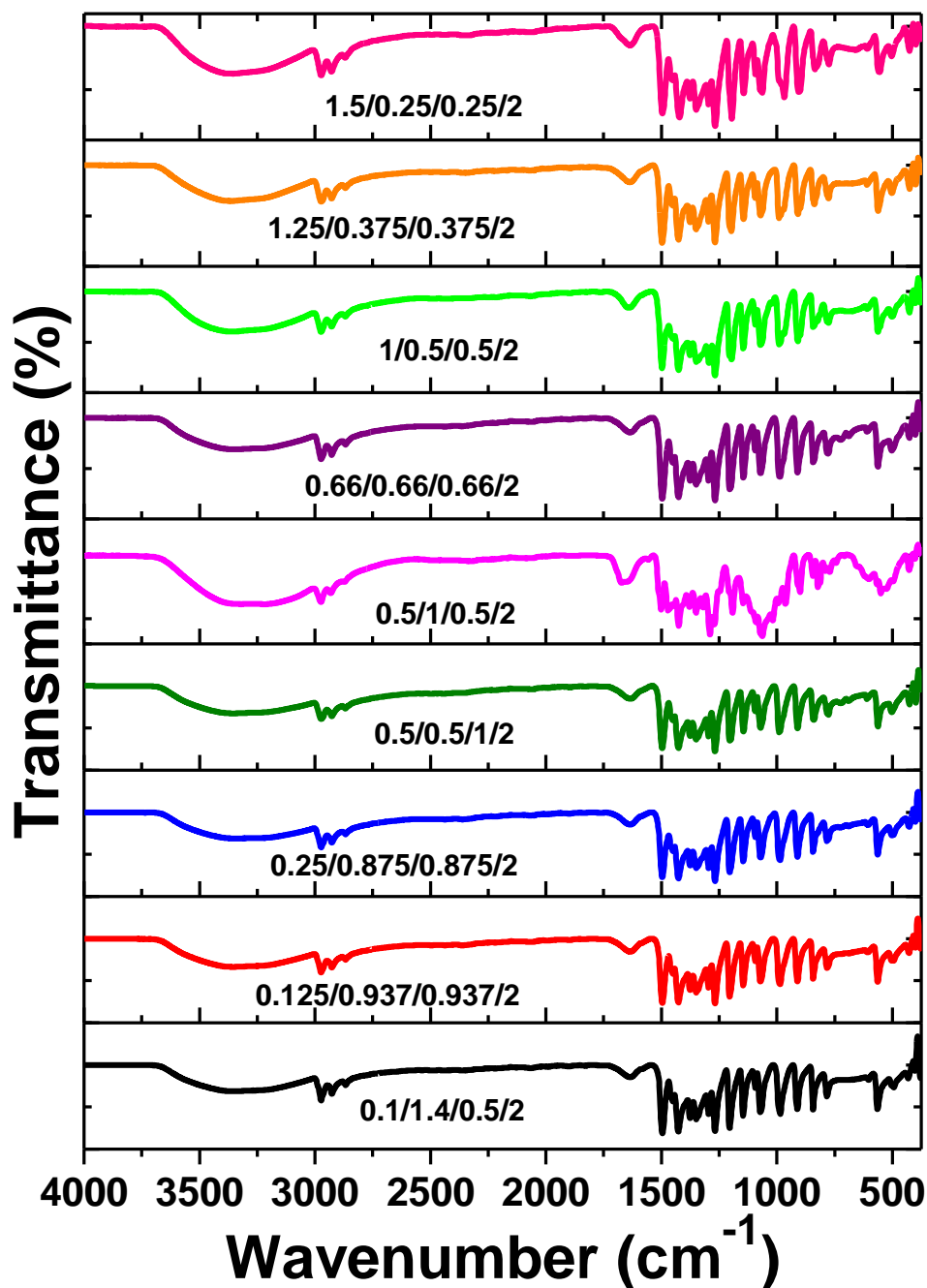


Figure 4.3. FT-IR spectra of AIGZS precursors

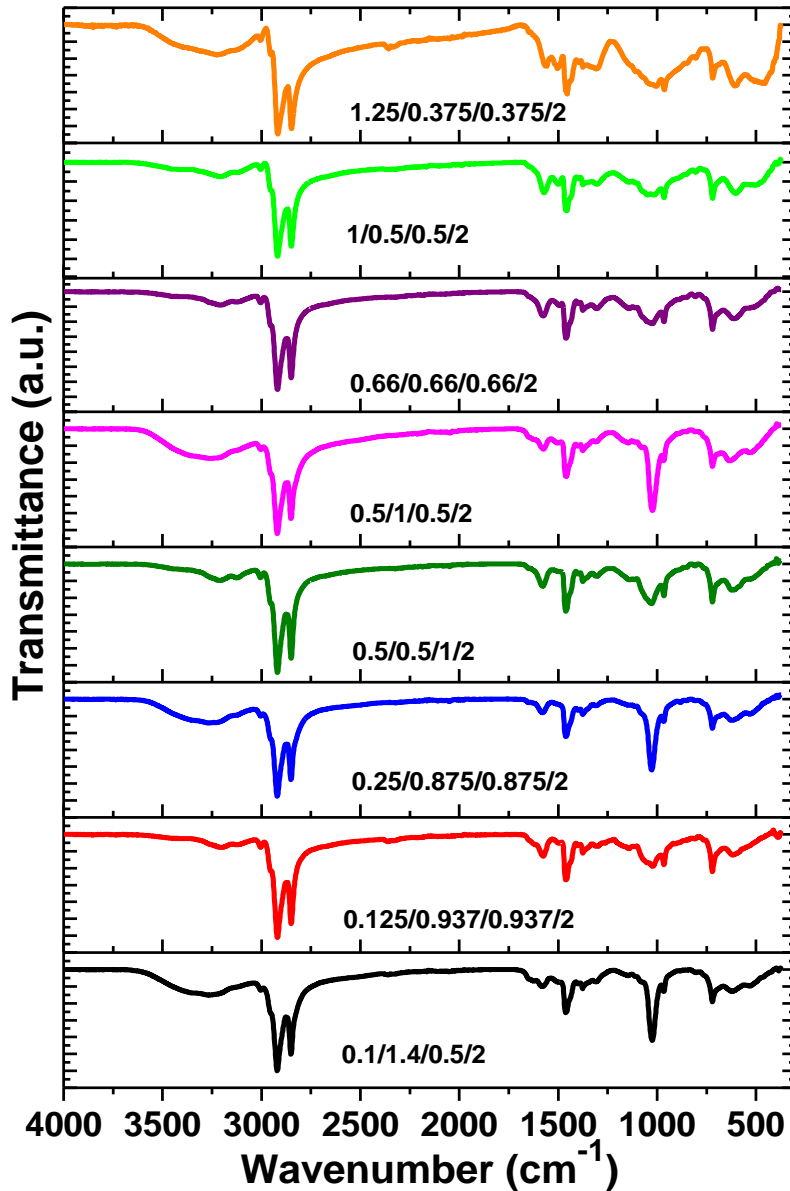


Figure 4.4. FT-IR spectra of OAm-capped AIGZS QDs obtained after heating at 220°C

The crystal structure, the size and the size distribution of AIGZS QDs were studied by XRD, TEM and SAED. The reflection peaks are characteristic of a tetragonal chalcopyrite phase and their broadness is indicative of the small size of the nanocrystals (Fig. 4.5a). The mean crystalline size, calculated from the (112) reflection by the Scherrer formula, is of ca. 2 nm. It can also be observed that changes in the Ag/In/Ga/Zn ratio does not affect the crystalline structure of the dots. Finally, no diffraction peaks of Ag_2S , In_2S_3 , Ga_2S_3 or ZnS could be observed in the XRD patterns, indicating the high purity of AIGZS QDs.

A representative TEM image of AIGZS QDs prepared with a Ag/In/Ga/Zn ratio of 1/0.5/0.5/2 is shown in Fig. 4.5b and Fig. 4.6. Regardless of the Ag/In/Ga/Zn ratio used for the synthesis of the precursors, AIGZS exhibit a spherical shape and a relatively narrow size distribution (2.0 ± 0.4 nm). The clear lattice planes observed in the HR-TEM image (Fig. 4.5c) and the electron diffraction pattern (inset of Fig. 4.5b) confirm their good crystallinity. The lattice spacing of 0.31 nm is consistent with the (112) plane of the tetragonal structure. The EDX analysis shows the characteristic peaks of Ag, In, Ga and Zn (Fig. 4.7). The atomic ratio Ag/In/Ga/Zn is 1.03/0.47/0.5/2, value close to the feeding ratio, which confirms that all metals are well incorporated in the QDs.

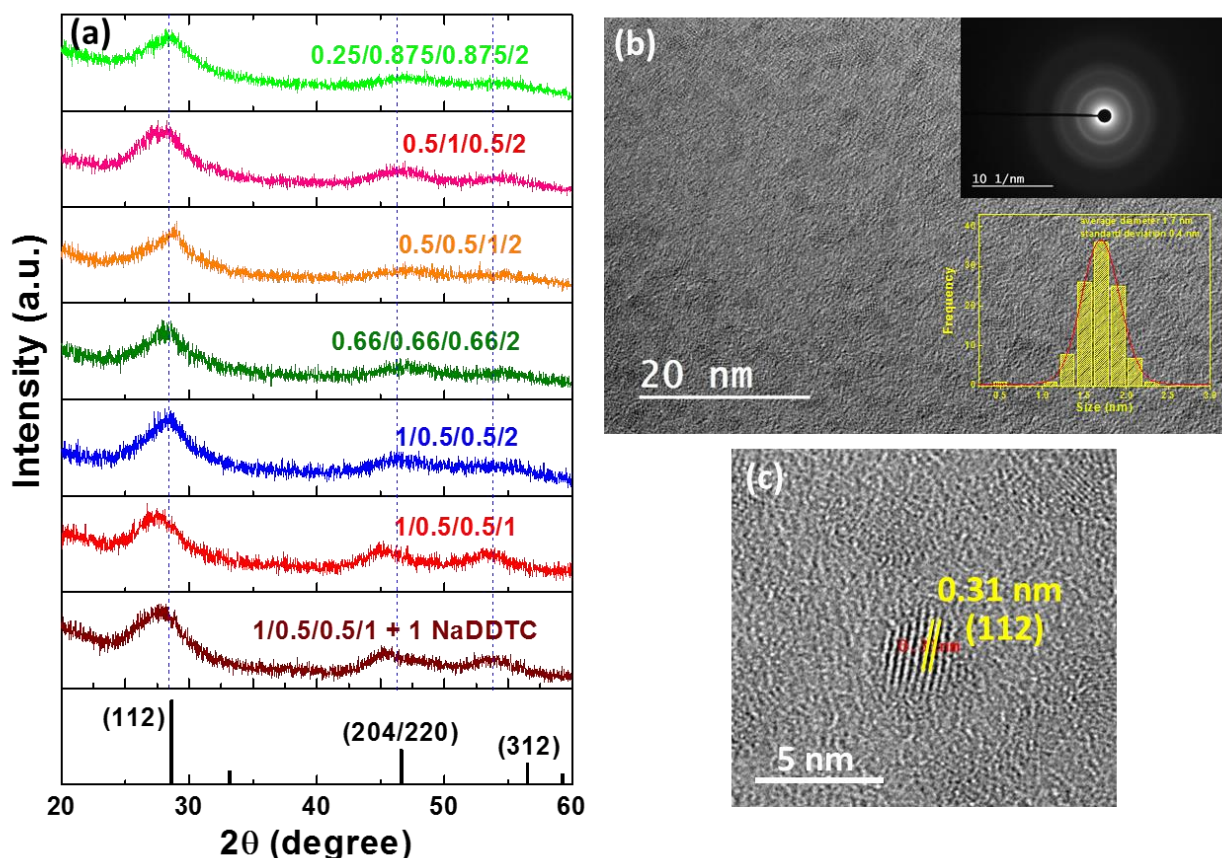


Figure 4.5. (a) XRD patterns of AIGZS QDs, (b) TEM image and (c) HR-TEM image of AIGZS QDs prepared with a Ag/In/Ga/Zn ratio of 1/0.5/0.5/2. The insets of (b) are the SAED pattern and the size distribution

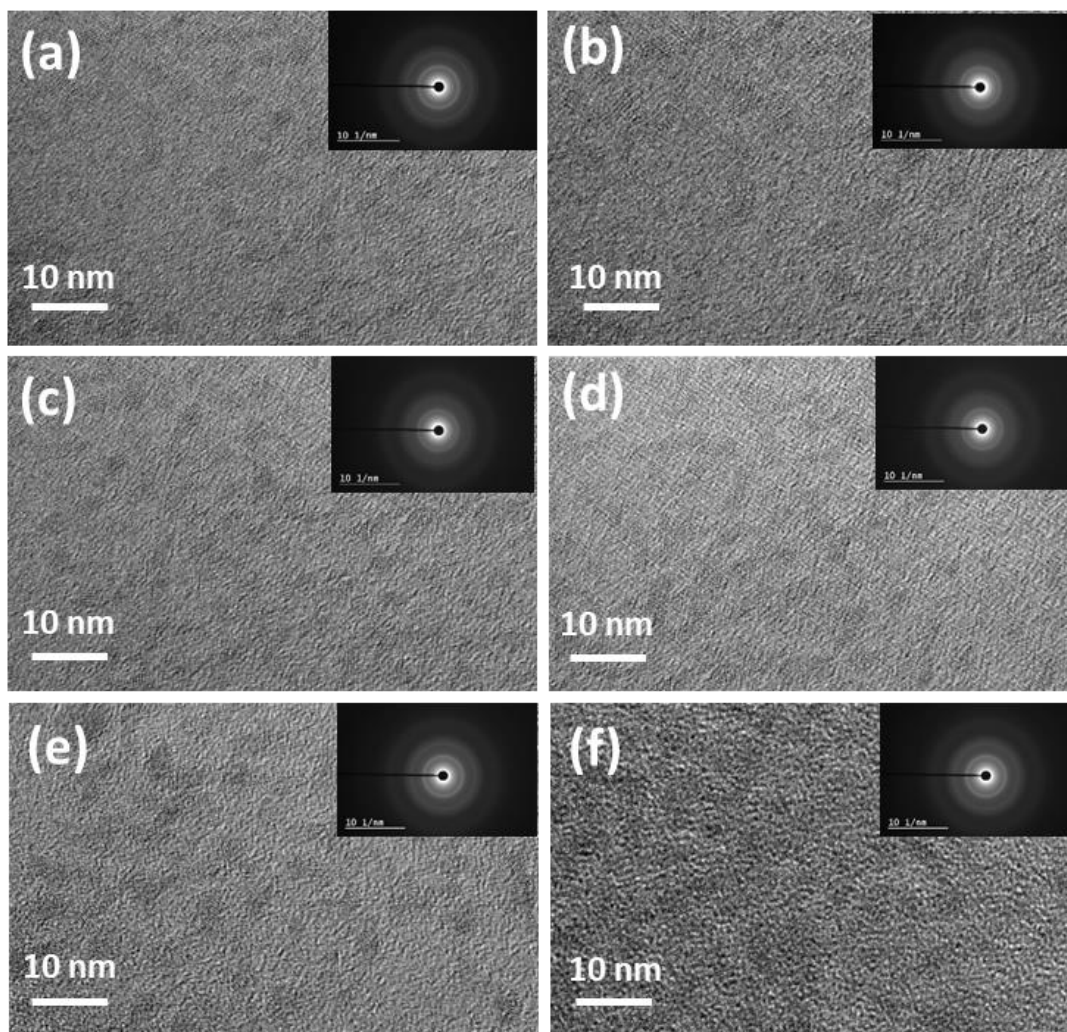


Figure 4.6. TEM images of AIGZS QDs prepared with Ag/In/Ga/Zn ratios of (a) 0.25/0.875/0.875/2, (b) 0.5/1/0.5/2, (c) 0.5/0.5/1/2, (d) 0.66/0.66/0.66/2, (e) 1/0.5/0.5/1 and (f) 1/0.5/0.5/1 + 1 NaDDTC

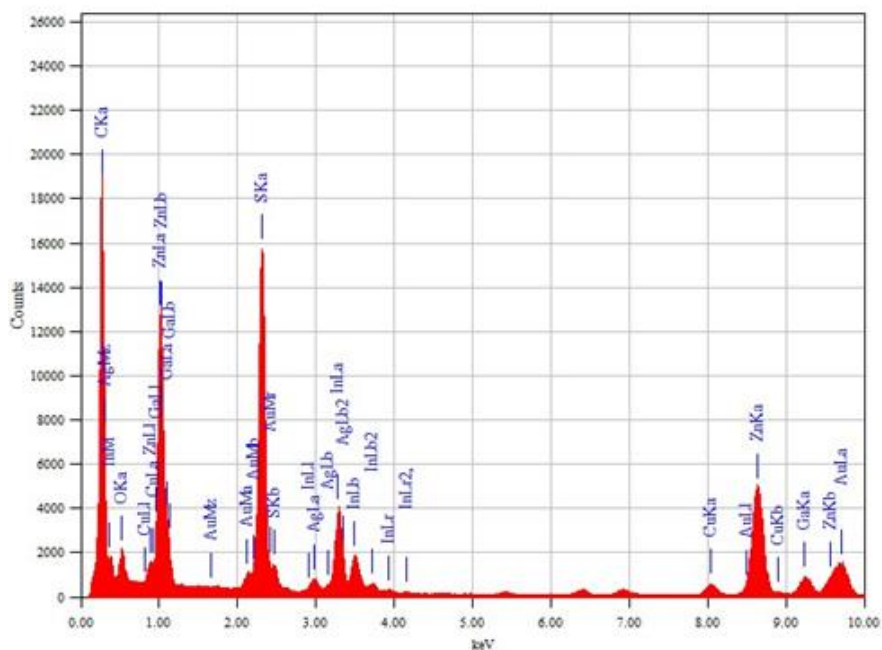


Figure 4.7. EDX analysis of AIGZS QDs prepared with a Ag/In/Ga/Zn ratio of 1/0.5/0.5/2

To determine the accurate composition of AIGZS QDs, the samples were characterized by ICP-OES and the results are described in Table 4.1. As previously observed by EDX, the composition of the dots is consistent with the nominal Ag/In/Ga/Zn ratio of the precursors. These results further demonstrate that Ag, In, Ga and Zn elements in the various precursors synthesized participate uniformly in the nucleation and growth and that the synthetic route developed allows the preparation of composition controlled AIGZS QDs.

Table 4.1. Theoretical and experimental composition of AIGZS QDs

Theoretical Ag/In/Ga/Zn ratio	Ag/In/Ga/Zn ratio determined by ICP-OES^a
0.25/0.875/0.875/2	0.27/0.83/0.90/2
0.5/1/0.5/2	0.51/0.97/0.52/2
0.5/0.5/1/2	0.53/0.46/1.01/2
0.66/0.66/0.66/2	0.68/0.65/0.67/2
1/0.5/0.5/2	1.01/0.51/0.48/2
1/0.5/0.5/1	1.03/0.48/0.49/1

^a Results were normalized to the Zn content of AIGZS QDs.

XPS was also used to investigate the chemical state and the composition of AIGZS QDs. The XPS survey spectrum shows the presence of Ag, In, Ga, Zn and S elements along with C and N originating from the OAm capping ligand (Fig. 4.8). The signals at 367.67, 445.04, 452.57, 1118.26 and 1021.79 eV can be assigned to Ag 3d_{5/2}, In 3d_{5/2}, In 3d_{3/2}, Ga 2p_{3/2} and Zn 2p_{3/2}, respectively, and confirm the valence states of Ag⁺, In³⁺, Ga³⁺ and Zn²⁺. The deconvoluted signals at 161.49 and 162.69 eV correspond to S 2p_{3/2} and S 2p_{1/2}, respectively, indicating that the metal cations are associated to S²⁻.

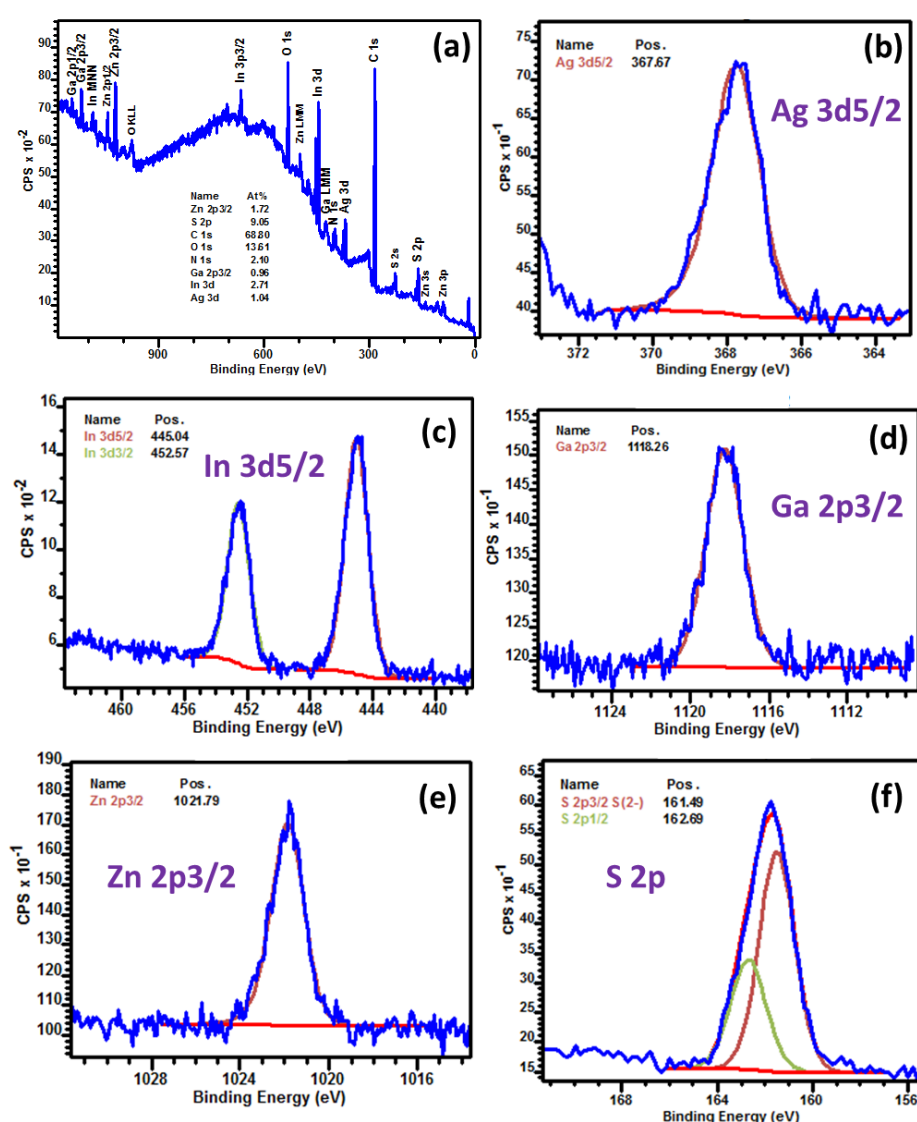


Figure 4.8. XPS analysis of AIGZS QDs prepared with a Ag/In/Ga/Zn ratio of 0.5/1/0.5/2. (a) Survey scan and high resolution scans of (b) Ag 3d_{5/2} region, (c) In 3d_{5/2} region, (d) Ga 2p_{3/2}, (e) Zn 2p_{3/2} and (f) S 2p

4.4. Optical properties

In preliminary experiments conducted with the precursor prepared with a Ag/In/Ga/Zn ratio of 0.5/1/0.5/2, we varied the temperature during the preparation of AIGZS QDs (190, 220 or 250°C). A gradual redshift of the PL emission wavelength was observed with the increase of the temperature (560, 583 and 601 nm for reactions conducted at 190, 220 and 250°C, respectively), likely due to an increase of the nanocrystals size (Fig. 4.9a). The highest PL QY (11%) was measured for nanocrystals prepared at 220°C and this temperature was kept in further experiments.

After heating at 220°C for 10 min (step 1), some aggregates formed in the reaction flask. These large sized particles were removed by centrifugation and the AIGZS QDs contained in the supernatant were re-heated at 220°C in the presence of OAm (step 2). A red-shift of the PL emission from 570 to 583 nm was observed after 10 min of heating and extending the heating period had no further influence of the PL emission peak (Fig. 4.9b). A marked increase of the PL QY from 11 to 20.2% was also observed after the second heating at 220°C, suggesting an improvement of nanocrystals surface passivation by OAm and the removal of surface defects that may serve as nonradiative channels. Finally, TGA analysis of the dots shows only one weight loss starting at ca. 250°C, likely originating from the removal of the OAm capping ligand (Fig. 4.1). The remaining mass is of ca. 80%, which confirms that AIGZS QDs are covered by a thick OAm shell.

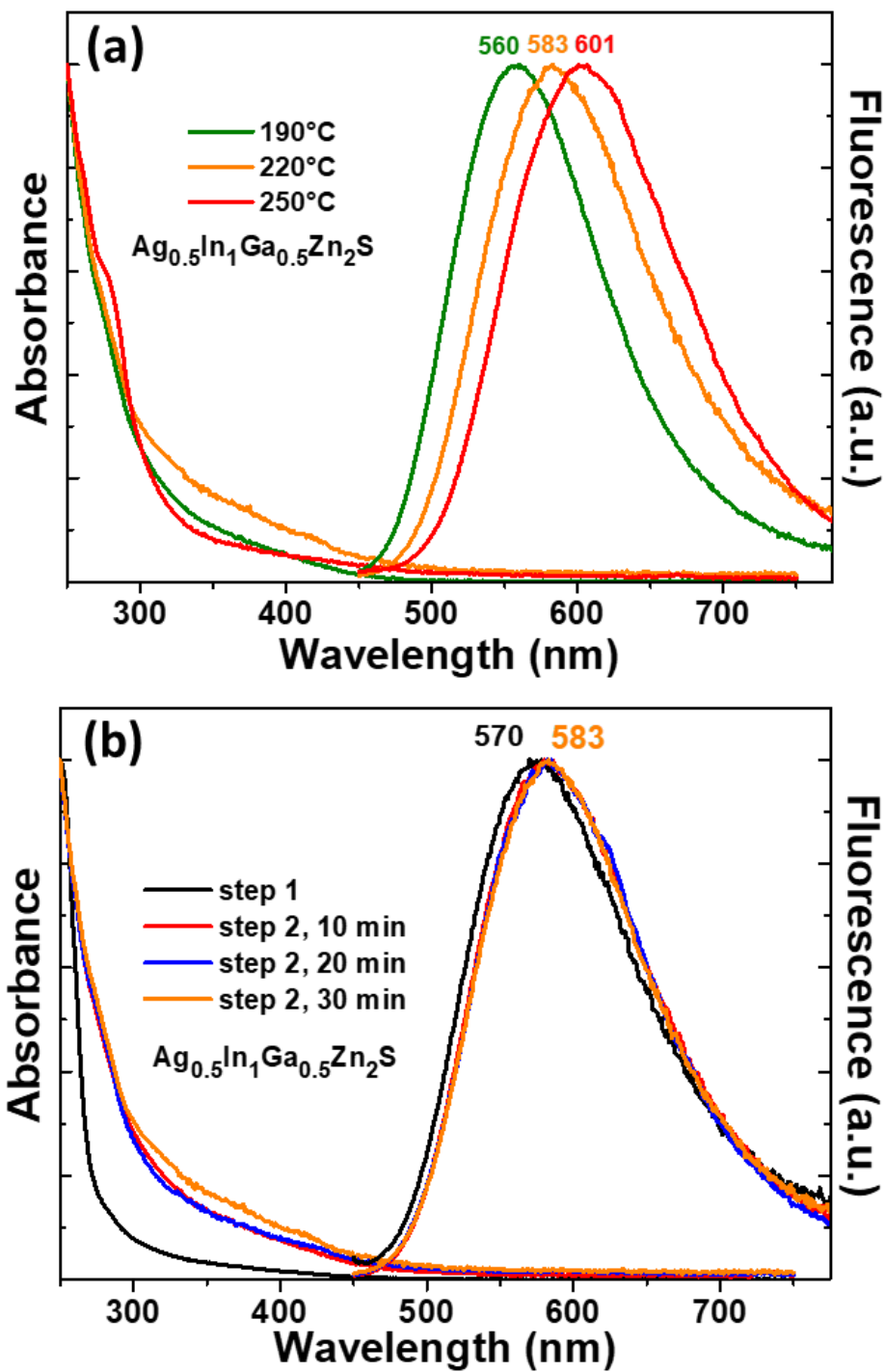


Figure 4.9. UV-visible and normalized PL emission spectra of AIGZS QDs (a) when varying the heating temperature and (b) after a first heating at 220°C and after re-heating at the same temperature

Fig. 4.10a-b show the evolution of UV-visible absorption and PL emission spectra of AIGZS QDS dispersed in chloroform. All absorption spectra exhibit almost similar features regardless of the Ag/In/Ga/Zn ratio. A relatively well resolved absorption peak can be observed at ca. 290 nm and all QDs absorb in the visible region up to ca. 550 nm. However, no marked exciton peak can be observed in the visible region likely due to the distribution of vibrational states in AIGZS QDs, which is a common feature for ternary or quaternary QDs.^{61,174} The steady state PL emission spectra are broad with a fwhm varying between 131 and 170 nm, which is characteristic of donor-acceptor (D-A) transitions and trap-state emissions (*vide infra*).^{61,174}

We first varied the Ag/In/Ga ratio without altering the amount of Zn(DDTC)₂ (nAg + In + Ga/nZn = 1). Only the nanocrystals prepared with a low Ag content (ratio of 0.25/0.875/0.75/2) exhibit a strong emission located at 515 nm associated to a defect related emission at lower energy. For all other dots, a single component emission was observed. A redshift of the PL emission from 515 to 650 nm can be observed with the increase of the Ag content due to the lower bandgap of Ag₂S (0.85-1.1 eV)²⁰⁰ compared to In₂S₃ (1.98-2.2 eV)²⁰¹ and Ga₂S₃ (ca. 3.4 eV)²⁰² in the bulk state. Next, by decreasing the Zn content (nAg + In + Ga/nZn = 0.5), a significant redshift of the PL emission to 699 nm was observed due to the lower contribution of the wide bandgap ZnS material (3.6 eV). These results indicate that the PL emission can be tailored by changing the Ag/In/Ga/Zn ratio. It should be noted that the metal/S ratio was also modified during this experiment as DDTC serves as sulfur source. By maintaining the S concentration by addition of NaDDTC, the PL emission wavelength is further shifted to 716 nm. The bandgap values were determined from the Tauc plots of $(\alpha h\nu)^2$ vs. $h\nu$ (where α is the absorption coefficient and $h\nu$ is the photon energy) and were found to decrease from 2.94 to 2.08 eV (Fig. 4.12).

The optical attributes of AIGZS QDs, namely the broad PL emission with a large Stokes shift, are typical of ternary and quaternary semiconductor nanocrystals and originate from surface states (vacancies and dangling bonds) and interstitial states (interstitial atoms and vacancies) that usually dominate the PL emission. The changes of the PL emission wavelength observed when varying the Ag/In/Ga/Zn ratio result from the lower bandgap of Ag-richer AIGZS QDs and from the wider bandgap of In, Ga or Zn-rich AIGZS QDs and thus from the shift of the intragap donor and acceptor levels. As can be seen from Table 4.2, the PL QYs of AIGZS QDs increase with the Ag content of the nanocrystals. The highest PL QYs were measured for AIGZS QDs prepared with Ag/In/Ga/Zn ratios of 0.66/0.66/0.66/2 and 1/0.5/0.5/2 (48.3 and 47.3%, respectively) (entries c and d). These results suggest that Ag vacancies and Ag

interstitials play a key role in the PL mechanism as previously observed for AIS and AIZS QDs.^{9,10} Contrary to PL QY values determined for Ag-In-Ga-S or Cu-In-Ga-Zn-S QDs,¹⁹ the increase of the Ga content in AIGZS QDs was found to be less deleterious than that of In (compare entries b and c). A decrease of the PL QY (25.4%) was also observed with the decrease of the Zn and S loading in AIGZS QDs (entry f). A similar PL QY (23.6%) was determined when adding NaDDTC in the reaction medium, indicating that the decrease was linked to the Zn loading (entry g).

To investigate the dynamic properties of photo-generated electron/hole pairs, time-resolved decays of AIGZS QDs at the maximum emission wavelength were carried out (Fig. 4.10c). The data were best fitted using a bi-exponential function $I(t) = A_1 \exp(-t/\tau_1) + A_2 \exp(-t/\tau_2)$ where τ_1 and τ_2 are the time constants of the PL and A_1 and A_2 the normalized amplitudes of the components. The average lifetime τ_{av} was determined using the formula $\tau_{av} = (A_1\tau_1 + A_2\tau_2)/(A_1 + A_2)$. The time constants and fitting parameters are listed in Table 4.2. Two radiative channels were observed. The fast decay component τ_1 is attributed to surface trap state recombination and the slow decay component τ_2 to the recombination of electrons via defect states located within the bandgap (D-A recombination).^{61,69,80,81,174} AIGZS QDs prepared with the Ag/In/Ga/Zn ratio of 0.25/0.875/0.875/2 exhibit the shortest PL lifetime (99.9 ns) due to the high contribution of surface defects. For QDs prepared with a stoichiometric ratio of (Ag + In + Ga)/Zn of 1, τ_{av} is the highest (278.8 ns) when equimolar amounts of Ag, In and Ga are used for the synthesis (entry d). This long PL decay is characteristic of intragap state-involved radiative recombinations of QDs exhibiting inherent lattice defects.^{61,174} The highest A_2 contributions were determined for AIGZS QDs prepared with Ag/In/Ga/Zn ratios of 0.66/0.66/0.66/2 and 1/0.5/0.5/2, which is in good agreement with the PL QYs of these dots (entries c and d). For QDs prepared with a (Ag + In + Ga)/Zn molar ratio of 0.5, a marked increase of τ_1 and τ_2 is observed and τ_{av} could reach 915 ns (entry g), suggesting that new surface and lattice defects generated by the default in Zn^{2+} ions to be involved in the transitions.

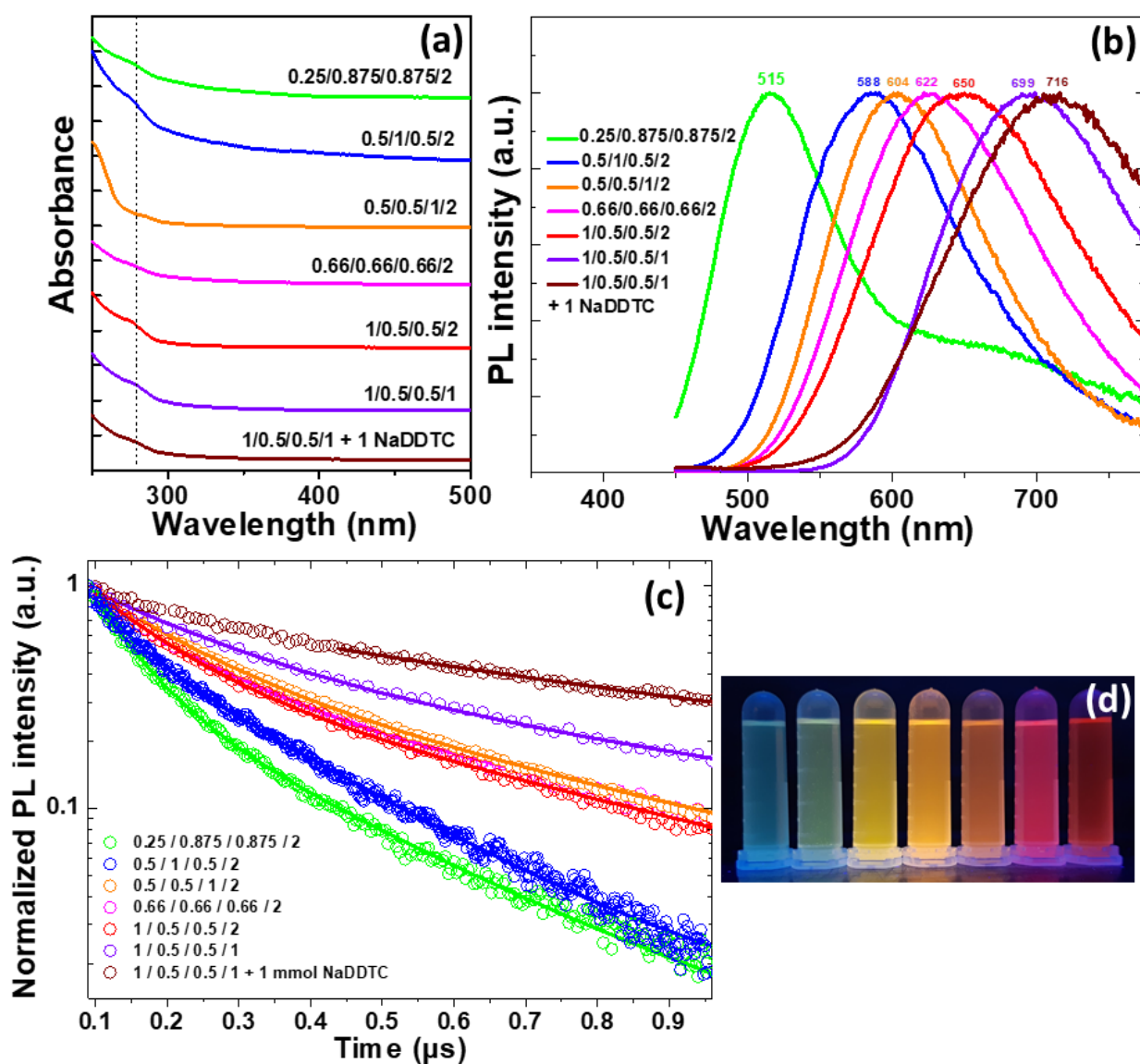


Figure 4.10. (a) UV-visible and (b) normalized PL emission spectra of AIGZS QDs when varying the Ag/In/Ga/Zn ratio, (c) Time resolved decay profiles of AIGZS QDs recorded at the maximum emission wavelength and (d) digital photograph of the dots under UV light illumination

Table 4.2. PL QYs, time constant τ_1 and τ_2 and the contributions of decays A_1 and A_2 of AIGZS QDs when varying the Ag/In/Ga/Zn ratio

Entry	Ag/In/Ga/Zn ratio	PL QY (%) ^a	A_1	τ_1 (ns)	A_2	τ_2 (ns)	τ_{av} (ns)
a	0.25/0.875/0.875/2	14.3	0.82865	66.3	0.17135	262.3	99.9
b	0.5/1/0.5/2	20.2	0.67945	52.9	0.32055	228.7	109.3
c	0.5/0.5/1/2	41.9	0.6819	143.5	0.3181	549.3	272.6
d	0.66/0.66/0.66/2	48.3	0.59008	121.6	0.40992	505.1	278.8
e	1/0.5/0.5/2	47.8	0.62873	116.6	0.37127	521.1	226.3
f	1/0.5/0.5/1	25.4	0.66339	189.9	0.33661	883.3	423.3
g	1/0.5/0.5/1 + 1 NaDDTC	23.6	0.49488	424.9	0.50512	1395.7	915.3

^a Determined using chloroform as solvent.

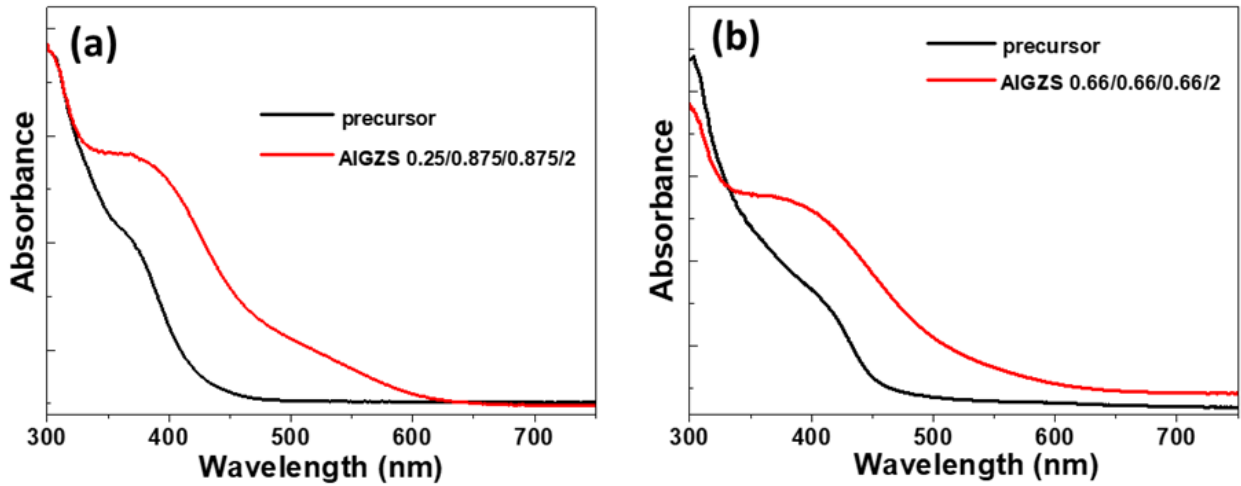


Figure 4.11. UV-visible absorption spectra of AIGZS precursors prepared with Ag/In/Ga/Zn ratios of 0.25/0.875/0.875/2 (a) and 0.66/0.66/0.66/2 (b) and of the corresponding QDs

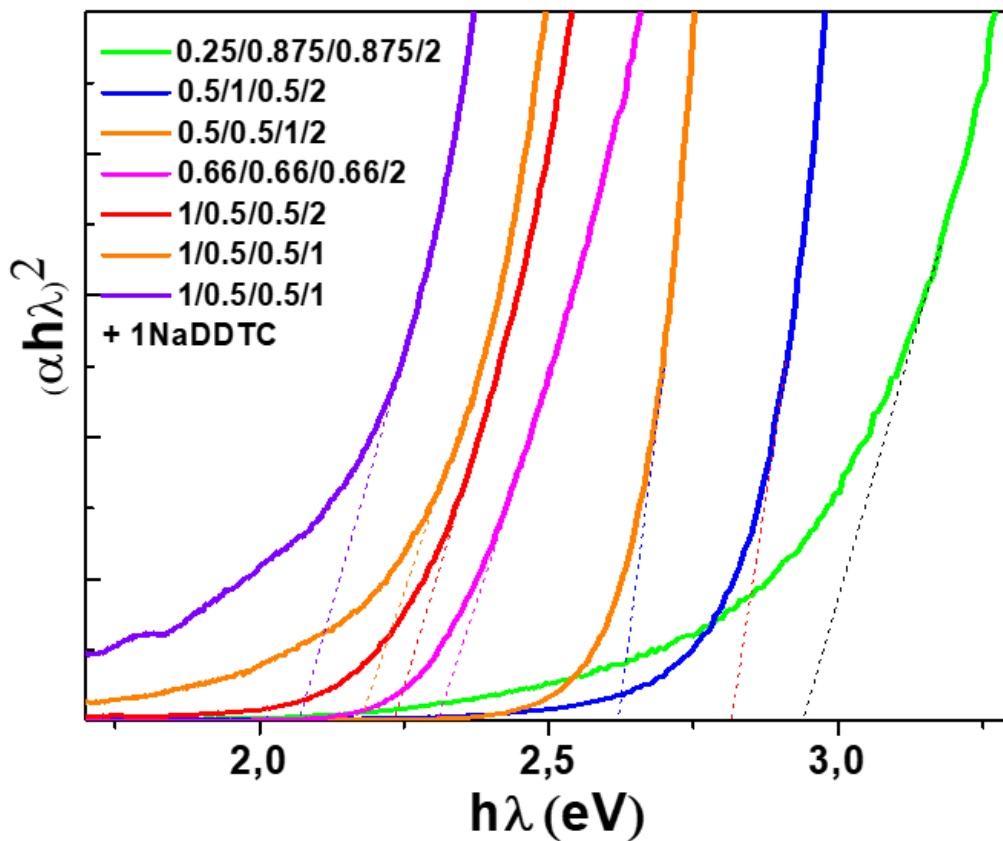


Figure 4.12. Determination of the optical bandgap of AIGZS QDs when varying the Ag/In/Ga/Zn ratio

4.5. Aqueous phase transfer

After post-preparation treatments and removal of unreacted precursors, AIGZS QDs were successfully transferred into aqueous phase via exchange of the hydrophobic OAm ligand with glutathione tetramethylammonium (GTMA) or glycine dithiocarbamate (Gly-DTC) (Fig. 4.13).^{62,196}

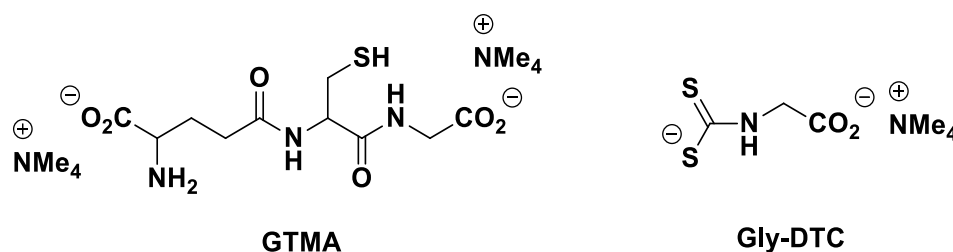


Figure 4.13. Structures of GTMA and Gly-DTC ligands used to transfer AIGZS QDs into aqueous solution.

The thiol function of GTMA and the dithiocarbamate function of Gly-DTC enable the removal of the OAm ligand and convert the native oil soluble nanocrystals into hydrophilic ones (Fig. 4.14a). Fig. 4.14b shows the UV-visible and the PL emission spectra before and after the ligand exchange. No significant changes could be observed in the UV-visible spectrum of AIGZS@GTMA QDs compared to the native dots. For Gly-DTC, a strong and well resolved peak appears at ca. 305 nm, which confirms that the dots are well capped by dithiocarbamate functions. The PL emission signals exhibit a clear redshift upon ligand exchange from 622 nm to 648 and 685 nm for AIGZS@GTMA and AIGZS@Gly-DTC QDs, respectively. The QDs are well dispersed in aqueous solution as demonstrated by DLS which shows hydrodynamic diameters of 14.6 ± 1.3 and 9.4 ± 1.8 nm for AIGZS@GTMA and AIGZS@Gly-DTC QDs, respectively, which indicate that the redshift originates from the changing of the environment around the dots and not from their aggregation (Fig. 4.15). The Zeta potential values of AIGZS@GTMA and AIGZS@Gly-DTC QDs are of -23.1 and -34.5 mV, respectively. Finally, the ligand exchange was accompanied by a slight decrease of the PL QY (from 48.3 to 43.7 and 37.4% for QDs capped with GTMA and Gly-DTC, respectively).

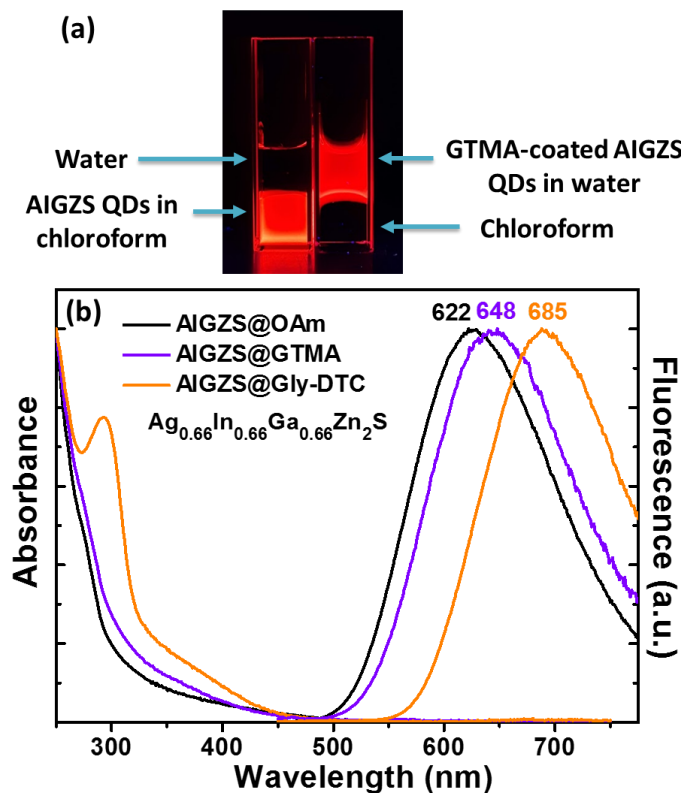


Figure 4.14. (a) Digital photograph taken under UV light illumination of dispersions of AIGZS QDs before and after the ligand exchange with GTMA. (b) UV-visible and normalized PL emission spectra of AIGZS QDs capped with OAm and after their transfer into water using GTMA and Gly-DDTC ligands

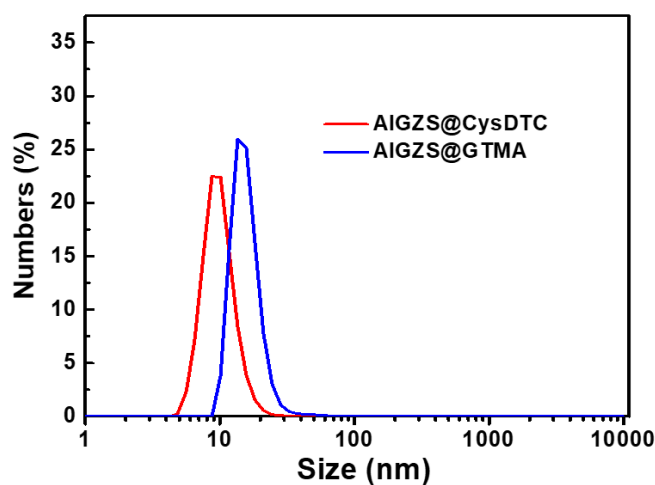


Figure 4.15. Hydrodynamic diameter AIGZS QDs capped with CysDTC and GTMA

4.6. Conclusion

A single source molecular precursor synthesis was developed for the preparation of new quinary AIGZS QDs. The dots exhibit an average diameter of ca. 2 nm and their PL emission can be tuned from the blue-green to the near-infrared by varying the Ag/In/Ga/Zn ratio. AIGZS QDs exhibit PL QYs up to 48.3%. The recombination of photogenerated electron-hole pairs occurs via surface-related trap states and intragap defect-related states and the PL lifetime could reach 915 ns for AIGZS QDs prepared with a Ag/In/Ga/Zn ratio of 1/0.5/0.5/1. These results show the high potential of AIGZS QDs as novel environmental-friendly fluorescence emitters.

Chapter 5. Synthesis of AIGZS and Mn:AIGZS QDs

5.1. Introduction

Fluorescence imaging and magnetic resonance imaging have played important roles in imaging and diagnosis of tumor cells, and they provide valuable informations with different imaging depths, sensitivity and resolutions. For example, magnetic resonance imaging with its soft-tissue based contrast provides high spatial resolution, while fluorescence imaging shows high sensitivity with temporal resolution²⁰³. Bimodal imaging probes offer advantages of these both imaging techniques. QDs possessing fluorescent and magnetic properties should be of high interest as fluorescent/magnetic imaging probes^{58,83,204–212}.

Ag-based ternary QDs and their ZnS shelled derivatives have been synthesized with highly fluorescent properties. Due to their unique optical characteristics, they have found applications in various fields like sensing, detection or imaging. Additionally, their multi-component composition allows to tune their PL emission peak position, by adjusting the size or the composition over the visible region and up to the near-infrared region. This enhances their ability to serve as fluorescent imaging probes, since in the 650–900 nm region, the tissue autofluorescence is low and less fluorescence extinction enhances a deep tissue penetration with minimal background interference²¹³.

Doping paramagnetic metal ions into fluorescent QDs core is the method commonly used to prepare magnetic QDs for application as contrast agents in MRI. MRI contrast agents shorten either T_1 or T_2 relaxation times of surrounding water protons. Therefore, there are two types of imaging contrast agents: (i) Type T_1 , shorten the T_1 relaxation time and yield a signal brightening; (ii) Type T_2 , shorten the T_2 relaxation time and yield a signal darkening²⁰⁷. Most paramagnetic agents, such as dysprosium (Dy^{3+}), gadolinium (Gd^{3+}), or manganese (Mn^{2+}), are T_1 contrast agents and therefore appear bright in T_1 -weighted images²¹⁴. Doping of Mn^{2+} ions is the best substitute when considering the toxicity of the dopant as it has been identified with gadolinium-based contrast agents (GBCAs) : the use of GBCAs is associated with the development of nephrogenic systemic fibrosis in patients with impaired renal function^{215–217}.

Doping Mn^{2+} ions into the QDs also leads to the change in their optical properties. Usually, the Mn-dopant related PL emission is located at ca. 600 nm and is originating from the $\text{Mn}^{2+} \ ^4\text{T}_1 \rightarrow \ ^6\text{A}_1$ transition^{82,84,131}. Moreover, a red-shift of the PL emission peak was also observed while increasing the Mn loading due to Mn-Mn interactions³⁵. However, the studies related to the Mn-doping in I-II-III-VI QDs and its influence on the optical and magnetic properties of the QDs has only faintly been studied.

In this chapter, the single precursor thermal decomposition synthesis described in the previous chapter was used for the preparation of Mn-doped Ag-In-Ga-Zn-S QDs. Their structural and morphological characterizations along with their optical and magnetic properties will also be discussed. The transfer of these QDs into the aqueous phase using glutathione tetramethylammonium in a fast and easily reproducible way was also conducted. Moreover, these particles retain excellent optical and magnetic properties after transfer into the aqueous phase.

5.2. Experimental part

Materials

Silver nitrate AgNO_3 , gallium nitrate hydrate $\text{Ga}(\text{NO}_3)_3 \cdot x\text{H}_2\text{O}$, indium nitrate hydrate $\text{In}(\text{NO}_3)_3 \cdot x\text{H}_2\text{O}$, zinc diethyldithiocarbamate $\text{Zn}(\text{DDTC})_2$, sodium diethyldithiocarbamate NaDDTC , manganese stearate MnSt_2 , oleylamine, glutathione, tetramethylammonium hydroxide pentahydrate, glycine, carbon disulfide, poly(maleic anhydride-alt-1-octadecene) PMAO, chloroform and methanol were used as received.

Preparation of $\text{Ag}_x\text{In}_y\text{Ga}_{2-x-y}\text{Zn}_2(\text{S}_2\text{CN}(\text{C}_2\text{H}_5)_2)_4$ precursors.

AgNO_3 , $\text{In}(\text{NO}_3)_3$, $\text{Ga}(\text{NO}_3)_3$ and $\text{Zn}(\text{DDTC})_2$ with a Ag/In/Ga/Zn ratio of 0.25/0.875/0.875/2 were mixed in 10 mL of a 1:1 water-methanol mixture. The solution was stirred for 2 h at room temperature to form $\text{Ag}_x\text{In}_y\text{Ga}_{2-x-y}\text{Zn}_2(\text{S}_2\text{CN}(\text{C}_2\text{H}_5)_2)_4$ precursors. The product then collected by centrifugation (4000 rpm for 15 min), dried under vacuum and stored at 4°C before use.

Synthesis of Mn(+2) stearate (MnSt_2)

Under a nitrogen atmosphere, stearic acid (10 mmol) in 15 mL of methanol was heated to 50-60 °C to make a homogeneous solution. After cooling the reaction mixture to room temperature, TMAH (10 mmol) in 20 mL of methanol was added and the mixture was further stirred for 15 min. Next, $\text{MnCl}_2 \cdot 4\text{H}_2\text{O}$ (5 mmol) in 10 mL of methanol was added dropwise under vigorous stirring. The white MnSt_2 precipitate was collected by centrifugation, washed several times with methanol and dried under vacuum. The dried MnSt_2 was stored at 4°C under N_2 before use.

Preparation of Mn-doped Ag-In-Ga-Zn-S (AIGZS) QDs

Mn-doping of AIGZS QDs was tested out using two approaches. One approach was named “precursor containing Mn^{2+} ions”. In this method, the diethyldithiocarbamate precursor was prepared in the presence of MnSt_2 along with AgNO_3 , $\text{In}(\text{NO}_3)_3$, $\text{Ga}(\text{NO}_3)_3$ and $\text{Zn}(\text{DDTC})_2$ salts. The amount of MnSt_2 was calculated according to the percentage of doping with manganese. Thus, a corresponding precursor was prepared for each doping. Further, the

appropriate precursor containing Mn^{2+} ions was used for each (1 %, 2.5 %, 5 %, 10 %) Mn-doped AIGZS QDs synthesis.

In the second approach, which was named “precursor + MnSt_2 ”, the Mn-doped AIGZS QDs were synthesized by thermolysis of $\text{Ag}_x\text{In}_y\text{Ga}_{2-x-y}\text{Zn}_2(\text{S}_2\text{CN}(\text{C}_2\text{H}_5)_2)_4$ in the presence of MnSt_2 precursors using oleylamine OAm as solvent. First, the precursor (100 mg) with the appropriate amount of MnSt_2 were dispersed in OAm (6 mL) and the mixture was stirred under argon flow until homogenization. Then, the solution was heated at 220°C for 10 min and the color changed to dark. After cooling, the large sized crystals were removed by centrifugation (5000 rpm for 10 min). The supernatant was precipitated by adding an excess of methanol and the powder was collected by centrifugation (5000 rpm for 10 min) and dried under vacuum. Next, the dried product was redispersed in OAm (6 mL) and the solution was heated at 220°C for 30 min. The obtained Mn:AIGZS QDs were precipitated by adding an excess of methanol, recovered by centrifugation (5000 rpm for 10 min) and purified by washing with methanol.

Transfer of Mn:AIGZS QDs into water

Glutathione tetramethylammonium coating. GTMA-coating was conducted using a previously described method¹⁹⁶. Briefly, GTMA was prepared by dissolving GSH (30 mg) and TMAH (54 mg) in 1 mL of methanol. Separately, 5 mg of Mn:AIGZS@OAm QDs were dispersed in 1 mL toluene, then 5 mL of chloroform were added. Next, 0.5 mL of the GTMA solution was dropwise added to the QDs solution and the mixture was vigorously stirred for 2 h. Then, water (4.5 mL) was added and the two-layer mixture was slightly shaken to transfer QDs into the water layer before being left for 1 h to reach equilibrium. Finally, the top water layer containing GTMA-capped AIGZS QDs was collected.

Poly(maleic anhydride-alt-1-octadecene coating). To disperse Mn:AIGZS@DDT QDs in water, the amphiphilic polymer poly(maleic-alt-1-octadecene) was used⁷⁵. A mixture of Mn:AIGZS@OAm QDs (6 mg), PMAO (9.4 mg) and 10 mL of chloroform was stirred vigorously for 2 h at ambient temperature. Next, the solvent was removed at room temperature by using a rotary evaporator. The obtained product was dissolved in 1 mL of chloroform and 6 mL of a 0.05 M aqueous solution of NaOH was added. This mixture was sonicated for 1 h at 50°C before being centrifuged for 15 min at 5000 rpm to remove the aggregates. Next, the supernatant was centrifuged for 30 min at 15 000 rpm and the pellet obtained was dispersed in a Borate Buffer solution (pH 9) and stored at 4°C .

Relaxivity measurements and MR images

Relaxation rates at 60 and 100 MHz were obtained using on a Bruker Minispec MQ60 equipment. Longitudinal (T1) and transverse (T2) relaxation times of water protons were measured with the following parameters :

T1 measurements at 25 °C: 8 accumulations, repetition time 10 s, inversion-recovery with 16 evolution times between 0.001s and 4xT1 ;

T2 measurements at 25 °C: 16 accumulations, repetition time 10 s, CPMG with 2000 points and $t / 2 = 0.6$ ms.

MRI images were recorded using a Bruker Biospec Avance 24/40 with a 2.34 T magnetic field (proton resonance frequency: 60 MHz). The 100 mg/mL solutions of 0 %, 1 % and 2.5 % Mn:AIGZS QDs were put in 4 mL vials and imaged with the following parameters :

Field of View: 6 cm; Matrix: 256*256 pixels; slice thickness: 2 mm.

Two sets of images were acquired: the first one with a 200 ms repetition time and 14 s echo time in order to achieve a good T1 contrast and the T2-weighted images were recorded with 5000 ms repetition time and 120 s echo time.

5.3. Morphology and structure characterization

Mn-doped Ag-In-Ga-Zn-S (Mn:AIGZS) QDs were synthesized in two-stage process. First, the $\text{Ag}_x\text{In}_y\text{Ga}_{2-x-y}\text{Zn}_2(\text{S}_2\text{CN}(\text{C}_2\text{H}_5)_2)_4$ complex precursor was prepared in a water-methanol. Next, the vacuum dried precursor and MnSt_2 were thermally decomposed in the presence of OAm as a solvent and a capping ligand.

AIGZS QDs were prepared using different Ag/In/Ga/Zn ratios: 0.25/0.875/0.875/2; 0.5/1/0.5/2; 0.5/0.5/1/2; 0.66/0.66/0.66/2; 1/0.5/0.5/2; 1/0.5/0.5/1; 1/0.5/0.5/1 + 1 mmol NaDDTC, while amount of sulfur precursors was kept constant.

For the studies of Mn-doping, the Ag/In/Ga/Zn ratio of 0,25/0,875/0,875/2 was selected. The amount of MnSt_2 dopant was calculated relative to the total amount of cations and added with the precursor during the thermal decomposition step. The reaction was conducted at 220°C, both first and second steps. This temperature was chosen from previous experiments conducted at 190°C, 220°C and 250°C. The QDs show optimal optical properties when synthesized at

220°C. The first step of the thermal decomposition with a duration of 10 min produces a brown suspension containing large sized particles which were removed by centrifugation. Then, the QDs were collected from the supernatant by precipitation with an excess amount of methanol. The collected precipitate was dried and redissolved in OAm for the second step of the synthesis consisting in the re-heating of the colloidal solution at 220°C for 30 min.

Two approaches for introducing the MnSt₂ dopant were tested. The first approach, which was named “precursor + MnSt₂”, is based on the addition of MnSt₂ to the precursor in the first thermal decomposition step of the synthesis. In the second approach, a precursor containing Mn²⁺ ions was prepared. The optical properties of the undoped, 5% and 10% Mn-doped QDs using these two synthetic approaches showed almost similar results (Fig. 5.1). Therefore, for further studies, the first approach was selected due to its simplicity.

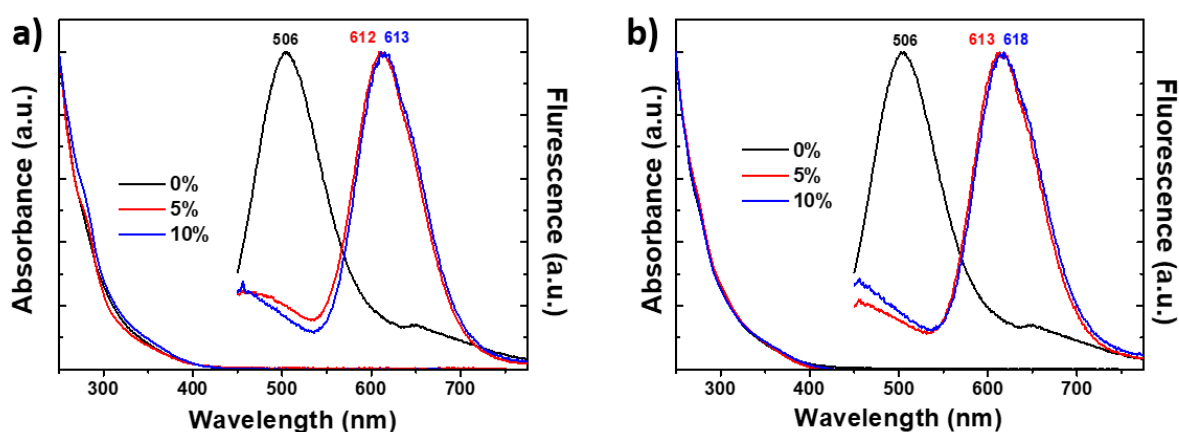


Figure 5.1. UV-Vis and PL emission spectra of Mn-doped AgInGaZnS QDs at Ag/In/Ga/Zn=0.25/0.875/0.875/2 ratio: a) “precursor + MnSt₂” method; b) “precursor containing Mn²⁺ ions”

X-Ray diffraction analysis was used to characterize the chemical structure of synthesized QDs. Fig. 5.2 shows the XRD patterns of Mn-doped AIGZS@OAm QDs prepared with a Ag/In/Ga/Zn/S ratio of 0.25/0.875/0.875/2 and when varying the Mn²⁺ loading from 0 to 10%. The broadness of the peaks originates from the small sizes of the nanoparticles. The peaks located at 28.63, 47.63 and 56.52° correspond to the (112), (204/220) and (312) planes of the tetragonal chalcopyrite phase, respectively. As can be seen from the figure, the peaks are shifted towards lower angles when the doping in Mn increases. This likely originates from the diffusion

of Mn^{2+} ions into the QDs core which leads to a lattice shrinkage since the ion radii of Mn^{2+} (0.070 nm) is smaller than the ion radii of In^{3+} (0.094 nm) and Ag^+ (0.115 nm).

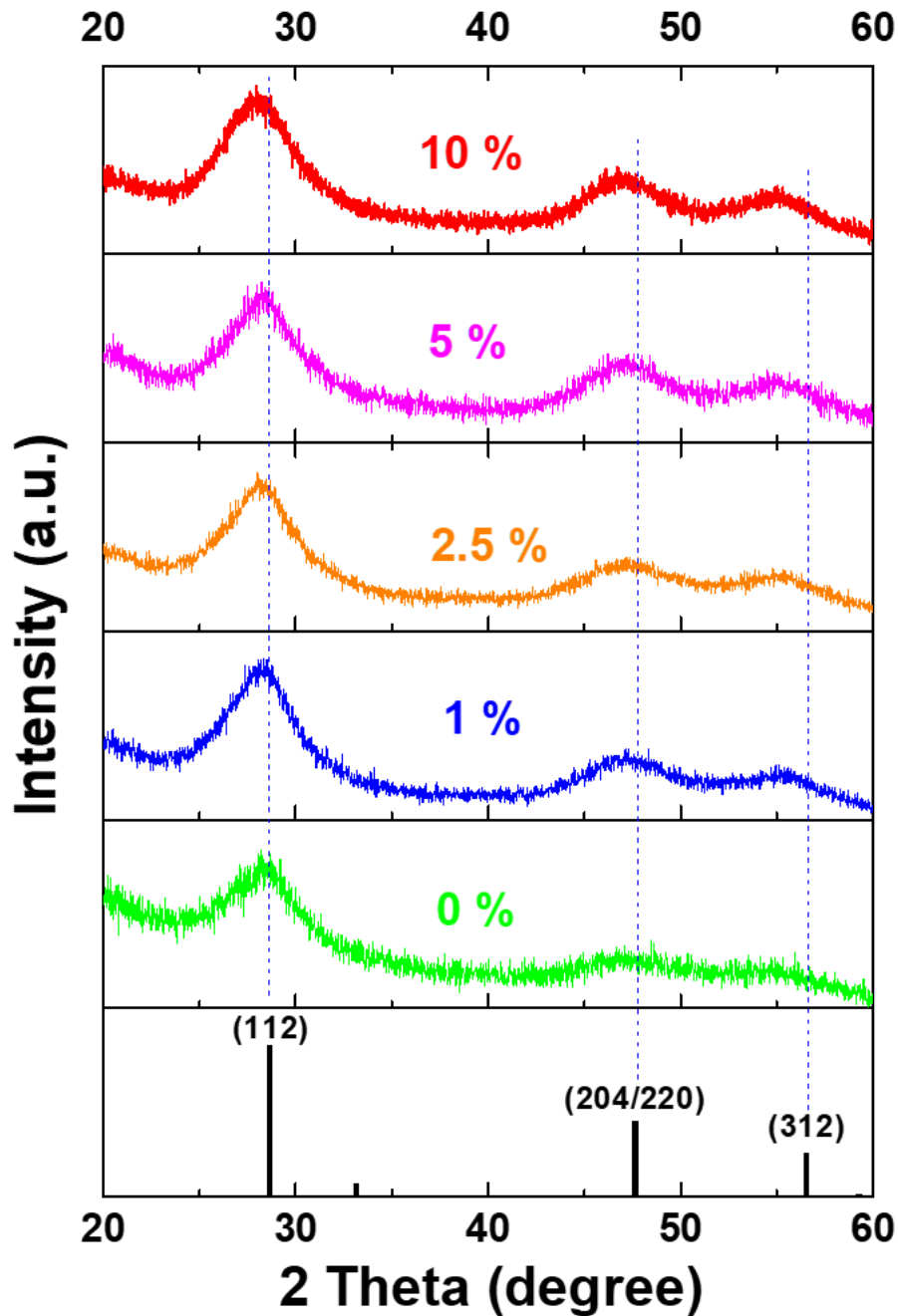


Figure 5.2. XRD patterns of Mn-doped AgInGaZnS QDs prepared using a Ag/In/Ga/Zn of 0.25/0.875/0.875/2

TEM was applied to characterize the size and the shape of AIGZS and Mn:AIGZS QDs. The images in Fig. 5.3 show that the average size of the nanocrystals varies between 1.8 and 2.0 nm by analyzing at least 100 nanocrystals in the TEM images. As can be seen from the TEM images, AIGZS and Mn:AIGZS QDs exhibit spherical and ellipsoidal shapes. A few larger particles with sizes around 7-9 nm were observed in some TEM images but they cannot be considered as one particle since they composed of a few small particles. The lattice spacing measured is of ca. 0.31 nm and corresponds to the (112) diffraction plane of the tetragonal chalcopyrite phase. The high crystallinity of the dots is confirmed from the selected area electron diffraction (SAED) patterns (see the insets of Fig. 5.3).

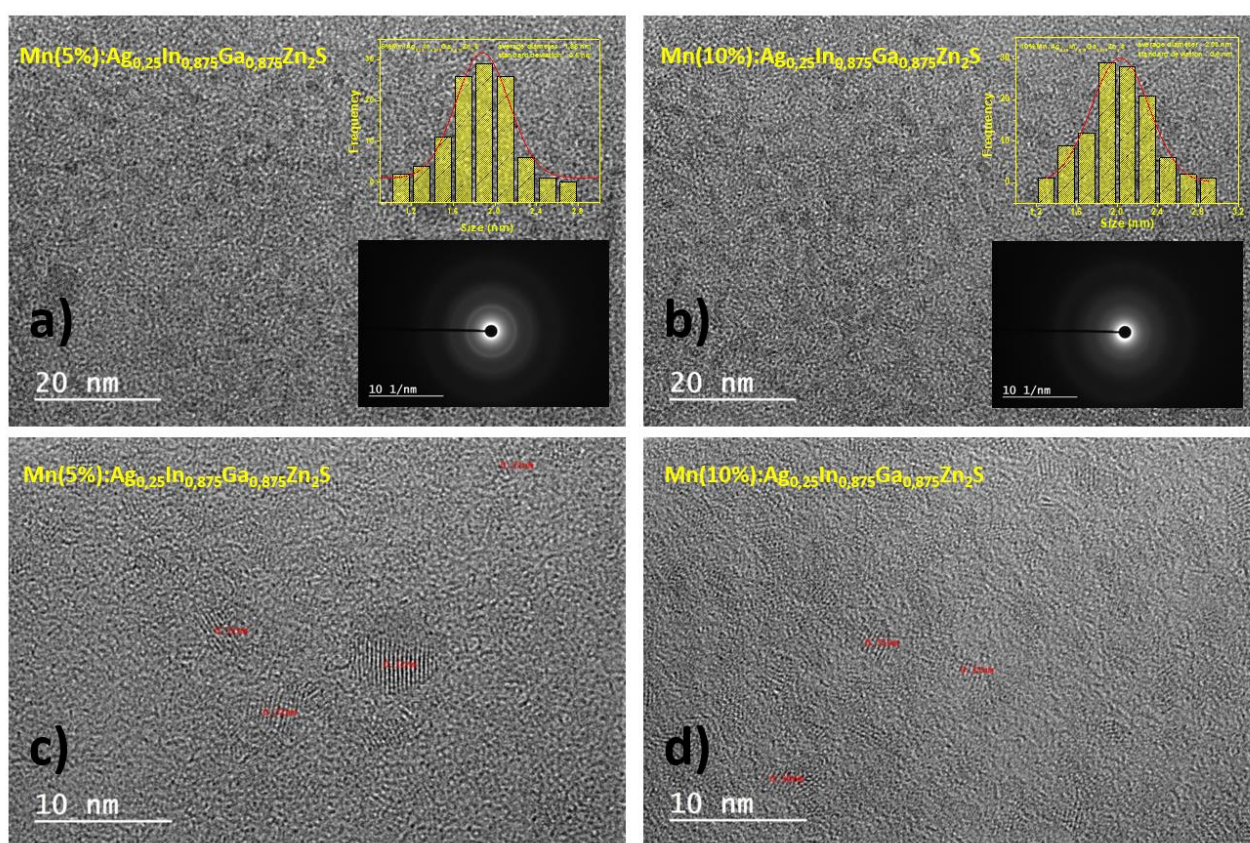


Figure 5.3. TEM images of Mn:AIGZS QDs at the Ag/In/Ga/Zn ratio of 0.25/0.875/0.875/2: a) 5%; b) 10% and HR-TEM images of 5% (c) and 10% Mn-doped QDs

Elemental analysis of synthesized AIGZS and Mn:AIGZS QDs was carried out by X-ray photoelectron spectroscopy. The results confirm the presence of Ag, In, Zn, Mn, Ga and S

elements in the AIGZS QDs and the stoichiometry is different from that used for the synthesis (Fig. 5.4 and Table 5.1). As the results show, the percentage of introduced Mn amount is significantly lower than the amount used for the synthesis, which indicates that the Mn ions were faintly doped into AIGZS cores. XPS was also used to investigate the chemical state and the composition of Mn:AIGZS QDs. The XPS survey spectrum shows the presence of Ag, In, Ga, Mn, Zn and S elements along with C and N originating from the GSH capping ligand (Fig. 5.4). The peaks at 367.67, 445.75, 452.28, 1118.26, 1021.79 and around 641 eV can be assigned to Ag 3d_{5/2}, In 3d_{5/2}, In 3d_{3/2}, Ga 2p_{3/2}, Zn 2p_{3/2} and Mn 2p_{3/2}, respectively, and confirm the valence states of Ag⁺, In³⁺, Ga³⁺, Zn²⁺ and Mn²⁺. The deconvoluted signals at 161.49 and 162.69 eV correspond to S 2p_{3/2} and S 2p_{1/2}, respectively, indicating that the metal cations are associated to S²⁻.

Table 5.1. Ag/In/Ga/Zn ratio determined by XPS

Element	Ag/In/Ga/Zn ratio, At. %		
	Mn(1%): 0.25/0.875/0.875/2	Mn(2.5%): 0.25/0.875/0.875/2	Mn(5%): 0.25/0.875/0.875/2
Ag	4.41	4.25	4.20
In	16.04	17.20	12.78
Ga	5.64	5.60	4.16
Zn	15.51	11.22	18.30
S	58.40	58.73	58.36
Mn	-	-	2.19

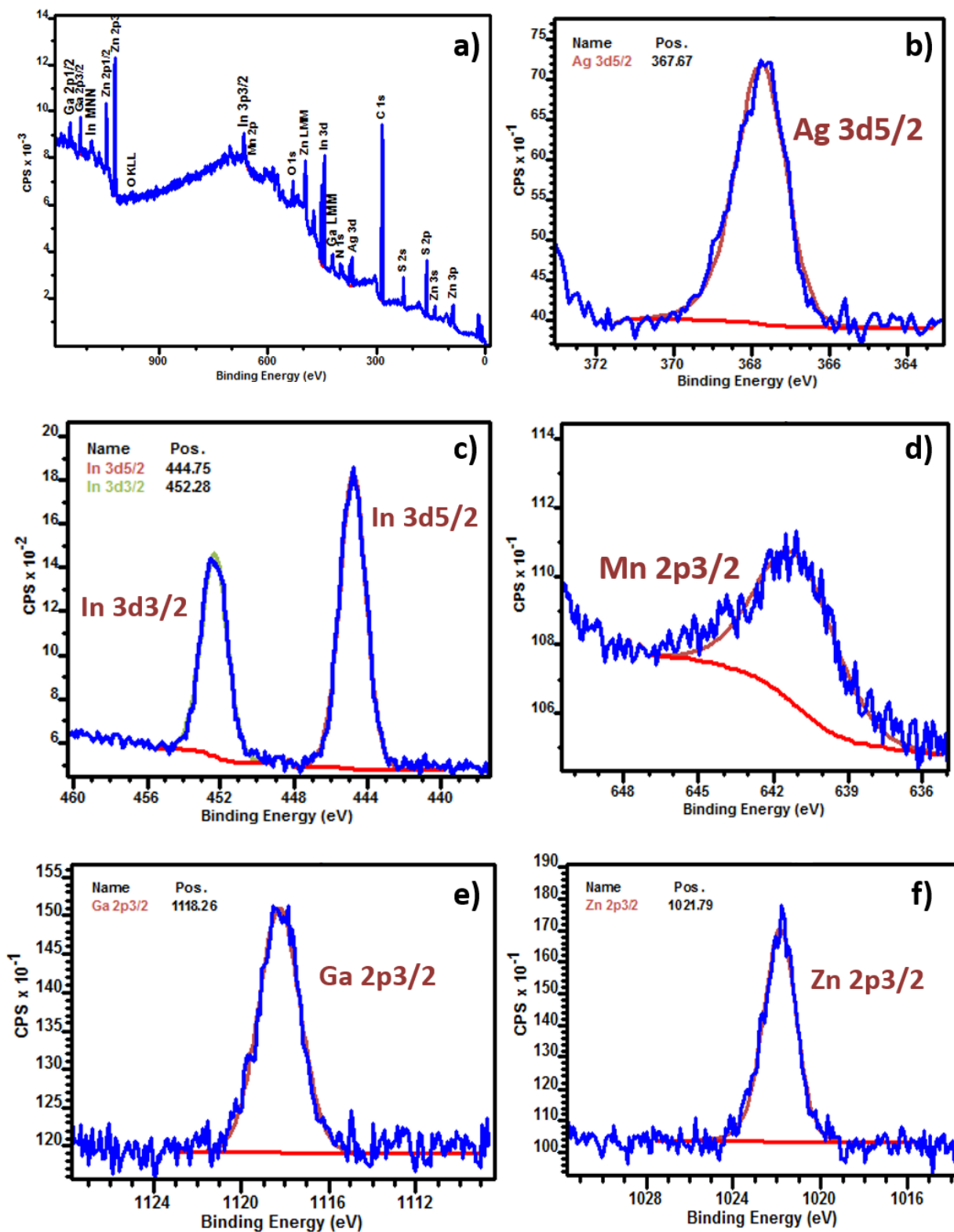


Figure 5.4. XPS analysis of AIGZS QDs: (a) wide scan of Mn(5%):AIGZS QDs and high resolution scans of Ag 3d_{5/2} region (b), In 3d_{3/2} and 3d_{5/2} regions (c), Mn 2p_{3/2} region (d), Ga 2p_{3/2} region (e), Zn 2p_{3/2} region

Electron paramagnetic resonance spectra recorded for the Mn:AIGZS QDs further confirm the doping of Mn^{2+} into the AIGZS nanocrystals (Fig. 5.5). The spectra show six clear hyperfine splittings separated by about 80 G for 1 %, 2.5 % and 5 % loading Mn, which is related to the coupling of the electronic spin with the 5/2 nuclear spin of Mn^{2+} . For 10 % doping AIGZS QDs poorly resolved hyperfine coupling was observed. The broad signal is observed in all spectra centred on $g = 2$. The broadness signal typically observed for AIZS, CIZS QDs can be associated to the complex environment of Mn^{2+} surrounded by Ag^+ , In^{3+} and Zn^{2+} ions³⁴.

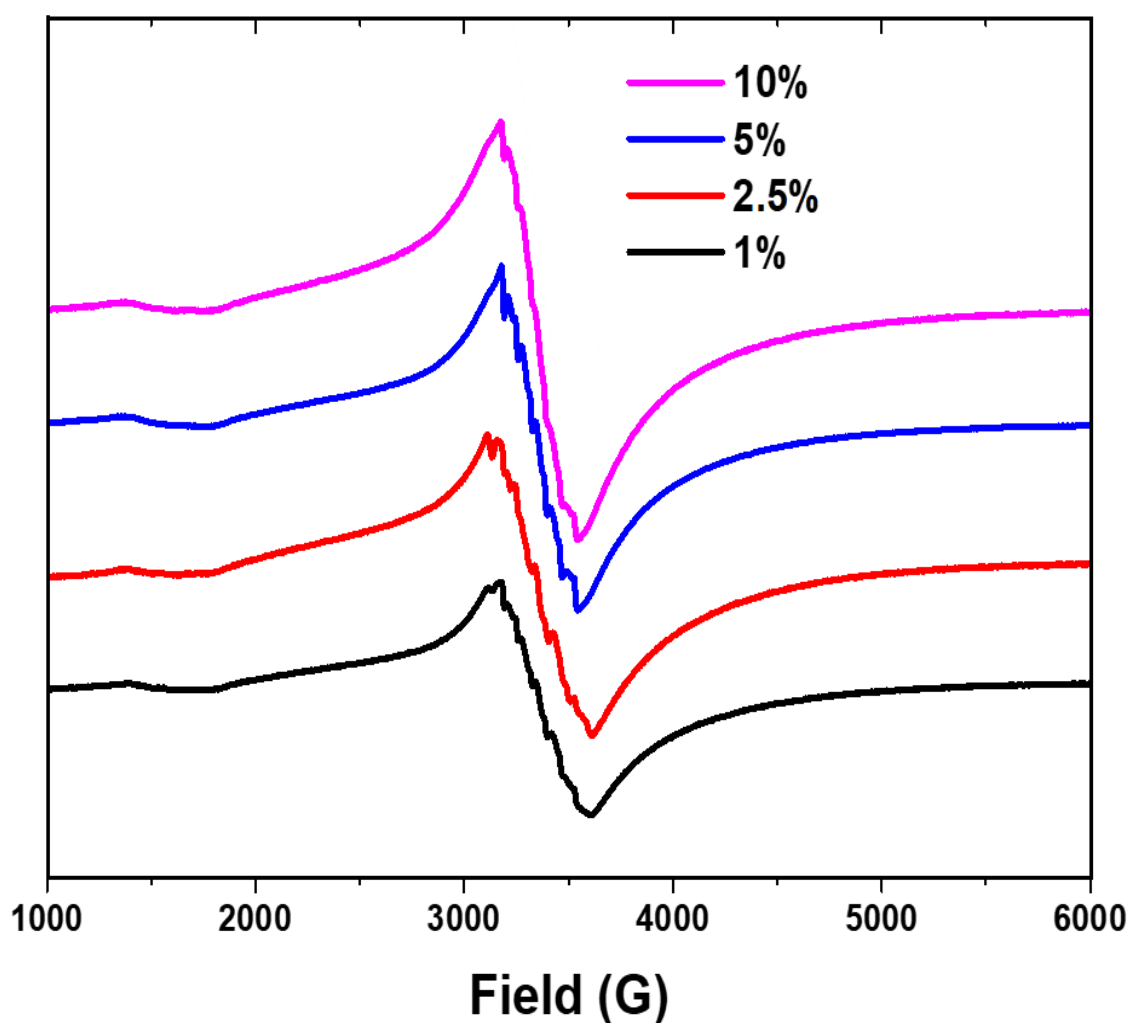


Figure 5.5. EPR spectra recorded at 20 K of Mn:AIGZS QDs at $\text{Ag/In/Ga/Zn}=0.25/0.875/0.875/2$ ratio

5.4. Optical characteristics

Fig. 5.6 shows the UV-vis absorption and the PL emission spectra and the digital photographs under UV light of the AIGZS QDs with the Ag/In/Ga/Zn ratio of 0.25 / 0.875 / 0.875 / 2 when increasing the amount of Mn²⁺ ion doping into these particles.

The emission peak of the undoped AIGZS QDs is located at 515 nm and a defect-related emission centered at ca. 650 nm can also be observed. After doping with Mn²⁺ ions, a marked red shift of PL emission is observed, which also accompanied by decreasing of the bandgap, suggesting modification of the electronic states of the AIGZS core (Fig. 5.8, Table 5.2). The bandgap values were determined from the Tauc plots of $(\alpha h\nu)^2$ vs $h\nu$, where α is the absorption coefficient and $h\nu$ is the photon energy, and were found to decrease from 2.94 to 2.58 eV with increasing the Mn loading.

When increasing the doping in Mn²⁺ ions only slight changes in the PL positions were detected and the emission peaks of 1 %, 2.5 %, 5 % and 10 % Mn-doped AIGZS QDs are located at 622, 627, 629 and 628 nm, respectively. As showed above, the XRD patterns showed shifts (Fig. 2), thus the shift to lower energies when doping with Mn²⁺ ions may be caused by the lattice shrinkage originating from the diffusion of Mn²⁺ ions into the AIGZS core structure.

The observed red shift from 515 nm for undoped AIGZS QDs to ca. 630 nm for Mn-doped AIGZS QDs indicates that Mn²⁺ ions contribute to the PL emission mechanism. It is likely that the $^4T_1 \rightarrow ^6A_1$ transition of the Mn²⁺ ions³⁴ inhibits, which was also demonstrated by PL lifetimes close to milliseconds, according to the PL decay measurements. (Table 5.3).

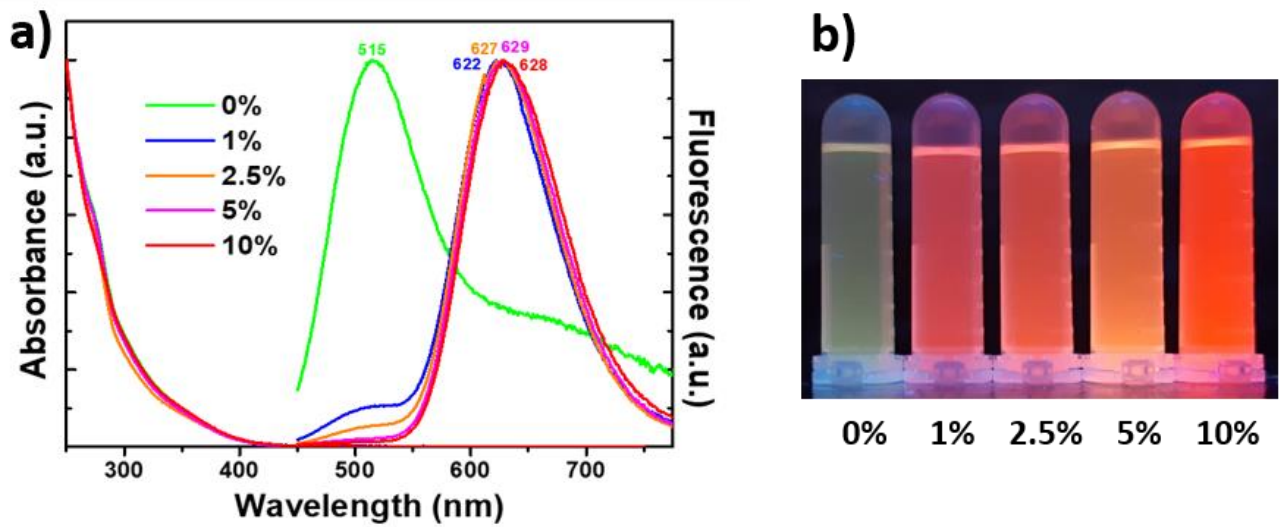


Figure 5.6. a) UV-Vis and PL spectra of Mn-doped AgInGaZnS QDs at Ag/In/Ga/Zn=0.25/0.875/0.875/2 ratio; b) photographs of these QDs under UV light

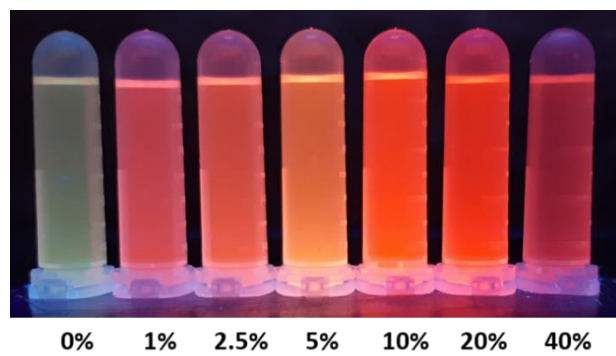


Figure 5.7. Digital photographs of Mn-doped AgInGaZnS QDs at Ag/In/Ga/Zn=0.25/0.875/0.875/2 ratio under UV light

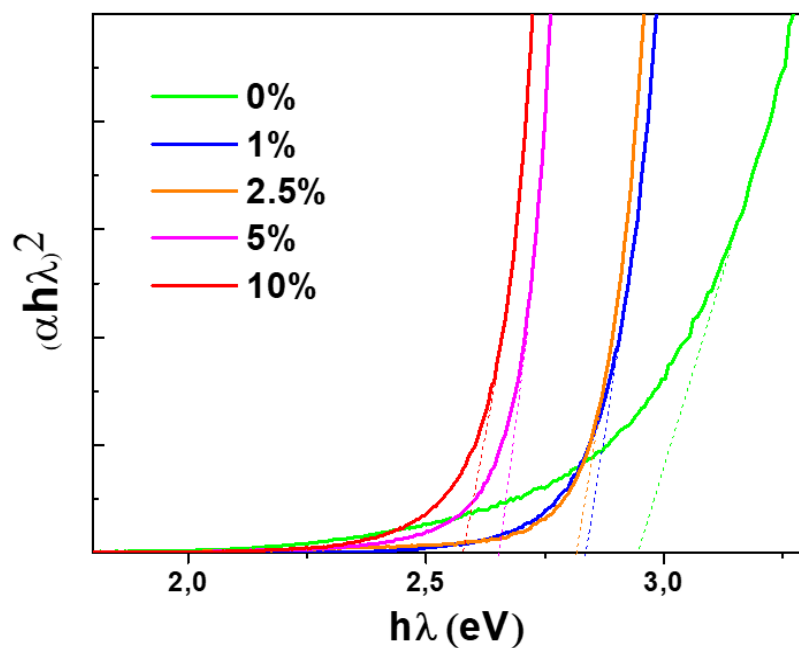


Figure 5.8. Determination of optical bandgaps of Mn-doped AgInGaZnS QDs at Ag/In/Ga/Zn=0.25/0.875/0.875/2 ratio

Table 5.2. The optical bandgap values of Mn-doped AgInGaZnS QDs

Mn:AIGZS QDs	E_g , eV
(Ag/In/Ga/Zn = 0.25/0.875/0.875/2)	
0%	2.94
1% Mn	2.83
2.5% Mn	2.81
5% Mn	2.66
10% Mn	2.58

The fluorescence quantum yields of the AIGZS QDs at room temperature were determined from the integrated fluorescence intensities of the QDs and reference, which is rhodamine 6G with

the QY of 95% in water, at 400 nm excitation (Table 5.3). All the samples for spectral measurement were diluted to yield an absorbance between 0.01-0.02 at the excitation wavelength. The PL QYs of the samples were calculated using the formula:

$$QY = \frac{F_s \times A_r \times QY_r}{F_r \times A_s}$$

where, F is the integrated fluorescence emission, A is the absorbance at the excitation wavelength of samples (s) and reference (r).

To further study of the PL emission mechanism, time-resolved PL decay measurements were carried out. Representative time-resolved PL decay spectra were recorded at the PL emission maxima of AIGZS and Mn:AIGZS QDs obtained from Fig. 5.6 and the results are shown in Fig. 5.9 and Table 5.3. The data were best fitted using a biexponential function $I(t) = A_1 \exp(-t/\tau_1) + A_2 \exp(-t/\tau_2)$, where τ_1 and τ_2 are the time constants of the PL and A_1 and A_2 the normalized amplitudes of the components. The fitting parameters are summarized in Table 5.3 when the Mn-doping increases. The PL lifetimes curve were the best fitted using two components: the first (fast) component τ_1 is associated with surface trap-state recombination, while the second (slow) component τ_2 is associated with defect states (D-A recombination).

The average PL lifetimes (τ_{av}) were determined using $\tau_{av} = (A_1\tau_1 + A_2\tau_2)/(A_1 + A_2)$ and was 99.9 ns for undoped AIGZS QDs, which shows the higher contribution of surface defects. Upon Mn-doping of AIGZS QDs, an increase of the decay time of both components was observed. The longer PL decay can be attributed to the radiative recombination, involving intragap states of QDs exhibiting inherent lattice defects. However, increasing Mn^{2+} concentration leads to the increasing contribution of the first component, suggesting a more pronounced influence of Mn^{2+} to surface-related defect recombination.

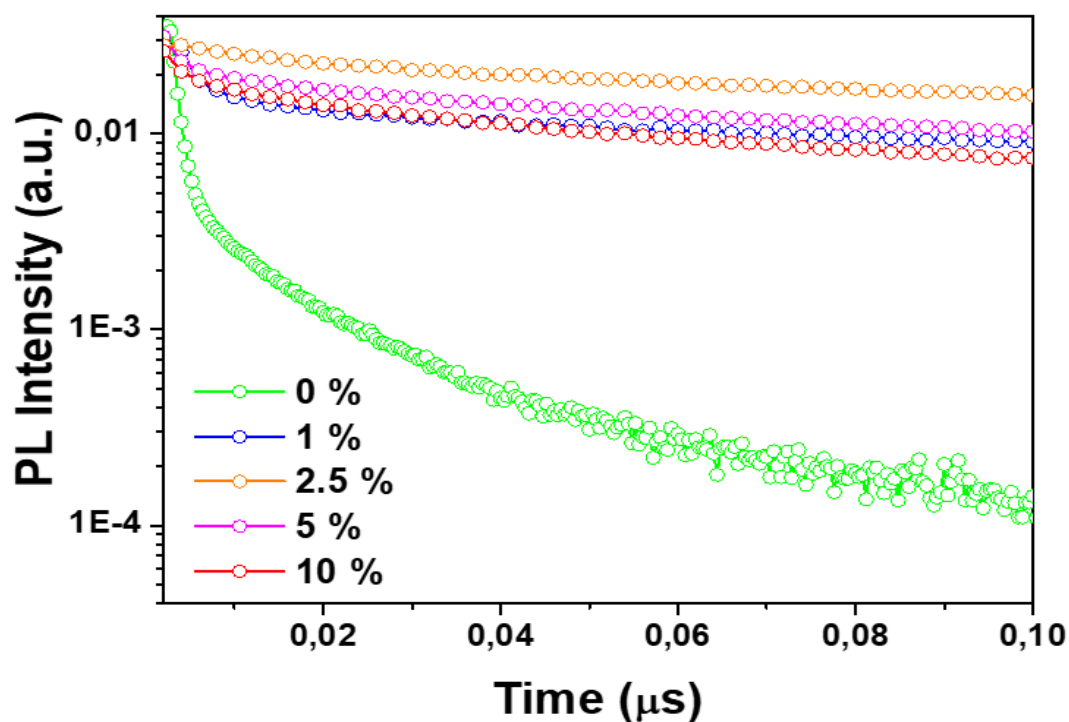


Figure 5.9. PL lifetimes of AIGZS and Mn-doped AIGZS QDs at PL maximum wavelength

Table 5.3. PL QYs, τ_1 and τ_2 time constants and the contributions of decays A_1 and A_2 of undoped and Mn-doped AIGZS QDs

Mn:AIGZS QDs	PL QYs, %	A_1	$\tau_1, \mu\text{s}$	A_2	$\tau_2, \mu\text{s}$	$\tau_{av}, \mu\text{s}$
Ag/In/Ga/Zn = 0.25/0.875/0.875/2						
0%	14.3	0.829	$66.3 \cdot 10^{-3}$	0.171	$262.3 \cdot 10^{-3}$	$99.9 \cdot 10^{-3}$
1% Mn	9.6	0.482	232.5	0.518	1497.4	887.9
2,5% Mn	18.1	0.577	192.4	0.423	1212.3	624.3
5% Mn	19.1	0.643	127.5	0.357	946.3	419.9
10% Mn	8.6	0.702	105.7	0.298	734.5	293.2

5.5. Magnetic properties

Magnetic measurements using VSM were carried out for undoped and Mn-doped AIGZS QDs with Ag/In/Ga/Zn ratio of 0.25/0.875/0.875/2 in a wide temperature range. Fig. 5.10 shows magnetization curves of Mn-doped samples at 10 K and 310 K. It can be seen from the figure that undoped AIGZS QDs exhibit diamagnetic behavior. For Mn-doped QDs, the magnetization curves show that the samples have both paramagnetic and superparamagnetic behaviors. Also, this figure demonstrates an increase of the magnetization with the Mn loading, which is the result of paramagnetic Mn^{2+} ions doping combined to the small sizes of nanoparticles. Magnetic measurements showed that these nanoparticles exhibit superparamagnetic behavior at 10 K and paramagnetic behavior at 310 K.

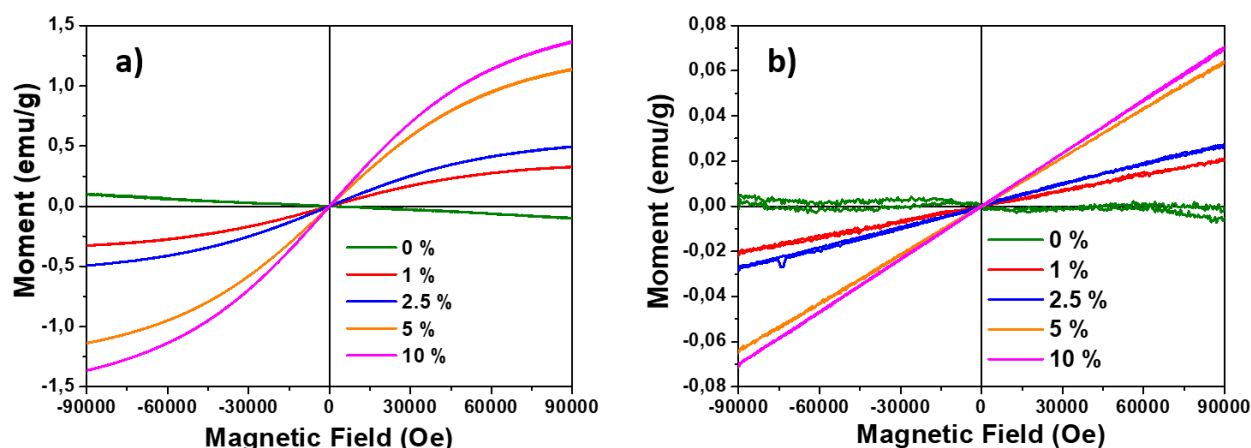


Figure 5.10. M(H) loop curves of Mn-doped AIGZS QDs at different temperatures: a) 10 K; b) 310 K

Temperature dependent magnetization curves of 1, 2.5, 5 and 10% Mn-doped AIGZS QDS are shown in the Fig. 5.11. The coercivity H_c (the applied field required for zero net moment) and the remanence M_r (the magnetic moment at zero applied field) for 10 % Mn-doped QDs at different temperatures are shown in the close-up magnetization curves in Fig. 5.12. The samples synthesized at high concentration of Mn^{2+} exhibit the highest saturation magnetization, up to 1.3 emu/g for 10% doping (at 10 K) (Fig. 5.10a), and decrease at higher temperatures. The

decrease of the amount of Mn^{2+} leads to the decrease of M_s values, and the temperature dependence is drastically increased.

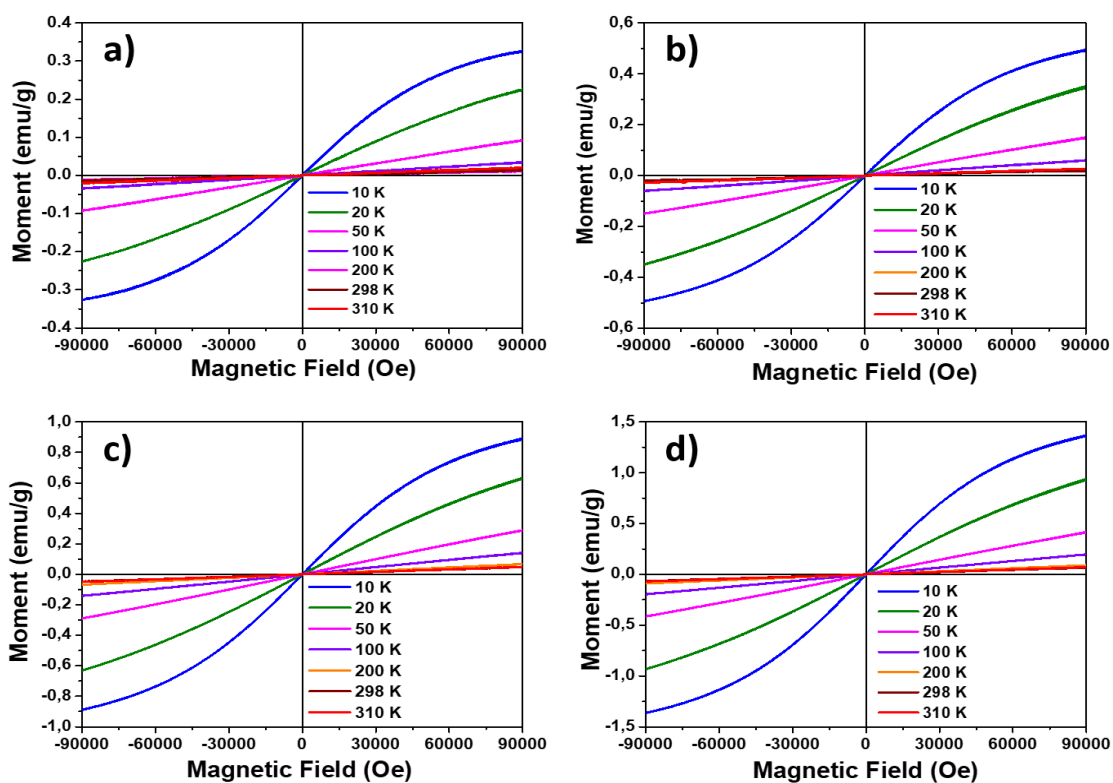


Figure 5.11. $M(H)$ loop curves of Mn-doped AIGZS QDs at different temperatures: a) 1%; b) 2.5%; c) 5%; d) 10%

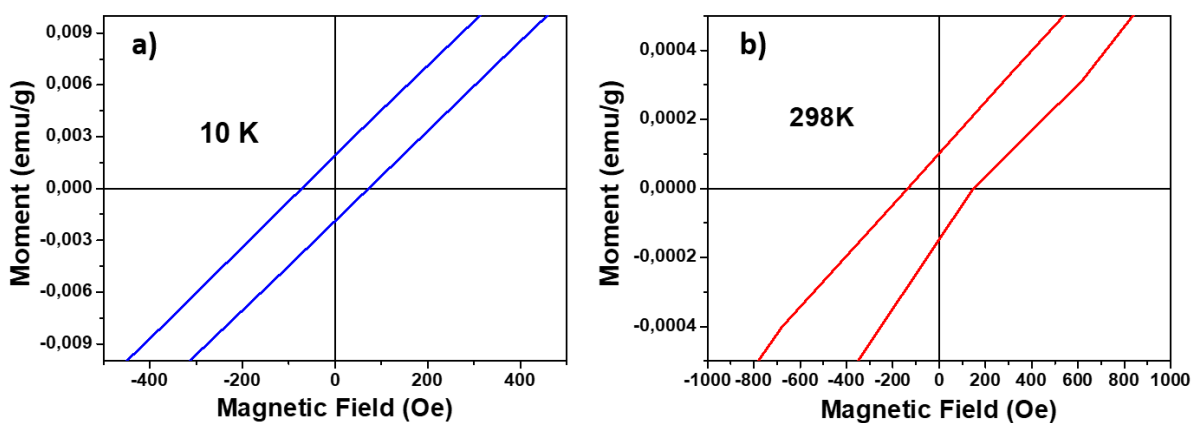


Figure 5.12. $M(H)$ loop curves of 10% Mn-doped AIGZS QDs at zero field: a) at 10 K; b) at 298 K

5.6. Aqueous phase transfer

To demonstrate the potential uses of Mn-doped AIGZS QDs in biological applications, the dots were transferred into aqueous phase. Undoped and paramagnetic metal Mn-doped AIGZS QDs behave similarly while transferring into the water medium. The transfer methods and synthetic conditions are presented in the previous chapter. Here the 5 % Mn-doped AIGZS QDs were aqueous phase transferred using amphiphilic ligand PMAO and GTMA, and their stability tested at pH values between 3 and 13 (Fig. 5.13 and 5.14). As can be seen, the position of the PL peaks does not change when the QDs transferred to aqueous media, and the photoluminescence intensity remains high within the physiologically appropriate range of 5 to 9, which demonstrates the potential of these QDs for biological applications. A marked decrease of the PL intensity is observed at pH below 5 due to the protonation of the carboxylate functions present at the periphery of the dots. In basic medium, the dots remain stable until pH 12.

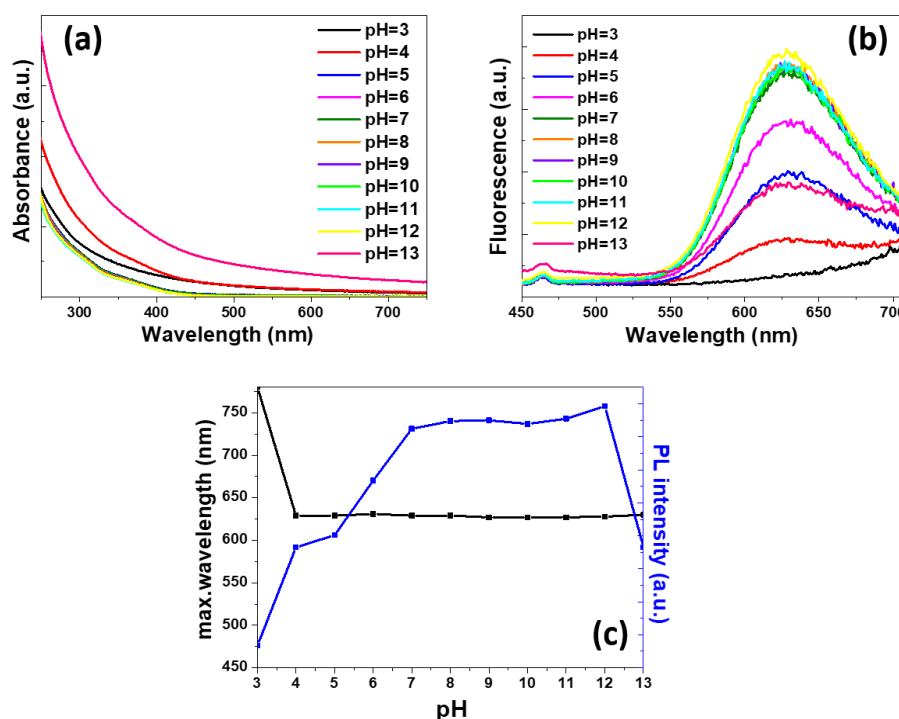


Figure 5.13. UV-Vis (a) and PL (b) spectra of 5% Mn-doped AIGZS QDs water transferred using PMAO recorded at different pH values, (c) shows the PL peak position and PL intensity changing in media with different pH values

Using GTMA as capping ligand shows similar results. Fig. 5.14 shows the UV-visible and PL spectra, as well as the position of the PL peak and the change in PL intensity in media with different pH values. In the same way as in capping with PMAO, the photoluminescence intensity remains high within the physiologically acceptable range of 5 to 9 and remains stable up to pH 12, which demonstrates the potential of the GTMA-coated QDs for biological applications. At pH below 4, a decrease in the PL intensity is observed due to the protonation of carboxylate functions. The position of the PL peaks does not change upon transfer of QDs to an aqueous medium.

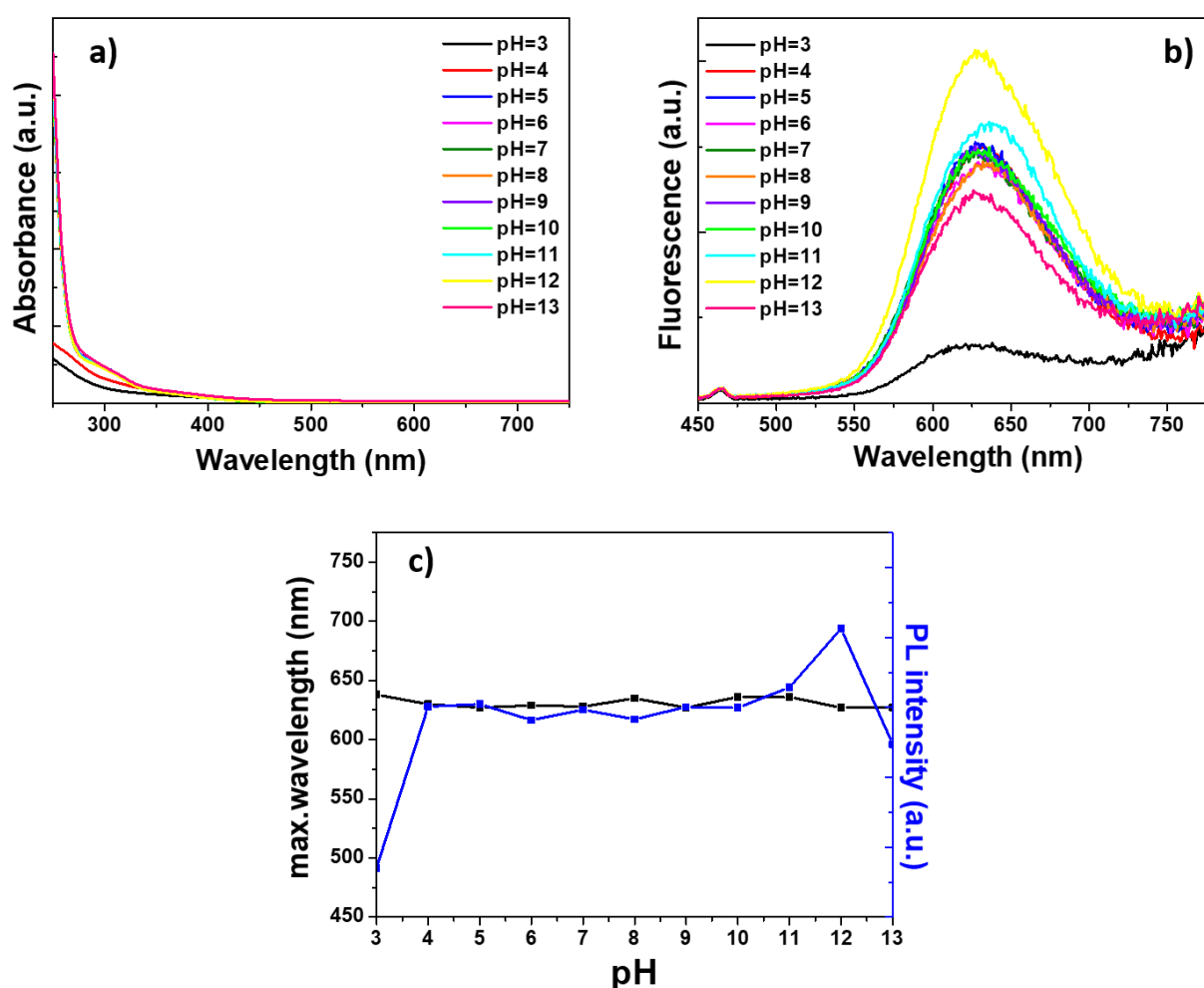


Figure 5.14. UV-Vis (a) and PL (b) spectra of 5% Mn-doped AIGZS QDs water transferred using GTMA recorded at different pH values, (c) shows the PL peak position and PL intensity changing in media with different pH values

5.7. Mn:AIGZS QDs as MRI probes

1 % and 2.5 % Mn-doped AIGZS QDs were *in-vitro* investigated as contrast agents (CAs) for MRI (experiments were also conducted with the QDs doped with 5% Mn but similar results to those observed with the 2.5% Mn doping were observed). As mentioned in the previous chapters, the Mn^{2+} ions show paramagnetic signals, thus these ions in Mn-doped AIGZS QDs are expected to increase the image intensity in T1-weighted imaging. One of the most important parameters of MRI CAs is their relaxivity, which can be determined as the slopes from the relaxation rates dependences on the CA concentrations. The relaxation rates are the inverses of relaxation times. Therefore, longitudinal relaxation times and transverse relaxation times were measured at 60 and 100 MHz (resonance frequency of ^1H) and ambient temperature for AIGZS QDs doped with Mn (Fig. 5.15). The relaxivity values at room temperature were found to be as follows: $r_1 = 0.19 \text{ mM}^{-1}\text{s}^{-1}$, $r_2 = 0.49 \text{ mM}^{-1}\text{s}^{-1}$ at 1.4 T and $r_1 = 0.11 \text{ mM}^{-1}\text{s}^{-1}$, $r_2 = 0.42 \text{ mM}^{-1}\text{s}^{-1}$ at 2.35 T for R1, R2 relaxation rates, respectively.

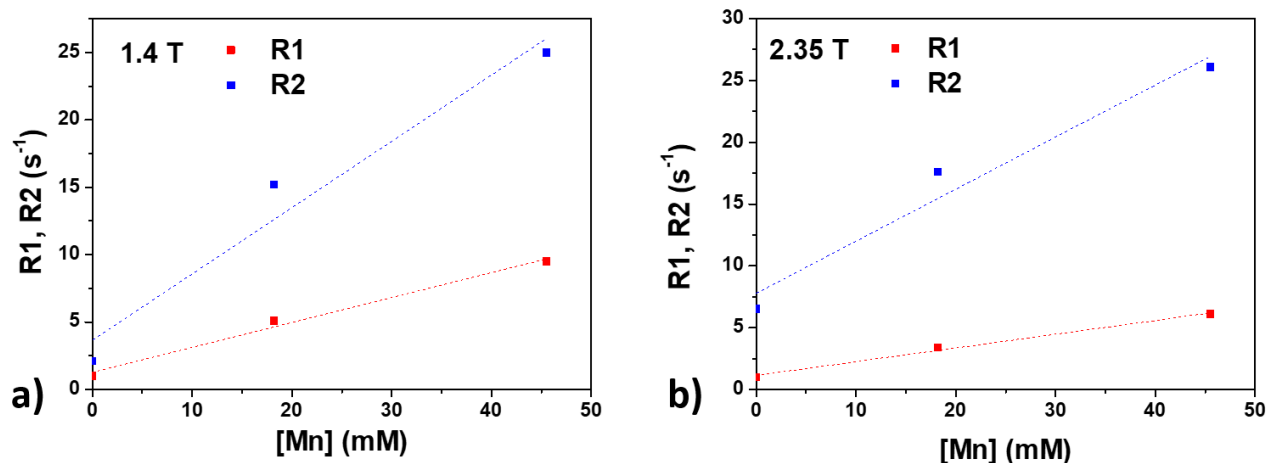


Figure 5.15. Longitudinal (R1) and transverse relaxation rates (R2) of Mn-doped AIGZS QDs as a function of Mn (II) concentrations in aqueous solution: a) at 1.4 T, 60 MHz (resonance frequency of ^1H) and 298 K, $r_1 = 0.19 \text{ mM}^{-1}\text{s}^{-1}$, $r_2 = 0.49 \text{ mM}^{-1}\text{s}^{-1}$; b) at 2.35 T, 100 MHz (resonance frequency of ^1H) and 298 K, $r_1 = 0.11 \text{ mM}^{-1}\text{s}^{-1}$, $r_2 = 0.42 \text{ mM}^{-1}\text{s}^{-1}$

s^{-1}

These relaxivity values are relatively lower than those of commercially available gadolinium-based contrast agents²¹⁸ (for example, $r_1 = 3.3 \text{ L mmol}^{-1} \text{ s}^{-1}$ and $r_2 = 3.9 \text{ L mmol}^{-1} \text{ s}^{-1}$ at 310 K in water, GADOVIST) in typical MRI field of 1.5 T and medically appropriate frequency range of 64–128 MHz. It was reported that the relaxivity of paramagnetic metal based CAs is attributed to their high surface-to-volume ratio, paramagnetic properties of metal ions as well as the numbers of unpaired electrons²¹⁹.

Nevertheless, the CAs are expected to enhance the contrast in MR images. Fig. 5.16 shows the MR images of Mn-doped AIGZS QDs. The T1-weighted and T2-weighted MRI images were recorded. As can be seen, with the increasing in Mn loading, an increase in the signal in both T1-weighted and T2-weighted images was observed. This shows that these Mn-doped AIGZS QDs can be potentially used as dual-modal MRI contrast agents.

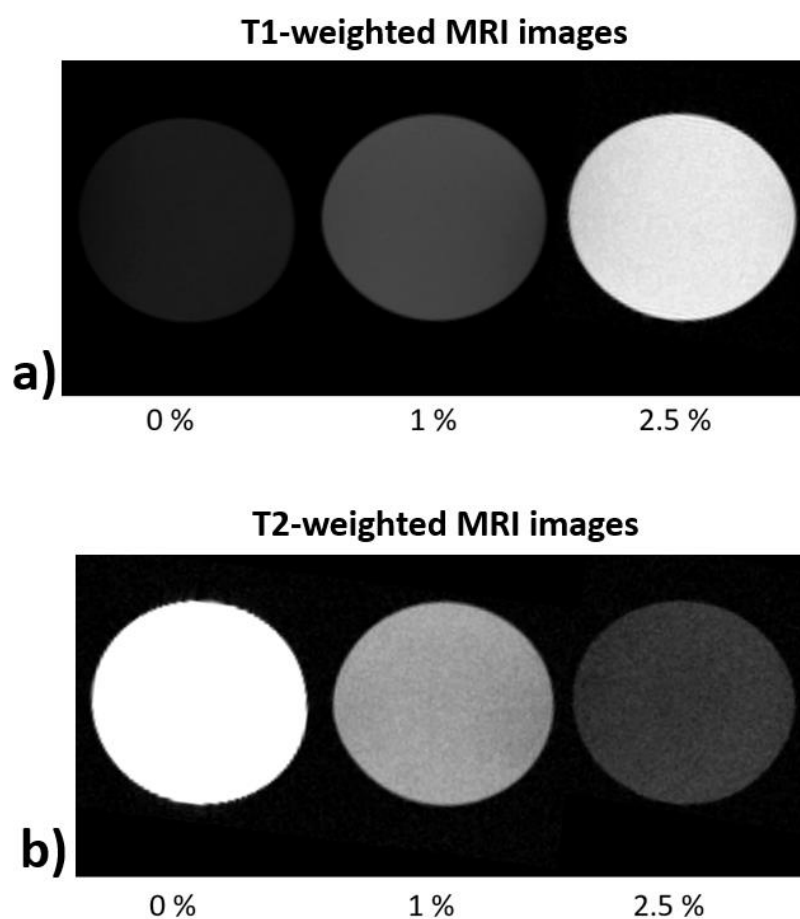


Figure 5.16. T1-weighted (a) and T2-weighted (b) MRI images of undoped, 1 % and 2.5 % Mn-doped AIGZS QDs

5.8. Conclusion

Mn-doped Ag-In-Ga-Zn-S QDs were synthesized using a Ag/In/Ga/Zn ratio of 0.25/0.875/0.875/2 using the thermal decomposition method. The metal diethyldithiocarbamate precursor was first prepared in a water-methanol mixture, then the dried precursor was heated at 220 °C in the presence of MnSt₂ as a dopant and oleylamine as a solvent and capping ligand. The synthesized QDs sizes in the range of 1.6 and 2.1 nm and have tetragonal structure. Mn-doped QDs exhibit both superparamagnetic and paramagnetic behaviors and were demonstrated to be of high potential as MRI contrast agents.

General conclusions and perspectives

During the past three years of preparing this dissertation, an important work has been done to prepare QDs for biomedical use in fluorescence imaging and magnetic resonance imaging. For this, Ag-In-Zn-S QDs were synthesized in organic and aqueous phases, doped with paramagnetic ions such as manganese, iron and gadolinium, and the origin of the fluorescence in doped QDs was investigated. In addition, new quinary Ag-In-Ga-Zn-S QDs were synthesized and their doping with manganese investigated. Further, the surfaces of these nanocrystals were modified with hydrophilic ligands for biomedical uses. At the end, primary tests were carried out using the prepared QDs as fluorescent and magnetic probes.

First, AIZS and Mn-doped AIZS QDs were prepared in organic phase using a one-step synthesis method. The dots produced are of $(\text{AgInS}_2)_x(\text{MnS})_y(\text{ZnS})_{1-x-y}$ general formula. The synthesized QDs with sizes from 3.3 to 3.7 nm show high fluorescence with a quantum yield of up to 62% for orange-emitting ones. It was found that the origin of fluorescence after doping differs from previously described results: continuous shifts to higher wavelengths for the PL peak positions were observed with the increase of the loading in Mn^{2+} , which indicates a modification of the electronic states of the dots. As shown by TEM results, these shifts do not originate from an increase in the size of the dots. The PL emission does not originate from Mn^{2+} related $^4\text{T}_1 \rightarrow ^6\text{A}_1$ transition, but rather from the new electronic energy levels of Mn^{2+} ions in the AIZS core. Further investigations of the origin of PL emission were conducted by time-resolved PL decay measurements and showed that the average PL lifetimes to be in the range of 1 to 10 μs . Such values are usually observed for undoped AIZS nanocrystals, which further confirms that the PL emission does not originate from $^4\text{T}_1 \rightarrow ^6\text{A}_1$ transition of Mn^{2+} ions (a millisecond PL lifetime should be observed). As a result, the Mn^{2+} loading dependence of the PL emission peak position indicates that there are new Mn^{2+} -dependent states with a relatively higher energy and located above the $^6\text{A}_1$ state. Further, doping of the QDs with Mn^{2+} ions led to a magnetic response to an applied field compared to undoped QDs. Mn-doped AIZS QDs, regardless of the doping percentage with manganese, showed a merge of a ferromagnetic signal with a paramagnetic and/or superparamagnetic signal. Moreover, AIZS and Mn-doped AIZS QDs were easily transferred to the aqueous phase using the amphiphilic polymer poly(maleic anhydride-alt-1-octadecene) without alteration of their optical properties.

In the following step, AIZS and Mn-, Gd- or Fe-doped AIZS QDs were synthesized directly in aqueous media using GSH as a capping ligand. When the application of synthesized QDs for biomedical purposes is considered, aqueous phase synthesis is preferable since as-synthesized QDs are water-dispersible. Thus, these particles do not require any modification for their transfer to the aqueous phase. These QDs showed high colloidal stability in a pH range of 5 to 9, and high photostability after 3 h under UV light illumination. Moreover, according to MTT-assay results, Mn-, Gd- or Fe-doped GSH-capped and GSH-PEI-capped AIZS QDs exhibit a good biocompatibility showing only weak toxicity until a concentration of 1 mg/mL. Further, capping with FA does not decrease the cell viability, the lowest cell viability, 76.4 %, being found for 5% Mn-doped AIZS QDs. Finally, GSH-PEI-FA-capped AIZS QDs entered into the cells, and through the cytoplasm labeled the nuclei of the cells. These results show that the FA ligand allows to target the dots into the cells and promotes specific intracellular uptake through receptor-mediated endocytosis.

Next, new Ag-In-Ga-Zn-S QDs were prepared via a single precursor thermal decomposition synthesis using OAm as both capping ligand and solvent. The sizes of the QDs were ca. 2 nm and their structure corresponds to the tetragonal chalcopyrite phase. It was found that changing the Ag/In/Ga/Zn ratio allows tuning the PL emission of the QDs from blue-green to the near-infrared. Further, the synthesized AIGZS QDs showed the highest PL QY of 48.3% at the Ag/In/Ga/Zn ratio of 0.66/0.66/0.66/2. Moreover, the PL lifetime was found to reach the 915 ns for AIGZS QDs prepared with the Ag/In/Ga/Zn ratio of 1/0.5/0.5/1. Finally, AIGZS QDs were aqueous phase transferred using glutathione tetramethylammonium as well as glycine dithiocarbamate. The aqueous transferred QDs show hydrodynamic diameters of 14.6 ± 1.3 nm and 9.4 ± 1.8 nm for AIGZS@GTMA and AIGZS@Gly-DTC QDs, respectively, according to DLS measurements.

In the last part of the work, Mn-doped Ag-In-Ga-Zn-S QDs were synthesized using the same single precursor thermal decomposition method. These QDs possess a size ranging from 1.8 to 2.0 nm and a tetragonal chalcopyrite structure. Their PL emission is a defect-related emission, which consists of two components: the fast component τ_1 is associated with surface trap-state recombination, the slow component τ_2 is associated with defect-states (D-A recombination). Mn-doping of AIGZS QDs resulted an increase of the decay time of both components. To transfer these QDs to the aqueous phase, glutathione tetramethylammonium was chosen as surface ligand due to the simplicity and rapidity of this method. Finally, T1 and T2-weighted

images of Mn-doped AIGZS QDs show that with increasing the Mn^{2+} ions concentration in AIGZS QDs results in increasing the contrast in T1 and T2-weighted MR images.

Summing up, the following perspectives of this dissertation can be emphasized:

- experiments to improve some properties (quantum yields, magnetic signal, colloidal and photostabilities) of the studied QDs both undoped and doped using facile one-pot thermal decomposition methods;
- doping of QDs with other elements (such as Ni, Co, Cr) in order to obtain effective magnetic signal. This will allow efficiently use them as dual-modal probes in bioimaging purposes;
- synthesis and characterization of AIZ-based quaternary QDs with substituting one of the elements in the structure, for example Ag-Cu-In-Zn-S QDs and their doping with paramagnetic ions such as Mn^{2+} , Gd^{3+} , Fe^{3+} followed by testing them as potential dual-modal probes in bioimaging purposes;
- in vivo bioimaging experiments aimed to better understanding of real application of prepared QDs as dual-modal fluorescent and magnetic probes;
- conduct research and experiments in order to scale up the synthesis.

References

- (1) Ekimov, A. I.; Onushchenko, A. A. Quantum Size Effect in 3-Dimensional Microscopic Semiconductor Crystals. *JETP Lett.* **1981**, *34* (6), 345–349.
- (2) Micić, O. I.; Nozik, A. J. Synthesis and Characterization of Binary and Ternary III–V Quantum Dots. *J. Lumin.* **1996**, *70* (1–6), 95–107. [https://doi.org/10.1016/0022-2313\(96\)00047-6](https://doi.org/10.1016/0022-2313(96)00047-6).
- (3) Berends, A. C.; Mangnus, M. J. J.; Xia, C.; Rabouw, F. T.; de Mello Donega, C. Optoelectronic Properties of Ternary I–III–VI₂ Semiconductor Nanocrystals: Bright Prospects with Elusive Origins. *J. Phys. Chem. Lett.* **2019**, *10* (7), 1600–1616. <https://doi.org/10.1021/acs.jpcclett.8b03653>.
- (4) Galsin, J. S. Crystal Structure of Solids. In *Solid State Physics*; Elsevier, 2019; pp 1–36. <https://doi.org/10.1016/B978-0-12-817103-5.00001-3>.
- (5) Zhang, S. B.; Wei, S.-H.; Zunger, A.; Katayama-Yoshida, H. Defect Physics of the CuInSe₂ Chalcopyrite Semiconductor. *Phys. Rev. B* **1998**, *57* (16), 9642–9656. <https://doi.org/10.1103/PhysRevB.57.9642>.
- (6) Hong, S. P.; Park, H. K.; Oh, J. H.; Yang, H.; Do, Y. R. Comparisons of the Structural and Optical Properties of O-AgInS₂, t-AgInS₂, and c-AgIn₅S₈ Nanocrystals and Their Solid-Solution Nanocrystals with ZnS. *J. Mater. Chem.* **2012**, *22* (36), 18939. <https://doi.org/10.1039/c2jm33879c>.
- (7) Rogers, B.; Adams, J.; Pennathur, S. *Nanotechnology: Understanding Small Systems*, Third edition.; Mechanical engineering series; CRC Press, Taylor & Francis Group: Boca Raton, 2015.
- (8) Dembski, S.; Schneider, C.; Christ, B.; Retter, M. Core-Shell Nanoparticles and Their Use for in Vitro and in Vivo Diagnostics. In *Core-Shell Nanostructures for Drug Delivery and Theranostics*; Elsevier, 2018; pp 119–141. <https://doi.org/10.1016/B978-0-08-102198-9.00005-3>.
- (9) Ghosh Chaudhuri, R.; Paria, S. Core/Shell Nanoparticles: Classes, Properties, Synthesis Mechanisms, Characterization, and Applications. *Chem. Rev.* **2012**, *112* (4), 2373–2433. <https://doi.org/10.1021/cr100449n>.
- (10) Zhao, H.; Rosei, F. Colloidal Quantum Dots for Solar Technologies. *Chem* **2017**, *3* (2), 229–258. <https://doi.org/10.1016/j.chempr.2017.07.007>.

- (11) Girma, W. M.; Fahmi, M. Z.; Permadi, A.; Abate, M. A.; Chang, J.-Y. Synthetic Strategies and Biomedical Applications of I–III–VI Ternary Quantum Dots. *J. Mater. Chem. B* **2017**, *5* (31), 6193–6216. <https://doi.org/10.1039/C7TB01156C>.
- (12) Ivanov, S. A.; Piryatinski, A.; Nanda, J.; Tretiak, S.; Zavadil, K. R.; Wallace, W. O.; Werder, D.; Klimov, V. I. Type-II Core/Shell CdS/ZnSe Nanocrystals: Synthesis, Electronic Structures, and Spectroscopic Properties. *J. Am. Chem. Soc.* **2007**, *129* (38), 11708–11719. <https://doi.org/10.1021/ja068351m>.
- (13) Zhong, H.; Bai, Z.; Zou, B. Tuning the Luminescence Properties of Colloidal I–III–VI Semiconductor Nanocrystals for Optoelectronics and Biotechnology Applications. *J. Phys. Chem. Lett.* **2012**, *3* (21), 3167–3175. <https://doi.org/10.1021/jz301345x>.
- (14) Li, S.; Tang, X.; Zang, Z.; Yao, Y.; Yao, Z.; Zhong, H.; Chen, B. I–III–VI Chalcogenide Semiconductor Nanocrystals: Synthesis, Properties, and Applications. *Chin. J. Catal.* **2018**, *39* (4), 590–605. [https://doi.org/10.1016/S1872-2067\(18\)63052-9](https://doi.org/10.1016/S1872-2067(18)63052-9).
- (15) Reiss, P.; Protière, M.; Li, L. Core/Shell Semiconductor Nanocrystals. *Small* **2009**, *5* (2), 154–168. <https://doi.org/10.1002/sml.200800841>.
- (16) Wang, D.; Zheng, W.; Hao, C.; Peng, Q.; Li, Y. General Synthesis of I–III–VI₂ Ternary Semiconductor Nanocrystals. *Chem. Commun.* **2008**, No. 22, 2556. <https://doi.org/10.1039/b800726h>.
- (17) Torimoto, T.; Adachi, T.; Okazaki, K.; Sakuraoka, M.; Shibayama, T.; Ohtani, B.; Kudo, A.; Kuwabata, S. Facile Synthesis of ZnS–AgInS₂ Solid Solution Nanoparticles for a Color-Adjustable Luminophore. *J. Am. Chem. Soc.* **2007**, *129* (41), 12388–12389. <https://doi.org/10.1021/ja0750470>.
- (18) Zhang, J.; Tse, K.; Wong, M.; Zhang, Y.; Zhu, J. A Brief Review of Co-Doping. *Front. Phys.* **2016**, *11* (6), 117405. <https://doi.org/10.1007/s11467-016-0577-2>.
- (19) Yang, Y.; Chen, O.; Angerhofer, A.; Cao, Y. C. Radial-Position-Controlled Doping in CdS/ZnS Core/Shell Nanocrystals. *J. Am. Chem. Soc.* **2006**, *128* (38), 12428–12429. <https://doi.org/10.1021/ja064818h>.
- (20) Koole, R.; Mulder, W. J. M.; van Schooneveld, M. M.; Strijkers, G. J.; Meijerink, A.; Nicolay, K. Magnetic Quantum Dots for Multimodal Imaging: Magnetic QDs for Multimodal Imaging. *Wiley Interdiscip. Rev. Nanomed. Nanobiotechnol.* **2009**, *1* (5), 475–491. <https://doi.org/10.1002/wnan.14>.
- (21) Torimoto, T.; Ogawa, S.; Adachi, T.; Kameyama, T.; Okazaki, K.; Shibayama, T.; Kudo, A.; Kuwabata, S. Remarkable Photoluminescence Enhancement of ZnS–AgInS₂

- Solid Solution Nanoparticles by Post-Synthesis Treatment. *Chem. Commun.* **2010**, 46 (12), 2082. <https://doi.org/10.1039/b924186h>.
- (22) Du, W.; Qian, X.; Yin, J.; Gong, Q. Shape- and Phase-Controlled Synthesis of Monodisperse, Single-Crystalline Ternary Chalcogenide Colloids through a Convenient Solution Synthesis Strategy. *Chem. - Eur. J.* **2007**, 13 (31), 8840–8846. <https://doi.org/10.1002/chem.200700618>.
- (23) Xie, R.; Rutherford, M.; Peng, X. Formation of High-Quality I–III–VI Semiconductor Nanocrystals by Tuning Relative Reactivity of Cationic Precursors. *J. Am. Chem. Soc.* **2009**, 131 (15), 5691–5697. <https://doi.org/10.1021/ja9005767>.
- (24) Ogawa, T.; Kuzuya, T.; Hamanaka, Y.; Sumiyama, K. Synthesis of Ag–In Binary Sulfide Nanoparticles—Structural Tuning and Their Photoluminescence Properties. *J. Mater. Chem.* **2010**, 20 (11), 2226. <https://doi.org/10.1039/b920732e>.
- (25) Luo, Z.; Zhang, H.; Huang, J.; Zhong, X. One-Step Synthesis of Water-Soluble AgInS₂ and ZnS–AgInS₂ Composite Nanocrystals and Their Photocatalytic Activities. *J. Colloid Interface Sci.* **2012**, 377 (1), 27–33. <https://doi.org/10.1016/j.jcis.2012.03.074>.
- (26) Peng, S.; Zhang, S.; Mhaisalkar, S. G.; Ramakrishna, S. Synthesis of AgInS₂ Nanocrystal Ink and Its Photoelectrical Application. *Phys. Chem. Chem. Phys.* **2012**, 14 (24), 8523. <https://doi.org/10.1039/c2cp40848a>.
- (27) Liu, L.; Hu, R.; Law, W.-C.; Roy, I.; Zhu, J.; Ye, L.; Hu, S.; Zhang, X.; Yong, K.-T. Optimizing the Synthesis of Red- and near-Infrared CuInS₂ and AgInS₂ Semiconductor Nanocrystals for Bioimaging. *The Analyst* **2013**, 138 (20), 6144. <https://doi.org/10.1039/c3an01030a>.
- (28) Xiang, W.; Xie, C.; Wang, J.; Zhong, J.; Liang, X.; Yang, H.; Luo, L.; Chen, Z. Studies on Highly Luminescent AgInS₂ and Ag–Zn–In–S Quantum Dots. *J. Alloys Compd.* **2014**, 588, 114–121. <https://doi.org/10.1016/j.jallcom.2013.10.188>.
- (29) Yoon, H. C.; Oh, J. H.; Ko, M.; Yoo, H.; Do, Y. R. Synthesis and Characterization of Green Zn–Ag–In–S and Red Zn–Cu–In–S Quantum Dots for Ultrahigh Color Quality of Down-Converted White LEDs. *ACS Appl. Mater. Interfaces* **2015**, 7 (13), 7342–7350. <https://doi.org/10.1021/acsami.5b00664>.
- (30) Murray, C. B.; Norris, D. J.; Bawendi, M. G. Synthesis and Characterization of Nearly Monodisperse CdE (E = Sulfur, Selenium, Tellurium) Semiconductor Nanocrystallites. *J. Am. Chem. Soc.* **1993**, 115 (19), 8706–8715. <https://doi.org/10.1021/ja00072a025>.

- (31) Mao, B.; Chuang, C.-H.; Wang, J.; Burda, C. Synthesis and Photophysical Properties of Ternary I–III–VI AgInS₂ Nanocrystals: Intrinsic versus Surface States. *J. Phys. Chem. C* **2011**, *115* (18), 8945–8954. <https://doi.org/10.1021/jp2011183>.
- (32) Mao, B.; Chuang, C.-H.; Lu, F.; Sang, L.; Zhu, J.; Burda, C. Study of the Partial Ag-to-Zn Cation Exchange in AgInS₂/ZnS Nanocrystals. *J. Phys. Chem. C* **2013**, *117* (1), 648–656. <https://doi.org/10.1021/jp309202g>.
- (33) Ko, M.; Yoon, H. C.; Yoo, H.; Oh, J. H.; Yang, H.; Do, Y. R. Highly Efficient Green Zn-Ag-In-S/Zn-In-S/ZnS QDs by a Strong Exothermic Reaction for Down-Converted Green and Tripackage White LEDs. *Adv. Funct. Mater.* **2017**, *27* (4), 1602638. <https://doi.org/10.1002/adfm.201602638>.
- (34) Manna, G.; Jana, S.; Bose, R.; Pradhan, N. Mn-Doped Multinary CIZS and AIZS Nanocrystals. *J. Phys. Chem. Lett.* **2012**, *3* (18), 2528–2534. <https://doi.org/10.1021/jz300978r>.
- (35) Chen, S.; Zaeimian, M. S.; Monteiro, J. H. S. K.; Zhao, J.; Mamalis, A. G.; de Bettencourt-Dias, A.; Zhu, X. Mn Doped AIZS/ZnS Nanocrystals: Synthesis and Optical Properties. *J. Alloys Compd.* **2017**, *725*, 1077–1083. <https://doi.org/10.1016/j.jallcom.2017.07.262>.
- (36) Kameyama, T.; Takahashi, T.; Machida, T.; Kamiya, Y.; Yamamoto, T.; Kuwabata, S.; Torimoto, T. Controlling the Electronic Energy Structure of ZnS–AgInS₂ Solid Solution Nanocrystals for Photoluminescence and Photocatalytic Hydrogen Evolution. *J. Phys. Chem. C* **2015**, *119* (44), 24740–24749. <https://doi.org/10.1021/acs.jpcc.5b07994>.
- (37) Hu, J.; Lu, Q.; Tang, K.; Qian, Y.; Zhou, G.; Liu, X. Solvothermal Reaction Route to Nanocrystalline Semiconductors AgMS₂ (M = Ga, In). *Chem. Commun.* **1999**, No. 12, 1093–1094.
- (38) Yuan, Y.; Zai, J.; Su, Y.; Qian, X. Controlled Synthesis of Monodispersed AgGaS₂ 3D Nanoflowers and the Shape Evolution from Nanoflowers to Colloids. *J. Solid State Chem.* **2011**, *184* (5), 1227–1235. <https://doi.org/10.1016/j.jssc.2011.03.022>.
- (39) Uematsu, T.; Doi, T.; Torimoto, T.; Kuwabata, S. Preparation of Luminescent AgInS₂–AgGaS₂ Solid Solution Nanoparticles and Their Optical Properties. *J. Phys. Chem. Lett.* **2010**, *1* (22), 3283–3287. <https://doi.org/10.1021/jz101295w>.
- (40) Sh. Maeda, T. Uematsu, T. Doi, J. Tokuda, T. Fujita, T. Torimoto, and S. K. Long Term Optical Properties of ZnS-AgInS₂ and AgInS₂-AgGaS₂ Solid-Solution

- Semiconductor Nanoparticles Dispersed in Polymer Matrices. *Electrochemistry* **2011**, *67* (2), 117–125.
- (41) Huang, F.; Zhou, J.; Xu, J.; Wang, Y. Formation of AgGaS₂ Nano-Pyramids from Ag₂S Nanospheres through Intermediate Ag₂S-AgGaS₂ Heterostructures and AgGaS₂ Sensitized Mn²⁺ Emission. *Nanoscale* **2014**, *6* (4), 2340–2344. <https://doi.org/10.1039/c3nr04765b>.
- (42) Fan, C. M.; Regulacio, M. D.; Ye, C.; Lim, S. H.; Zheng, Y.; Xu, Q. H.; Xu, A. W.; Han, M. Y. Colloidal Synthesis and Photocatalytic Properties of Orthorhombic AgGaS₂ Nanocrystals. *Chem. Commun.* **2014**, *50* (54), 7128–7131. <https://doi.org/10.1039/c4cc01778a>.
- (43) Kim, J. H.; Kim, B. Y.; Jang, E. P.; Yoon, S. Y.; Kim, K. H.; Do, Y. R.; Yang, H. Synthesis of Widely Emission-Tunable Ag-Ga-S and Its Quaternary Derivative Quantum Dots. *Chem. Eng. J.* **2018**, *347* (April), 791–797. <https://doi.org/10.1016/j.cej.2018.04.167>.
- (44) Kameyama, T.; Kishi, M.; Miyamae, C.; Sharma, D. K.; Hirata, S.; Yamamoto, T.; Uematsu, T.; Vacha, M.; Kuwabata, S.; Torimoto, T. Wavelength-Tunable Band-Edge Photoluminescence of Nonstoichiometric Ag-In-S Nanoparticles via Ga³⁺ Doping. *ACS Appl. Mater. Interfaces* **2018**, *10* (49), 42844–42855. <https://doi.org/10.1021/acsami.8b15222>.
- (45) Uematsu, T.; Wajima, K.; Sharma, D. K.; Hirata, S.; Yamamoto, T.; Kameyama, T.; Vacha, M.; Torimoto, T.; Kuwabata, S. Narrow Band-Edge Photoluminescence from AgInS₂ Semiconductor Nanoparticles by the Formation of Amorphous III–VI Semiconductor Shells. *NPG Asia Mater.* **2018**, *10* (8), 713–726. <https://doi.org/10.1038/s41427-018-0067-9>.
- (46) Song, J.; Zhang, Y.; Dai, Y.; Hu, J.; Zhu, L.; Xu, X.; Yu, Y.; Li, H.; Yao, B.; Zhou, H. Polyelectrolyte-Mediated Nontoxic AgGa_xIn_{1-x}S₂ QDs/Low-Density Lipoprotein Nanoprobe for Selective 3D Fluorescence Imaging of Cancer Stem Cells. *ACS Appl. Mater. Interfaces* **2019**, *11* (10), 9884–9892. <https://doi.org/10.1021/acsami.9b00121>.
- (47) Hoisang, W.; Uematsu, T.; Yamamoto, T.; Torimoto, T.; Kuwabata, S. Core Nanoparticle Engineering for Narrower and More Intense Band-Edge Emission from AgInS₂/Ga_x Core/Shell Quantum Dots. *Nanomaterials* **2019**, *9* (12). <https://doi.org/10.3390/nano9121763>.

- (48) Deng, D.; Cao, J.; Qu, L.; Achilefu, S.; Gu, Y. Highly Luminescent Water-Soluble Quaternary Zn–Ag–In–S Quantum Dots for Tumor Cell-Targeted Imaging. *Phys. Chem. Chem. Phys.* **2013**, *15* (14), 5078. <https://doi.org/10.1039/c3cp00046j>.
- (49) Xiong, W.-W.; Yang, G.-H.; Wu, X.-C.; Zhu, J.-J. Microwave-Assisted Synthesis of Highly Luminescent AgInS₂/ZnS Nanocrystals for Dynamic Intracellular Cu(II) Detection. *J. Mater. Chem. B* **2013**, *1* (33), 4160. <https://doi.org/10.1039/c3tb20638f>.
- (50) Liu, Y.; Tang, X.; Deng, M.; Zhu, T.; Bai, Y.; Qu, D.; Huang, X.; Qiu, F. One-Step Aqueous Synthesis of Highly Luminescent Hydrophilic AgInZnS Quantum Dots. *J. Lumin.* **2018**, *202*, 71–76. <https://doi.org/10.1016/j.jlumin.2018.05.040>.
- (51) Regulacio, M. D.; Win, K. Y.; Lo, S. L.; Zhang, S.-Y.; Zhang, X.; Wang, S.; Han, M.-Y.; Zheng, Y. Aqueous Synthesis of Highly Luminescent AgInS₂–ZnS Quantum Dots and Their Biological Applications. *Nanoscale* **2013**, *5* (6), 2322. <https://doi.org/10.1039/c3nr34159c>.
- (52) Chen, Y.; Wang, Q.; Zha, T.; Min, J.; Gao, J.; Zhou, C.; Li, J.; Zhao, M.; Li, S. Green and Facile Synthesis of High-Quality Water-Soluble Ag-In-S/ZnS Core/Shell Quantum Dots with Obvious Bandgap and Sub-Bandgap Excitations. *J. Alloys Compd.* **2018**, *753*, 364–370. <https://doi.org/10.1016/j.jallcom.2018.04.242>.
- (53) Kurshanov, D. A.; Gromova, Yu. A.; Cherevko, S. A.; Ushakova, E. V.; Kormilina, T. K.; Dubavik, A.; Fedorov, A. V.; Baranov, A. V. Non-Toxic Ternary Quantum Dots AgInS₂ and AgInS₂/ZnS: Synthesis and Optical Properties. *Opt. Spectrosc.* **2018**, *125* (6), 1041–1046. <https://doi.org/10.1134/S0030400X1812010X>.
- (54) Pu, Y.; Cai, F.; Wang, D.; Wang, J.-X.; Chen, J.-F. Colloidal Synthesis of Semiconductor Quantum Dots toward Large-Scale Production: A Review. *Ind. Eng. Chem. Res.* **2018**, *57* (6), 1790–1802. <https://doi.org/10.1021/acs.iecr.7b04836>.
- (55) Chen, H.; Liu, X.-Y.; Wang, S.; Wang, X.; Wei, Q.; Jiang, X.; Wang, F.; Xu, K.; Ke, J.; Zhang, Q.; Gao, Q.; Ke, Y.; Long, Y.-T.; Ning, Z. Quaternary Two Dimensional Zn–Ag–In–S Nanosheets for Highly Efficient Photocatalytic Hydrogen Generation. *J. Mater. Chem. A* **2018**, *6* (25), 11670–11675. <https://doi.org/10.1039/C8TA03726D>.
- (56) Mansur, A. A. P.; Mansur, H. S.; Carvalho, S. M.; Caires, A. J. One-Pot Aqueous Synthesis of Fluorescent Ag-In-Zn-S Quantum Dot/Polymer Bioconjugates for Multiplex Optical Bioimaging of Glioblastoma Cells. *Contrast Media Mol. Imaging* **2017**, *2017*, 1–15. <https://doi.org/10.1155/2017/3896107>.

- (57) Kang, X.; Huang, L.; Yang, Y.; Pan, D. Scaling up the Aqueous Synthesis of Visible Light Emitting Multinary AgInS₂/ZnS Core/Shell Quantum Dots. *J. Phys. Chem. C* **2015**, *119* (14), 7933–7940. <https://doi.org/10.1021/acs.jpcc.5b00413>.
- (58) Lai, P.-Y.; Huang, C.-C.; Chou, T.-H.; Ou, K.-L.; Chang, J.-Y. Aqueous Synthesis of Ag and Mn Co-Doped In₂S₃/ZnS Quantum Dots with Tunable Emission for Dual-Modal Targeted Imaging. *Acta Biomater.* **2017**, *50*, 522–533. <https://doi.org/10.1016/j.actbio.2016.12.028>.
- (59) Singh, R. K.; Kumar, R.; Singh, D. P.; Savu, R.; Moshkalev, S. A. Progress in Microwave-Assisted Synthesis of Quantum Dots (Graphene/Carbon/Semiconducting) for Bioapplications: A Review. *Mater. Today Chem.* **2019**, *12*, 282–314. <https://doi.org/10.1016/j.mtchem.2019.03.001>.
- (60) Raevskaya, A.; Lesnyak, V.; Haubold, D.; Dzhagan, V.; Stroyuk, O.; Gaponik, N.; Zahn, D. R. T.; Eychmüller, A. A Fine Size Selection of Brightly Luminescent Water-Soluble Ag–In–S and Ag–In–S/ZnS Quantum Dots. *J. Phys. Chem. C* **2017**, *121* (16), 9032–9042. <https://doi.org/10.1021/acs.jpcc.7b00849>.
- (61) Mrad, M.; Ben Chaabane, T.; Rinnert, H.; Lavinia, B.; Jasniewski, J.; Medjahdi, G.; Schneider, R. Aqueous Synthesis for Highly Emissive 3-Mercaptopropionic Acid-Capped AIZS Quantum Dots. *Inorg. Chem.* **2020**, *59* (9), 6220–6231. <https://doi.org/10.1021/acs.inorgchem.0c00347>.
- (62) Dubois, F.; Mahler, B.; Dubertret, B.; Doris, E.; Mioskowski, C. A Versatile Strategy for Quantum Dot Ligand Exchange. *J. Am. Chem. Soc.* **2007**, *129* (3), 482–483. <https://doi.org/10.1021/ja067742y>.
- (63) Hong, R.; Fischer, N. O.; Verma, A.; Goodman, C. M.; Emrick, T.; Rotello, V. M. Control of Protein Structure and Function through Surface Recognition by Tailored Nanoparticle Scaffolds. *J. Am. Chem. Soc.* **2004**, *126* (3), 739–743. <https://doi.org/10.1021/ja037470o>.
- (64) Zylstra, J.; Amey, J.; Miska, N. J.; Pang, L.; Hine, C. R.; Langer, J.; Doyle, R. P.; Maye, M. M. A Modular Phase Transfer and Ligand Exchange Protocol for Quantum Dots. *Langmuir* **2011**, *27* (8), 4371–4379. <https://doi.org/10.1021/la104542n>.
- (65) Clapp, A. R.; Goldman, E. R.; Mattoussi, H. Capping of CdSe–ZnS Quantum Dots with DHLA and Subsequent Conjugation with Proteins. *Nat. Protoc.* **2006**, *1* (3), 1258–1266. <https://doi.org/10.1038/nprot.2006.184>.

- (66) Breus, V. V.; Heyes, C. D.; Nienhaus, G. U. Quenching of CdSe–ZnS Core–Shell Quantum Dot Luminescence by Water-Soluble Thiolated Ligands. *J. Phys. Chem. C* **2007**, *111* (50), 18589–18594. <https://doi.org/10.1021/jp075848p>.
- (67) Zhao, C.; Bai, Z.; Liu, X.; Zhang, Y.; Zou, B.; Zhong, H. Small GSH-Capped CuInS₂ Quantum Dots: MPA-Assisted Aqueous Phase Transfer and Bioimaging Applications. *ACS Appl. Mater. Interfaces* **2015**, *7* (32), 17623–17629. <https://doi.org/10.1021/acsami.5b05503>.
- (68) Tamang, S.; Beaune, G.; Texier, I.; Reiss, P. Aqueous Phase Transfer of InP/ZnS Nanocrystals Conserving Fluorescence and High Colloidal Stability. *ACS Nano* **2011**, *5* (12), 9392–9402. <https://doi.org/10.1021/nn203598c>.
- (69) Mao, B.; Chuang, C.-H.; McCleese, C.; Zhu, J.; Burda, C. Near-Infrared Emitting AgInS₂/ZnS Nanocrystals. *J. Phys. Chem. C* **2014**, *118* (25), 13883–13889. <https://doi.org/10.1021/jp500872w>.
- (70) Bujak, P.; Wróbel, Z.; Penkala, M.; Kotwica, K.; Kmita, A.; Gajewska, M.; Ostrowski, A.; Kowalik, P.; Pron, A. Highly Luminescent Ag–In–Zn–S Quaternary Nanocrystals: Growth Mechanism and Surface Chemistry Elucidation. *Inorg. Chem.* **2019**, *58* (2), 1358–1370. <https://doi.org/10.1021/acs.inorgchem.8b02916>.
- (71) Pong, B.-K.; Trout, B. L.; Lee, J.-Y. Modified Ligand-Exchange for Efficient Solubilization of CdSe/ZnS Quantum Dots in Water: A Procedure Guided by Computational Studies. *Langmuir* **2008**, *24* (10), 5270–5276. <https://doi.org/10.1021/la703431j>.
- (72) Kulkarni, S. A.; Feng, S.-S. Effects of Particle Size and Surface Modification on Cellular Uptake and Biodistribution of Polymeric Nanoparticles for Drug Delivery. *Pharm. Res.* **2013**, *30* (10), 2512–2522. <https://doi.org/10.1007/s11095-012-0958-3>.
- (73) Bilan, R.; Fleury, F.; Nabiev, I.; Sukhanova, A. Quantum Dot Surface Chemistry and Functionalization for Cell Targeting and Imaging. *Bioconjug. Chem.* **2015**, *26* (4), 609–624. <https://doi.org/10.1021/acs.bioconjchem.5b00069>.
- (74) Pellegrino, T.; Manna, L.; Kudera, S.; Liedl, T.; Koktysh, D.; Rogach, A. L.; Keller, S.; Rädler, J.; Natile, G.; Parak, W. J. Hydrophobic Nanocrystals Coated with an Amphiphilic Polymer Shell: A General Route to Water Soluble Nanocrystals. *Nano Lett.* **2004**, *4* (4), 703–707. <https://doi.org/10.1021/nl035172j>.
- (75) Michalska, M.; Florczak, A.; Dams-Kozłowska, H.; Gapinski, J.; Jurga, S.; Schneider, R. Peptide-Functionalized ZCIS QDs as Fluorescent Nanoprobe for Targeted HER2-

- Positive Breast Cancer Cells Imaging. *Acta Biomater.* **2016**, *35*, 293–304. <https://doi.org/10.1016/j.actbio.2016.02.002>.
- (76) Wang, T.; Sridhar, R.; Korotcov, A.; Ting, A. H.; Francis, K.; Mitchell, J.; Wang, P. C. Synthesis of Amphiphilic Triblock Copolymers as Multidentate Ligands for Biocompatible Coating of Quantum Dots. *Colloids Surf. Physicochem. Eng. Asp.* **2011**, *375* (1–3), 147–155. <https://doi.org/10.1016/j.colsurfa.2010.11.079>.
- (77) Hamanaka, Y.; Ozawa, K.; Kuzuya, T. Enhancement of Donor–Acceptor Pair Emissions in Colloidal AgInS₂ Quantum Dots with High Concentrations of Defects. *J. Phys. Chem. C* **2014**, *118* (26), 14562–14568. <https://doi.org/10.1021/jp501429f>.
- (78) Hamanaka, Y.; Ogawa, T.; Tsuzuki, M.; Kuzuya, T. Photoluminescence Properties and Its Origin of AgInS₂ Quantum Dots with Chalcopyrite Structure. *J. Phys. Chem. C* **2011**, *115* (5), 1786–1792. <https://doi.org/10.1021/jp110409q>.
- (79) Rao, M. J.; Shibata, T.; Chattopadhyay, S.; Nag, A. Origin of Photoluminescence and XAFS Study of (ZnS)_{1-x}(AgInS₂)_x Nanocrystals. *J. Phys. Chem. Lett.* **2014**, *5* (1), 167–173. <https://doi.org/10.1021/jz402443y>.
- (80) Jeong, S.; Yoon, H. C.; Han, N. S.; Oh, J. H.; Park, S. M.; Min, B. K.; Do, Y. R.; Song, J. K. Band-Gap States of AgIn₅S₈ and ZnS–AgIn₅S₈ Nanoparticles. *J. Phys. Chem. C* **2017**, *121* (5), 3149–3155. <https://doi.org/10.1021/acs.jpcc.7b00043>.
- (81) Stroyuk, O.; Raevskaya, A.; Spranger, F.; Selyshchev, O.; Dzhagan, V.; Schulze, S.; Zahn, D. R. T.; Eychmüller, A. Origin and Dynamics of Highly Efficient Broadband Photoluminescence of Aqueous Glutathione-Capped Size-Selected Ag–In–S Quantum Dots. *J. Phys. Chem. C* **2018**, *122* (25), 13648–13658. <https://doi.org/10.1021/acs.jpcc.8b00106>.
- (82) Tang, X.; Zu, Z.; Bian, L.; Du, J.; Chen, W.; Zeng, X.; Wen, M.; Zang, Z.; Xue, J. Synthesis of Mn Doping Ag–In–Zn–S Nanoparticles and Their Photoluminescence Properties. *Mater. Des.* **2016**, *91*, 256–261. <https://doi.org/10.1016/j.matdes.2015.11.080>.
- (83) Ding, K.; Jing, L.; Liu, C.; Hou, Y.; Gao, M. Magnetically Engineered Cd-Free Quantum Dots as Dual-Modality Probes for Fluorescence/Magnetic Resonance Imaging of Tumors. *Biomaterials* **2014**, *35* (5), 1608–1617. <https://doi.org/10.1016/j.biomaterials.2013.10.078>.
- (84) Huang, B.; Dai, Q.; Zhuo, N.; Jiang, Q.; Shi, F.; Wang, H.; Zhang, H.; Liao, C.; Cui, Y.; Zhang, J. Bicolor Mn-Doped CuInS₂/ZnS Core/Shell Nanocrystals for White

- Light-Emitting Diode with High Color Rendering Index. *J. Appl. Phys.* **2014**, *116* (9), 094303. <https://doi.org/10.1063/1.4894246>.
- (85) Zhou, P.; Zhang, X.; Li, L.; Liu, X.; Yuan, L.; Zhang, X. Temperature-Dependent Photoluminescence Properties of Mn:ZnCuInS Nanocrystals. *Opt. Mater. Express* **2015**, *5* (9), 2069. <https://doi.org/10.1364/OME.5.002069>.
- (86) Pradhan, N. Red-Tuned Mn d-d Emission in Doped Semiconductor Nanocrystals. *ChemPhysChem* **2016**, *17* (8), 1087–1094. <https://doi.org/10.1002/cphc.201500953>.
- (87) Gabka, G.; Bujak, P.; Giedyk, K.; Ostrowski, A.; Malinowska, K.; Herbich, J.; Golec, B.; Wielgus, I.; Pron, A. A Simple Route to Alloyed Quaternary Nanocrystals Ag–In–Zn–S with Shape and Size Control. *Inorg. Chem.* **2014**, *53* (10), 5002–5012. <https://doi.org/10.1021/ic500046m>.
- (88) Jeong, S.; Yoon, S.; Chun, S. Y.; Yoon, H. C.; Han, N. S.; Oh, J. H.; Park, S. M.; Do, Y. R.; Song, J. K. Enhancement Mechanism of the Photoluminescence Quantum Yield in Highly Efficient ZnS–AgIn₅S₈ Quantum Dots with Core/Shell Structures. *J. Phys. Chem. C* **2018**, *122* (18), 10125–10132. <https://doi.org/10.1021/acs.jpcc.8b01774>.
- (89) Dai, M.; Ogawa, S.; Kameyama, T.; Okazaki, K.; Kudo, A.; Kuwabata, S.; Tsuboi, Y.; Torimoto, T. Tunable Photoluminescence from the Visible to Near-Infrared Wavelength Region of Non-Stoichiometric AgInS₂ Nanoparticles. *J. Mater. Chem.* **2012**, *22* (25), 12851. <https://doi.org/10.1039/c2jm31463k>.
- (90) Hamanaka, Y.; Yukioki, D.; Kuzuya, T. Structural Transformation and Photoluminescence Modification of AgInS₂ Nanoparticles Induced by ZnS Shell Formation. *Appl. Phys. Express* **2015**, *8* (9), 095001. <https://doi.org/10.7567/APEX.8.095001>.
- (91) Deng, D.; Qu, L.; Cheng, Z.; Achilefu, S.; Gu, Y. Highly Luminescent Water-Soluble Quaternary Zn–Ag–In–S Quantum Dots and Their Unique Precursor S/In Ratio-Dependent Spectral Shifts. *J. Lumin.* **2014**, *146*, 364–370. <https://doi.org/10.1016/j.jlumin.2013.09.063>.
- (92) Chang, J.-Y.; Wang, G.-Q.; Cheng, C.-Y.; Lin, W.-X.; Hsu, J.-C. Strategies for Photoluminescence Enhancement of AgInS₂ Quantum Dots and Their Application as Bioimaging Probes. *J. Mater. Chem.* **2012**, *22* (21), 10609. <https://doi.org/10.1039/c2jm30679d>.
- (93) Zeng, B.; Chen, F.; Liu, Z.; Guan, Z.; Li, X.; Teng, F.; Tang, A. Seeded-Mediated Growth of Ternary Ag–In–S and Quaternary Ag–In–Zn–S Nanocrystals from Binary

- Ag₂S Seeds and the Composition-Tunable Optical Properties. *J. Mater. Chem. C* **2019**, 7 (5), 1307–1315. <https://doi.org/10.1039/C8TC05755A>.
- (94) Martynenko, I. V.; Baimuratov, A. S.; Weigert, F.; Soares, J. X.; Dharmo, L.; Nickl, P.; Doerfel, I.; Pauli, J.; Rukhlenko, I. D.; Baranov, A. V.; Resch-Genger, U. Photoluminescence of Ag-In-S/ZnS Quantum Dots: Excitation Energy Dependence and Low-Energy Electronic Structure. *Nano Res.* **2019**, 12 (7), 1595–1603. <https://doi.org/10.1007/s12274-019-2398-4>.
- (95) Tang, X.; Ho, W. B. A.; Xue, J. M. Synthesis of Zn-Doped AgInS₂ Nanocrystals and Their Fluorescence Properties. *J. Phys. Chem. C* **2012**, 116 (17), 9769–9773. <https://doi.org/10.1021/jp207711p>.
- (96) Colombo, M.; Carregal-Romero, S.; Casula, M. F.; Gutiérrez, L.; Morales, M. P.; Böhm, I. B.; Heverhagen, J. T.; Prospero, D.; Parak, Wolfgang. J. Biological Applications of Magnetic Nanoparticles. *Chem. Soc. Rev.* **2012**, 41 (11), 4306. <https://doi.org/10.1039/c2cs15337h>.
- (97) Si, P. Z.; Brück, E.; Zhang, Z. D.; Tegus, O.; Zhang, W. S.; Buschow, K. H. J.; Klaasse, J. C. P. Structural and Magnetic Properties of Mn Nanoparticles Prepared by Arc-Discharge. *Mater. Res. Bull.* **2005**, 40 (1), 29–37. <https://doi.org/10.1016/j.materresbull.2004.09.010>.
- (98) Agrahari, V.; Tripathi, A. K.; Mathpal, M. C.; Pandey, A. C.; Mishra, S. K.; Shukla, R. K.; Agarwal, A. Effect of Mn Doping on Structural, Optical and Magnetic Properties of SnO₂ Nanoparticles. *J. Mater. Sci. Mater. Electron.* **2015**, 26 (12), 9571–9582. <https://doi.org/10.1007/s10854-015-3620-0>.
- (99) Amaranatha Reddy, D.; Sambasivam, S.; Murali, G.; Poornaprakash, B.; Vijayalakshmi, R. P.; Aparna, Y.; Reddy, B. K.; Rao, J. L. Effect of Mn Co-Doping on the Structural, Optical and Magnetic Properties of ZnS:Cr Nanoparticles. *J. Alloys Compd.* **2012**, 537, 208–215. <https://doi.org/10.1016/j.jallcom.2012.04.115>.
- (100) Sharma, A. D.; Sharma, H. B. Electrical and Magnetic Properties of Mn-Doped BiFeO₃ Nanomaterials. *Integr. Ferroelectr.* **2019**, 203 (1), 81–90. <https://doi.org/10.1080/10584587.2019.1674969>.
- (101) Zaeimian, M. S.; Gallian, B.; Harrison, C.; Wang, Y.; Zhao, J.; Zhu, X. Mn Doped AZIS/ZnS Nanocrystals (NCs): Effects of Ag and Mn Levels on NC Optical Properties. *J. Alloys Compd.* **2018**, 765, 236–244. <https://doi.org/10.1016/j.jallcom.2018.06.173>.

- (102) Resch-Genger, U.; Grabolle, M.; Cavaliere-Jaricot, S.; Nitschke, R.; Nann, T. Quantum Dots versus Organic Dyes as Fluorescent Labels. *Nat. Methods* **2008**, *5* (9), 763–775. <https://doi.org/10.1038/nmeth.1248>.
- (103) Ruan, C.; Zhang, Y.; Lu, M.; Ji, C.; Sun, C.; Chen, X.; Chen, H.; Colvin, V.; Yu, W. White Light-Emitting Diodes Based on AgInS₂/ZnS Quantum Dots with Improved Bandwidth in Visible Light Communication. *Nanomaterials* **2016**, *6* (1), 13. <https://doi.org/10.3390/nano6010013>.
- (104) Kim, E.; Ruankham, P.; Lee, J.; Hachiya, K.; Sagawa, T. Ag–In–Zn–S Quantum Dots for Hybrid Organic–Inorganic Solar Cells. *Jpn. J. Appl. Phys.* **2016**, *55* (2S), 02BF06. <https://doi.org/10.7567/JJAP.55.02BF06>.
- (105) Chen, T.; Hu, X.; Xu, Y.; Wang, L.; Jiang, W.; Jiang, W.; Xie, Z. Hydrothermal Synthesis of Highly Fluorescent Ag–In–S/ZnS Core/Shell Quantum Dots for White Light-Emitting Diodes. *J. Alloys Compd.* **2019**, *804*, 119–127. <https://doi.org/10.1016/j.jallcom.2019.06.134>.
- (106) Chung, W.; Jung, H.; Lee, C. H.; Kim, S. H. Extremely High Color Rendering White Light from Surface Passivated Carbon Dots and Zn-Doped AgInS₂ Nanocrystals. *J Mater Chem C* **2014**, *2* (21), 4227–4232. <https://doi.org/10.1039/C3TC32559H>.
- (107) Zhu, B.; Ji, W.; Duan, Z.; Sheng, Y.; Wang, T.; Yuan, Q.; Zhang, H.; Tang, X.; Zhang, H. Low Turn-on Voltage and Highly Bright Ag–In–Zn–S Quantum Dot Light-Emitting Diodes. *J. Mater. Chem. C* **2018**, *6* (17), 4683–4690. <https://doi.org/10.1039/C8TC01022F>.
- (108) Cheng, K.-C.; Law, W.-C.; Yong, K.-T.; Nevins, J. S.; Watson, D. F.; Ho, H.-P.; Prasad, P. N. Synthesis of Near-Infrared Silver-Indium-Sulfide (AgInS₂) Quantum Dots as Heavy-Metal Free Photosensitizer for Solar Cell Applications. *Chem. Phys. Lett.* **2011**, *515* (4–6), 254–257. <https://doi.org/10.1016/j.cplett.2011.09.027>.
- (109) Choi, D. B.; Kim, S.; Yoon, H. C.; Ko, M.; Yang, H.; Do, Y. R. Color-Tunable Ag-In-Zn-S Quantum-Dot Light-Emitting Devices Realizing Green, Yellow and Amber Emissions. *J. Mater. Chem. C* **2017**, *5* (4), 953–959. <https://doi.org/10.1039/C6TC04798J>.
- (110) Li, S.; Chen, Y.; Huang, L.; Pan, D. Simple Continuous-Flow Synthesis of Cu–In–Zn–S/ZnS and Ag–In–Zn–S/ZnS Core/Shell Quantum Dots. *Nanotechnology* **2013**, *24* (39), 395705. <https://doi.org/10.1088/0957-4484/24/39/395705>.

- (111) Yu, R.; Yin, F.; Pu, C.; Song, H.; Xu, X.; Zhang, H.; Ji, W. Highly Efficient Ag–In–Zn–S Quantum Dot Light-Emitting Diodes with a Hole-Spacing Interlayer. *Org. Electron.* **2020**, *84*, 105809. <https://doi.org/10.1016/j.orgel.2020.105809>.
- (112) Guan, H.; Zhao, S.; Wang, H.; Yan, D.; Wang, M.; Zang, Z. Room Temperature Synthesis of Stable Single Silica-Coated CsPbBr₃ Quantum Dots Combining Tunable Red Emission of Ag–In–Zn–S for High-CRI White Light-Emitting Diodes. *Nano Energy* **2020**, *67*, 104279. <https://doi.org/10.1016/j.nanoen.2019.104279>.
- (113) Kameyama, T.; Koyama, S.; Yamamoto, T.; Kuwabata, S.; Torimoto, T. Enhanced Photocatalytic Activity of Zn–Ag–In–S Semiconductor Nanocrystals with a Dumbbell-Shaped Heterostructure. *J. Phys. Chem. C* **2018**, *122* (25), 13705–13715. <https://doi.org/10.1021/acs.jpcc.8b00255>.
- (114) Yang, Y.; Liu, Y.; Mao, B.; Luo, B.; Zhang, K.; Wei, W.; Kang, Z.; Shi, W.; Yuan, S. Facile Surface Engineering of Ag–In–Zn–S Quantum Dot Photocatalysts by Mixed-Ligand Passivation with Improved Charge Carrier Lifetime. *Catal. Lett.* **2019**, *149* (7), 1800–1812. <https://doi.org/10.1007/s10562-019-02718-6>.
- (115) Liu, Y.; Zhu, T.; Deng, M.; Tang, X.; Han, S.; Liu, A.; Bai, Y.; Qu, D.; Huang, X.; Qiu, F. Selective and Sensitive Detection of Copper(II) Based on Fluorescent Zinc-Doped AgInS₂ Quantum Dots. *J. Lumin.* **2018**, *201*, 182–188. <https://doi.org/10.1016/j.jlumin.2018.04.046>.
- (116) Liu, Y.; Tang, X.; Huang, W.; Yin, G.; Deng, M.; Cao, Y.; Shi, L.; Zhu, T.; Huang, L.; Ikechukwu, I. P.; Gong, Y.; Bai, Y.; Qu, D.; Huang, X.; Qiu, F. A Fluorometric Optical Fiber Nanoprobe for Copper(II) by Using AgInZnS Quantum Dots. *Microchim. Acta* **2020**, *187* (2), 146. <https://doi.org/10.1007/s00604-020-4110-5>.
- (117) Matsuda, Y.; Torimoto, T.; Kameya, T.; Kameyama, T.; Kuwabata, S.; Yamaguchi, H.; Niimi, T. ZnS–AgInS₂ Nanoparticles as a Temperature Sensor. *Sens. Actuators B Chem.* **2013**, *176*, 505–508. <https://doi.org/10.1016/j.snb.2012.09.005>.
- (118) Hardman, R. A Toxicologic Review of Quantum Dots: Toxicity Depends on Physicochemical and Environmental Factors. *Environ. Health Perspect.* **2006**, *114* (2), 165–172. <https://doi.org/10.1289/ehp.8284>.
- (119) Istomina, M. S.; Pechnikova, N. A.; Korolev, D. V.; Pochkayeva, E. I.; Mazing, D. S.; Galagudza, M. M.; Moshnikov, V. A.; Shlyakhto, E. V. ZAIS-Based Colloidal QDs as Fluorescent Labels for Theranostics: Physical Properties, Biodistribution and

- Biocompatibility. *Bull. Russ. State Med. Univ.* **2019**, No. 6, 94–101. <https://doi.org/10.24075/brsmu.2018.073>.
- (120) Chen, S.; Ahmadiantehrani, M.; Publicover, N. G.; Hunter, K. W.; Zhu, X. Thermal Decomposition Based Synthesis of Ag-In-S/ZnS Quantum Dots and Their Chlorotoxin-Modified Micelles for Brain Tumor Cell Targeting. *RSC Adv.* **2015**, 5 (74), 60612–60620. <https://doi.org/10.1039/C5RA11250H>.
- (121) Liu, S.; Su, X. The Synthesis and Application of I–III–VI Type Quantum Dots. *RSC Adv* **2014**, 4 (82), 43415–43428. <https://doi.org/10.1039/C4RA05677A>.
- (122) Xu, G.; Zeng, S.; Zhang, B.; Swihart, M. T.; Yong, K.-T.; Prasad, P. N. New Generation Cadmium-Free Quantum Dots for Biophotonics and Nanomedicine. *Chem. Rev.* **2016**, 116 (19), 12234–12327. <https://doi.org/10.1021/acs.chemrev.6b00290>.
- (123) Abdullah, H.; Kuo, D.-H. Facile Synthesis of N-Type $(\text{AgIn})_x \text{Zn}_{2(1-x)} \text{S}_2$ /p-Type $\text{Ag}_2 \text{S}$ Nanocomposite for Visible Light Photocatalytic Reduction To Detoxify Hexavalent Chromium. *ACS Appl. Mater. Interfaces* **2015**, 7 (48), 26941–26951. <https://doi.org/10.1021/acsami.5b09647>.
- (124) Boonsin, R.; Barros, A.; Donat, F.; Boyer, D.; Chadeyron, G.; Schneider, R.; Boutinaud, P.; Mahiou, R. Optical Properties and Reliability Studies of Gradient Alloyed Green Emitting $(\text{CdSe})_x (\text{ZnS})_{1-x}$ and Red Emitting $(\text{CuInS}_2)_x (\text{ZnS})_{1-x}$ Quantum Dots for White Light-Emitting Diodes. *ACS Photonics* **2018**, 5 (2), 462–470. <https://doi.org/10.1021/acsphotonics.7b00980>.
- (125) Jagadeeswararao, M.; Swarnkar, A.; Markad, G. B.; Nag, A. Defect-Mediated Electron–Hole Separation in Colloidal $\text{Ag}_2 \text{S}$ – AgInS_2 Hetero Dimer Nanocrystals Tailoring Luminescence and Solar Cell Properties. *J. Phys. Chem. C* **2016**, 120 (34), 19461–19469. <https://doi.org/10.1021/acs.jpcc.6b06394>.
- (126) Song, J.; Ma, C.; Zhang, W.; Yang, S.; Wang, S.; Lv, L.; Zhu, L.; Xia, R.; Xu, X. Tumor Cell-Targeted $\text{Zn}_3 \text{In}_2 \text{S}_6$ and Ag–Zn–In–S Quantum Dots for Color Adjustable Luminophores. *J. Mater. Chem. B* **2016**, 4 (48), 7909–7918. <https://doi.org/10.1039/C6TB02297A>.
- (127) Shinchi, H.; Wakao, M.; Nagata, N.; Sakamoto, M.; Mochizuki, E.; Uematsu, T.; Kuwabata, S.; Suda, Y. Cadmium-Free Sugar-Chain-Immobilized Fluorescent Nanoparticles Containing Low-Toxicity ZnS – AgInS_2 Cores for Probing Lectin and Cells. *Bioconjug. Chem.* **2014**, 25 (2), 286–295. <https://doi.org/10.1021/bc400425w>.

- (128) Wang, L.; Kang, X.; Pan, D. Gram-Scale Synthesis of Hydrophilic PEI-Coated AgInS₂ Quantum Dots and Its Application in Hydrogen Peroxide/Glucose Detection and Cell Imaging. *Inorg. Chem.* **2017**, *56* (11), 6122–6130. <https://doi.org/10.1021/acs.inorgchem.7b00053>.
- (129) Hattori, K.; Akamatsu, K.; Kamegashira, N. Electrical Properties of Polycrystalline Chalcopyrite AgInS₂ Films. *J. Appl. Phys.* **1992**, *71* (7), 3414–3418. <https://doi.org/10.1063/1.350938>.
- (130) You, S. H.; Hong, K. J.; Youn, C. J.; Jeong, T. S.; Moon, J. D.; Kim, H. S.; Park, J. S. Origin of Point Defects in AgInS₂/GaAs Epilayer Obtained from Photoluminescence Measurement. *J. Appl. Phys.* **2001**, *90* (8), 3894–3898. <https://doi.org/10.1063/1.1405132>.
- (131) Takahashi, T.; Kudo, A.; Kuwabata, S.; Ishikawa, A.; Ishihara, H.; Tsuboi, Y.; Torimoto, T. Plasmon-Enhanced Photoluminescence and Photocatalytic Activities of Visible-Light-Responsive ZnS-AgInS₂ Solid Solution Nanoparticles. *J. Phys. Chem. C* **2013**, *117* (6), 2511–2520. <https://doi.org/10.1021/jp3064257>.
- (132) Aboulaich, A.; Geszke, M.; Balan, L.; Ghanbaja, J.; Medjahdi, G.; Schneider, R. Water-Based Route to Colloidal Mn-Doped ZnSe and Core/Shell ZnSe/ZnS Quantum Dots. *Inorg. Chem.* **2010**, *49* (23), 10940–10948. <https://doi.org/10.1021/ic101302q>.
- (133) Zhou, R.; Sun, S.; Li, C.; Wu, L.; Hou, X.; Wu, P. Enriching Mn-Doped ZnSe Quantum Dots onto Mesoporous Silica Nanoparticles for Enhanced Fluorescence/Magnetic Resonance Imaging Dual-Modal Bio-Imaging. *ACS Appl. Mater. Interfaces* **2018**, *10* (40), 34060–34067. <https://doi.org/10.1021/acsami.8b14554>.
- (134) Aldeek, F.; Balan, L.; Medjahdi, G.; Roques-Carmes, T.; Malval, J.-P.; Mustin, C.; Ghanbaja, J.; Schneider, R. Enhanced Optical Properties of Core/Shell/Shell CdTe/CdS/ZnO Quantum Dots Prepared in Aqueous Solution. *J. Phys. Chem. C* **2009**, *113* (45), 19458–19467. <https://doi.org/10.1021/jp905695f>.
- (135) Albert manoharan, A.; Chandramohan, R.; David prabu, R.; Valanarasu, S.; Ganesh, V.; Shkir, M.; Kathalingam, A.; AlFaify, S. Facile Synthesis and Characterization of Undoped, Mn Doped and Nd Co-Doped CuO Nanoparticles for Optoelectronic and Magnetic Applications. *J. Mol. Struct.* **2018**, *1171*, 388–395. <https://doi.org/10.1016/j.molstruc.2018.06.018>.

- (136) Ravi, S.; Winfred Shashikanth, F. Ferromagnetism in Mn Doped Copper Oxide Nanoflake like Structures with High Neel Temperature. *Mater. Lett.* **2015**, *141*, 132–134. <https://doi.org/10.1016/j.matlet.2014.11.089>.
- (137) Zhu, S.; Chen, C.; Li, Z. Magnetic Enhancement and Magnetic Signal Tunability of (Mn, Co) Co-Doped SnO₂ Dilute Magnetic Semiconductor Nanoparticles. *J. Magn. Magn. Mater.* **2019**, *471*, 370–380. <https://doi.org/10.1016/j.jmmm.2018.09.106>.
- (138) Sharma, N.; Gaur, A.; Kotnala, R. K. Signature of Weak Ferroelectricity and Ferromagnetism in Mn Doped CuO Nanostructures. *J. Magn. Magn. Mater.* **2015**, *377*, 183–189. <https://doi.org/10.1016/j.jmmm.2014.10.055>.
- (139) Amighian, J.; Karimzadeh, E.; Mozaffari, M. The Effect of Mn²⁺ Substitution on Magnetic Properties of Mn_xFe_{3-x}O₄ Nanoparticles Prepared by Coprecipitation Method. *J. Magn. Magn. Mater.* **2013**, *332*, 157–162. <https://doi.org/10.1016/j.jmmm.2012.12.005>.
- (140) Booth, M.; Peel, R.; Partanen, R.; Hondow, N.; Vasilca, V.; Jeuken, L. J. C.; Critchley, K. Amphipol-Encapsulated CuInS₂/ZnS Quantum Dots with Excellent Colloidal Stability. *RSC Adv.* **2013**, *3* (43), 20559. <https://doi.org/10.1039/c3ra43846e>.
- (141) Han, C.-Y.; Yang, H. Development of Colloidal Quantum Dots for Electrically Driven Light-Emitting Devices. *J. Korean Ceram. Soc.* **2017**, *54* (6), 449–469. <https://doi.org/10.4191/kcers.2017.54.6.03>.
- (142) Yang, Z.; Gao, M.; Wu, W.; Yang, X.; Sun, X. W.; Zhang, J.; Wang, H.-C.; Liu, R.-S.; Han, C.-Y.; Yang, H.; Li, W. Recent Advances in Quantum Dot-Based Light-Emitting Devices: Challenges and Possible Solutions. *Mater. Today* **2019**, *24*, 69–93. <https://doi.org/10.1016/j.mattod.2018.09.002>.
- (143) Feng, J.; Yang, X.; Li, R.; Yang, X.; Feng, G. The Composition-Dependent Photoluminescence Properties of Non-Stoichiometric Zn_xAgyInS_{1.5+x+0.5y} Nanocrystals. *Micromachines* **2019**, *10* (7), 439. <https://doi.org/10.3390/mi10070439>.
- (144) Wei, J.; Li, F.; Chang, C.; Zhang, Q. Synthesis of Emission Tunable AgInS₂/ZnS Quantum Dots and Application for Light Emitting Diodes. *J. Phys. Commun.* **2020**, *4* (4), 045016. <https://doi.org/10.1088/2399-6528/ab885a>.
- (145) Sharma, V. K.; Gokyar, S.; Kelestemur, Y.; Erdem, T.; Unal, E.; Demir, H. V. Manganese Doped Fluorescent Paramagnetic Nanocrystals for Dual-Modal Imaging. *Small* **2014**, *10* (23), 4961–4966. <https://doi.org/10.1002/sml.201401143>.

- (146) Ji, Z.; Ai, P.; Shao, C.; Wang, T.; Yan, C.; Ye, L.; Gu, W. Manganese-Doped Carbon Dots for Magnetic Resonance/Optical Dual-Modal Imaging of Tiny Brain Glioma. *ACS Biomater. Sci. Eng.* **2018**, *4* (6), 2089–2094. <https://doi.org/10.1021/acsbiomaterials.7b01008>.
- (147) Pellico, J.; Ellis, C. M.; Davis, J. J. Nanoparticle-Based Paramagnetic Contrast Agents for Magnetic Resonance Imaging. *Contrast Media Mol. Imaging* **2019**, *2019*, 1–13. <https://doi.org/10.1155/2019/1845637>.
- (148) Wang, J.; Liu, J. PEI–Folic Acid Modified Carbon Nanodots for Cancer Cell-Targeted Delivery and Two-Photon Excitation Imaging. *RSC Adv.* **2016**, *6* (24), 19662–19668. <https://doi.org/10.1039/C5RA27249A>.
- (149) Hu, X.; Chen, T.; Xu, Y.; Wang, M.; Jiang, W.; Jiang, W. Hydrothermal Synthesis of Bright and Stable AgInS₂ Quantum Dots with Tunable Visible Emission. *J. Lumin.* **2018**, *200*, 189–195. <https://doi.org/10.1016/j.jlumin.2018.04.025>.
- (150) Wang, X.; Liang, Z.; Xu, X.; Wang, N.; Fang, J.; Wang, J.; Xu, G. A High Efficient Photoluminescence Zn–Cu–In–S/ZnS Quantum Dots with Long Lifetime. *J. Alloys Compd.* **2015**, *640*, 134–140. <https://doi.org/10.1016/j.jallcom.2015.03.249>.
- (151) Nithyaa, N.; Jaya, N. V. Structural, Optical, and Magnetic Properties of Gd-Doped TiO₂ Nanoparticles. *J. Supercond. Nov. Magn.* **2018**, *31* (12), 4117–4126. <https://doi.org/10.1007/s10948-018-4693-9>.
- (152) Zhuo, S.; Guan, Y.; Li, H.; Fang, J.; Zhang, P.; Du, J.; Zhu, C. Facile Fabrication of Fluorescent Fe-Doped Carbon Quantum Dots for Dopamine Sensing and Bioimaging Application. *The Analyst* **2019**, *144* (2), 656–662. <https://doi.org/10.1039/C8AN01741G>.
- (153) Sakamoto, S.; Fujimori, A. Chemical Trend in the Electronic Structure of Fe-Doped III–V Semiconductors and Possible Origin of Ferromagnetism: A First-Principles Study. *J. Appl. Phys.* **2019**, *126* (17), 173910. <https://doi.org/10.1063/1.5124704>.
- (154) Obeid, M. M.; Jappor, H. R.; Al-Marzoki, K.; Al-Hydary, I. A.; Edrees, S. J.; Shukur, M. M. Unraveling the Effect of Gd Doping on the Structural, Optical, and Magnetic Properties of ZnO Based Diluted Magnetic Semiconductor Nanorods. *RSC Adv.* **2019**, *9* (57), 33207–33221. <https://doi.org/10.1039/C9RA04750F>.
- (155) Chen, Z.; Li, Z.; Lin, Y.; Yin, M.; Ren, J.; Qu, X. Bioresponsive Hyaluronic Acid-Capped Mesoporous Silica Nanoparticles for Targeted Drug Delivery. *Chem. - Eur. J.* **2013**, *19* (5), 1778–1783. <https://doi.org/10.1002/chem.201202038>.

- (156) Arpicco, S.; Milla, P.; Stella, B.; Dosio, F. Hyaluronic Acid Conjugates as Vectors for the Active Targeting of Drugs, Genes and Nanocomposites in Cancer Treatment. *Molecules* **2014**, *19* (3), 3193–3230. <https://doi.org/10.3390/molecules19033193>.
- (157) Yang, Y.; Jing, L.; Li, X.; Lin, L.; Yue, X.; Dai, Z. Hyaluronic Acid Conjugated Magnetic Prussian Blue@Quantum Dot Nanoparticles for Cancer Theranostics. *Theranostics* **2017**, *7* (2), 466–481. <https://doi.org/10.7150/thno.17411>.
- (158) Wang, X.; Niu, D.; Hu, C.; Li, P. Polyethyleneimine-Based Nanocarriers for Gene Delivery. *Curr. Pharm. Des.* **2015**, *21* (42), 6140–6156(17).
- (159) Hunter, A. Molecular Hurdles in Polyfectin Design and Mechanistic Background to Polycation Induced Cytotoxicity☆. *Adv. Drug Deliv. Rev.* **2006**, *58* (14), 1523–1531. <https://doi.org/10.1016/j.addr.2006.09.008>.
- (160) Aravindan, L.; Bicknell, K. A.; Brooks, G.; Khutoryanskiy, V. V.; Williams, A. C. Effect of Acyl Chain Length on Transfection Efficiency and Toxicity of Polyethylenimine. *Int. J. Pharm.* **2009**, *378* (1–2), 201–210. <https://doi.org/10.1016/j.ijpharm.2009.05.052>.
- (161) Wen, S.; Zheng, F.; Shen, M.; Shi, X. Surface Modification and PEGylation of Branched Polyethyleneimine for Improved Biocompatibility. *J. Appl. Polym. Sci.* **2013**, *128* (6), 3807–3813. <https://doi.org/10.1002/app.38444>.
- (162) Morosini, V.; Bastogne, T.; Frochot, C.; Schneider, R.; François, A.; Guillemin, F.; Barberi-Heyob, M. Quantum Dot–Folic Acid Conjugates as Potential Photosensitizers in Photodynamic Therapy of Cancer. *Photochem. Photobiol. Sci.* **2011**, *10* (5), 842. <https://doi.org/10.1039/c0pp00380h>.
- (163) Zwicke, G. L.; Ali Mansoori, G.; Jeffery, C. J. Utilizing the Folate Receptor for Active Targeting of Cancer Nanotherapeutics. *Nano Rev.* **2012**, *3* (1), 18496. <https://doi.org/10.3402/nano.v3i0.18496>.
- (164) Fernández, M.; Javaid, F.; Chudasama, V. Advances in Targeting the Folate Receptor in the Treatment/Imaging of Cancers. *Chem. Sci.* **2018**, *9* (4), 790–810. <https://doi.org/10.1039/C7SC04004K>.
- (165) Frigerio, B.; Bizzoni, C.; Jansen, G.; Leamon, C. P.; Peters, G. J.; Low, P. S.; Matherly, L. H.; Figini, M. Folate Receptors and Transporters: Biological Role and Diagnostic/Therapeutic Targets in Cancer and Other Diseases. *J. Exp. Clin. Cancer Res.* **2019**, *38* (1), 125. <https://doi.org/10.1186/s13046-019-1123-1>.

- (166) Costantino, L.; Tosi, G.; Ruozi, B.; Bondioli, L.; Vandelli, M. A.; Forni, F. Colloidal Systems for CNS Drug Delivery. In *Progress in Brain Research*; Elsevier, 2009; Vol. 180, pp 35–69. [https://doi.org/10.1016/S0079-6123\(08\)80003-9](https://doi.org/10.1016/S0079-6123(08)80003-9).
- (167) Rengasamy, G.; Venkataraman, A.; Veeraraghavan, V. P.; Jainu, M. Cytotoxic and Apoptotic Potential of *Myristica Fragrans* Houtt. (Mace) Extract on Human Oral Epidermal Carcinoma KB Cell Lines. *Braz. J. Pharm. Sci.* **2018**, *54* (3). <https://doi.org/10.1590/s2175-97902018000318028>.
- (168) Bai, X.; Purcell-Milton, F.; Gun'ko, Y. Optical Properties, Synthesis, and Potential Applications of Cu-Based Ternary or Quaternary Anisotropic Quantum Dots, Polytypic Nanocrystals, and Core/Shell Heterostructures. *Nanomaterials* **2019**, *9* (1), 85. <https://doi.org/10.3390/nano9010085>.
- (169) Chen, B.; Pradhan, N.; Zhong, H. From Large-Scale Synthesis to Lighting Device Applications of Ternary I–III–VI Semiconductor Nanocrystals: Inspiring Greener Material Emitters. *J. Phys. Chem. Lett.* **2018**, *9* (2), 435–445. <https://doi.org/10.1021/acs.jpcclett.7b03037>.
- (170) Regulacio, M. D.; Han, M.-Y. Multinary I–III–VI₂ and I₂–II–IV–VI₄ Semiconductor Nanostructures for Photocatalytic Applications. *Acc. Chem. Res.* **2016**, *49* (3), 511–519. <https://doi.org/10.1021/acs.accounts.5b00535>.
- (171) Kolny-Olesiak, J.; Weller, H. Synthesis and Application of Colloidal CuInS₂ Semiconductor Nanocrystals. *ACS Appl. Mater. Interfaces* **2013**, *5* (23), 12221–12237. <https://doi.org/10.1021/am404084d>.
- (172) Leach, A. D. P.; Macdonald, J. E. Optoelectronic Properties of CuInS₂ Nanocrystals and Their Origin. *J. Phys. Chem. Lett.* **2016**, *7* (3), 572–583. <https://doi.org/10.1021/acs.jpcclett.5b02211>.
- (173) Torimoto, T.; Kameyama, T.; Kuwabata, S. Photofunctional Materials Fabricated with Chalcopyrite-Type Semiconductor Nanoparticles Composed of AgInS₂ and Its Solid Solutions. *J. Phys. Chem. Lett.* **2014**, *5* (2), 336–347. <https://doi.org/10.1021/jz402378x>.
- (174) Galiyeva, P.; Alem, H.; Rinnert, H.; Balan, L.; Blanchard, S.; Medjahdi, G.; Uralbekov, B.; Schneider, R. Highly Fluorescent, Color Tunable and Magnetic Quaternary Ag–In–Mn–Zn–S Quantum Dots. *Inorg. Chem. Front.* **2019**, *6* (6), 1422–1431. <https://doi.org/10.1039/C9QI00131J>.

- (175) Torimoto, T.; Kamiya, Y.; Kameyama, T.; Nishi, H.; Uematsu, T.; Kuwabata, S.; Shibayama, T. Controlling Shape Anisotropy of ZnS–AgInS₂ Solid Solution Nanoparticles for Improving Photocatalytic Activity. *ACS Appl. Mater. Interfaces* **2016**, *8* (40), 27151–27161. <https://doi.org/10.1021/acsami.6b10408>.
- (176) Bergren, M. R.; Makarov, N. S.; Ramasamy, K.; Jackson, A.; Guglielmetti, R.; McDaniel, H. High-Performance CuInS₂ Quantum Dot Laminated Glass Luminescent Solar Concentrators for Windows. *ACS Energy Lett.* **2018**, *3* (3), 520–525. <https://doi.org/10.1021/acseenergylett.7b01346>.
- (177) Wang, Z.; Zhang, X.; Xin, W.; Yao, D.; Liu, Y.; Zhang, L.; Liu, W.; Zhang, W.; Zheng, W.; Yang, B.; Zhang, H. Facile Synthesis of Cu–In–S/ZnS Core/Shell Quantum Dots in 1-Dodecanethiol for Efficient Light-Emitting Diodes with an External Quantum Efficiency of 7.8%. *Chem. Mater.* **2018**, *30* (24), 8939–8947. <https://doi.org/10.1021/acs.chemmater.8b04282>.
- (178) Shamirian, A.; Appelbe, O.; Zhang, Q.; Ganesh, B.; Kron, S. J.; Snee, P. T. A Toolkit for Bioimaging Using Near-Infrared AgInS₂/ZnS Quantum Dots. *J. Mater. Chem. B* **2015**, *3* (41), 8188–8196. <https://doi.org/10.1039/C5TB00247H>.
- (179) Perera, S. D.; Zhang, H.; Ding, X.; Nelson, A.; Robinson, R. D. Nanocluster Seed-Mediated Synthesis of CuInS₂ Quantum Dots, Nanodisks, Nanorods, and Doped Zn–CuInGaS₂ Quantum Dots. *J. Mater. Chem. C* **2015**, *3* (5), 1044–1055. <https://doi.org/10.1039/C4TC01887G>.
- (180) Song, W.-S.; Kim, J.-H.; Lee, J.-H.; Lee, H.-S.; Do, Y. R.; Yang, H. Synthesis of Color-Tunable Cu–In–Ga–S Solid Solution Quantum Dots with High Quantum Yields for Application to White Light-Emitting Diodes. *J. Mater. Chem.* **2012**, *22* (41), 21901. <https://doi.org/10.1039/c2jm35150a>.
- (181) Hu, Z. M.; Fei, G. T.; Zhang, L. D. Synthesis of Green-to-Red-Emitting Cu–Ga–S/ZnS Core/Shell Quantum Dots for Application in White Light-Emitting Diodes. *J. Lumin.* **2019**, *208*, 18–23. <https://doi.org/10.1016/j.jlumin.2018.12.023>.
- (182) Mei, S.; Zhang, G.; Yang, W.; Wei, X.; Zhang, W.; Zhu, J.; Guo, R. A Facile Route for Highly Efficient Color-Tunable Cu–Ga–Se/ZnSe Quantum Dots. *Appl. Surf. Sci.* **2018**, *456*, 876–881. <https://doi.org/10.1016/j.apsusc.2018.06.199>.
- (183) Kim, J.-H.; Kim, K.-H.; Yoon, S.-Y.; Kim, Y.; Lee, S.-H.; Kim, H.-S.; Yang, H. Tunable Emission of Bluish Zn–Cu–Ga–S Quantum Dots by Mn Doping and Their

- Electroluminescence. *ACS Appl. Mater. Interfaces* **2019**, *11* (8), 8250–8257. <https://doi.org/10.1021/acsami.8b20894>.
- (184) Jo, D.-Y.; Kim, D.; Kim, J.-H.; Chae, H.; Seo, H. J.; Do, Y. R.; Yang, H. Tunable White Fluorescent Copper Gallium Sulfide Quantum Dots Enabled by Mn Doping. *ACS Appl. Mater. Interfaces* **2016**, *8* (19), 12291–12297. <https://doi.org/10.1021/acsami.6b01763>.
- (185) Kim, J.-H.; Kim, B.-Y.; Jang, E.-P.; Yoon, S.-Y.; Kim, K.-H.; Do, Y. R.; Yang, H. Synthesis of Widely Emission-Tunable Ag–Ga–S and Its Quaternary Derivative Quantum Dots. *Chem. Eng. J.* **2018**, *347*, 791–797. <https://doi.org/10.1016/j.cej.2018.04.167>.
- (186) Zhang, W.-J.; Pan, C.-Y.; Cao, F.; Wang, H.; Yang, X. Bright Violet-to-Aqua-Emitting Cadmium-Free Ag-Doped Zn–Ga–S Quantum Dots with High Stability. *Chem. Commun.* **2018**, *54* (33), 4176–4179. <https://doi.org/10.1039/C8CC01293H>.
- (187) Kameyama, T.; Kishi, M.; Miyamae, C.; Sharma, D. K.; Hirata, S.; Yamamoto, T.; Uematsu, T.; Vacha, M.; Kuwabata, S.; Torimoto, T. Wavelength-Tunable Band-Edge Photoluminescence of Nonstoichiometric Ag–In–S Nanoparticles via Ga³⁺ Doping. *ACS Appl. Mater. Interfaces* **2018**, *10* (49), 42844–42855. <https://doi.org/10.1021/acsami.8b15222>.
- (188) Song, J.; Zhang, Y.; Dai, Y.; Hu, J.; Zhu, L.; Xu, X.; Yu, Y.; Li, H.; Yao, B.; Zhou, H. Polyelectrolyte-Mediated Nontoxic AgGa_xIn_{1-x}S₂ QDs/Low-Density Lipoprotein Nanoprobe for Selective 3D Fluorescence Imaging of Cancer Stem Cells. *ACS Appl. Mater. Interfaces* **2019**, *11* (10), 9884–9892. <https://doi.org/10.1021/acsami.9b00121>.
- (189) Fan, C.-M.; Regulacio, M. D.; Ye, C.; Lim, S. H.; Zheng, Y.; Xu, Q.-H.; Xu, A.-W.; Han, M.-Y. Colloidal Synthesis and Photocatalytic Properties of Orthorhombic AgGaS₂ Nanocrystals. *Chem. Commun.* **2014**, *50* (54), 7128. <https://doi.org/10.1039/c4cc01778a>.
- (190) Wei, S.; Liu, Y.; Ma, M.; Wu, Y.; Huang, L.; Pan, D. Thin-Shell CdSe/ZnCdS Core/Shell Quantum Dots and Their Electroluminescent Device Application. *J. Mater. Chem. C* **2018**, *6* (41), 11104–11110. <https://doi.org/10.1039/C8TC03906B>.
- (191) Shen, S.; Zhang, Y.; Peng, L.; Xu, B.; Du, Y.; Deng, M.; Xu, H.; Wang, Q. Generalized Synthesis of Metal Sulfide Nanocrystals from Single-Source Precursors: Size, Shape and Chemical Composition Control and Their Properties. *CrystEngComm* **2011**, *13* (14), 4572. <https://doi.org/10.1039/c0ce00982b>.

- (192) Bear, J. C.; Hollingsworth, N.; Roffey, A.; McNaughten, P. D.; Mayes, A. G.; Macdonald, T. J.; Nann, T.; Ng, W. H.; Kenyon, A. J.; Hogarth, G.; Parkin, I. P. Doping Group IIB Metal Ions into Quantum Dot Shells via the One-Pot Decomposition of Metal-Dithiocarbamates. *Adv. Opt. Mater.* **2015**, *3* (5), 704–712. <https://doi.org/10.1002/adom.201400570>.
- (193) Chen, D.; Zhao, F.; Qi, H.; Rutherford, M.; Peng, X. Bright and Stable Purple/Blue Emitting CdS/ZnS Core/Shell Nanocrystals Grown by Thermal Cycling Using a Single-Source Precursor. *Chem. Mater.* **2010**, *22* (4), 1437–1444. <https://doi.org/10.1021/cm902516f>.
- (194) Cai, J.; Wang, S.; Zhu, K.; Wu, Y.; Zhou, L.; Zhang, Y.; Wu, Q.; Wang, X.; Hu, Z. Synthesis of Alloyed $Zn_{1-x}Mn_xS$ Nanowires with Completely Controlled Compositions and Tunable Bandgaps. *RSC Adv.* **2018**, *8* (1), 374–379. <https://doi.org/10.1039/C7RA12714F>.
- (195) Wang, Y.; Wu, J.; Zheng, J.; Jiang, R.; Xu, R. Ni²⁺-Doped $Zn_xCd_{1-x}S$ Photocatalysts from Single-Source Precursors for Efficient Solar Hydrogen Production under Visible Light Irradiation. *Catal Sci Technol* **2012**, *2* (3), 581–588. <https://doi.org/10.1039/C2CY00310D>.
- (196) Wei, Y.; Yang, J.; Ying, J. Y. Reversible Phase Transfer of Quantum Dots and Metal Nanoparticles. *Chem. Commun.* **2010**, *46* (18), 3179. <https://doi.org/10.1039/b926194j>.
- (197) Pearson, R. G. Hard and Soft Acids and Bases, HSAB, Part 1: Fundamental Principles. *J. Chem. Educ.* **1968**, *45* (9), 581. <https://doi.org/10.1021/ed045p581>.
- (198) Liu, W. Low Temperature Synthesis of Hexagonal Phase ZnS Nanocrystals by Thermolysis of an Air-Stable Single-Source Molecular Precursor in Air. *Mater. Lett.* **2006**, *60* (4), 551–554. <https://doi.org/10.1016/j.matlet.2005.09.033>.
- (199) Costa, A. C.; Ondar, G. F.; Versiane, O.; Ramos, J. M.; Santos, T. G.; Martin, A. A.; Raniero, L.; Bussi, G. G. A.; Téllez Soto, C. A. DFT: B3LYP/6-311G (d, p) Vibrational Analysis of Bis-(Diethyldithiocarbamate)Zinc (II) and Natural Bond Orbitals. *Spectrochim. Acta. A. Mol. Biomol. Spectrosc.* **2013**, *105*, 251–258. <https://doi.org/10.1016/j.saa.2012.11.097>.
- (200) Vogel, R.; Hoyer, P.; Weller, H. Quantum-Sized PbS, CdS, Ag₂S, Sb₂S₃, and Bi₂S₃ Particles as Sensitizers for Various Nanoporous Wide-Bandgap Semiconductors. *J. Phys. Chem.* **1994**, *98* (12), 3183–3188. <https://doi.org/10.1021/j100063a022>.

- (201) Khanchandani, S.; Kundu, S.; Patra, A.; Ganguli, A. K. Band Gap Tuning of ZnO/In₂S₃ Core/Shell Nanorod Arrays for Enhanced Visible-Light-Driven Photocatalysis. *J. Phys. Chem. C* **2013**, *117* (11), 5558–5567. <https://doi.org/10.1021/jp310495j>.
- (202) Zhou, N.; Gan, L.; Yang, R.; Wang, F.; Li, L.; Chen, Y.; Li, D.; Zhai, T. Nonlayered Two-Dimensional Defective Semiconductor γ -Ga₂S₃ toward Broadband Photodetection. *ACS Nano* **2019**, *13* (6), 6297–6307. <https://doi.org/10.1021/acsnano.9b00276>.
- (203) Park, Y. I.; Kim, H. M.; Kim, J. H.; Moon, K. C.; Yoo, B.; Lee, K. T.; Lee, N.; Choi, Y.; Park, W.; Ling, D.; Na, K.; Moon, W. K.; Choi, S. H.; Park, H. S.; Yoon, S.-Y.; Suh, Y. D.; Lee, S. H.; Hyeon, T. Theranostic Probe Based on Lanthanide-Doped Nanoparticles for Simultaneous In Vivo Dual-Modal Imaging and Photodynamic Therapy. *Adv. Mater.* **2012**, *24* (42), 5755–5761. <https://doi.org/10.1002/adma.201202433>.
- (204) Jańczewski, D.; Zhang, Y.; Das, G. K.; Yi, D. K.; Padmanabhan, P.; Bhakoo, K. K.; Tan, T. T. Y.; Selvan, S. T. Bimodal Magnetic-Fluorescent Probes for Bioimaging. *Microsc. Res. Tech.* **2011**, *74* (7), 563–576. <https://doi.org/10.1002/jemt.20912>.
- (205) Li, K.; Ding, D.; Huo, D.; Pu, K.-Y.; Thao, N. N. P.; Hu, Y.; Li, Z.; Liu, B. Conjugated Polymer Based Nanoparticles as Dual-Modal Probes for Targeted In Vivo Fluorescence and Magnetic Resonance Imaging. *Adv. Funct. Mater.* **2012**, *22* (15), 3107–3115. <https://doi.org/10.1002/adfm.201102234>.
- (206) Zeng, S.; Tsang, M.-K.; Chan, C.-F.; Wong, K.-L.; Fei, B.; Hao, J. Dual-Modal Fluorescent/Magnetic Bioprobes Based on Small Sized Upconversion Nanoparticles of Amine-Functionalized BaGdF₅:Yb/Er. *Nanoscale* **2012**, *4* (16), 5118. <https://doi.org/10.1039/c2nr31294h>.
- (207) Jing, L.; Ding, K.; Kershaw, S. V.; Kempson, I. M.; Rogach, A. L.; Gao, M. Magnetically Engineered Semiconductor Quantum Dots as Multimodal Imaging Probes. *Adv. Mater.* **2014**, *26* (37), 6367–6386. <https://doi.org/10.1002/adma.201402296>.
- (208) Walia, S.; Acharya, A. Silica Micro/Nanospheres for Theranostics: From Bimodal MRI and Fluorescent Imaging Probes to Cancer Therapy. *Beilstein J. Nanotechnol.* **2015**, *6*, 546–558. <https://doi.org/10.3762/bjnano.6.57>.
- (209) Labiadh, H.; Ben Chaabane, T.; Sibille, R.; Balan, L.; Schneider, R. A Facile Method for the Preparation of Bifunctional Mn:ZnS/ZnS/Fe₃O₄ Magnetic and Fluorescent

- Nanocrystals. *Beilstein J. Nanotechnol.* **2015**, *6*, 1743–1751. <https://doi.org/10.3762/bjnano.6.178>.
- (210) Zhang, F.; Kong, X.-Q.; Li, Q.; Sun, T.-T.; Chai, C.; Shen, W.; Hong, Z.-Y.; He, X.-W.; Li, W.-Y.; Zhang, Y.-K. Facile Synthesis of CdTe@GdS Fluorescent-Magnetic Nanoparticles for Tumor-Targeted Dual-Modal Imaging. *Talanta* **2016**, *148*, 108–115. <https://doi.org/10.1016/j.talanta.2015.10.046>.
- (211) Chen, H.; Wang, Y.; Wang, T.; Shi, D.; Sun, Z.; Xia, C.; Wang, B. Application Prospective of Nanoprobes with MRI and FI Dual-Modality Imaging on Breast Cancer Stem Cells in Tumor. *J. Nanobiotechnology* **2016**, *14* (1), 52. <https://doi.org/10.1186/s12951-016-0195-8>.
- (212) Gedda, G.; Chen, G.-R.; Yao, Y.-Y.; Girma, W. M.; Li, J.-D.; Yen, C.-L.; Ling, Y.-C.; Chang, J.-Y. Aqueous Synthesis of Dual-Targeting Gd-Doped CuInS₂/ZnS Quantum Dots for Cancer-Specific Bi-Modal Imaging. *New J. Chem.* **2017**, *41* (23), 14161–14170. <https://doi.org/10.1039/C7NJ02252B>.
- (213) Würth, C.; Hoffmann, K.; Behnke, T.; Ohnesorge, M.; Resch-Genger, U. Polymer- and Glass-Based Fluorescence Standards for the Near Infrared (NIR) Spectral Region. *J. Fluoresc.* **2011**, *21* (3), 953–961. <https://doi.org/10.1007/s10895-010-0650-0>.
- (214) Xiao, Y.-D.; Paudel, R.; Liu, J.; Ma, C.; Zhang, Z.-S.; Zhou, S.-K. MRI Contrast Agents: Classification and Application (Review). *Int. J. Mol. Med.* **2016**, *38* (5), 1319–1326. <https://doi.org/10.3892/ijmm.2016.2744>.
- (215) Cheng, S.; Abramova, L.; Saab, G.; Turabelidze, G.; Patel, P.; Arduino, M.; Hess, T.; Kallen, A.; Jhung, M. Nephrogenic Fibrosing Dermopathy Associated with Exposure to Gadolinium-Containing Contrast Agents - St. Louis, Missouri, 2002-2006. *Morb. Mortal. Wkly. Rep.* **2007**, *56* (7), 137–141.
- (216) Kueny-Stotz, M.; Garofalo, A.; Felder-Flesch, D. Manganese-Enhanced MRI Contrast Agents: From Small Chelates to Nanosized Hybrids. *Eur. J. Inorg. Chem.* **2012**, *2012* (12), 1987–2005. <https://doi.org/10.1002/ejic.201101163>.
- (217) Botta, M.; Carniato, F.; Esteban-Gómez, D.; Platas-Iglesias, C.; Tei, L. Mn(II) Compounds as an Alternative to Gd-Based MRI Probes. *Future Med. Chem.* **2019**, *11* (12), 1461–1483. <https://doi.org/10.4155/fmc-2018-0608>.
- (218) Rohrer, M.; Bauer, H.; Mintorovitch, J.; Requardt, M.; Weinmann, H.-J. Comparison of Magnetic Properties of MRI Contrast Media Solutions at Different Magnetic Field

Strengths. *Invest. Radiol.* **2005**, *40* (11), 715–724.
<https://doi.org/10.1097/01.rli.0000184756.66360.d3>.

- (219) Baek, M. J.; Park, J. Y.; Xu, W.; Kattel, K.; Kim, H. G.; Lee, E. J.; Patel, A. K.; Lee, J. J.; Chang, Y.; Kim, T. J.; Bae, J. E.; Chae, K. S.; Lee, G. H. Water-Soluble MnO Nanocolloid for a Molecular T_1 MR Imaging: A Facile One-Pot Synthesis, In Vivo T_1 MR Images, and Account for Relaxivities. *ACS Appl. Mater. Interfaces* **2010**, *2* (10), 2949–2955. <https://doi.org/10.1021/am100641z>.

List of figures

Figure 1.1. Schematic illustration of a QD stabilized with 1-Dodecanethiol (DDT).....	15
Figure 1.2. Schematic illustrations of a) binary zinc blende ³ ; b) ternary chalcopyrite ³ and c) binary wurtzite ⁴ structures.....	18
Figure 1.3. Schematic illustrations of: a) smaller the diameter the particle the more portion of atoms on the surface of particle; b) decreasing diameter decreases melting temperature of gold particles ⁷	19
Figure 1.4. Type I and Type II band-edge alignments at the interface of core and shell semiconductors ¹¹	21
Figure 1.5. Figure of the bandgap energy dependence on particle size	22
Figure 1.6. Schematic illustration of the equipment for the hot-injection synthesis of QDs ...	27
Figure 1.7. Left: schematic of the relaxation dynamics in the investigated AgInS ₂ nanocrystals; Right: TEM images of the NCs: (b) AIS, 2.3±0.4 nm; (d) AIS/ZnS, 2.4±0.4 nm ³¹	28
Figure 1.8. Left: digital images of PL tunable AIZS and their Mn-doped NCs obtained under UV irradiation; Right: (d) and (e) are TEM and HR-TEM images of Mn-doped AIZS QDs, respectively, (f) is the XRD pattern of AIZS QDs ³⁴	30
Figure 1.9. Schematic illustration of aqueous phase transfer methods: A – ligand overcoating; B – ligand exchange ⁶²	37
Figure 1.10. Schematic diagram of PL mechanism for (ZnS) _{1-x} (AgInS ₂) _x NCs when a) x = 1; and b) x < 1 ⁷⁹	40
Figure 1.11. Schematic diagram of PL mechanisms: a) original hole transfer and appearance of defect levels in ternary NCs that emits trap-state emission; b) quenching of trap-state emission with Mn ²⁺ ⁴ T ₁ → ⁶ A ₁ transition in CIZS and AIZS QDs, while Zn content is sufficient; c) case in CIZS and AIZS QDs, while Zn content is insufficient for dopant emission to evolve ³⁴	41
Figure 1.12. Absorption and PL spectra of CIS, CIS/ZnS, CIS/ZnS:Mn, and CIS/ ZnS:Mn/ZnS nanocrystals ⁸⁴	42
Figure 1.13. a) Temperature-dependent PL spectra of Mn:CIZS QDs; b) Schematic diagram of PL mechanism for Mn:ZCIS nanocrystals ⁸⁵	43
Figure 1.14. Illustration of two possible pathways for electron-hole recombination in Mn doped AIZS/ZnS NCs (a) one is from the alloy or trap states (caused by Mn-AIZS alloying or Mn-induced defects in the Mn-doped layer) to the valence band, which contributes to the fast PL	

decay; and (b) the other one is Mn 4T_1 to 6A_1 from a few of Mn pairs or diluted Mn dopants out of the Mn-doped layer, which is responsible for the slow PL decay ³⁵	44
Figure 1.15. Photographs of the chloroform solution containing AIS particles under room (upper) and UV (lower) light irradiation (numbers show x value in $(Ag_xIn_{(1-x)}[S_2CN(C_2H_5)_2]_{(3-2x)})$) ⁸⁹	46
Figure 1.16. Absorption (A), PL (B) spectra and photographs of Zn-doped AIS QDs prepared at different temperatures ⁹⁵	48
Figure 1.17. Temperature variation of ZAIS $((AgIn)_xZn_{2(1-x)}(S_2CN(C_2H_5)_2)_4)$ QDs luminescent spectra ¹¹⁷	52
Figure 1.18. Confocal images of HepG2 cells stained with a solution of FA-conjugated $AgInS_2$ -ZnS QDs for 1 h as well as fixed with alcohol and subsequently stained with DAPI: a) under visible light; b) DAPI emission at 460 nm, showing the location of the HepG2 cell nuclei; c) red fluorescence originating from $AgInS_2$ -ZnS QDs; d) composite image. Scale bar represents 20 μm ⁹²	54
Figure 2.1. Schematic illustration of DDT-capped $(AgInS_2)_x(ZnS)_{1-x}$ (AIZS) QDs synthesis	58
Figure 2.2. Schematic illustration of aqueous phase transfer of hydrophobic ligand capped QDs by overcoating with PMAO	59
Figure 2.3. Schematic illustration of aqueous phase transfer by ligand exchange using L-Cysteine	60
Figure 2.4. XRD patterns of red-emitting AIZS and Mn:AIZS QDs when varying the Mn^{2+} loading	63
Figure 2.5. XRD patterns of green-emitting AIZS and Mn:AIZS QDs when varying the Mn^{2+} loading	64
Figure 2.6. Rietveld refinement result (red curve) of the powder XRD data of AIZS QDs (black curve) using the orthorhombic phase of $AgInS_2$. The blue curve corresponds to the difference between the experimental data and the simulation. Data were obtained considering the lattice parameters $a = 0.7008$ nm, $b = 0.8162$ nm and $c = 0.6585$ nm and an average size of 5 nm for the QDs	65
Figure 2.7. EDX analyses of orange-emitting AIZS and of Mn:AIZS QDs loaded with 25, 50 and 75% Mn^{2+} , respectively	67
Figure 2.8. EDX analyses of orange-emitting AIZS and of Mn:AIZS QDs loaded with 25, 50 and 75% Mn^{2+} , respectively	68

Figure 2.9. EPR spectra recorded at 20 K of orange-emitting AIZS QDs loaded with 25, 50 and 75% Mn ²⁺	69
Figure 2.10. TEM and HR-TEM images of (a) orange-emitting AIZS and (b-d) Mn:AIZS QDs loaded with 25, 50 and 75% Mn ²⁺ , respectively. The insets shows SAED patterns	70
Figure 2.11. Average sizes and standard deviations of (a) orange-emitting AIZS, (b) Mn (25%):AIZS, (c) Mn (50%):AIZS and (d) Mn (75%):AIZS QDs.....	70
Figure 2.12. TGA trace (a) and FT-IR spectrum (b) of Mn (50%):AIZS QDs.....	72
Figure 2.13. UV-visible absorption and normalized PL emission spectra of (a) green and (b) orange emitting QDs when increasing the Mn ²⁺ loading from 25 to 75% ($\lambda_{ex} = 400$ nm). The insets are digital photographs of the dots dispersed in chloroform under UV light illumination	74
Figure 2.14. PL excitation (dotted red lines) and PL emission (black lines) spectra of (a) AIZS and (b) Mn (25%):AIZS QDs in chloroform. Excitation spectra were monitored at the corresponding emission peak of each sample taken from Fig. 2.13	76
Figure 2.15. Determination of the optical bandgap of AIZS and Mn:AIZS QDs when increasing the loading in Mn ²⁺ ions in (a) green-emitting AIZS QDs and (b) orange-emitting AIZS QDs	77
Figure 2.16. Schematic illustration of the PL mechanism of (a) AIZS and (b-c) Mn:AIZS QDs. The solid arrows correspond to radiative relations while the dotted arrows show the non-radiative relaxations	78
Figure 2.17. PL lifetimes of orange-emitting AIZS and of the corresponding Mn:AIZS QDs at the PL maximum wavelength.....	79
Figure 2.18. (a) M(H) loop curves of Mn (25%):AIZS QDs at different temperatures and (b) the magnetic properties at zero field. (c) and (e) are the M(H) loop curves of AIZS and Mn:AIZS QDs at 10K and 300K, respectively. (d) and (f) describe the magnetic properties at zero field of 75% and 25% Mn-doped AIZS QDs, respectively.....	82
Figure 2.19. (a) UV-visible and PL emission spectra of AIZS and Mn:AIZS QDs after transfer in water using the PMAO polymer and (b) digital photograph taken under UV light illumination of Mn (25%):AIZS QDs before and after their transfer into water.....	84
Figure 2.20. UV-Vis (a) and PL (b) spectra of undoped AIZS QDs water transferred using PMAO at different pH, and the PL peak positions and the PL intensities changing (c) in media with different pH values	85

Figure 2.21. UV-visible and PL emission spectra of undoped AIZS QDs after transfer in water using different ligands	87
Figure 2.22. DLS and zeta-potential curves of AIZS QDs after transfer in water using different ligands	87
Figure 2.23. UV-Vis (a) and PL (b) spectra of undoped AIZS QDs water transferred using L-Cys recorded at different pH, (c) shows the PL peak position and PL intensity changing in media with different pH values	88
Figure 3.1. Schematic illustration of aqueous phase synthesis of magnetic metal doped GSH-capped quaternary Ag-In-Zn-Me-S QDs.....	92
Figure 3.2. Schematic illustration of cationization with PEI and HA-capping of GSH-capped AIZS QDs.....	93
Figure 3.3. XRD patterns of aqueous synthesized AIZS@GSH QDs when varying the metal-doping percentage: a) Mn-doped; b) Gd-doped; c) Fe-doped.....	96
Figure 3.4. TEM images, SAED patterns and size distributions of 5% Mn-doped (a) and 10% Mn-doped (b) AIZS@GSH QDs.....	97
Figure 3.5. TEM images, SAED patterns and size distributions of 5% Gd-doped (a) and 10% Gd-doped (b) AIZS@GSH QDs	97
Figure 3.6. TEM images, SAED patterns and size distributions of 5% Fe-doped (a) and 10% Fe-doped (b) AIZS@GSH QDs	97
Figure 3.7. TGA curves of AIZS@GSH QDs when varying the: a) Mn-doping, b) Gd-doping, and c) Fe-doping.....	98
Figure 3.8. EDX analyses of AIZS@GSH QDs when varying the: a) Mn-doping, b) Gd-doping, and c) Fe-doping.....	99
Figure 3.9. EPR spectra of Mn-doped AIZS@GSH QDs.....	101
Figure 3.10. UV-Vis absorption and PL emission spectra of 5% Mn-doped AIZS@GSH QDs during core, 1 st shell and 2 nd shell processing	103
Figure 3.11. Determination of the optical bandgap of AIZS QDs during nanoparticles growth	103
Figure 3.12. (a) UV-Vis absorption and PL emission spectra undoped and Mn-doped AIZS@GSH QDs and (b) photograph of aqueous dispersions of the dots under UV light irradiation	104
Figure 3.13. Determination of the optical bandgap of AIZS and Mn:AIZS QDs when increasing the loading in Mn ²⁺ ions.....	105

Figure 3.14. (a) UV-Vis absorption and PL emission spectra of undoped and Gd-doped AIZS@GSH QDs and (b) photograph of aqueous dispersions of the dots under UV light irradiation	106
Figure 3.15. (a) UV-Vis absorption and PL emission spectra of undoped and Gd-doped AIZS@GSH QDs and (b) photograph of aqueous dispersions of the dots under UV light irradiation	107
Figure 3.16. PL lifetimes of AIZS and Mn-, Gd-, Fe-doped AIZS QDs at PL maximum wavelength	109
Figure 3.17. M(H) loop curves of 5 % (a) and 10 % (b) Mn-doped AIZS QDs at different temperatures and the magnetic properties of 10% Mn-doped QDs at zero field at 10 K (c) and 300 K (d)	111
Figure 3.18. M(H) loop curves of 5 % and 10 % Gd-doped AIZS QDs at different temperatures (a and b, respectively) and the magnetic properties of 10% Gd-doped QDs at zero field at 10 K and 300 K (c and d, respectively).....	112
Figure 3.19. M(H) loop curves of AIZS QDs at different temperatures: a) 5 % and b) 10 % Fe-doped	113
Figure 3.20. Structures of (a) hyaluronic acid and (b) branched polyethylene imine.....	113
Figure 3.21. Structure of folic acid	114
Figure 3.22. Schema of PEI-FA conjugate preparation	114
Figure 3.23. FT-IR spectra of (a) hyaluronic acid sodium salt and 10% Gd-doped AIZS QDs capped with (b) GSH, (c) GSH-PEI and (d) GSH-PEI-HA	116
Figure 3.24. (a) DLS and (b) zeta-potential analyses of 10% Mn-doped AIZS QDs capped with glutathione, polyethylene imine and hyaluronic acid.....	117
Figure 3.25. (a) Colloidal and (b) photostability of aqueous phase synthesized 10% Mn-doped AIZS@GSH QDs	118
Figure 3.26. KB cells viability detected by the MTT assay after 24 h incubation in GSH and GSH@PEI-capped Mn-doped (a and b, respectively), Gd-doped (c and d, respectively), and Fe-doped (e and f, respectively) AIZS QDs at different concentrations	120
Figure 3.27. KB cells viability determined by MTT assay after 24 h incubation with GSH-PEI-FA-capped AIZS QDs (concentration of 1 mg/mL)	121
Figure 3.28. Confocal microscopic images of AIZS QDs: a) 10 % Mn, GSH; b) 10% Mn, GSH-PEI-FA; c) 10% Gd, GSH-PEI-FA; d) 10% Fe, GSH-PEI-FA.....	123

Figure 4.1. TGA traces of Zn(DDTC) ₂ , AIGZS precursors prepared with Ag/In/Ga/Zn ratios of 0.5/0.5/1/2, 1/0.5/0.5/1, 0.5/1/0.5/2 and 1.5/0.25/0.25/2 and the corresponding AIGZS QDs	131
Figure 4.2. XRD patterns of Zn(DDTC) ₂ and of the precursors prepared with Ag/In/Ga/Zn ratios of 0.25/0.875/0.875/2 and 0.5/1/0.5/2	132
Figure 4.3. FT-IR spectra of AIGZS precursors	133
Figure 4.4. FT-IR spectra of OAm-capped AIGZS QDs obtained after heating at 220°C	134
Figure 4.5. (a) XRD patterns of AIGZS QDs, (b) TEM image and (c) HR-TEM image of AIGZS QDs prepared with a Ag/In/Ga/Zn ratio of 1/0.5/0.5/2. The insets of (b) are the SAED pattern and the size distribution.....	135
Figure 4.6. TEM images of AIGZS QDs prepared with Ag/In/Ga/Zn ratios of (a) 0.25/0.875/0.875/2, (b) 0.5/1/0.5/2, (c) 0.5/0.5/1/2, (d) 0.66/0.66/0.66/2, (e) 1/0.5/0.5/1 and (f) 1/0.5/0.5/1 + 1 NaDDTC.....	136
Figure 4.7. EDX analysis of AIGZS QDs prepared with a Ag/In/Ga/Zn ratio of 1/0.5/0.5/2	137
Figure 4.8. XPS analysis of AIGZS QDs prepared with a Ag/In/Ga/Zn ratio of 0.5/1/0.5/2. (a) Survey scan and high resolution scans of (b) Ag 3d _{5/2} region, (c) In 3d _{5/2} region, (d) Ga 2p _{3/2} , (e) Zn 2p _{3/2} and (f) S 2p.....	138
Figure 4.9. UV-visible and normalized PL emission spectra of AIGZS QDs (a) when varying the heating temperature and (b) after a first heating at 220°C and after re-heating at the same temperature.....	140
Figure 4.10. (a) UV-visible and (b) normalized PL emission spectra of AIGZS QDs when varying the Ag/In/Ga/Zn ratio, (c) Time resolved decay profiles of AIGZS QDs recorded at the maximum emission wavelength and (d) digital photograph of the dots under UV light illumination	143
Figure 4.11. UV-visible absorption spectra of AIGZS precursors prepared with Ag/In/Ga/Zn ratios of 0.25/0.875/0.875/2 (a) and 0.66/0.66/0.66/2 (b) and of the corresponding QDs.....	145
Figure 4.12. Determination of the optical bandgap of AIGZS QDs when varying the Ag/In/Ga/Zn ratio.....	145
Figure 4.13. Structures of GTMA and Gly-DTC ligands used to transfer AIGZS QDs into aqueous solution.....	146
Figure 4.14. (a) Digital photograph taken under UV light illumination of dispersions of AIGZS QDs before and after the ligand exchange with GTMA. (b) UV-visible and normalized PL	

emission spectra of AIGZS QDs capped with OAm and after their transfer into water using GTMA and Gly-DDTC ligands.....	147
Figure 4.15. Hydrodynamic diameter AIGZS QDs capped with CysDTC and GTMA	147
Figure 5.1. UV-Vis and PL emission spectra of Mn-doped AgInGaZnS QDs at Ag/In/Ga/Zn=0.25/0.875/0.875/2 ratio: a) “precursor + MnSt ₂ ” method; b) “precursor containing Mn ²⁺ ions”	154
Figure 5.2. XRD patterns of Mn-doped AgInGaZnS QDs prepared using a Ag/In/Ga/Zn of 0.25/0.875/0.875/2.....	155
Figure 5.3. TEM images of Mn:AIGZS QDs at the Ag/In/Ga/Zn ratio of 0.25/0.875/0.875/2: a) 5%; b) 10% and HR-TEM images of 5% (c) and 10% Mn-doped QDs	156
Figure 5.4. XPS analysis of AIGZS QDs: (a) wide scan of Mn(5%):AIGZS QDs and high resolution scans of Ag 3d _{5/2} region (b), In 3d _{3/2} and 3d _{5/2} regions (c), Mn 2p _{3/2} region (d), Ga 2p _{3/2} region (e), Zn 2p _{3/2} region.....	158
Figure 5.5. EPR spectra recorded at 20 K of Mn:AIGZS QDs at Ag/In/Ga/Zn=0.25/0.875/0.875/2 ratio	159
Figure 5.6. a) UV-Vis and PL spectra of Mn-doped AgInGaZnS QDs at Ag/In/Ga/Zn=0.25/0.875/0.875/2 ratio; b) photographs of these QDs under UV light.....	161
Figure 5.7. Digital photographs of Mn-doped AgInGaZnS QDs at Ag/In/Ga/Zn=0.25/0.875/0.875/2 ratio under UV light.....	161
Figure 5.8. Determination of optical bandgaps of Mn-doped AgInGaZnS QDs at Ag/In/Ga/Zn=0.25/0.875/0.875/2 ratio	162
Figure 5.9. PL lifetimes of AIGZS and Mn-doped AIGZS QDs at PL maximum wavelength	164
Figure 5.10. M(H) loop curves of Mn-doped AIGZS QDs at different temperatures: a) 10 K; b) 310 K.....	165
Figure 5.11. M(H) loop curves of Mn-doped AIGZS QDs at different temperatures: a) 1%; b) 2.5%; c) 5%; d) 10%	166
Figure 5.12. M(H) loop curves of 10% Mn-doped AIGZS QDs at zero field: a) at 10 K; b) at 298 K.....	166
Figure 5.13. UV-Vis (a) and PL (b) spectra of 5% Mn-doped AIGZS QDs water transferred using PMAO recorded at different pH values, (c) shows the PL peak position and PL intensity changing in media with different pH values	167

Figure 5.14. UV-Vis (a) and PL (b) spectra of 5% Mn-doped AIGZS QDs water transferred using GTMA recorded at different pH values, (c) shows the PL peak position and PL intensity changing in media with different pH values 168

Figure 5.15. Longitudinal (R1) and transverse relaxation rates (R2) of Mn-doped AIGZS QDs as a function of Mn (II) concentrations in aqueous solution: a) at 1.4 T, 60 MHz (resonance frequency of ^1H) and 298 K, $r_1 = 0.19 \text{ mM}^{-1}\text{s}^{-1}$, $r_2 = 0.49 \text{ mM}^{-1}\text{s}^{-1}$; b) at 2.35 T, 100 MHz (resonance frequency of ^1H) and 298 K, $r_1 = 0.11 \text{ mM}^{-1}\text{s}^{-1}$, $r_2 = 0.42 \text{ mM}^{-1}\text{s}^{-1}$ 169

Figure 5.16. T1-weighted (a) and T2-weighted (b) MRI images of undoped, 1 % and 2.5 % Mn-doped AIGZS QDs 170

List of tables

Table 1.1. Evolution of QDs classes with examples	16
Table 2.1. Theoretical and actual Ag/In/Mn/Zn ratios determined by ICP-OES for orange-emitting AIZS QDs when varying the Mn ²⁺ loading QDs	66
Table 2.2 Atomic ratios in AIZS and Mn:AIZS QDs determined by EDX analyses	67
Table 2.3. Lifetimes and fitting parameters of orange-emitting AIZS and Mn:AIZS nanocrystals	80
Table 2.4. The structural and chemical formulas of the ligands used for the synthesis and ligand exchange	86
Table 3.1. EDX results of AIZS@GSH QDs when varying the metal-doping	100
Table 3.2. Theoretical and actual Ag/In/Zn/Me ratios determined by EDX for Me-doped AIZS QDs	100
Table 3.3. PL QYs of aqueous synthesized AIZS@GSH QDs doped with different metals.	105
Table 3.4. Lifetimes and fitting parameters of AIZS and Mn:AIZS, Gd:AIZS, Fe:AIZS QDs	108
Table 4.1. Theoretical and experimental composition of AIGZS QDs	137
Table 4.2. PL QYs, time constant τ_1 and τ_2 and the contributions of decays A ₁ and A ₂ of AIGZS QDs when varying the Ag/In/Ga/Zn ratio	144
Table 5.1. Ag/In/Ga/Zn ratio determined by XPS	157
Table 5.2. The optical bandgap values of Mn-doped AgInGaZnS QDs	162
Table 5.3. PL QYs, τ_1 and τ_2 time constants and the contributions of decays A ₁ and A ₂ of undoped and Mn-doped AIGZS QDs	164

Summary

Key words: quantum dots (QDs), I-II-III-VI QDs, one-pot synthesis, single precursor synthesis, magnetic nanoparticles, toxicity, fluorescent imaging, fluorescent/magnetic dual-modal probes.

Since fluorescence imaging (FI) and magnetic resonance imaging (MRI) are among the most effective diagnostic tools, QDs with fluorescent and magnetic properties are of great interest as dual-modal probes. In this work, undoped and doped Ag-In-Zn-S (AIZS) and Ag-In-Ga-Zn-S (AIGZS) QDs were synthesized and investigated as bimodal probes for FI and MRI. Highly fluorescent AIZS QDs were prepared in organic media using DDT and OAm as capping ligands. Mn:AIZS QDs showed paramagnetic and superparamagnetic properties. AIZS and Mn:AIZS QDs were also transferred into aqueous phase using the amphiphilic PMAO polymer. Further, Mn, Gd or Fe-doped AIZS QDs were prepared in aqueous media, showed low cytotoxicity toward KB cells, and demonstrated potential as fluorescent probes for FI. Finally, AIGZS and Mn:AIGZS QDs, synthesized via a novel single precursor thermal decomposition method, showed high fluorescence and paramagnetic/superparamagnetic properties. Mn-doped aqueous transferred AIGZS QDs increased contrast in both T1-weighted and T2-weighted images with increasing in Mn loading.

Résumé

Mots clés: quantum dots (QDs), I-II-III-VI QDs, synthèse one-pot, synthèse mono-précurseur, nanoparticules magnétiques, toxicité, imagerie de fluorescence, sondes pour l'imagerie bimodale.

L'imagerie par fluorescence (IF) et l'imagerie de résonance magnétique (IRM) comptent parmi les outils de diagnostic les plus efficaces. Dans ce contexte, des QDs possédant à la fois des propriétés fluorescentes et magnétiques sont d'un grand intérêt en tant que sondes bimodales. Dans ce travail, des QDs Ag-In-Zn-S (AIZS) et Ag-In-Ga-Zn-S (AIGZS) ont été préparés et dopés afin de développer de nouvelles sondes de sondes bimodales pour l'IF et l'IRM. Des QDs AIZS très fluorescents ont été préparés en milieu organique à l'aide de DDT et d'OAm comme ligands. Les QDs Mn:AIZS possèdent des propriétés paramagnétiques et superparamagnétiques. Les QDs AIZS et Mn:AIZS ont également été transférés en phase aqueuse à l'aide du polymère amphiphile PMAO. Par la suite, des QDs AIZS dopés Mn, Gd ou

Fe ont été préparés en milieu. Des études toxicologiques et d'imagerie ont montré une bonne biocompatibilité avec les cellules KB ainsi que le fort potentiel de ces nanocristaux pour l'IF. Dans la dernière partie de ce travail, des QDs AIGZS and Mn:AIGZS QDs ont été préparés via un procédé de décomposition thermique n'utilisant qu'un seul précurseur. Ces QDs possèdent de très bonnes propriétés optiques et magnétiques. Les QDs dopés Mn ont été transférés en phase aqueuse et ont montré un fort potentiel comme agent de contraste pour l'imagerie T1 et T2.